UNIVERSITY OF CALIFORNIA, SAN DIEGO

Molecular Modeling of Atmospheric Aerosols: from Clusters to Langmuir Monolayers

A dissertation submitted in partial satisfaction of the requirements for the degree of

Doctor of Philosophy

in

Chemistry

by

Wei Lin

Committee in charge:

Professor Francesco Paesani, Chair
Professor Henry D. I. Abarbanel
Professor Judy E. Kim
Professor Andrew C. Kummel
Professor Katja Lindenberg
Professor Tadeusz F. Molinski

2014

The dissertation of Wei Lin is approved, and it is acceptable in quality and form for publication on microfilm and electronically:

_____

_____

_____

_____

_____

_____

Chair

University of California, San Diego

2014

Table of Contents

Signature iii
Table of Contents iv
List of Figures vii
List of Tables xi
Acknowledgements xiii
Vita xvi
Abstract of the Dissertation xviii

Chapter 1: Atmospheric aerosols formed from nucleation of gas-phase species and sea spray 1
1.1. Aerosols formed through nucleation of gas-phase species 1
1.2. Aerosols formed from sea spray 5
1.3. References 7

Chapter 2. Systematic study of structural and thermodynamic properties of $HCl(H_2O)_n$ clusters from semiempirical replica exchange simulation 12
2.1. Abstract 12
2.2. Introduction 13
2.3. Computational methodology 15
2.4. Results and discussion 17
2.4.1. Minimum energy structures 17
2.4.2. $HCl(H_2O)_4$ 20
2.4.3. $HCl(H_2O)_5$ 21
2.4.4. $HCl(H_2O)_6$ 23
2.4.5. $HCl(H_2O)_7$ 24
2.4.6. $HCl(H_2O)_8$ 26
2.4.7. $HCl(H_2O)_9$ 28
2.4.8. $HCl(H_2O)_{10}$ 29
2.5. Conclusions 30
2.6. Acknowledgments 31
2.7. References 48

Chapter 3. Infrared spectra of $HCl(H_2O)_n$ clusters from semiempirical Born-Oppenheimer molecular dynamics simulations 54
3.1. Abstract 54
3.2. Introduction 54
3.3. Methodology 57
3.3.1. Computational details 57
3.3.2. Infrared spectra calculation and frequency assignment 57
3.4. Results and discussion 59
3.4.1. Eigen-type complexes 60
3.4.2. Eigen-like-type complexes 62
3.4.3. Zundel- and $H_7O_3^+$-type complexes 64

3.4.4. Intermediate Zundel-Eigen-type complexes 66
3.4.5. IR spectra of $HCl(H_2O)_{10}$ and $HCl(H_2O)_{21}$ clusters 68
3.5. Conclusions 69
3.6. Acknowledgments 70
3.7. References 79

Chapter 4. Negative ion photoelectron spectroscopy reveals thermodynamic advantage of organic acids in facilitating formation of bisulfate ion clusters: atmospheric implications 82
4.1. Abstract 82
4.2. Introduction 83
4.3. Combination of experimental and computational results 85
4.4. Conclusions 92
4.5. Acknowledgments 93
4.6. References 98

Chapter 5. A refined MS-EVB model for proton transport in the aqueous environments 103
5.1. Abstract 103
5.2. Introduction 103
5.3. Computational methodology 107
5.3.1. The anharmonic aSPC/Fw water model 107
5.3.2. The anharmonic aMS-EVB3 model 109
5.4. Results and discussion 113
5.4.1. aSPC/Fw model 113
5.4.2. aMS-EVB3 119
5.5. Conclusions 122
5.6. Acknowledgments 124
5.7. References 136

Chapter 6. Fast and slow proton transfer in ice: the role of the quasi-liquid layer and hydrogen-bond network 140
6.1. Abstract 140
6.2. Introduction 140
6.3. Computational methodology 143
6.3.1. The anharmonic aSPC/Fw/ice model 143
6.3.2. The anharmonic aMS-EVB3/ice model 144
6.3.3. Ice I_h and amorphous ice configurations 145
6.3.4. Molecular dynamics simulations of protonated ice 146
6.4. Results 148
6.4.1. Proton mobility on ice surfaces 148
6.4.2. Proton mobility in bulk ice I_h 150
6.4.3. Fast and trapped protons in bulk ice I_h 151
6.5. Discussion 153
6.5.1. Fast proton transfer/transport in bulk ice I_h 153
6.5.2 Proton hopping relay vs. Bjerrum defect transfer 155

6.5.3 Proton transfer/transport and the role of the quasi-liquid layer... 156
6.6. Summary 158
6.7. Acknowledgments..... 159
6.8. References 173

Chapter 7. Effect of lipid size on the phase behavior and physical properties of Langmuir monolayers: implications in atmospheric chemistry 178
7.1. Abstract 178
7.2. Introduction 179
7.3. Computational methodology 181
7.4. Results and discussion..... 183
7.4.1. Surface pressure-are isotherms..... 183
7.4.2. Structural properties of PA monolayers..... 185
7.4.3. Electron density profiles..... 187
7.4.4. Structures of tail groups: Gauche defects..... 188
7.5. Conclusions 189
7.6. Acknowledgments..... 190
7.7. References 198

List of Figures

Figure 2.1. Global minimum-energy structures of $HCl(H_2O)_n$ clusters with n = 4 – 15 and n = 21 obtained at the PM3-MAIS level of theory. Cl, O and H atoms are shown in cyan, red and gray, respectively..... 33
Figure 2.2. Temperature dependence of the constant-volume configurational heat capacity (C_v/k_B) of $HCl(H_2O)_n$ clusters with n = 4 – 10..... 34
Figure 2.3. PM3-MAIS low-energy structures (top panel) and isomer populations (bottom panel) of the $HCl(H_2O)_4$ isomers. The relative energies (in kcal/mol) are reported in parenthesis. See main text for details on the notation. 34
Figure 2.4. Low-energy structures (top panel) and isomer populations (bottom panel) of the $HCl(H_2O)_5$ isomers. (a – h) are the structures obtained with PM3-MAIS, while (i, j) correspond to the optimized structures calculated at the B3LYP/6-311++g(d,p) level of theory. See main text for details on the notation..... 35
Figure 2.5. Selected low-energy structures of the $HCl(H_2O)_6$ isomers obtained at the PM3-MAIS level of theory. See main text for details on the notation..... 36
Figure 2.6. PM3-MAIS low-energy structures (top panel) and isomer populations (bottom panel) of the $HCl(H_2O)_7$ isomers. See main text for details on the notation..... 37
Figure 2.7. PM3-MAIS low-energy structures (top panel) and isomer populations (bottom panel) of the $HCl(H_2O)_8$ isomers. See main text for details on the notation..... 38
Figure 2.8. PM3-MAIS low-energy structures (top panel) and isomer populations (bottom panel) of the $HCl(H_2O)_9$ isomers. See main text for details on the notation..... 39
Figure 2.9. PM3-MAIS low-energy structures (top panel) and isomer populations (bottom panel) of the $HCl(H_2O)_{10}$ isomers. See main text for details on the notation..... 40

Figure 3.1. Infrared spectra of $HCl(H_2O)_n$ clusters containing Eigen-type structures. The H_3O^+ asymmetric and symmetric stretches are shown in red and green, respectively. The blue feature is assigned to the OH stretch of H_2O that is H-bonded to the chloride ion. The corresponding cluster structures are shown next to each IR spectrum..... 71
Figure 3.2. IR spectra of $HCl(H_2O)_n$ clusters with Eigen-like-type structures, $H_3O^+(H_2O)_2Cl^-$, in which one H_2O molecule of the Eigen ion is replaced by Cl^-. The H_3O^+ asymmetric stretches are shown in red, and the OH stretch of H_3O^+ H-bonded to the chloride ion is shown in green..... 72
Figure 3.3. IR spectra of $HCl(H_2O)_n$ clusters with Zundel (top two traces) and $H_7O_3^+$ (bottom two traces) type structures. The red feature indicates the shared proton oscillation. OH stretches of H_2O in $H_5O_2^+$ are shown in green..... 73
Figure 3.4. Left: $\delta = r_{O_aH^*} - r_{O_bH^*}$ calculated for the $H_7O_3^+$ moiety in the structure 9D1Z of the $HCl(H_2O)_9$ cluster along the MD trajectory. Right: three representative configurations of $H_7O_3^+$..... 74
Figure 3.5. IR spectra of the $HCl(H_2O)_n$ clusters with intermediate Zundel-Eigen-type structures. The red feature indicates the shared proton oscillation. The H_2O molecule in $H_5O_2^+$ (water "b" in Figure 3.6c) displays two different stretches..... 75
Figure 3.6. (a) Global minimum-energy structure of the $HCl(H_2O)_{21}$ cluster in which the $H_5O_2^+$ complex is shown in blue. The AADD-type (A indicates a H-bond acceptor and D

indicates a H-bond donor) water molecule is shown in black. (b) Global minimum-energy structure of the $HCl(H_2O)_{10}$ cluster..... 76
Figure 3.7. Normalized distributions of the quantity $\delta = r_{O_aH^*} - r_{O_bH^*}$ calculated for the $H_5O_2^+$ moiety in the $HCl(H_2O)_{10}$ and $HCl(H_2O)_{21}$ clusters. O_a and O_b indicate the oxygen atoms of the water molecules labeled as "a" and "b" in Figure 3.6c, respectively..... 77
Figure 3.8. Calculated IR spectra for the global minimum-energy structures of the $HCl(H_2O)_{10}$ and $HCl(H_2O)_{21}$ clusters. The red feature indicates the shared proton oscillation in $H_5O_2^+$. The OH stretches of the H_2O molecule "a" in Figure 3.6c are shown in green..... 78

Figure 4.1. The 20 K photoelectron spectra of $HSO_4^-(Sol)_{0-2}$ (Sol = SUA, H_2SO_4, and H_2O) at 157 nm (7.867 eV). The vibrational progression of the C band of HSO_4^- is indicated..... 95
Figure 4.2. The most stable structures and low-lying isomers that show good agreement with the experiments of $HSO_4^-(Sol)_{0-2}$ (Sol = H_2DC_2 (SUA), H_2SO_4 and H_2O) at the B3LYP/6-311++G(3df, 3pd) level. Selected bond lengths (Å), bond angles (^{o}) and relative energies (kcal/mol) are indicated..... 96

Figure 5.1. Geometries of protonated water dimer (Zundel ion), trimer, tetramers (Eigen ion and linear structure) and pentamers. The geometrical parameters indicated in the figure are listed in Table 5.4..... 125
Figure 5.2. Radial distribution functions for oxygen-oxygen (bottom), oxygen-hydrogen (middle panel), and hydrogen-hydrogen (top panel) atom pairs computed with the *a*SPC/Fw water model. The experimental data for the set (a) are from Ref.[44], for the set (b) are from Ref.[45], and for set (c) are from Ref. 46..... 126
Figure 5.3. PES curves for the proton shuttling in the Zundel ion with O---O distances of 2.2, 2.4, 2.6 and 2.8 Å. The proton shuttling coordinate, *q,* is defined as the difference in the distance of the central hydrogen from its position at the center. See the section 5.4.2 for the details..... 127
Figure 5.4. RDF curves of bulk water with an excess proton. a) Top left curve: RDF describing the spatial correlation between the oxygen atom of the pivot hydronium ion (O*) and the water oxygen atoms (O)..... 128
Figure 5.5. Mean-square displacement (MSD) of the excess proton center of the excess charge as a function of time. The data for the MS-EVB3 model are from Ref. 30..... 129
Figure 5.6. Comparison of the *a*MS-EVB3 (red) and MS-EVB3 (black) free energy profiles for the proton-transfer reaction calculated as a function of the difference between two largest MS-EVB amplitudes, $c_1^2 - c_2^2$. The MS-EVB3 results are from Ref. 30…..130

Figure 6.1. Snapshots from aMS-EVB3 simulations of an excess proton on the surface of ice I_h (a) and amorphous ice (b) at 265 K. The yellow circles identify the instantaneous location of the hydronium ion on both surfaces, while the dashed orange lines correspond to hydrogen bonds between the water molecules..... 160
Figure 6.2. Parallel and perpendicular components of the self-diffusion coefficient of the center of excess charge calculated from aMS-EVB3 simulations of ice I_h (cold colors) and amorphous ice (warm colors) surfaces..... 160

Figure 6.3. Distribution of proton hopping frequencies in bulk ice I_h calculated at 190 K by averaging over 500 aMS-EVB3 trajectories of 50 ps each..... 161
Figure 6.4. a) Schematic representation of proton hopping in ice I_h. b) Variation of the O-O distances along an aMS-EVB3 trajectory displaying fast proton-hopping events in ice I_h. O_c corresponds to the oxygen atom of the initial hydronium ion while O_a is the oxygen atom of the final hydronium ion that is formed after proton hopping..... 162
Figure 6.5. (a) Variation of O*-O_i distances along an aMS-EVB3 trajectory displaying a proton-trapping event. O* indicates the oxygen atom in the hydronium ion, and O_i corresponds to the oxygen atom of each of the four water molecules coordinated with the hydronium ion within the lattice..... 163
Figure 6.6. Schematic representation of the formation of a long-lived H/L complex (proton tramp) in ice I_h..... 163
Figure 6.7. Small protonated water clusters. All values for the indicated bonds and angles are listed in Table 7.5..... 164
Figure 6.8. Potential energy curves corresponding to proton shuttling in the Zundel ion ($H_5O_2^+$)calculated for different O_a---O_b distances (R_{OO} = 2.2, 2.4, 2.6, and 2.8 Å), where O_a and O_b are the oxygen atoms of the two water molecules. The proton shuttling coordinate is defined as $q = R_{OaH^*} - R_{ObH^*}$, where H* is the shared proton..... 165
Figure 6.9. 2-dimensional projections of ice-water coexistence structures extracted from aSPC/Fw/ice simulations. a) Initial configuration. b) Final configuration after a 10 ns long NPTsimulation at T = 265 K. c) Final configuration after a 10 ns long NPT simulation at T = 270 K..... 166
Figure 6.10. Ice (black solid lines) and liquid water (red dashed lines) oxygen-oxygen RDFs calculated from ice-water coexistence simulations at: a) T = 265K, b) T = 270K and c) T = 275K. Each RDF curve was obtained by averaging over each 1 ns interval of a 10 ns long simulation..... 167

Figure 7.1. Structures of (a) PA, (b) DPPA, (c) Lipid-A and (d) DPPA monolayers for molecualr dynamics simulations. In (d), the water molecules are in blue, the tail groups of DPPA are in green, the head groups of DPPA are in red and the Na^+ ions are in yellow 192
Figure 7.2. Surface pressure-area isotherms of monolayers at T = 300 K: (a) the PA monolayer with water subphase, (b) the DPPA monolayer with Na^+/water subphase, and (c) the Lipid-A monolayers with Na^+/water subphase..... 192
Figure 7.3. Snapshots of PA monolayers. (a) PA monolayers at untilted condensed phase with surface pressure at 34.6 mN/m and surface area per PA molecule at 19.25 $Å^2$. (b) PA monolayers at tilted condensed phase with surface pressure at 5.6 mN/m and surface area per PA molecule at 22.00 $Å^2$..... 193
Figure 7.4. (a) The radial distribution functions of C---C of carboxylic groups of PA monolayers. The 2D nuclear density of carbon in carboxylic groups of PA monolayer at (b) high surface pressure and (c) low surface pressure along the molecular dynamics trajectories..... 194
Figure 7.5. Tilted angle of acyl chains of (a) PA, (b) DPPA and (c) Lipid-A monolayers.......... 195

Figure 7.6. Electronic density profiles along z-axis of (a) PA, (b) DPPA and (c) Lipid-A monolayers. Carton demonstration of (d) tail and (e) head group dominations along the packing process..... 196
Figure 7.7. The *trans* probabilities of acyl chains of PA, DPPA and Lipid-A monolayers..... 197
Figure 7.8. The radial distribution functions of O---H distances of head groups of PA and DPPA monolayers. (a) Distance of hydrogen and carbonyl oxygen of carboxyl group of PA monolayers and (b) distance of hydrogen and phosphate oxygen of hydrogen phosphate group of DPPA monolayers..... 197

List of Tables

Table 2.1. Number of replicas (N), lowest (T_{low}) and highest (T_{high}) temperatures, and radius of the spherical cavity (r_o) used to prevent water evaporation in SE-BO-REMD simulations of $HCl(H_2O)_n$ clusters with n = 4 - 21..... 41
Table 2.2. Relative energies (in kcal/mol) of the first low-energy isomers of $HCl(H_2O)_5$ calculated with PM3-MAIS and B3LYP/6-311++g(d,p) [with (E_{ZPE}) and without zero-point energy corrections (E_0)]..... 42
Table 2.3. Relative energies (in kcal/mol) of the first low-energy isomers of $HCl(H_2O)_6$ calculated with PM3-MAIS and B3LYP/6-311++g(d,p) [with (E_{ZPE}) and without zero-point energy corrections (E_0)]..... 43
Table 2.4. Relative energies (in kcal/mol) of the first low-energy isomers of $HCl(H_2O)_7$ calculated with PM3-MAIS and B3LYP/6-311++g(d,p) [with (E_{ZPE}) and without zero-point energy corrections (E_0)]..... 44
Table 2.5. Relative energies (in kcal/mol) of the first low-energy isomers of $HCl(H_2O)_8$ calculated with PM3-MAIS and B3LYP/6-311++g(d,p) [with (E_{ZPE}) and without zero-point energy corrections (E_0)]..... 45
Table 2.6. Relative energies (in kcal/mol) of the first low-energy isomers of $HCl(H_2O)_9$ calculated with PM3-MAIS and B3LYP/6-311++g(d,p) [with (E_{ZPE}) and without zero-point energy corrections (E_0)]..... 46
Table 2.7. Relative energies (in kcal/mol) of the first low-energy isomers of $HCl(H_2O)_{10}$ calculated with PM3-MAIS and B3LYP/6-311++g(d,p) [with (E_{ZPE}) and without zero-point energy corrections (E_0)]..... 47

Table 4.1. The experimentally measured and theoretically calculated adiabatic (ADE) and vertical detachment energy (VDE) for $HSO_4^-(Sol)_n$ (Sol = SUA, H_2O and H_2SO_4) (n = 0-2) (in eV)..... 97

Table 5.1. Parameters for the *a*SPC/Fw model..... 131
Table 5.2. Parameters for the *a*MS-EVB3 model..... 132
Table 5.3. Comparison between the water properties calculated with the *a*SPC/Fw model and the corresponding experimental data. Also shown are the results obtained in Ref. 11 with the SPC/Fw model. All properties are described in the text..... 133
Table 5.4. Geometries of protonated water clusters..... 134
Table 5.5. Comparison of binding energies of protonated water clusters..... 135

Table 6.1. Parallel $\left(D_{CEC}^{\parallel}\right)$ and perpendicular $\left(D_{CEC}^{\perp}\right)$ components of the center of excess charge self-diffusion coefficient (eqs 6.2 and 6.3), and average proton hopping frequency (PHF) calculated from aMS-EVB3 simulations of an excess proton on ice I_h and amorphous ice surfaces..... 168

Table 6.2. Isotropic $\left(D_{CEC}\right)$ center of excess charge self-diffusion coefficient and average proton hopping frequency (PHF) calculated from aMS-EVB3 simulations of an excess proton in bulk ice I_h..... 168
Table 6.3. Parameters for the *a*SPC/Fw model for ice..... 169
Table 6.4. Parameters for the *a*MS-EVB3 model for ice..... 170
Table 6.5. Geometries of protonated water clusters with bonds in Å and angles in degree……171
Table 6.6. Binding energies for small protonated water clusters 172

Table 7.1. Structure information of PA monolayers..... 198

Acknowledgements

I would like to thank Professor Francesco Paesani for his continuous support and guidance in my graduate studies. He has set an example of excellence as a researcher, instructor and role model. The Paesani group is a continually evolving group of brilliant minds which I have had the great pleasure of being a part of during my graduate studies. I thank Dr. Andy Gotez for his guidance in the implementation of PM3-MAIS into Amber. I also thank Dr. Kyoyeon Park for her collaboration and valuable discussions in my initial graduate studies. I would like to thank Dr. Volodymyr Babin for providing and tutoring the REPIMD code. I thank Drs. Anthony J. Clark and Chungwen Liang for their valuable discussions on Langmuir monolayer projects. I also must thank Dr. Jordi Cirera-Fernandez and Greg Medders for their great ideas, conversations and friendship.

I also must thank Professor Katja Lindenberg for her altruistic support and understanding during my entire graduate studies.

Most importantly I appreciate my wife, Yang Yang, who has suffered what I suffered and joyed what I enjoyed, and with my sons, Dan-Yi and Ming-Yi, who have given me great joy, love and comfort of my life. Special thanks should also be given to my parents and parents-in-law.

Chapter 2 contains materials from "Systematic Study of Structural and Thermodynamic Properties of $HCl(H_2O)_n$ Clusters from Semiempirical Replica Exchange Simulations" published in 2013 in *Journal of Physical Chemistry A. (Volume* 117, pages 7131 to 7141), authored by Wei Lin and Francesco Paesani. All material has been reproduced with the consent of all other authors.

Chapter 3 contains materials from "Infrared Spectra of $HCl(H_2O)_n$ Clusters: A Born-Oppenheimer Molecular Dynamics Simulations" currently being prepared for submission for publication authored by Wei Lin and Francesco Paesani. All material has been reproduced with the consent of all other authors.

Chapter 4 contains materials from "Negative Ion Photoelectron Spectroscopy Reveals Thermodynamic Advantage of Organic Acids in Facilitating Formation of Bisulfate Ion Clusters: Atmospheric Implications" published in 2013 in *Journal of Physical Chemistry Letters (Volume* 4, pages 779 to 785), authored by Gao-Lei Hou, Wei Lin, Shi-Hu Deng, Jian Zhang, Wei-Jun Zheng, Francesco Paesani, Xue-Bin Wang. All material has been reproduced with the consent of all other authors.

Chapter 5 contains materials from "A Refined MS-EVB Model for Proton Transport in Aqueous Environments" published in 2012 in *Journal of Physical Chemistry B. (Volume* 116, pages 343 to 352), authored by Kyoyeon Park, Wei Lin and Francesco Paesani. All material has been reproduced with the consent of all other authors.

Chapter 6 contains materials from "Fast and Slow Proton Transfer in ice: the Role of the Quasi-liquid Layer and Hydrogen-bond Network" published in 2014 in *Journal of Physical Chemistry B. (*DOI: 10.1021/jp501116d), authored by Kyoyeon Park, Wei Lin and Francesco Paesani. All material has been reproduced with the consent of all other authors.

Chapter 7 includes materials from "Effect of Lipid Complexity and Surface Pressure on the Structural Properties of Langmuir Monolayers: Atmospheric Implications" currently being prepared for submission for publication authored by Wei Lin, Anthony J.

Clark and Francesco Paesani. All material has been reproduced with the consent of all other authors.

VITA

2003 Bachelor of Science, Chemistry, Fuzhou University

2006 Master of Engineering, Materials Physics and Chemistry, Fuzhou University

2009 Master of Science, Chemistry, California State University, Los Angeles

2014 Doctor of Philosophy, Chemistry, University of California, San Diego

PUBLICATIONS

W. Lin, F. Paesani* "Infrared Spectra of $HCl(H_2O)_n$ Clusters: A Born-Oppenheimer Molecular Dynamics Simulations" *To be submitted*

K. Park, **W. Lin**, F. Paesani* "Fast and Slow Proton Transfer in ice: the Role of the Quasi-liquid Layer and Hydrogen-bond Network" *J. Phys. Chem. B., (In press)*

W. Lin, F. Paesani* "Systematic Study of Structural and Thermodynamic Properties of $HCl(H_2O)_n$ Clusters from Semiempirical Replica Exchange Simulations" *J. Phys. Chem. A.*, 117, 7131 (2013)

G. Hou, **W. Lin**, S. Deng, J. Zhang, W. Zheng, F. Paesani, X. Wang* "Negative Ion Photoelectron Spectroscopy Reveals Thermodynamic Advantage of Organic Acids in Facilitating Formation of Bisulfate Ion Clusters: Atmospheric Implications" *J. Phys. Chem. Lett*., 4, 779 (2013)

K. Park†, **W. Lin**†, F. Paesani* "A Refined MS-EVB Model for Proton Transport in Aqueous Environments" *J. Phys. Chem. B.*,116, 443 (2012) (Co-first author)

H. Jin, **W. Lin**, Y. Zhang, J. Zhu, Y. Li, Y. F. Zhang*, K. Ding, X. Huang, W. Chen, " Effects of Ti doping at the Reduced SnO_2(110) Surface with Different Oxygen Vacancies: A First Principles Study" *Theor. Chem. Acc.*, 131(6), 1231 (2012)

Y. Mao, **W. Lin**, Y. Ba* "Antifreeze Protein NMR Sensor to Detect Water Molecular Reorientation in the Surface of Ice" *J. Chem. Phys*., 131, 101102 (2009)

Y. F. Zhang*, **W. Lin**, Q. Wang, Y. Li, J. Li, "Theoretical Study on the Structural and Electronic Properties of the Reduced SnO_2(110) Surface" *Chinese J. Struct. Chem.*, 26(5), 606 (2007)

W. Lin, Y. F. Zhang*, Y. Li, K. Ding, J. Li, Y. Xu "Structural Characterizations and Electronic Properties of Ti-doped SnO_2(110) Surface: A First Principles Study" *J. Chem. Phys.* 124, 054704 (2006)

W. Lin, Y. F. Zhang*, Y. Li, Y. Chen, J. Li, "First Principles Studies on the Geometry and Electronic Structures of the SnO_2(110) Surface" *Acta Phys.-Chim. Sin.*, 22 (1), 76 (2006)

Y. F. Zhang*, **W. Lin**, Y. Li, K. Ding, J. Li, "A Theoretical Study on the Electronic Structures of TiO_2: Effect of Hartree-Fock Exchange". *J. Phys. Chem. B* 109(41), 19270 (2005)

ABSTRACT OF THE DISSERTATION

Molecular Modeling of Atmospheric Aerosols: from Clusters to Langmuir Monolayers

by

Wei Lin

Doctor of Philosophy in Chemistry

University of California San Diego, 2014

Professor Francesco Paesani, Chair

Aerosols are tiny particles suspended in the atmosphere, which can directly be generated by biogenic and anthropogenic processes or be formed through nucleation of gas-phase species. Aerosols influence the chemical composition of the atmosphere, and have both direct and indirect effects on the Earth's radiative balance. These processes have major implications for climate, ecosystems, and public health. In this dissertation, we first discuss computational studies aimed at providing fundamental insights into the molecular mechanisms of aerosol nucleation through the characterization of structural, thermodynamic, and spectroscopic properties of important nucleation species, with a particular focus on $HCl(H_2O)_n$ and $HSO_4^-(HO_2C(CH_2)_2CO_2H)_n$ binary systems. We then

describe the development and application of molecular models for characterizing proton transfer and transport in water and ice. In particular, we use computer simulations with our improved multistate empirical valence bond models to characterize the mechanisms responsible for proton mobility in ice I_h as well as on the surface of both ice I_h and amorphous ice. Based on our simulation results, we thus develop a unified picture of proton transfer and transport in and on ice.

The last part of this dissertation focuses on the properties of sea spray particles, which represent one of the most important components of biogenic aerosols. Field measurements have demonstrated that sea-spray particles contain a large fraction of organic material, which correlates with the extent of biological activity at the surface microlayer of the ocean. In this context, we perform molecular dynamics simulations to characterize the properties of model sea-spray aerosol surfaces. Specifically, we study the phase behavior and structural properties of three Langmuir monolayers (palmitic acid, dipalmitoyl phosphatidic acid, and Lipid-A) at the air/water interface. Through a detailed analysis of the molecular dynamics trajectories, direct connections between order/disorder transitions of the Langmuir monolayers and water structure/dynamics are determined as a function of surface pressure and structural complexity of the monolayers. Our results provide key molecular-level insights into the physical behavior of organic material at aqueous interfaces which can help understand the reactivity and nucleation properties of sea-spray aerosols.

Chapter 1. Atmospheric aerosols formed from nucleation of gas-phase species and sea spray

1.1. Aerosols formed through nucleation of gas-phase species

Atmospheric aerosols have attracted considerable interest because of their impact on climate, atmospheric chemistry, air quality, ecosystems, and public health.[1-3] Despite much recent progress in characterizing aerosol properties, large uncertainties are still associated with estimates of aerosol contributions to the total radiative forcing of the atmosphere indicated by the latest report to the Intergovernmental Panel on Climate Change (Climate Change 2013: the Physical Science Basis).

Aerosols originate from different sources, being generated by both biogenic (e.g., dust storms, wave breaking) and anthropogenic (e.g., combustion) processes or formed through nucleation of gas-phase species.[1,2,4] New particle formation by nucleation has been observed in different atmospheric environments, including the lower stratosphere, the free troposphere, the continental boundary layer just above Earth's surface, and coastal environments.[1,2] As the new particles grow in size, they can participate in cloud condensation and influence the radiation balance of the atmosphere. Aerosol formation by nucleation involves two distinct steps: 1) Aggregation of a small cluster of gaseous molecules with water molecules until the "critical nucleus" size is reached, at which point the particle becomes stable; 2) Spontaneous growth of the particle after reaching the critical size.[1,2,4,5]

The most common nucleating species is sulfuric acid (H_2SO_4). H_2SO_4 has a low vapor pressure at atmospheric temperatures, which becomes even lower when mixed with water.[5] Ammonia, amines, organic acids, and hydrochloric acid have also been proposed as nucleating precursors.[4-6] In this regard, noncovalent interactions such as hydrogen bonding have been recognized as playing a key role in the formation of the initial clusters. As the clusters growth, proton transfers between an acid moiety (e.g., HCl or H_2SO_4) and a base moiety (e.g., NH_3) become possible because the resulting ion pair is stabilized by interactions with surrounding polar molecules (e.g., H_2O).[7] The formation of the ion pair significantly increases the nucleation rate by reducing the free energy of the system,[5,8] although the associated molecular mechanisms remain poorly understood.[5,9]

The first aim of this dissertation research is to provide fundamental insights into the molecular mechanisms of aerosol nucleation in the atmosphere through computational studies focusing on the characterization of important nucleation species. Specifically, the properties of the $HCl(H_2O)_n$, $HSO_4^-(H_2O)_n$, $HSO_4^-(H_2SO_4)_n$, and $HSO_4^-(HO_2C(CH_2)_2CO_2H)_n$ systems are studied in Chapters 2 - 4. The second aim of my dissertation is to develop accurate molecular models for characterizing proton transfer and transport in aqueous environments and in ice (both bulk and surface) under atmospheric conditions. Finally, the third aim of my dissertation is to characterize the properties of Langmuir monolayers at the air/water interface as proxies of sea-spray aerosol surfaces.

Chapter 2 presents a systematic study of the structural and thermodynamic properties of $HCl(H_2O)_n$ clusters with n = 4 - 10. Due to the presence of the dissociated

proton, different local structures are determined within each cluster, including Zundel, Eigen, Eigen-like, $H_7O_3^+$, and intermediate Zundel−Eigen configurations. As the cluster size increases, several groups of isomers are identified, whose relative stabilities vary as a function of temperature. Importantly, the heat capacity indicates that the melting behavior of these clusters is highly size dependent. In particular, melting has been observed in clusters with n = 7 ~ 10 in the temperature range between 100 ~ 160 K.

Chapter 3 reports on infrared spectra of $HCl(H_2O)_n$ clusters with n = 4 - 10, 21. The calculated IR spectra associated with the different isomers show that the charge redistribution within the clusters leads to large variations in the vibrational frequencies associated with the excess proton. Specifically, vibrational shifts of up to 1645 cm^{-1} are found in the IR spectra, which correspond to structural changes in the solvation of the excess proton. This is in excellent agreement with the experimental value of ~1600 cm^{-1} that has been measured in the IR spectra of analogous protonated water clusters with n = 2 – 11.[10] Unique spectroscopic signatures are identified for each excess proton-containing "core ion" structure and hydrogen-bonding topology. These unique signatures directly relate structural and dynamical properties that can guide the interpretation of the experimental measurements.

Chapter 4 describes the role of organic acids in enhancing the formation of new aerosol particles through the determination of structural and thermodynamic properties of clusters formed by HSO_4^- and succinic acid [$HO_2C(CH_2)_2CO_2H$] (SUA).[11] In this regard, we have collaborated with experimentalists at the Pacific Northwest National Laboratory to combine negative ion photoelectron spectroscopy and theoretical modeling for characterizing the properties of $HSO_4^-(SUA)_n$, $HSO_4^-(H_2O)_n$, and $HSO_4^-(H_2SO_4)_n$ with

with n = 0-2. The experimental results show that one SUA molecule can stabilize HSO_4^- by ~39 kcal/mol, which is approximately three times the stabilization obtained with one water molecule (~13 kcal/mol). Our molecular dynamics simulations and quantum chemical calculations reveal the most plausible structures of these clusters and attribute the stability of these clusters to the formation of strong hydrogen bonds. Our study provides direct evidence indicating that organic acid molecules can promote both the formation and growth of aerosols.

Chapter 5 presents the development of an anharmonic water force field (*a*SPC/Fw) model, in which the OH bond potential is described through a quartic approximation to a Morse potential. The new *a*SPC/Fw model provides an accurate description of water at ambient conditions and reproduces the available experimental data for several structural, thermodynamic, and dynamical properties. Based on the *a*SPC/Fw model, a revised multistate empirical valence bond (*a*MS-EVB3) model was developed for proton transport in aqueous solution. The new *a*MS-EVB3 model is able to accurately describe the solvation structure around an excess proton when applied to the study of proton solvation and transport in bulk water. Importantly, the *a*MS-EVB3 model also predicts a significantly larger proton diffusion coefficient than previous models, which largely improves the agreement with the available experimental data.[12]

Chapter 6 describes the development and application of an ab initio-based reactive force field, *a*MS-EVB3/ice, for proton transfer in ice. The *a*MS-EVB3/ice model builds upon the *a*SPC/Fw/ice water model, which was developed to correctly reproduce the melting/freezing behavior of ice. The *a*MS-EVB3/ice was used to analyze both structural and dynamical properties of protonated ice as a function of temperature. Our

simulation results indicate that the mobility of excess protons at ice surfaces is largely suppressed, with protons becoming essentially immobile at temperatures below 200 K. In contrast, fast proton transfer/transport can exist in bulk ice I_h at low temperature due to the presence of connected regions of the proton-disordered hydrogen bond network. The simulation results indicate that the mechanisms associated with proton transfer/transport in both bulk and interfacial regions of ice are largely dependent on the local hydrogen bond structure surrounding the charge defect. A molecular-level picture of the mechanisms responsible for proton transfer/transport in ice is then developed and used to interpret the available experimental data.[13-18]

1.2. Aerosols formed from sea spray

Marine aerosols constitute one of the most important natural aerosol systems and are known to play an important role in the regulation of the Earth's climate.[1] Marine aerosols comprise primary and secondary aerosol components. The primary aerosol components originate from the interaction of wind stress at the ocean surface that results in the mechanical production of sea-spray aerosol.[19] Sea salts and organic compounds are the main components of these aerosols.[20,21] The concentration of organic components in aerosols depends upon biological processes taking place in the ocean surface microlayer, resulting in particles with markedly different physical and chemical properties.[22,23] The chemical composition plays an important role in determining morphological, optical and chemical properties of the aerosols.[24-29] For instance, the organic component affects ability of aerosols to act as a cloud condensation nuclei and to scatter light.[30-32]

The organic composition of aerosols has been shown to be extremely variable.[33] Different chemical species, including alkanes,[34,35] alcohols,[36] polycyclic aromatic hydrocarbons (PAHs),[37] sterols,[38] free fatty acids (FFAs),[39-41] and carbohydrates,[42] have been detected on aerosol particles. Among these species, FFAs are commonly identified with palmitic acid (PA), a saturated 16 carbon chain. Recent studies have revealed that lipopolysaccharides can also be found within the ocean surface microlayer and in atmospheric aerosols.[43-46] The chemical composition is ultimately responsible for the physical and chemical properties of the aerosol. For example, the surface morphology of an aerosol is dependent upon the nature of the organic film, as soluble and insoluble surfactants form expanded and close-packed films, respectively.[47] Packing of the surface film affects uptake and evaporation of water, which can then alter other properties of the aerosol particles.[29]

Chapter 7 describes the results of molecule dynamics simulations performed to characterize the phase behavior and structural properties of Langmuir monolayers at the air/water interface. Specifically, the phase behaviors of three different monolayers, namely palmitic acid (PA), dipalmitoyl phosphatidic acid (DPPA) and Lipid-A, are investigated through molecular dynamics simulations with atomistic force fields. The complexity of both hydrophobic tail and hydrophilic head groups in these systems increases from PA to DPPA and Lipid-A. Our results show that at T=300 K a second-order phase transition appears as a kink in the PA isotherm as the monolayer transitions from the uniformly tilted condensed to the untilted condensed phase. A first-order phase transition instead appears in the Lipid-A isotherm as the corresponding monolayer undergoes a liquid-condensed to liquid-expanded phase transition in the experimental

data. The analysis of the lipid structures indicates that the conformation of the acyl chains is more disordered in the Lipid-A monolayer than in PA and DPPA monolayers, which is attributed to the presence of a larger number of gauche defects. It is also found that the tilt angles calculated for the acyl chains with respect to the normal to the interface become wider in all monolayers as the area per molecule increases (i.e., as the surface pressure decreases). Our simulations provide fundamental insights into the molecular structure and physical properties of Langmuir monolayers at air/water interfaces that can affect chemical processes on aerosol particles in the atmosphere.

1.3 References

(1) Finlayson-Pitts, B. J.; Pitts, J. N., Jr. *Chemistry of the upper and lower atmosphere: Theory, experiments and applications*; Academic Press, 2000.

(2) J. H. Seinfeld, S. N. P. *Atmospheric Chemistry and Physics - From Air Pollution to Climate Change*; John Wiley & Sons: New York, NY, 2006.

(3) Kulmala, M.; How particles nucleate and grow; *Science* **2003**, *302*, 1000-1001.

(4) Kulmala, M.; Kontkanen, J.; Junninen, H.; Lehtipalo, K.; Manninen, H. E.; Nieminen, T.; Petaja, T.; Sipila, M.; Schobesberger, S.; Rantala, P.; Franchin, A.; Jokinen, T.; Jarvinen, E.; Aijala, M.; Kangasluoma, J.; Hakala, J.; Aalto, P. P.; Paasonen, P.; Mikkila, J.; Vanhanen, J.; Aalto, J.; Hakola, H.; Makkonen, U.; Ruuskanen, T.; Mauldin, R. L.; Duplissy, J.; Vehkamaki, H.; Back, J.; Kortelainen, A.; Riipinen, I.; Kurten, T.; Johnston, M. V.; Smith, J. N.; Ehn, M.; Mentel, T. F.; Lehtinen, K. E. J.; Laaksonen, A.; Kerminen, V. M.; Worsnop, D. R.; Direct Observations of Atmospheric Aerosol Nucleation; *Science* **2013**, *339*, 943-946.

(5) Zhang, R. Y.; Khalizov, A.; Wang, L.; Hu, M.; Xu, W.; Nucleation and Growth of Nanoparticles in the Atmosphere; *Chem Rev* **2012**, *112*, 1957-2011.

(6) Wang, L.; Khalizov, A. F.; Zheng, J.; Xu, W.; Ma, Y.; Lal, V.; Zhang, R. Y.; Atmospheric nanoparticles formed from heterogeneous reactions of organics; *Nat Geosci* **2010**, *3*, 238-242.

(7) Leopold, K. R.; Hydrated Acid Clusters; *Annu Rev Phys Chem* **2011**, *62*, 327-349.

(8) Kathmann, S. M.; Schenter, G. K.; Garrett, B. C.; Chen, B.; Siepmann, J. I.; Thermodynamics and Kinetics of Nanoclusters Controlling Gas-to-Particle Nucleation; *J Phys Chem C* **2009**, *113*, 10354-10370.

(9) McNeill, V. F.; Loerting, T.; Geiger, F. M.; Trout, B. L.; Molina, M. J.; Hydrogen chloride-induced surface disordering on ice; *P Natl Acad Sci USA* **2006**, *103*, 9422-9427.

(10) Headrick, J. M.; Diken, E. G.; Walters, R. S.; Hammer, N. I.; Christie, R. A.; Cui, J.; Myshakin, E. M.; Duncan, M. A.; Johnson, M. A.; Jordan, K. D.; Spectral signatures of hydrated proton vibrations in water clusters; *Science* **2005**, *308*, 1765-1769.

(11) Zhang, R. Y.; Suh, I.; Zhao, J.; Zhang, D.; Fortner, E. C.; Tie, X. X.; Molina, L. T.; Molina, M. J.; Atmospheric new particle formation enhanced by organic acids; *Science* **2004**, *304*, 1487-1490.

(12) Roberts, N. K.; Northey, H. L.; Proton and Deuteron Mobility in Normal and Heavy-Water Solutions of Electrolytes; *J Chem Soc Farad T 1* **1974**, *70*, 253-262.

(13) Cowin, J. P.; Tsekouras, A. A.; Iedema, M. J.; Wu, K.; Ellison, G. B.; Immobility of protons in ice from 30 to 190 K; *Nature* **1999**, *398*, 405-407.

(14) Collier, W. B.; Ritzhaupt, G.; Devlin, J. P.; Spectroscopically Evaluated Rates and Energies for Proton-Transfer and Bjerrum Defect Migration in Cubic Ice; *J Phys Chem-Us* **1984**, *88*, 363-368.

(15) Uras-Aytemiz, N.; Joyce, C.; Devlin, J. P.; Protonic and Bjerrum defect activity near the surface of ice at T < 145 K; *J Chem Phys* **2001**, *115*, 9835-9842.

(16) Lee, C. W.; Lee, P. R.; Kang, H.; Protons at ice surfaces; *Angew Chem Int Edit* **2006**, *45*, 5529-5533.

(17) Lee, C. W.; Lee, P. R.; Kim, Y. K.; Kang, H.; Mechanistic study of proton transfer and H/D exchange in ice films at low temperatures (100-140 K); *J Chem Phys* **2007**, *127*.

(18) Moon, E. S.; Yoon, J.; Kang, H.; Energy barrier of proton transfer at ice surfaces; *J Chem Phys* **2010**, *133*.

(19) Ellison, G. B.; Tuck, A. F.; Vaida, V.; Atmospheric processing of organic aerosols; *J Geophys Res-Atmos* **1999**, *104*, 11633-11641.

(20) Jimenez, J. L.; Canagaratna, M. R.; Donahue, N. M.; Prevot, A. S. H.; Zhang, Q.; Kroll, J. H.; DeCarlo, P. F.; Allan, J. D.; Coe, H.; Ng, N. L.; Aiken, A. C.; Docherty, K. S.; Ulbrich, I. M.; Grieshop, A. P.; Robinson, A. L.; Duplissy, J.; Smith, J. D.; Wilson, K. R.; Lanz, V. A.; Hueglin, C.; Sun, Y. L.; Tian, J.; Laaksonen, A.; Raatikainen, T.; Rautiainen, J.; Vaattovaara, P.; Ehn, M.; Kulmala, M.; Tomlinson, J. M.; Collins, D. R.; Cubison, M. J.; Dunlea, E. J.; Huffman, J. A.; Onasch, T. B.; Alfarra, M. R.; Williams, P. I.; Bower, K.; Kondo, Y.; Schneider, J.; Drewnick, F.; Borrmann, S.; Weimer, S.; Demerjian, K.; Salcedo, D.; Cottrell, L.; Griffin, R.; Takami, A.; Miyoshi, T.; Hatakeyama, S.; Shimono, A.; Sun, J. Y.; Zhang, Y. M.; Dzepina, K.; Kimmel, J. R.; Sueper, D.; Jayne, J. T.; Herndon, S. C.; Trimborn, A. M.; Williams, L. R.; Wood, E. C.;

Middlebrook, A. M.; Kolb, C. E.; Baltensperger, U.; Worsnop, D. R.; Evolution of Organic Aerosols in the Atmosphere; *Science* **2009**, *326*, 1525-1529.

(21) Rinaldi, M.; Decesari, S.; Finessi, E.; Giulianelli, L.; Carbone, C.; Fuzzi, S.; O'Dowd, C. D.; Ceburnis, D.; Facchini, M. C.; Primary and Secondary Organic Marine Aerosol and Oceanic Biological Activity: Recent Results and New Perspectives for Future Studies; *Adv Meteorol* **2010**.

(22) O'Dowd, C. D.; Facchini, M. C.; Cavalli, F.; Ceburnis, D.; Mircea, M.; Decesari, S.; Fuzzi, S.; Yoon, Y. J.; Putaud, J. P.; Biogenically driven organic contribution to marine aerosol; *Nature* **2004**, *431*, 676-680.

(23) Wojciechowski, J. C.; Schumacher, M. V.; Pires, C. A. D.; Madruga, P. R. D.; Kilca, R. D.; Brun, E. J.; da Silva, C. R. S.; Vaccaro, S.; Neto, R. M. R.; Geostatistics Applied to the Study of Soil Physiochemical Characteristics in Seasonal Deciduous Forest Areas; *Cienc Florest* **2009**, *19*, 383-391.

(24) Laurain, A. M. C.; Reid, J. P.; Characterizing Internally Mixed Insoluble Organic Inclusions in Aqueous Aerosol Droplets and Their Influence on Light Absorption; *J Phys Chem A* **2009**, *113*, 7039-7047.

(25) Sierra-Hernandez, M. R.; Allen, H. C.; Incorporation and Exclusion of Long Chain Alkyl Halides in Fatty Acid Monolayers at the Air-Water Interface; *Langmuir* **2010**, *26*, 18806-18816.

(26) Quinn, P. K.; Kapustin, V. N.; Bates, T. S.; Covert, D. S.; Chemical and optical properties of marine boundary layer aerosol particles of the mid-Pacific in relation to sources and meteorological transport; *J Geophys Res-Atmos* **1996**, *101*, 6931-6951.

(27) Beaver, M. R.; Freedman, M. A.; Hasenkopf, C. A.; Tolbert, M. A.; Cooling Enhancement of Aerosol Particles Due to Surfactant Precipitation; *J Phys Chem A* **2010**, *114*, 7070-7076.

(28) Novakov, T.; Corrigan, C. E.; Penner, J. E.; Chuang, C. C.; Rosario, O.; Bracero, O. L. M.; Organic aerosols in the Caribbean trade winds: A natural source?; *J Geophys Res-Atmos* **1997**, *102*, 21307-21313.

(29) Garland, R. M.; Wise, M. E.; Beaver, M. R.; DeWitt, H. L.; Aiken, A. C.; Jimenez, J. L.; Tolbert, M. A.; Impact of palmitic acid coating on the water uptake and loss of ammonium sulfate particles; *Atmos Chem Phys* **2005**, *5*, 1951-1961.

(30) Abbatt, J. P. D.; Broekhuizen, K.; Kumal, P. P.; Cloud condensation nucleus activity of internally mixed ammonium sulfate/organic acid aerosol particles; *Atmos Environ* **2005**, *39*, 4767-4778.

(31) Fuzzi, S.; Andreae, M. O.; Huebert, B. J.; Kulmala, M.; Bond, T. C.; Boy, M.; Doherty, S. J.; Guenther, A.; Kanakidou, M.; Kawamura, K.; Kerminen, V. M.; Lohmann, U.; Russell, L. M.; Poschl, U.; Critical assessment of the current state of scientific knowledge, terminology, and research needs concerning the role of organic aerosols in the atmosphere, climate, and global change; *Atmos Chem Phys* **2006**, *6*, 2017-2038.

(32) Rudich, Y.; Laboratory perspectives on the chemical transformations of organic matter in atmospheric particles; *Chem Rev* **2003**, *103*, 5097-5124.

(33) Rogge, W. F.; Mazurek, M. A.; Hildemann, L. M.; Cass, G. R.; Simoneit, B. R. T.; Quantification of Urban Organic Aerosols at a Molecular-Level - Identification, Abundance and Seasonal-Variation; *Atmos Environ a-Gen* **1993**, *27*, 1309-1330.

(34) Simoneit, B. R. T.; Application of Molecular Marker Analysis to Reconcile Sources of Carbonaceous Particulates in Tropospheric Aerosols; *Sci Total Environ* **1984**, *36*, 61-72.

(35) Sicre, M. A.; Marty, J. C.; Saliot, A.; N-Alkanes, Fatty-Acid Esters, and Fatty-Acid Salts in Size Fractionated Aerosols Collected over the Mediterranean-Sea; *J Geophys Res-Atmos* **1990**, *95*, 3649-3657.

(36) Gogou, A. I.; Apostolaki, M.; Stephanou, E. G.; Determination of organic molecular markers in marine aerosols and sediments: one-step flash chromatography compound class fractionation and capillary gas chromatographic analysis; *J Chromatogr A* **1998**, *799*, 215-231.

(37) Gogou, A.; Stratigakis, N.; Kanakidou, M.; Stephanou, E. G.; Organic aerosols in Eastern Mediterranean: Components source reconciliation by using molecular markers and atmospheric back trajectories; *Org Geochem* **1996**, *25*, 79-96.

(38) Barbier, M.; Tusseau, D.; Marty, J. C.; Saliot, A.; Sterols in Aerosols, Surface Microlayer and Subsurface Water in the Northeastern Tropical Atlantic; *Oceanol Acta* **1981**, *4*, 77-84.

(39) Barger, W. R.; Garrett, W. D.; Surface Active Organic Material in Marine Atmosphere; *J Geophys Res* **1970**, *75*, 4561-&.

(40) Barger, W. R.; Garrett, W. D.; Surface-Active Organic Material in Air over Mediterranean and over Eastern Equatorial Pacific; *J Geophys Res-Oc Atm* **1976**, *81*, 3151-3157.

(41) Duce, R. A.; Mohnen, V. A.; Zimmerman, P. R.; Grosjean, D.; Cautreels, W.; Chatfield, R.; Jaenicke, R.; Ogren, J. A.; Pellizzari, E. D.; Wallace, G. T.; Organic Material in the Global Troposphere; *Rev Geophys* **1983**, *21*, 921-952.

(42) Crahan, K. K.; Hegg, D. A.; Covert, D. S.; Jonsson, H.; Reid, J. S.; Khelif, D.; Brooks, B. J.; Speciation of organic aerosols in the tropical mid-pacific and their relationship to light scattering; *J Atmos Sci* **2004**, *61*, 2544-2558.

(43) Lass, K.; Friedrichs, G.; Revealing structural properties of the marine nanolayer from vibrational sum frequency generation spectra; *J Geophys Res-Oceans* **2011**, *116*.

(44) Hawkins, L. N.; Russell, L.; Polysaccharides, Proteins, and Phytoplankton Fragments: Four Chemically Distinct Types of Marine Primary Organic Aerosol Classified by Single Particle Spectromicroscopy; *Adv Meteorol* **2010**.

(45) Russell, L. M.; Hawkins, L. N.; Frossard, A. A.; Quinn, P. K.; Bates, T. S.; Carbohydrate-like composition of submicron atmospheric particles and their production from ocean bubble bursting; *P Natl Acad Sci USA* **2010**, *107*, 6652-6657.

(46) Facchini, M. C.; Rinaldi, M.; Decesari, S.; Carbone, C.; Finessi, E.; Mircea, M.; Fuzzi, S.; Ceburnis, D.; Flanagan, R.; Nilsson, E. D.; de Leeuw, G.; Martino, M.; Woeltjen, J.; O'Dowd, C. D.; Primary submicron marine aerosol dominated by insoluble organic colloids and aggregates; *Geophys Res Lett* **2008**, *35*.

(47) Donaldson, D. J.; Vaida, V.; The influence of organic films at the air-aqueous boundary on atmospheric processes; *Chem Rev* **2006**, *106*, 1445-1461.

Chapter 2. Systematic study of structural and thermodynamic properties of $HCl(H_2O)_n$ clusters from semiempirical replica exchange simulations

2.1. Abstract

The structural and thermodynamic properties of $HCl(H_2O)_n$ clusters with n = 4 - 10 are studied using Born-Oppenheimer replica exchange molecular dynamics simulations with the PM3-MAIS semiempirical Hamiltonian. Independently of the cluster size, the simulations predict that HCl exists in the dissociated form in all low-energy isomers. Different local structures are identified within the clusters due to the presence of the dissociated proton, including Zundel, Eigen, Eigen-like, $H_7O_3^+$, and intermediate Zundel-Eigen configurations. As the cluster size increases, several groups of isomers are identified, whose relative stabilities vary as a function of temperature. A detailed analysis of the heat capacity indicates that the melting behavior of $HCl(H_2O)_n$ clusters is strongly size-dependent. In particular, melting is observed in clusters with n = 7 – 10 in the temperature range T = 100 – 150 K. By contrast, melting is not observed in clusters with n = 4 – 6. Minimum energy structures for $HCl(H_2O)_n$ clusters with n = 11 – 15 and n = 21 are also characterized.

2.2. Introduction

Water-containing complexes play an important role in the atmosphere mediating many physicochemical processes of relevance to climate and the environment.[1] It has been suggested that water clusters containing seed species act as key intermediates in new particle formation and nucleation.[2] Due to the importance of these physicochemical processes in the atmosphere, several theoretical and experimental studies have focused in recent years on the characterization of structural and thermodynamic properties, spectroscopic features, and reactivity of pure and doped water clusters.[3-9] In particular, because of its importance at the fundamental level and its repercussions in heterogeneous processes that take place on atmospheric particles, acid dissociation in water clusters has been the subject of intense research aimed at elucidating the molecular mechanisms associated with proton transfer events.[10]

In this regard, HCl-water clusters are used as prototypical systems to understand the molecular mechanisms determining acid dissociation in solution and, for this reason, have been the focus of numerous experimental[11-17] and theoretical studies.[18-34] Initial efforts were directed toward the determination of the minimum number of water molecules required to trigger the HCl dissociation.[10] Most theoretical studies show that (at least) four water molecules are necessary to form the so-called charge-separated solvent-shared ion pair.[19,26-28,33,34] However, infrared spectroscopy experiments carried out in low-temperature solid matrices and free-jet expansions have been unable to provide an unambiguous assignment of the dissociated forms of small $HCl(H_2O)_n$ clusters.[35-40] In a recent spectroscopic study carried out in helium droplets, a band at 2670 cm^{-1} was assigned to the dissociated $H_3O^+(H_2O)_3Cl^-$ ion pair.[41] This assignment is different from

that determined in a previous free-jet expansion study,[38] and it has recently been questioned.[42,43]

The low-energy minima structures of $HCl(H_2O)_n$ clusters with $n \leq 6$ have been explored using different electronic structure methods.[18-32] In the past decade, both Car-Parrinello (CPMD) and Born-Oppenheimer (BOMD) molecular dynamics simulations were carried for $HCl(H_2O)_n$ clusters with $n \leq 6$ and their deuterated analogs.[33,34,41,44-49] These ab initio molecular dynamics (AIMD) simulations show that the relative stability of different $HCl((H_2O)_6$ isomers is significantly affected by temperature.[47] CPMD simulations carried out for $DCl(D_2O)_n$ with n = 1 - 6 were also used to determine the relationships between energies, structures, and spectroscopic features.[33] An aggregation-induced chemical reaction mechanism was proposed based on the study of HCl dissociation in growing water clusters up to n = 4.[41,42] Nuclear quantum effects on the structural properties and HCl dissociation in $HCl(H_2O)_4$ were studied using path-integral molecular dynamics (PIMD) in combination with a semiempirical representation of the underlying molecular interactions.[45,46] It was found that both nuclear quantum effects and thermal fluctuations play a key role in determining the structural rearrangements of $HCl(H_2O)_4$.[37,38] The effects of nuclear quantization on the structural properties of the ionic $HCl(H_2O)_4$ cluster were also investigated using PI-CPMD simulations.[50] This study demonstrates that nuclear quantum effects significantly affect the structure of the contact ion pair isomer but appear to have only a marginal impact on the solvent-shared ion-pair isomer. Although much computational effort has been devoted to the investigation of $HCl(H_2O)_n$ clusters, previous studies have been limited to clusters with $n \leq 6$ water

molecules and very little is known about the relative stability of larger $HCl(H_2O)_n$ clusters as a function of temperature.

The present study reports on semiempirical Born-Oppenheimer replica exchange molecular dynamics (SE-BO-REMD) simulations that are used to determine the structural and thermodynamic properties of $HCl(H_2O)_n$ clusters with n = 4 – 10 in the temperature range 10 ~ 300 K as well as the global energy minimum structures of selected clusters with up to n = 21. The paper is organized as follows: In Section 2, the computational methodologies are described, while the results are discussed in Section 3. The conclusions are then given in Section 4.

2.3. Computational methodology

Since a detailed description of the REMD method can be found in Ref.[51] only a brief summary of the main concepts and numerical details specific to the present study are provided here. REMD is a method used to effectively sample high-dimensional rough energy landscapes. In current work, through running several independent and simultaneous simulations with different temperatures (replicas), conformations of system are sampled at each temperature and exchanged based on Metropolis criterion. In this way, configurations at low temperatures could be available to the simulations at high temperatures and vice versa, and thermodynamic properties can be precisely obtained as a function of temperature. All simulation results reported in Section 3 were obtained from SE-BO-REMD simulations using a variable number of temperature replicas, *N*, (Table 2.1). The temperature range was selected to guarantee a proper sampling of the phase space associated with each cluster size, while the number of replicas was chosen to

guarantee sufficient overlap between the energy distributions of adjacent replicas. The *N* temperatures were distributed between the lowest and highest values according to an appropriate exponential function.[51] To prevent evaporation, the clusters were confined inside a spherical volume through the application of a restraining harmonic potential, $V = \frac{1}{2}k\left(r - r_0\right)^2$. The temperature intervals along with the value of r_o used in the SE-BO-REMD simulations for each cluster are listed in Table 2.1.

In all simulations the molecular interactions were described by the PM3-MAIS semiempirical Hamiltonian.[52,53] PM3-MAIS was originally derived from the PM3 model through the optimization of the O-O, O-H, and H-H core-core interaction terms to describe hydrogen-bonded systems and proton transfer reactions.[52] Later, the PM3-MAIS parameterization was extended through the development of optimized H-Cl and O-Cl core-core interactions, which enabled the study of small HCl-containing water clusters.[53] Although PM3-MAIS method predicts a slight overestimation of HCl acidity in water environment, it has a huge improvement over PM3 and overall well agreement with ab initio calculations. Combined with its affordable computational cost, PM3-MAIS has attracted interest for applications to numerical simulations.[45,46,54,55]

For the purpose of the present study, the PM3-MAIS model was implemented in the AMBER 12 suite of codes,[56] which was then used in all SE-BO-REMD simulations. The equations of motion were propagated in the NVT ensemble according to the leapfrog algorithm with timestep Δt = 0.5 fs. The temperature was controlled using the Andersen thermostat with a random rescaling of the atom velocities every 100 steps.[57] Depending on the cluster size, after 1 - 2 ns of equilibration, the production runs were carried out for

additional 3 - 5 ns, which were then used to calculate the structural and thermodynamic properties of the clusters. Every 2000 steps exchanges between adjacent replicas were attempted, resulting in an acceptance rate of ~ 40%, independently of the cluster size. Clusters configurations sampled by each replica were stored every 2000 steps for subsequent structural and thermodynamic analysis. These configurations were first optimized at the PM3-MAIS level and the different low-energy minima were characterized according to their inherent topologies. These local-minimum structures were then reoptimized at the B3LYP/6-311++g(d,p) level of theory. The B3LYP calculations were performed using Gaussian 09.[58] To characterize the thermodynamic stability of each cluster, the constant volume heat capacity (C_V/k_B) was calculated from the fluctuations of the total energy[59]

$$\frac{C_V}{K_B} = \frac{1}{(K_B T)^2}\left(\langle E^2\rangle - \langle E\rangle^2\right) \quad (2.1)$$

where *E* is the total energy, *T* is the temperature, and the angular brackets indicate ensemble averages.

2.4. Results and discussion

2.4.1. Minimum energy structures

The lowest-energy structures of $HCl(H_2O)_n$ with n = 4 – 15, 21 calculated from SE- BO-REMD simulations with PM3-MAIS are shown in Figure 2.2.1. The simulations predict the dissociation of HCl independently of cluster size. The dissociated chloride ion (Cl^-) is predicted to form two, three, and four hydrogen bonds in clusters with n = 4, n = 5 – 8, and n = 9 – 21 H_2O molecules, respectively. Depending on the number of H_2O

molecules, the presence of the excess proton results in the appearance of Zundel-type structures (Z, $H_5O_2^+$) for n = 4, Eigen-type structures (E, $H_9O_4^+$) for n = 7 – 8, and n = 13 – 15, Eigen-like-type structures ($H_7O_3^+Cl^-$, with Cl^- replacing one of the H_2O molecules of the Eigen structure) for n = 5 – 6, and intermediate Zundel-Eigen-type structures (I) for n = 9 – 12, and 21. Zundel-, Eigen-, and intermediate Zundel-Eigen-type structures are defined in terms of a geometric criterion based on $\delta = r_{O_aH^*} - r_{O_bH^*}$, where $r_{O_aH^*}$ and $r_{O_bH^*}$ are the distances between the excess proton H^* and the two closest oxygen atoms O_a and O_b, respectively.[60] According to this definition, $|\delta|$ = 0.0 Å corresponds to the perfect Zundel structure, while $|\delta|$ = 0.35 Å corresponds to the perfect Eigen structure. It has recently been shown that $|\delta| \leq 0.05$ and $|\delta| \geq 0.2$ Å can be used to distinguish Zundel- and Eigen-type structures in protonated water clusters.[61] In the present analysis of $HCl(H_2O)_n$ clusters, $|\delta| \leq 0.05$ identifies Zundel-type structures, $|\delta| \geq 0.17$ Å corresponds to Eigen-type structures, while 0.05 Å < $|\delta|$ < 0.17 Å indicates intermediate Zundel-Eigen-type structures.

As shown in Figure 2.1, PM3-MAIS predicts a single five-member ring to be the most stable structure of $HCl(H_2O)_4$. Both $HCl(H_2O)_5$ and $HCl(H_2O)_6$ are characterized by two fused rings with all water molecules being single acceptor / single donor (AD). $HCl(H_2O)_7$ is the first cluster in which the H_2O molecules are not coplanar but arranged in a cubic-like geometry with C_{3v} symmetry. In this case, the H_2O molecules can be divided in two groups including double acceptor / single donor (AAD) and single acceptor / double donor (ADD) molecules. A similar structural arrangement was reported

for the $HF(H_2O)_7$ cluster.[62] Interestingly, the structure of the $HCl(H_2O)_7$ cluster can be considered as an extension of the charge-separated solvent-shared ion pair (SIP) species found in $HCl(H_2O)_4$ in which three H_2O molecules are "sandwiched" between Cl^- and the hydronium cation (H_3O^+).[34,41] In the case of $HCl(H_2O)_7$, six H_2O molecules are "sandwiched" between the two ionic moieties forming two solvation shells around H_3O^+. The minimum energy structure of $HCl(H_2O)_8$ is obtained by adding one H_2O molecule between the first and second solvation shells around Cl^- in the $HCl(H_2O)_7$ cluster, which leads to the formation of a distorted cuboid structure. The additional H_2O molecule is in the AD configuration while the other six H_2O molecules remain in the AAD and ADD configurations. A similar structural arrangement was reported for $(H_2O)_9$.[63] In $HCl(H_2O)_9$, the additional H_2O molecule acts as a bridge between one of the apexes of the $HCl(H_2O)_8$ cuboid and Cl^-. Clathrate-like structures are observed for all clusters with $n > 9$. In particular, for $n = 21$, Cl^- is embedded inside a water cage and forms four hydrogen bonds, three with double acceptor / double donor (AADD) H_2O molecules and one with a H_2O molecule that is part of the protonated complex.

For all clusters, the minimum energy structures obtained at the PM3-MAIS level display different local arrangements associated with the protonated complexes, including Zundel, Eigen, Eigen-like and intermediate Zundel-Eigen configurations. However, when these structures are reoptimized at the B3LYP/6-311++g(d,p) level, all clusters with $n \geq 5$ display only Eigen-type configurations. Similar differences were reported for $H^+(H_2O)_{22}$ from calculations carried out with SCC-DFTB and B3LYP.[64]

In the following, to distinguish between the different structural arrangements within each cluster, a notation is used in which each isomer is given a unique label

defined by two numbers and two letters. The first number indicates the number of H_2O molecules in the cluster and is followed by a letter that identifies the group to which the isomer belongs. The second number indicates the energy rank of the isomer within each group, while the last letter describes the type of protonated complex formed upon HCl dissociation, with Z, E or I, corresponding to Zundel, Eigen and Eigen-like, and intermediate Zundel-Eigen structures, respectively. Based on this notation, the minimum energy structure of $HCl(H_2O)_n$ is defined by the sequence nA1L, where L can be Z, E or I. For the $HCl(H_2O)_5$ cluster, an additional letter, B, is added at the beginning of the sequence, indicating that the optimized structure is obtained with B3LYP, but is not found in the corresponding PM3-MAIS calculations.

2.4.2. $HCl(H_2O)_4$

The low-energy structures of the $HCl(H_2O)_4$ cluster were previously studied with both PM3-MAIS[45,46] and ab initio methods.[19,20,24,26-32] At the PM3-MAIS level, the minimum-energy structure corresponds to the HCl-dissociated five-membered ring structure (4A1Z) shown in Figure 2.3. However, this isomer is not found at the B3LYP level, which instead predicts a five-membered ring containing a nearly undissociated HCl ($R_{HCl} \approx 1.4$ Å). The slight overestimation of HCl acidity by PM3-MAIS is believed to be the main reason for this difference.[45,46] As a consequence, the isomer 4B1E, corresponding to the charge-separated solvent-shared ion pair (SIP) $H_3O^+(H_2O)Cl^-$, is the second lowest-energy isomer at the PM3-MAIS level but the most stable structure at both the B3LYP and MP2 levels of theory.[27] The next isomer, 4C1I, can be described as a kite-like structure characterized by a four-membered ring with a dangling H_2O molecule. In

this case, the dissociated proton is found in an intermediated Zundel-Eigen-type configuration with $|\delta|$ = 0.12 Å. Reoptimization of 4C1I performed at the B3LYP level results in a closely related structure, with one OH of the dangling H_2O molecule forming a weak hydrogen bond with Cl^-. A compact contact ion pair $H_3O^+(H_2O)_3Cl^-$, labeled as 4D1E, is predicted to be the next isomer with both PM3-MAIS and higher-level electronic structure methods.

The relative stability of the four different groups of the $HCl(H_2O)_4$ isomers over the temperature range 10 K $\leq$ T $\leq$ 300 K is shown in Figure 2.3. At low temperatures (T < 70 K) only isomers of group 4A exist. The relative population of this group decreases gradually with increasing temperature, reaching 50% at ~160 K and 18% at ~300 K. At the same time, the population of the 4C group raises to almost 50% at 170 K and to 75% at 300 K due to the associated larger entropic contributions. The populations of 4B and 4D isomers are small at all temperatures (<3% and < 1%, respectively). Importantly, the present SE-BO-REMD simulations indicate that 4A isomers are also present at relatively high temperatures, which could not be found in conventional MD simulations carried out at 300 K.[45] The population crossover between groups 4A and 4C is reflected in the temperature dependence of the heat capacity (Figure 2.2), which remains approximately constant up to ~80 K before rising and reaching a shallow maximum at ~160 K.

2.4.3. $HCl(H_2O)_5$

Figure 2.4 shows the low-energy isomers of $HCl(H_2O)_5$ divided in six different groups according to their structural motif. For all isomers, PM3-MAIS predicts the dissociation of HCl. Previous studies of $HCl(H_2O)_5$ performed with high-level electronic

structure methods focused on the most stable structures of the groups 5A, 5B, and 5C, often reporting conflicting results.[24,27,31] Re et al. reported that 5B1E is the lowest-energy isomer at the B3LYP/D95(p,d) level of theory with 5A1E and 5C1E being respectively 0.4 kcal/mol and 1.4 kcal/mol higher in energy.[31] Cabaleiro-Lago et al. showed that 5A1E is the lowest-energy isomer followed by 5B1E and 5C1E at the MP2/TZVP level of theory with and without zero-point energy (ZPE) corrections.[24] The PM3-MAIS results display a trend similar to that predicted by MP2/TZVP. As shown in Figure 2.4, the isomers 5C1I and 5D1I correspond to intermediate Zundel-Eigen-type structures, while the isomers 5E1Z and 5F1Z can be described as Zundel-type structures. After reoptimization at the B3LYP level, the dangling water in the 5D1I, 5E1Z, and 5F1Z isomers forms a hydrogen bond with Cl^- (Figure 2.4i-j). It is worth noting that neither Zundel-type nor intermediate Zundel-Eigen-type structures are found at the B3LYP level. The optimized energies of the $HCl(H_2O)_5$ isomers calculated at both PM3-MAIS and B3LYP/6-311++g(d,p) levels of theory are listed in Table 2.

When PM3 Hamiltonian was developed, nuclear quantum effects were included implicitly since most reference functions were derived from experimental data. The choice of heats of formation as reference data implies that the parametrization must account for zero-point vibrational energies.[65] This certainly seems to be the case for PM3-MAIS, since it takes parameters of electronic terms from PM3 method. Therefore, we should expect that the electronic energies calculated from PM3-MAIS (partially) accounted zero-point energies for implicitly. It would be reasonable to find that electronic energies of PM3-MAIS have somehow better agreement with the corresponding B3LYP

ZPE energies. From isomers 5A1E to 5E1Z, the PM3-MAIS energies display the same trend as that obtained at the B3LYP level when ZPE corrections are taken into account.

The relative populations of the groups 5A, 5B, and 5C are shown in Figure 2.4 as a function of temperature up to T = 325 K. Group 5A provides the largest contribution, with the populations of all other groups being very small (~1%) at T < 250 K. Three structures of group 5A (a-c in Figure 2.4) effectively represent the entire population of the $HCl(H_2O)_5$ isomers at all temperatures. 5A1E is the only isomer that exists at low temperatures, while isomers 5A2E and 5A3E first appear at ~50 K and gradually increase in population as the temperature increases. Figure 2.4 indicates that no transitions between different groups of $HCl(H_2O)_5$ isomers occur as the temperature increases, which correlates with the absence of any peak in the temperature-dependent profile of the heat capacity (Figure 2.2).

2.4.4. $HCl(H_2O)_6$

As the cluster size increases, the number of low-energy isomers grows quickly. For $HCl(H_2O)_6$, ~100 distinct local minima within 3 kcal/mol of the global minimum exist at the PM3-MAIS level. The corresponding structures are assigned to nine groups (6A to 6I). The lowest-energy isomers of each group are shown in Figure 2.5 with their energies listed in Table 2.3. Within each group, the various isomers differ only in the positions of the free OH bonds. For example, the isomers in group 6A are all characterized by a double-ring structure with five free OH bonds that can rotate in and out of the plane. This results in $2^5 = 32$ possible structures. Reoptimization performed at the B3LYP/6-311++g(d,p) level of theory leads to a different global minimum-energy

structure that is related to 6E1I with the excess proton in an Eigen-type configuration. As reported in Table 2.3, the isomer 6B1E becomes the lowest-energy structure at the B3LYP level when ZPE correction are taken into account within the harmonic approximation. All Zundel-type and intermediate Zundel-Eigen-type isomers obtained with PM3-MAIS transform to Eigen-type structures after reoptimization at the B3LYP/6-311++g(d,p) level of theory.

The relative stability of the $HCl(H_2O)_6$ isomers as a function of temperature is similar to that obtained for the $HCl(H_2O)_5$ cluster, with isomers of group A being the only structures found over the entire temperature range examined in this study. Among them, 6A1E exists at all temperatures and is the only structure present at low temperatures, while 6A2E appears at T ~50 K and its population increases with the temperature, reaching ~10% for T > 100 K. All other 6A isomers contribute by less than 10%. Since only isomers belonging to group A are present at all temperatures, the heat capacity of $HCl(H_2O)_6$ shown in Figure 2.2 does not display any peak indicative of structural transitions.

2.4.5. $HCl(H_2O)_7$

The first fourteen low-energy isomers of $HCl(H_2O)_7$ are shown in Figure 2.6, while the corresponding energies calculated with PM3-MAIS and B3LYP (with and without ZPE corrections) are listed in Table 2.4. These isomers can be divided in seven different groups from 7A to 7G. As mentioned in Section 2.4.1, the global minimum-energy structure, 7A1E, corresponds to a cubic-like geometry with C_{3v} symmetry. The second lowest-energy structure (7A2E) is also a cubic-like geometry characterized by a

symmetric plane than includes the chloride ion, the hydronium oxygen, and two water molecules. The energy difference between isomers 7A1E and 7A2E calculated at the PM3-MAIS level is 1.3 kcal/mol, which becomes ~0.2 kcal/mol with B3LYP. The next low-energy isomer, 7B1I, display a structural arrangement similar to the global minimum-energy structure of the $H^+(H_2O)_8$ cluster.[66] Further optimization of 7B1I carried out at the B3LYP level leads to 7A2E (see Table 2.4).

The protonated water complexes found in the isomers of group 7C contain the $H_2O\cdots H_3O^+\cdots H_2O$ ($H_7O_3^+$) configuration. At the PM3-MAIS level, the isomers belonging to group 7C lie ~2 kcal/mol above the global minimum energy. This gap becomes ~4 kcal/mol and ~6.5 kcal/mol at the B3LYP level with and without ZPE corrections, respectively. The difference between the PM3-MAIS and B3LYP results can be attributed to the formation of the Eigen-type complex found in the B3LYP structures, which replaces the $H_7O_3^+$ complex obtained at the PM3-MAIS level.

The isomers of group 7D are characterized by two fused five-membered rings with the dissociated proton in an Eigen-type structure. By contrast, intermediate Zundel-Eigen-type complexes are found in the 7E isomers with $|\delta|$ between 0.06 and 0.1 Å. As the energy increases, cage-like structures are observed (groups 7F and 7G), which lie about 2 kcal/mol above the global minimum. For isomers belonging to groups 7D – 7G, the energy differences between PM3-MAIS and B3LYP with ZPE corrections are smaller than 0.8 kcal/mol.

The relative populations of the different groups associated with the $HCl(H_2O)_7$ cluster are shown in Figure 2.6. Below 70 K, only isomers of group 7A are observed, with their populations decreasing quickly to ~50% at ~100 K and becoming smaller than 2% at

~150 K. At the same time, groups 7B and 7E appear at T > 70 K. The populations of both groups 7C and 7D increase rapidly with temperature, with 7C reaching ~36% at 150 K and 7D rising up to ~53% at 270 K. Isomers of group 7E are observed with populations varying from 10% to 20% at T > 100 K. Very low populations (<3%) are instead found for groups 7F and 7G. These variations in the isomer populations are reflected in the calculated heat capacity that displays a pronounced peak at T ~110 K (Figure 2.2) before reaching a minimum at T ~150 K and increasing again at higher temperatures. The temperature dependence of the heat capacity clearly indicates that the peak observed at T ~110 K can be associated with the structural transition between group 7A and all other groups.

2.4.6. $HCl(H_2O)_8$

Figure 2.7 shows the first seventeen low-energy isomers of the $HCl(H_2O)_8$ cluster, divided into six groups (8A – 8F), while the corresponding energies calculated at both PM3-MAIS and B3LYP levels of theory are reported in Table 2.5. Seven isomers belong to group 8A in which the dissociated proton is found in Eigen-type configurations. These are cubic structures with two faces formed by five-membered rings and an additional water molecule acting as a bridge between two apexes of the cube. The various isomers of group 8A differ only in the positions of the bridging water and excess proton. A similar structural arrangement was also reported from simulations carried out at T ~100 K with a different semiempirical model (PM3-SSP2).[67] Interestingly, the $HCl(H_2O)_8$ isomers of group 8A display the same three-dimensional arrangement as the lowest-energy structure of the $(H_2O)_9$ cluster.[68]

The isomers of group 8B are characterized by basket-like structures, while those of group 8C can be described as cubic-like structures. The isomers of these two groups lie ~0.7 to ~1.0 kcal/mol above the global minimum energy (8A1E), respectively. Group 8D is characterized by "three-legs-chair"-like structures, while both 8E1E and 8F1Z can be described as fused-ring-type structures. The PM3-MAIS isomers of group 8C move to groups 8A or 8B after reoptimization at the B3LYP level. The most stable structure obtained with B3LYP corresponds to the isomer 8A4E with or without ZPE corrections. The differences between PM3-MAIS and B3LYP energies for isomers of groups 8D, 8E, and 8F are relatively large (> 2 kcal/mol). As seen above for smaller cluster sizes, the optimization carried out at the B3LYP level leads to structures in which the dissociated proton is always found in Eigen-type configurations. This structural arrangement is effectively responsible for the energy differences between PM3-MAIS and B3LYP isomers belonging to groups 8D, 8E, and 8F. Nevertheless, both PM3-MAIS and B3LYP predict the same five isomers (8A1E – 8A5E) to be the most stable structures of the $HCl(H_2O)_8$ cluster.

To characterize the isomer stability of $HCl(H_2O)_n$ clusters with $n \geq 8$, two independent criteria were used to classify the different isomers: 1) a criterion based on the potential energy (that was also used for smaller clusters with $n \leq 7$), and 2) a criterion based on the number of free OH (i.e., number of water OH that are not involved in any hydrogen bond). According to the second criterion, both groups 8A and 8B contain isomers with four free OH bonds, while isomers of groups 8C, 8D, and 8E have five free OH bonds, and isomers of group 8F contain six free OH. As shown in Figure 2.7, the combined population of groups 8A and 8B corresponds to the entire population of

isomers with 4 free OH groups over the entire temperature range. By contrast, the sum of populations of groups 8C, 8D, and 8E is appreciably smaller than the total population of isomers with five free OH, which implies that other (unidentified) isomers with five free OH exist at relatively higher energies.

Below 80 K, only isomers with four free OH have sizable populations. As the temperature increases, the population of isomers with five free OH also increases and reaches a maximum at ~150 K. A similar trend is observed for isomers with six free OH that contribute by ~60% and ~50% to the total cluster population at ~300 K and 350 K, respectively. The analysis of the heat capacity indicates the presence of a peak at ~110 K, which can be traced to the structural transition from isomers with four free OH to isomers with five free OH.

2.4.7. $HCl(H_2O)_9$

The first twelve lowest-energy structures of the $HCl(H_2O)_9$ cluster, divided into six groups, are shown in Figure 2.8. Half of these structures belong to the group 9A in which the dissociated proton forms Zundel-type or intermediate Zundel-Eigen-type complexes. Inspection of the structural arrangement of these isomers suggests that group 9A can effectively be considered as a natural extension of group 8A after addition of one H_2O molecule. Similarly, the chair-like isomers of group 9E are derived from those of the "three-legs-chair"-like group (8D), while the "basket"-like isomers of group 9F are derived from the corresponding group (8B) of $HCl(H_2O)_8$. The isomer 9D1I contains the $H_7O_3^+$ complex with two identical shared protons as the isomer 7C1Z.

The four lowest-energy isomers found at the PM3-MAIS level of theory belong to groups 9A, 9B, 9C, and 9D, respectively, and lie within ~0.3 kcal/mol of the global minimum energy (Table 2.6). As already observed for smaller $HCl(H_2O)_n$ clusters with n = 4 - 8, reoptimization of the PM3-MAIS structures carried out at the B3LYP level leads to the formation of Eigen-type complexes for all isomers. Interestingly, PM3-MAIS predicts the same global minimum energy structure (9A1Z) as B3LYP without ZPE corrections. After inclusion of ZPE corrections, the global minimum energy structure at the B3LYP level becomes 9C1E, which, however, lies only 0.03 kcal/mol below 9A1Z.

The isomers of groups 9A, 9D, and 9E have four free OH, while groups 9B, 9C, and 9F contain isomers with five free OH. Differently from $HCl(H_2O)_n$ clusters with n = 7 – 8 for which the population of group B is negligible below 50 K, isomers of group 9B appear already at very low temperature (~10 K). A comparison of the isomer populations indicates that groups 9A, 9D, and 9E effectively contain all isomers with four free OH bonds, while other unidentified structures with five free OH must exist above 80 K. The isomers with five and six free OH bonds represent the dominant structures at ~110 K and ~220 K, respectively. As a result of the variation in relative stability among the different isomers, the heat capacity of the $HCl(H_2O)_9$ cluster shows a broad peak between 70 K and 180 K. This corresponds to the transition from isomers with four free OH bonds to isomers with a larger number of free OH bonds.

2.4.8. $HCl(H_2O)_{10}$

The first eleven low-energy isomers of $HCl(H_2O)_{10}$ are shown in Figure 2.9. They are characterized by clathrate-like structures. Among the three isomers of group 10A, two

structures contain the dissociated proton in intermediate Zundel-Eigen-type complexes (10A1I and 10A2I), while the proton in 10A3E is found in an Eigen-type environment. The groups 10B, 10C, and 10D can be derived directly from group 9A after addition of one H_2O molecule. Table 2.7 lists the corresponding energies calculated at the PM3-MAIS and B3LYP levels of theory. Although the energy order predicted by the two methods is different, the corresponding energies lie within 1.0 kcal/mol in all cases.

The relative populations of the $HCl(H_2O)_{10}$ isomers are shown in Figure 2.9. The isomers with four free OH dominate at low temperature and start disappearing above ~200 K. Similar trends are also observed for isomers with five, six, and seven free OH, which reach maxima of 35 – 50 % at 150 K, 180 K, and 250 K, respectively. Figure 2.9 clearly shows that group 10A contains all possible isomers with four free OH. By contrast, while the population of group 10B is effectively identical to the population of all isomers with five free OH below 70 K, group 10C also contributes by ~5% at higher temperatures. The structural transition between isomers with four free OH bonds and those with five and six OH is reflected in the temperature dependence of the heat capacity that displays a pronounced peak at T ~ 150 K.

2.5. Conclusions

Semiempirical Born-Oppenheimer replica exchange molecular dynamics simulations have been used to investigate the structural and thermodynamic properties of $HCl(H_2O)_n$ with n = 4 – 10 as well as the global minimum-energy structures of larger clusters with n = 11 – 15, 21 clusters. All SE-BO-REMD simulations have been performed with the PM3-MAIS Hamiltonian. The optimized structures and energies of

several low-energy isomers for each cluster size have then been compared with the corresponding results obtained at the B3LYP/6-311++g(d,p) level of theory. For all isomers, independently of the cluster size, PM3-MAIS predicts the complete dissociation of HCl. The analysis of the local solvating environment around the excess proton indicates the formation of Zundel, Eigen, Eigen-like, $H_7O_3^+$, and intermediate Zundel-Eigen type structures. The temperature dependence of the heat capacity displays pronounced peaks for clusters with n = 7 – 10, while no peaks are observed for smaller clusters. The presence of peaks in the temperature-dependent profile of the heat capacity is associated with structural transitions that occur within each cluster size as a function of temperature. In turn, these features are directly related to the melting behavior of each cluster, leading to an increase in the number of free OH as the temperature increases. However, it should be awaked that the results achieved in current work are based on semiempirical electronic structure method. It is well known that PM3-MAIS method overestimates HCl acidity in water environment. Furthermore, using of minimal basis sets in PM3-MAIS limits the accuracy of non-additive effects, which might be of some importance for the study of larger systems.[53,55] Better performance of PM3-MAIS method might be possibly obtained with the reparameterization of electronic terms[45] as well as overcoming the minimal basis set limitation. Based on the present results for the structural and thermodynamic properties of the $HCl(H_2O)_n$ clusters, future studies will focus on the analysis of the vibrational spectroscopic features and nuclear quantum effects associated with acid dissociation and hydrogen bonding topologies.

2.6. Acknowledgments

This research was supported by the National Science Foundation through grant CHE-1111364. This work used the Extreme Science and Engineering Discovery Environment (XSEDE), which is supported by National Science Foundation grant number OCI-1053575 (allocation TG-CHE110009).

This chapter contains materials from "Systematic Study of Structural and Thermodynamic Properties of $HCl(H_2O)_n$ Clusters from Semiempirical Replica Exchange Simulations" published in 2013 in *Journal of Physical Chemistry A. (Volume* 117, pages 7131 to 7141), authored by Wei Lin and Francesco Paesani. All material has been reproduced with the consent of all other authors.

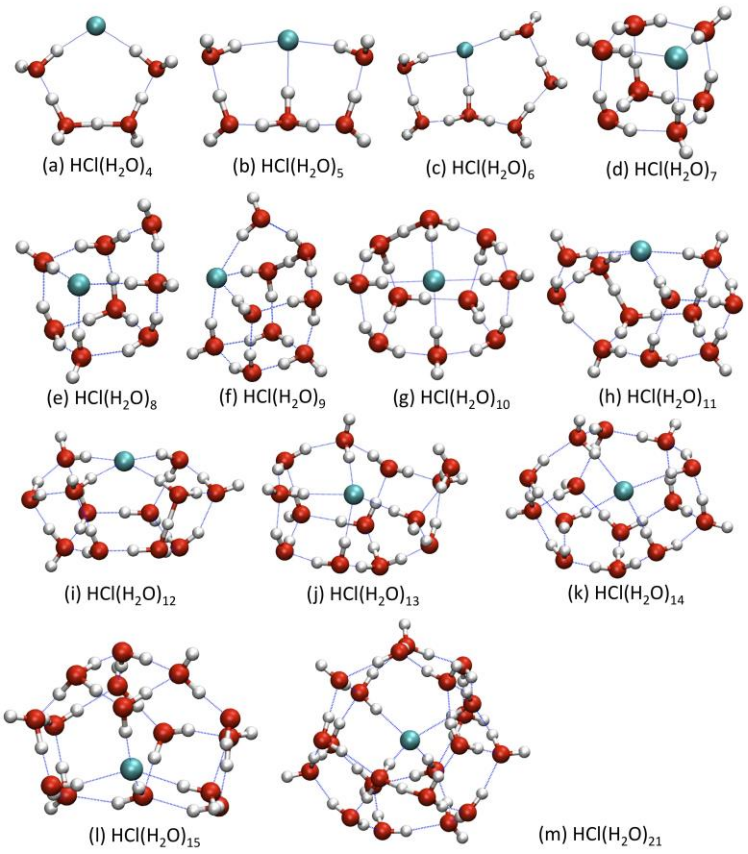

Figure 2.1. Global minimum-energy structures of $HCl(H_2O)_n$ clusters with n = 4 – 15 and n = 21 obtained at the PM3-MAIS level of theory. Cl, O and H atoms are shown in cyan, red and gray, respectively.

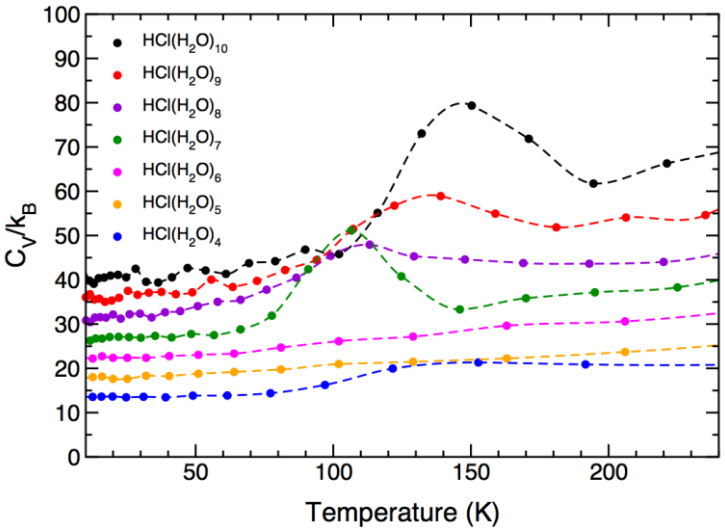

Figure 2.2. Temperature dependence of the constant-volume configurational heat capacity (C_v/k_B) of $HCl(H_2O)_n$ clusters with n = 4 – 10.

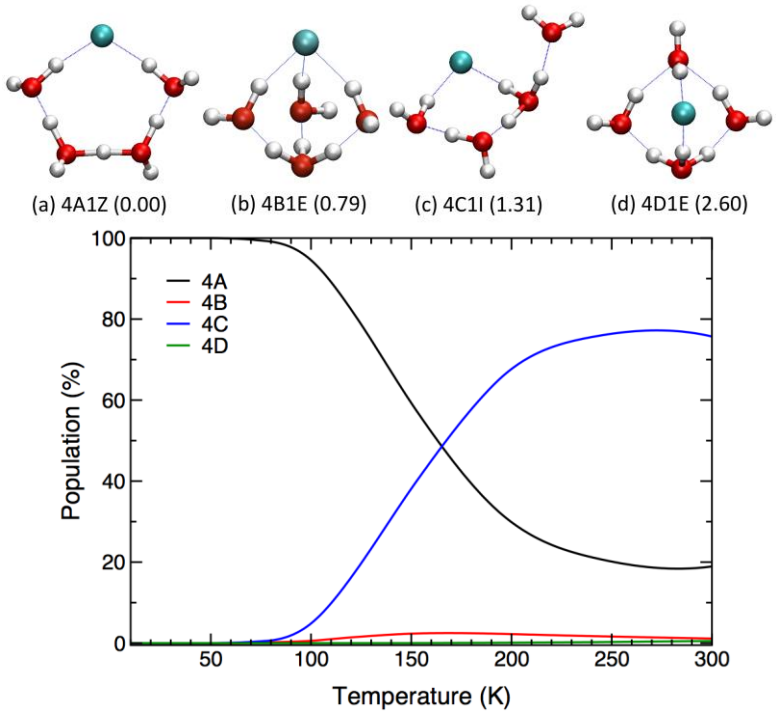

Figure 2.3. PM3-MAIS low-energy structures (top panel) and isomer populations (bottom panel) of the $HCl(H_2O)_4$ isomers. The relative energies (in kcal/mol) are reported in parenthesis. See main text for details on the notation.

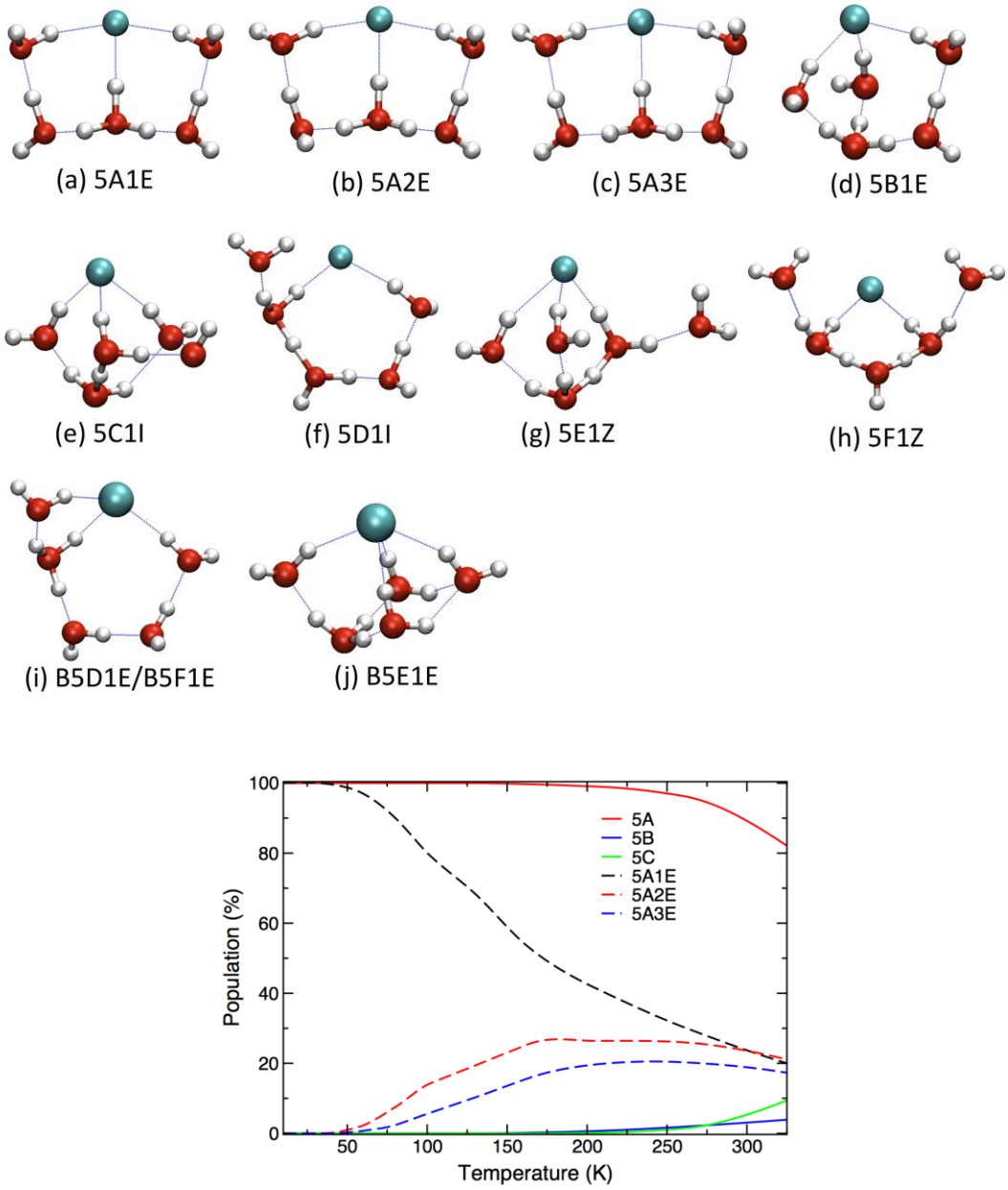

Figure 2.4. Low-energy structures (top panel) and isomer populations (bottom panel) of the $HCl(H_2O)_5$ isomers. (a – h) are the structures obtained with PM3-MAIS, while (i, j) correspond to the optimized structures calculated at the B3LYP/6-311++g(d,p) level of theory. See main text for details on the notation.

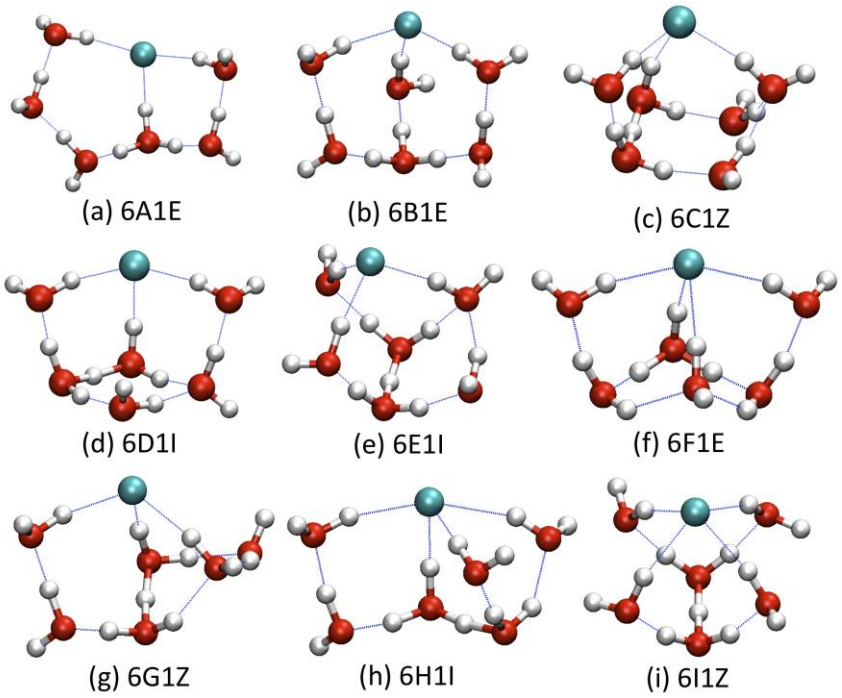

Figure 2.5. Selected low-energy structures of the $HCl(H_2O)_6$ isomers obtained at the PM3-MAIS level of theory. See main text for details on the notation.

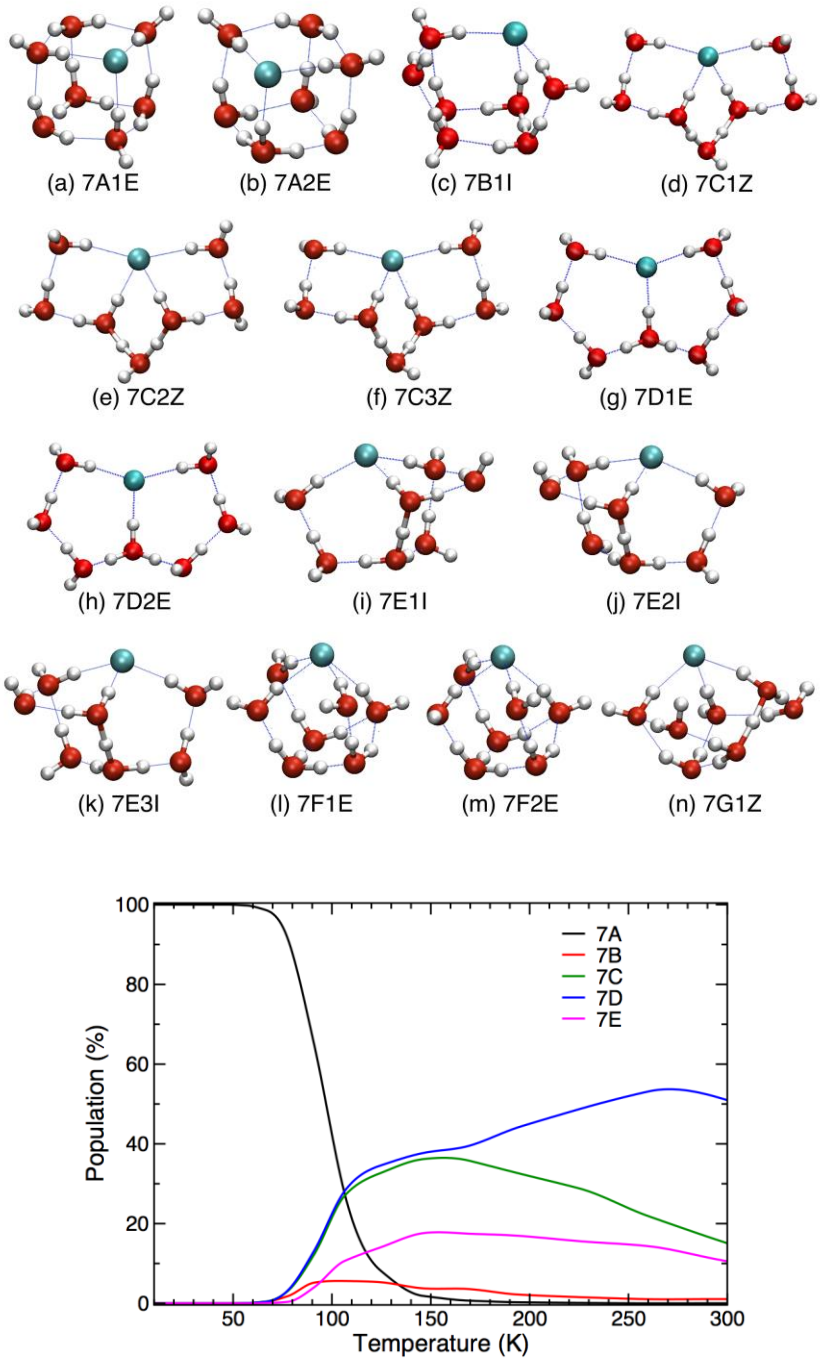

Figure 2.6. PM3-MAIS low-energy structures (top panel) and isomer populations (bottom panel) of the $HCl(H_2O)_7$ isomers. See main text for details on the notation.

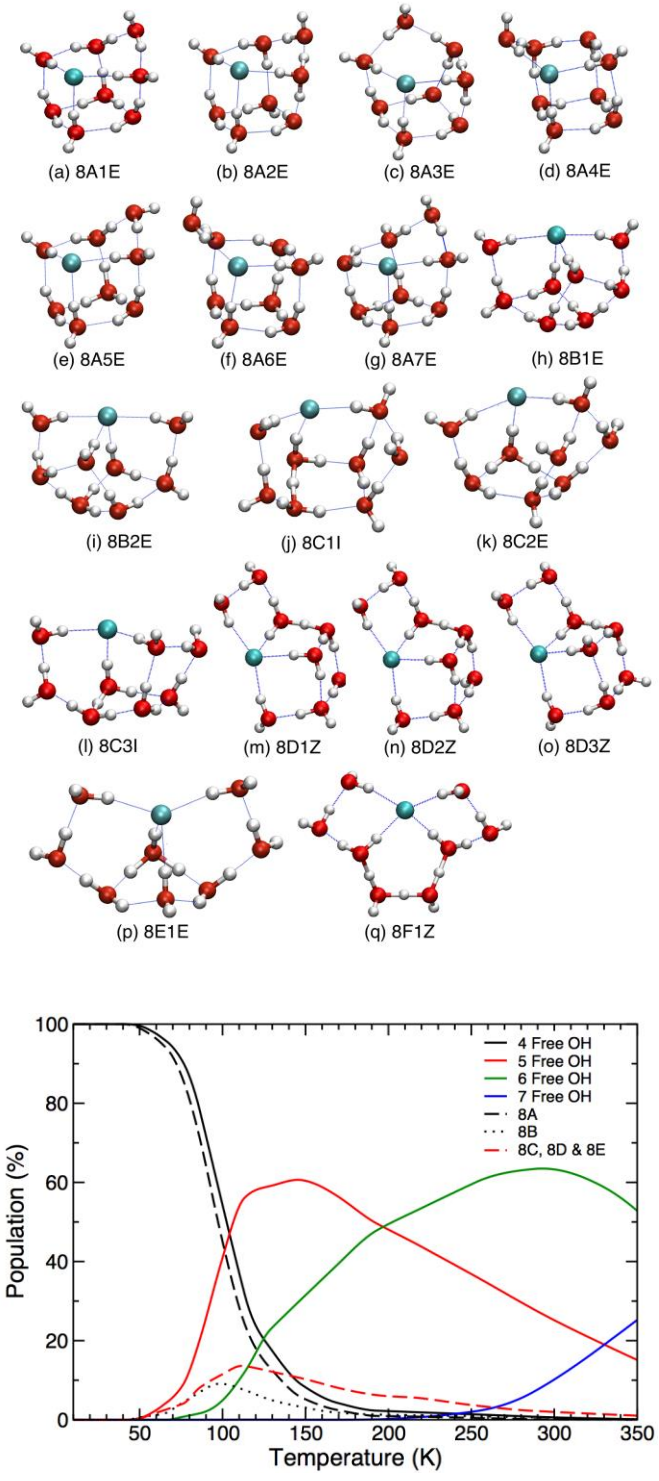

Figure 2.7. PM3-MAIS low-energy structures (top panel) and isomer populations (bottom panel) of the $HCl(H_2O)_8$ isomers. See main text for details on the notation.

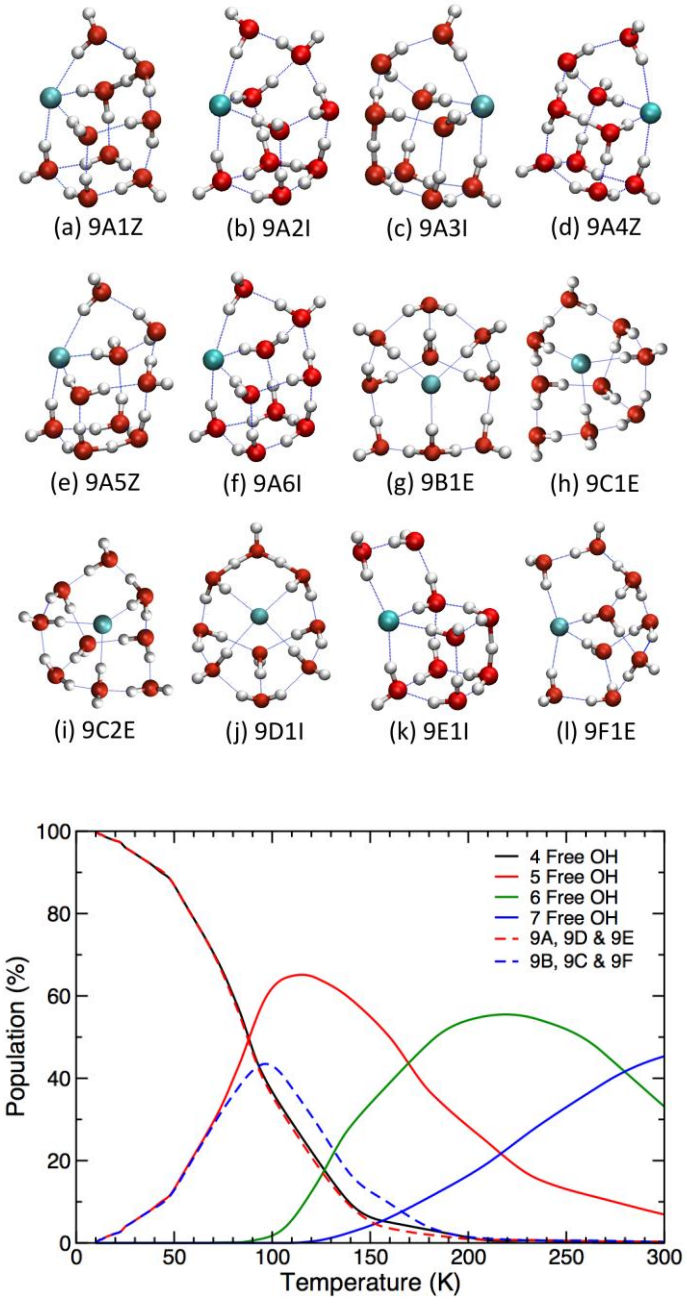

Figure 2.8. PM3-MAIS low-energy structures (top panel) and isomer populations (bottom panel) of the $HCl(H_2O)_9$ isomers. See main text for details on the notation.

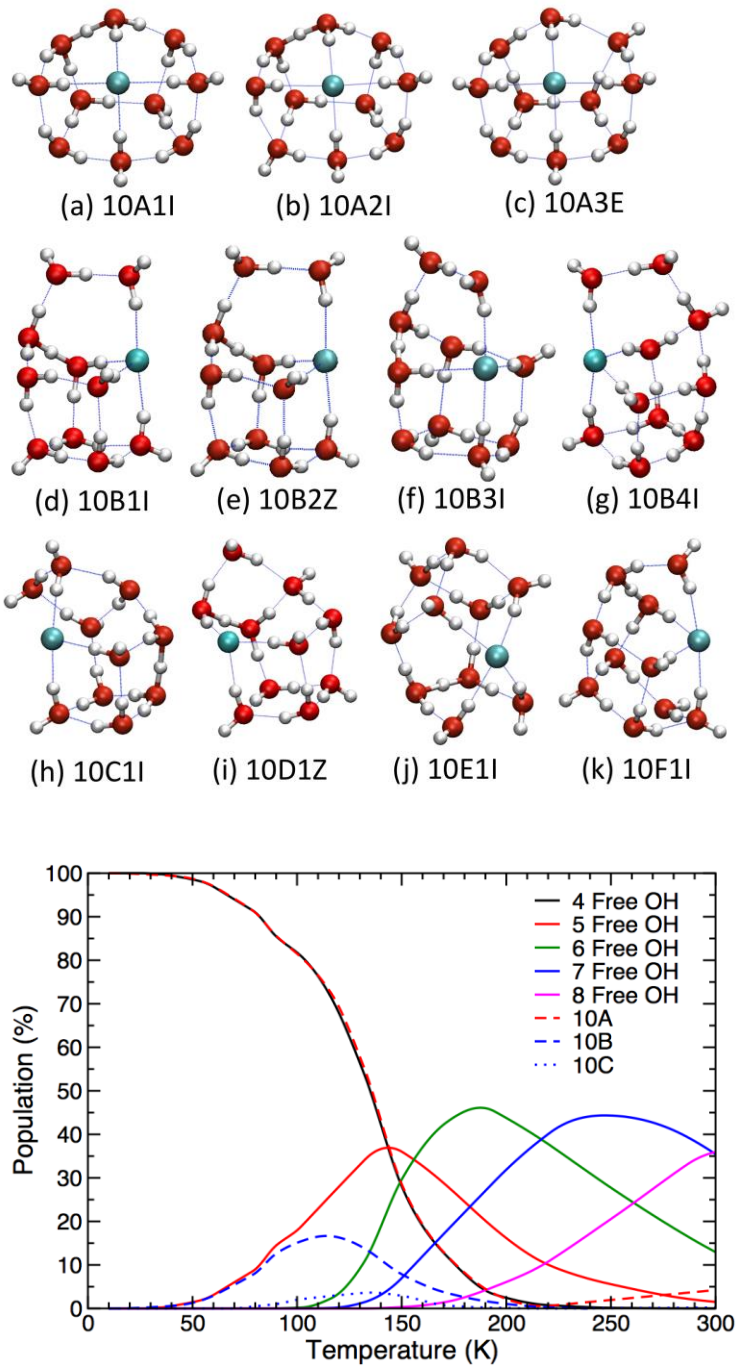

Figure 2.9. PM3-MAIS low-energy structures (top panel) and isomer populations (bottom panel) of the $HCl(H_2O)_{10}$ isomers. See main text for details on the notation.

Table 2.1. Number of replicas (N), lowest (T_{low}) and highest (T_{high}) temperatures, and radius of the spherical cavity (r_o) used to prevent water evaporation in SE-BO-REMD simulations of $HCl(H_2O)_n$ clusters with n = 4 - 21.

	N	T_{low} (K)	T_{high} (K)	r_o (Å)
$HCl(H_2O)_4$	16	10	300	10
$HCl(H_2O)_5$	16	10	325	10
$HCl(H_2O)_6$	16	10	325	10
$HCl(H_2O)_7$	24	10	350	10
$HCl(H_2O)_8$	24	10	375	10
$HCl(H_2O)_9$	32	6	350	10
$HCl(H_2O)_{10}$	32	6	325	12
$HCl(H_2O)_{11}$	32	6	325	12
$HCl(H_2O)_{12}$	32	6	325	12
$HCl(H_2O)_{13}$	32	6	325	12
$HCl(H_2O)_{14}$	32	6	300	13
$HCl(H_2O)_{15}$	32	6	300	13
$HCl(H_2O)_{21}$	32	6	275	15

Table 2.2. Relative energies (in kcal/mol) of the first low-energy isomers of $HCl(H_2O)_5$ calculated with PM3-MAIS and B3LYP/6-311++g(d,p) [with (E_{ZPE}) and without zero-point energy corrections (E_0)].

Isomers	PM3-MAIS		B3LYP/6-311++g(d,p)			
	Rank	$E_{PM3\text{-}MAIS}$	Rank	E_0	Order	E_{ZPE}
5A1E	1	0.000	2	0.008	1	0.000
5A2E	2	0.490	1	0.000	2	0.158
5A3E	3	0.715	4	0.211	3	0.234
5B1E	4	1.460	3	0.141	4	0.428
5C1I	5	3.303	5	1.680	5	2.353
5D1I	6	4.162	7	3.461	6	3.231
5E1Z	7	6.571	6	3.078	7	4.159
5F1Z	8	7.147	/	3.461(5D1I)	/	3.231(5D1I)

Table 2.3. Relative energies (in kcal/mol) of the first low-energy isomers of $HCl(H_2O)_6$ calculated with PM3-MAIS and B3LYP/6-311++g(d,p) [with (E_{ZPE}) and without zero-point energy corrections (E_0)].

Isomers	PM3-MAIS		B3LYP/6-311++g(d,p)			
	Rank	$E_{PM3\text{-}MAIS}$	Rank	E_0	Order	E_{ZPE}
6A1E	1	0.000	3	0.696	2	0.289
6B1E	2	0.621	2	0.300	1	0.000
6C1Z	3	1.418	4	0.713	4	0.921
6D1Z	4	1.448	6	1.249	6	1.523
6E1I	5	1.669	1	0.000	3	0.530
6F1E	6	1.811	7	1.277	7	1.647
6G1Z	7	2.071	9	2.120	9	2.196
6H1I	8	2.414	8	2.091	8	1.691
6I1Z	9	2.768	5	0.957	5	1.437

Table 2.4. Relative energies (in kcal/mol) of the first low-energy isomers of $HCl(H_2O)_7$ calculated with PM3-MAIS and B3LYP/6-311++g(d,p) [with (E_{ZPE}) and without zero-point energy corrections (E_0)].

	PM3-MAIS		B3LYP/6-311++g(d,p)			
Isomers	Rank	$E_{PM3\text{-}MAIS}$	Rank	E_0	Order	E_{ZPE}
7A1E	1	0.000	1	0.000	1	0.000
7A2E	2	1.306	2	0.244	2	0.203
7B1Z	3	1.414	/	0.244(7A2E)	/	0.203(7A2E)
7C1Z	4	1.532	11	6.489	11	3.992
7D1E	5	1.715	9	5.340	7	2.437
7E1Z	6	1.910	6	4.636	6	2.382
7C2Z	7	1.978	12	6.613	12	4.119
7E2Z	8	1.995	8	4.994	9	2.533
7E3Z	9	2.022	7	4.710	8	2.439
7F1E	10	2.028	3	2.687	3	1.306
7F2E	11	2.075	4	2.820	4	1.376
7G1Z	12	2.107	5	3.282	5	2.049
7D2E	13	2.143	10	5.788	10	2.895
7C3Z	14	2.144	13	6.793	13	4.132

Table 2.5. Relative energies (in kcal/mol) of the first low-energy isomers of $HCl(H_2O)_8$ calculated with PM3-MAIS and B3LYP/6-311++g(d,p) [with (E_{ZPE}) and without zero-point energy corrections (E_0)].

	PM3-MAIS		B3LYP/6-311++g(d,p)			
Isomers	Rank	$E_{PM3\text{-}MAIS}$	Rank	E_0	Rank	E_{ZPE}
8A1E	1	0.000	3	0.306	3	0.456
8A2E	2	0.131	2	0.179	2	0.190
8A3E	3	0.215	5	0.639	5	0.577
8A4E	4	0.216	1	0.000	1	0.000
8A5E	5	0.240	4	0.511	4	0.536
8A6E	6	0.401	6	1.826	7	1.940
8A7E	7	0.663	9	3.271	10	3.120
8B1E	8	0.676	7	2.283	6	1.896
8C1I	9	0.756	/	0.639(8A3E)	/	0.577(8A3E)
8B2E	10	0.822	8	2.548	8	2.125
8C2E	11	0.972	/	0.639(8A3E)	/	0.577(8A3E)
8C3I	12	0.990	10	3.301(8B)	9	2.675(8B)
8D1Z	13	1.096	13	5.458	12	3.405
8D2Z	14	1.232	11	5.342	14	3.594
8D3Z	15	1.428	14	5.729	13	3.527
8E1E	16	1.471	12	5.450	11	3.104
8F1Z	17	1.533	15	7.773	15	5.285

Table 2.6. Relative energies (in kcal/mol) of the first low-energy isomers of $HCl(H_2O)_9$ calculated with PM3-MAIS and B3LYP/6-311++g(d,p) [with (E_{ZPE}) and without zero-point energy corrections (E_0)].

	PM3-MAIS		B3LYP/6-311++g(d,p)			
Isomers	Rank	$E_{PM3\text{-}MAIS}$	Rank	E_0	Rank	E_{ZPE}
9A1Z	1	0.000	1	0.000	2	0.031
9B1E	2	0.101	5	0.687	4	0.320
9C1E	3	0.273	2	0.250	1	0.000
9D1I	4	0.288	12	2.917	12	2.889
9A2I	5	0.450	4	0.686	6	0.921
9A3I	6	0.594	7	1.004	7	1.049
9A4Z	7	0.607	6	0.957	5	0.744
9E1I	8	0.685	9	1.669	10	1.914
9C2E	9	0.748	3	0.656	3	0.179
9A5Z	10	0.753	10	2.399	11	2.253
9A6I	11	0.767	8	1.222	8	1.241
9F1E	12	0.822	11	2.696	9	1.840

Table 2.7. Relative energies (in kcal/mol) of the first low-energy isomers of $HCl(H_2O)_{10}$ calculated with PM3-MAIS and B3LYP/6-311++g(d,p) [with (E_{ZPE}) and without zero-point energy corrections (E_0)].

	PM3-MAIS		B3LYP/6-311++g(d,p)			
Isomers	Rank	$E_{PM3\text{-}MAIS}$	Rank	E_0	Rank	E_{ZPE}
10A1I	1	0.000	7	0.331	6	1.111
10B1I	2	0.399	3	0.124	4	0.227
10A2I	3	0.512	5	0.230	8	1.376
10B2Z	4	0.746	1	0.000	1	0.000
10A3E	5	0.779	2	0.025	7	1.181
10C1I	6	0.982	8	1.109 (10D)	9	1.709 (10D)
10B3I	7	1.026	4	0.183	2	0.040
10D1Z	8	1.136	10	1.697	10	2.132
10E1I	9	1.261	6	0.263	3	0.133
10F1I	10	1.422	9	1.245	5	1.011
10B4I	11	1.507	11	1.726	11	2.161

2.7. References

(1) Finlayson-Pitts, B. J.; Pitts, J. N., Jr. *Chemistry of the upper and lower atmosphere: Theory, experiments and applications*; Academic Press, 2000.

(2) Vaida, V. Water cluster mediated atmospheric chemistry *J. Chem. Phys.* **2011**, *135*, 020901.

(3) Lambrecht, D. S.; Clark, G. N. I.; Head-Gordon, T.; Head-Gordon, M. Exploring the Rich Energy Landscape of Sulfate-Water Clusters SO(4)(2-) (H(2)O)(n=3-7): An Electronic Structure Approach *J. Phys. Chem. A* **2011**, *115*, 11438-11454.

(4) Kaneko, T.; Akimoto, T.; Yasuoka, K.; Mitsutake, A.; Zeng, X. C. Size-Dependent Phase Changes in Water Clusters *J. Chem. Theory Comput.* **2011**, *7*, 3083-3087.

(5) Oncak, M.; Slavicek, P.; Farnik, M.; Buck, U. Photochemistry of Hydrogen Halides on Water Clusters: Simulations of Electronic Spectra and Photodynamics, and Comparison with Photodissociation Experiments *J. Phys. Chem. A* **2011**, *115*, 6155-6168.

(6) Hujo, W.; Gaus, M.; Schultze, M.; Kubar, T.; Grunenberg, J.; Elstner, M.; Bauerecker, S. Effect of Nitrogen Adsorption on the Mid-Infrared Spectrum of Water Clusters *J. Phys. Chem. A* **2011**, *115*, 6218-6225.

(7) Goken, E. G.; Joshi, K. L.; Russo, M. F.; van Duin, A. C. T.; Castleman, A. W. Effect of Formic Acid Addition on Water Cluster Stability and Structure *J. Phys. Chem. A* **2011**, *115*, 4657-4664.

(8) Yacovitch, T. I.; Wende, T.; Jiang, L.; Heine, N.; Meijer, G.; Neumark, D. M.; Asmis, K. R. Infrared Spectroscopy of Hydrated Bisulfate Anion Clusters: HSO(4)(-)(H(2)O)(1-16) *J. Phys. Chem. Lett.* **2011**, *2*, 2135-2140.

(9) Zhai, Y. T.; Laio, A.; Tosatti, E.; Gong, X. G. Finite Temperature Properties of Clusters by Replica Exchange Metadynamics: The Water Nonamer *J. Am. Chem. Soc.* **2011**, *133*, 2535-2540.

(10) Leopold, K. R. Hydrated Acid Clusters *Annu. Rev. Phys. Chem.* **2011**, *62*, 327-349.

(11) Molina, M. J.; Tso, T. L.; Molina, L. T.; Wang, F. C. Y. Antarctic Stratospheric Chemistry of Chlorine Nitrate, Hydrogen-Chloride and Ice - Release of Active Chlorine *Science* **1987**, *238*, 1253-1257.

(12) Kang, H.; Shin, T. H.; Park, S. C.; Kim, I. K.; Han, S. J. Acidity of hydrogen chloride on ice *J. Am. Chem. Soc.* **2000**, *122*, 9842-9843.

(13) Kondo, M.; Kawanowa, H.; Gotoh, Y.; Souda, R. Ionization and solvation of HCl adsorbed on the D2O-ice surface *J. Chem. Phys.* **2004**, *121*, 8589-8593.

(14) McNeill, V. F.; Loerting, T.; Geiger, F. M.; Trout, B. L.; Molina, M. J. Hydrogen chloride-induced surface disordering on ice *Proc. Natl. Acad. Sci. USA* **2006**, *103*, 9422-9427.

(15) Olanrewaju, B. O.; Herring-Captain, J.; Grieves, G. A.; Aleksandrov, A.; Orlando, T. M. Probing the Interaction of Hydrogen Chloride with Low-Temperature Water Ice Surfaces Using Thermal and Electron-Stimulated Desorption *J. Phys. Chem. A* **2011**, *115*, 5936-5942.

(16) McNeill, V. F.; Geiger, F. M.; Loerting, T.; Trout, B. L.; Molina, L. T.; Molina, M. J. Interaction of hydrogen chloride with ice surfaces: The effects of grain size, surface roughness, and surface disorder *J. Phys. Chem. A* **2007**, *111*, 6274-6284.

(17) Fulton, J. L.; Balasubramanian, M. Structure of Hydronium (H3O+)/Chloride (Cl-) Contact Ion Pairs in Aqueous Hydrochloric Acid Solution: A Zundel-like Local Configuration *J. Am. Chem. Soc.* **2010**, *132*, 12597-12604.

(18) Packer, M. J.; Clary, D. C. Interaction of Hcl with Water Clusters - (H2o)(N)Hcl, N=1-3 *J. Phys. Chem.* **1995**, *99*, 14323-14333.

(19) Lee, C. T.; Sosa, C.; Planas, M.; Novoa, J. J. A theoretical study of the ionic dissociation of HF, HCl, and H2S in water clusters *J. Chem. Phys.* **1996**, *104*, 7081-7085.

(20) Planas, M.; Lee, C.; Novoa, J. J. Kinetics of the proton transfer in X center dot center dot center dot(H2O)(4) cluster (X=H2O, NH3, H2S, and HCl): Evidence of a concerted mechanism *J. Phys. Chem.* **1996**, *100*, 16495-16501.

(21) Estrin, D. A.; Kohanoff, J.; Laria, D. H.; Weht, R. O. Hybrid quantum and classical mechanical Monte Carlo simulations of the interaction of hydrogen chloride with solid water clusters *Chem. Phys. Lett.* **1997**, *280*, 280-286.

(22) Ando, K.; Hynes, J. T. Molecular mechanism of HCl acid ionization in water: Ab initio potential energy surfaces and Monte Carlo simulations *J. Phys. Chem. B* **1997**, *101*, 10464-10478.

(23) Bolton, K. A QM/MM study of HCl adsorption at ice surface defect sites *J. Mol. Struc.-Theochem.* **2003**, *632*, 145-156.

(24) Cabaleiro-Lago, E. M.; Hermida-Ramon, J. M.; Rodriguez-Otero, J. Computational study of the dissociation of H-X acids (X=F, Cl, Br, I) in water clusters *J. Chem. Phys.* **2002**, *117*, 3160-3168.

(25) Chaban, G. M.; Gerber, R. B.; Janda, K. C. Transition from hydrogen bonding to ionization in (HCl)(n)(NH(3))(n) and (HCl)n(H2O)(n) clusters: Consequences or anharmonic vibrational spectroscopy *J. Phys. Chem. A* **2001**, *105*, 8323-8332.

(26) Bacelo, D. E.; Binning, R. C.; Ishikawa, Y. Ab initio Monte Carlo simulated annealing study of HCl(H2O)(n) (n=3, 4) clusters *J. Phys. Chem. A* **1999**, *103*, 4631-4640.

(27) Odde, S.; Mhin, B. J.; Lee, S.; Lee, H. M.; Kim, K. S. Dissociation chemistry of hydrogen halides in water *J. Chem. Phys.* **2004**, *120*, 9524-9535.

(28) Milet, A.; Struniewicz, C.; Moszynski, R.; Wormer, P. E. S. Theoretical study of the protolytic dissociation of HCl in water clusters *J. Chem. Phys.* **2001**, *115*, 349-356.

(29) Osamura, Y.; Tachikawa, M.; Mori, K. Isotope effect of hydrated clusters of hydrogen chloride, HCl(H2O)(n) and DCl(H2O)(n) (n = 0-4): application of dynamic extended molecular orbital method *Mol. Phys.* **1999**, *96*, 1207-1215.

(30) Pettersson, J. B. C.; Svanberg, M.; Bolton, K. Coupled QM/MM molecular dynamics simulations of HCl interacting with ice surfaces and water clusters - Evidence of rapid ionization *J. Phys. Chem. A* **2000**, *104*, 5787-5798.

(31) Re, S.; Osamura, Y.; Suzuki, Y.; Schaefer, H. F. Structures and stability of hydrated clusters of hydrogen chloride, HCl(H2O)(n), n=1-5 *J. Chem. Phys.* **1998**, *109*, 973-977.

(32) Sobolewski, A. L.; Domcke, W. Photochemistry of HCl(H2O)(4): Cluster model of the photodetachment of the chloride anion in water *J. Phys. Chem. A* **2003**, *107*, 1557-1562.

(33) Masia, M.; Forbert, H.; Marx, D. Connecting structure to infrared spectra of molecular and autodissociated HCl - Water aggregates *J. Phys. Chem. A* **2007**, *111*, 12181-12191.

(34) Forbert, H.; Masia, M.; Kaczmarek-Kedziera, A.; Nair, N. N.; Marx, D. Aggregation-Induced Chemical Reactions: Acid Dissociation in Growing Water Clusters *J. Am. Chem. Soc.* **2011**, *133*, 4062-4072.

(35) Ault, B. S.; Pimentel, G. C. Infrared-Spectrum of Water Hydrochloric Acid Complex in Solid Nitrogen *J. Phys. Chem.* **1973**, *77*, 57-61.

(36) Schriver, A.; Silvi, B.; Maillard, D.; Perchard, J. P. Structure of Water Hydrochloric Acid Complexes in Argon and Nitrogen Matrices from Ir-Spectra *J. Phys. Chem.* **1977**, *81*, 2095-2102.

(37) Amirand, C.; Maillard, D. Spectrum and Structure of Water-Rich Water Hydracid Complexes from Matrix-Isolation Spectroscopy - Evidence for Proton-Transfer *J. Mol. Struct.* **1988**, *176*, 181-201.

(38) Farnik, M.; Weimann, M.; Suhm, M. A. Acidic protons before take-off: A comparative jet Fourier transform infrared study of small HCl- and HBr-solvent complexes *J. Chem. Phys.* **2003**, *118*, 10120-10136.

(39) Devlin, J. P.; Farnik, M.; Suhm, M. A.; Buch, V. Comparative FTIR spectroscopy of HX adsorbed on solid water: Ragout-jet water clusters vs ice nanocrystal arrays *J. Phys. Chem. A* **2005**, *109*, 955-958.

(40) Weimann, M.; Farnik, M.; Suhm, M. A. A first glimpse at the acidic proton vibrations in HCl-water clusters via supersonic jet FTIR spectroscopy *Phys. Chem. Chem. Phys.* **2002**, *4*, 3933-3937.

(41) Gutberlet, A.; Schwaab, G.; Birer, O.; Masia, M.; Kaczmarek, A.; Forbert, H.; Havenith, M.; Marx, D. Aggregation-Induced Dissociation of HCl(H(2)O)(4) Below 1 K: The Smallest Droplet of Acid *Science* **2009**, *324*, 1545-1548.

(42) Flynn, S. D.; Skvortsov, D.; Morrison, A. M.; Liang, T.; Choi, M. Y.; Douberly, G. E.; Vilesov, A. F. Infrared Spectra of HCl-H2O Clusters in Helium Nanodroplets *J. Phys. Chem. Lett.* **2010**, *1*, 2233-2238.

(43) Morrison, A. M.; Flynn, S. D.; Liang, T.; Douberly, G. E. Infrared Spectroscopy of (HCl)(m)(H2O)(n) Clusters in Helium Nanodroplets: Definitive Assignments in the HCl Stretch Region *J. Phys. Chem. A* **2010**, *114*, 8090-8098.

(44) Sillanpaa, A.; Laasonen, K. Car-Parrinello molecular dynamics study of DCI hydrate crystals *Chem. Phys. Chem.* **2005**, *6*, 1879-1883.

(45) Sugawara, S.; Yoshikawa, T.; Takayanagi, T.; Tachikawa, M. Theoretical study on mechanisms of structural rearrangement and ionic dissociation in the HCl(H(2)O)(4) cluster with path-integral molecular dynamics simulations *Chem. Phys. Lett.* **2011**, *501*, 238-244.

(46) Takayanagi, T.; Takahashi, K.; Kakizaki, A.; Shiga, M.; Tachikawa, M. Path-integral molecular dynamics simulations of hydrated hydrogen chloride cluster HCl(H(2)O)(4) on a semiempirical potential energy surface *Chem. Phys.* **2009**, *358*, 196-202.

(47) Scandolo, S.; Ndongmouo, U. F. T.; Lee, M. S.; Rousseau, R.; Baletto, F. Finite-temperature effects on the stability and infrared spectra of HCl(H2O)(6) clusters *J. Phys. Chem. A* **2007**, *111*, 12810-12815.

(48) Buch, V.; Dubrovskiy, A.; Mohamed, F.; Parrinello, M.; Sadlej, J.; Hammerich, A. D.; Devlin, J. P. HCl hydrates as model systems for protonated water *J. Phys. Chem. A* **2008**, *112*, 2144-2161.

(49) Jansen, G.; Boese, A. D.; Forbert, H.; Masia, M.; Tekin, A.; Marx, D. Constructing simple yet accurate potentials for describing the solvation of HCl/water clusters in bulk helium and nanodroplets *Phys. Chem. Chem. Phys.* **2011**, *13*, 14550-14564.

(50) Walewski, L.; Forbert, H.; Marx, D. Quantum Induced Bond Centering in Microsolvated HCl *J. Phys. Chem. Lett.* **2011**, *2*, 3069-3074.

(51) Okamoto, Y.; Sugita, Y. Replica-exchange molecular dynamics method for protein folding *Chem. Phys. Lett.* **1999**, *314*, 141-151.

(52) Ruiz-Lopez, M. F.; Bernal-Uruchurtu, M. I. Basic ideas for the correction of semiempirical methods describing H-bonded systems *Chem. Phys. Lett.* **2000**, *330*, 118-124.

(53) Bernal-Uruchurtu, M. I.; Arillo-Flores, O. I.; Ruiz-Lopez, M. F. Can semi-empirical models describe HCl dissociation in water? *Theor. Chem. Acc.* **2007**, *118*, 425-435.

(54) Flores, O. I. A.; Bernal-Uruchurtu, M. I. Charge Separation Process in Water Clusters Containing HCl. Molecular Dynamics Study Using Semiempirical Hamiltonians *J. Phys. Chem. A* **2010**, *114*, 8975-8983.

(55) Park, K.; Gotz, A. W.; Walker, R. C.; Paesani, F. Application of Adaptive QM/MM Methods to Molecular Dynamics Simulations of Aqueous Systems *J. Chem. Theory Comput.* **2012**, *8*, 2868-2877.

(56) Case, D. A.; Darden, T. A.; Cheatham, T. E., III ; Simmerling, C. L.; Wang, J.; Duke, R. E.; Luo, R.; Walker, R. C.; Zhang, W.; Merz, K. M.; etal.; 12 ed.; University of California - San Francisco: San Francisco, 2012.

(57) Andrea, T. A.; Swope, W. C.; Andersen, H. C. The Role of Long Ranged Forces in Determining the Structure and Properties of Liquid Water *J. Chem. Phys.* **1983**, *79*, 4576-4584.

(58) Frisch, M. J.; Trucks, G. W.; Schlegel, H. B.; Scuseria, G. E.; Robb, M. A.; Cheeseman, J. R.; Scalmani, G.; Barone, V.; Mennucci, B.; Petersson, G. A.; etal.; Gaussian, Inc.: Wallingford, CT, 2009.

(59) Leach, A. R. *Molecular modelling: principle and applications*; Pearson Prentice Hakk, 2001.

(60) Tuckerman, M. E.; Marx, D.; Klein, M. L.; Parrinello, M. On the quantum nature of the shared proton in hydrogen bonds *Science* **1997**, *275*, 817-820.

(61) Agmon, N.; Markovitch, O.; Chen, H.; Izvekov, S.; Paesani, F.; Voth, G. A. Special pair dance and partner selection: Elementary steps in proton transport in liquid water *J. Phys. Chem. B* **2008**, *112*, 9456-9466.

(62) Kuo, J. L.; Xie, Z. Z.; Ong, Y. S. On the effects of basis-set in studying the hydration and dissociation of HF in cubic $HF(H_2O)_7$ clusters *Chem. Phys. Lett.* **2008**, *453*, 13-17.

(63) Buck, U.; Brudermann, J.; Buch, V. Isomerization and melting-like transition of size-selected water nonamers *J. Phys. Chem. A* **2002**, *106*, 453-457.

(64) Choi, T. H.; Jordan, K. D. Application of the SCC-DFTB Method to H(+)(H(2)O)(6), H(+)(H(2)O)(21), and H(+)(H(2)O)(22) *J. Phys. Chem. B* **2010**, *114*, 6932-6936.

(65) Dykstra, C. E. *Theory and applications of computational chemistry : the first forty years*; 1st ed.; Elsevier: Amsterdam ; Boston, 2005.

(66) Christie, R. A.; Jordan, K. D. Finite temperature behavior of H+(H2O)(6) and H+(H2O)(8) *J. Phys. Chem. B* **2002**, *106*, 8376-8381.

(67) Svanberg, M.; Pettersson, J. B. C.; Bolton, K. Coupled QM/MM molecular dynamics simulations of HCl interacting with ice surfaces and water clusters - Evidence of rapid ionization *J. Phys. Chem. A* **2000**, *104*, 5787-5798.

(68) Buck, U.; Ettischer, I.; Melzer, M.; Buch, V.; Sadlej, J. Structure and spectra of three-dimensional (H2O)(n) clusters, n = 8, 9, 10 *Phys. Rev. Lett.* **1998**, *80*, 2578-2581.

Chapter 3. Infrared spectra of $HCl(H_2O)_n$ clusters from semiempirical Born-Oppenheimer molecular dynamics simulations

3.1. Abstract

The infrared spectra of $HCl(H_2O)_n$ clusters, with n = 4 – 10 and n = 21, are calculated at T = 50 K from semiempirical Born-Oppenheimer molecular dynamics simulations performed with the PM3-MAIS model. A specific focus is on the relationship between spectroscopic features associated with the presence of the excess proton generated by the HCl dissociation and the underlying water hydrogen bonding topologies. Vibrational modes involving the motion of the excess proton are attributed to specific features appearing at ~1175 cm^{-1} for Zundel-type structures, in the 1670 – 1800 cm^{-1} range for intermediate Zundel-Eigen-type structures, and at ~2820 cm^{-1} for Eigen-type structures. This wide range of frequencies correlates with the position of the excess proton within the clusters, which determines the excess charge redistribution and, consequently, the bond strengths. For water molecules forming hydrogen bonds with the chloride ion, blue shifts of the OH stretching frequencies are obtained. Overall, the theoretical predictions are in good agreement with the available experimental data.

3.2. Introduction

Hydrated acid clusters have attracted significant attention due to their importance to fundamental chemistry and their role in physicochemical processes in the atmosphere.[1] Due to finite-size effects, structural (e.g., hydrogen bond topology), thermodynamic and

dynamical properties of acid-water clusters are different from those of the same acids in aqueous solution.[2] In introductory chemistry textbooks, strong acids are often described as fully ionized in water. However, since the ionization process depends at the molecular level on the nature of the aqueous environment, the number of water molecules that are effectively necessary for the formation of stable ion pairs depends on both thermodynamic conditions and system size.[3-5]

At the cluster level, many hydrated acid-water systems have been investigated both experimentally and theoretically.[2] For common strong acids, computational studies suggest that at least three to four water molecules are needed for the ion pair to become a minimum-energy structure on the potential energy surface.[2] In particular, for $HCl(H_2O)_n$ clusters, theoretical studies showed that four water molecules are necessary to form the so-called charge-separated solvent-shared ion pair.[6-9] An aggregation-induced chemical reaction mechanism was proposed to describe the processes of HCl dissociation with subsequent formation of a solvent-shared ion pair in the presence of four water molecules.[10,11] Nuclear quantum effects were also found to play an important role in determining both the structural rearrangements and the underlying hydrogen-bonding topology of the $HCl(H_2O)_4$ cluster.[12-14] Investigations of the low-energy structures of $HCl(H_2O)_n$ clusters with $n \geq 5$ predicted complete HCl dissociation.[7,15]

Both experimental measurements[16-20] and theoretical calculations[21-23] of the infrared (IR) spectra of undissociated $HCl(H_2O)_n$ clusters have been reported. As mentioned above, HCl is predicted to dissociate as the size of the cluster increases. Consequently, the HCl stretching vibration, which is characteristic of small clusters, gradually disappears in the IR spectra of larger (ionized) clusters. The latter are

characterized by several features corresponding to various vibrational modes associated with the solvated excess proton, including OH stretching vibrations of protonated water complexes. Car-Parrinello molecular dynamics (CPMD) simulations were carried out to investigate the relationship between structural and spectroscopic properties of $DCl(D_2O)_n$ clusters with n = 1 – 6.[23] Finite-temperature effects on the stability and infrared spectra of undissociated and dissociated $HCl(H_2O)_6$ clusters were also studied using "first principles" molecular dynamics simulations.[24] Recently, new experimental measurements have provided direct evidence for the presence of dissociated HCl molecules in $HCl(H_2O)_n$ clusters with $n \geq 4$.[11,25]

In a previous study, we investigated the low-energy structures of $HCl(H_2O)_{4\text{-}10}$ clusters.[15] In these clusters, various protonated water structures were identified, including Zundel, Eigen, Eigen-like, $H_7O_3^+$, and intermediate Zundel-Eigen type configurations.[15] Due to the variety of isomeric structures and corresponding charge delocalization, the OH stretching vibrations in larger $HCl(H_2O)_n$ clusters display pronounced frequency shifts that are often difficult to interpret experimentally. In the present study, infrared spectra of $HCl(H_2O)_n$ (n = 4 – 10, 21) clusters are calculated from classical semiempirical Born-Oppenheimer molecular dynamics (BOMD) simulations at T = 50 K. The equilibrium structures are obtained from our previous Born-Oppenheimer replica exchange molecular dynamics simulations.[15] The molecular interactions are described using the PM3-MAIS Hamiltonian,[26,27] which was derived from the PM3 model through a reparameterization of the core-core interactions.[26] Although it is known to slightly overestimate the acidity of HCl molecules in water environments, PM3-MAIS has been shown to provide a qualitatively correct description of the underlying physics of HCl-water systems, thus

enabling the study of large $HCl(H_2O)_n$ clusters which are difficult to characterize using other simulation approaches.[26] The main focus of this study is on determining the relationship between specific spectroscopic features associated with the presence of the excess proton resulting from the HCl dissociation and the underlying water hydrogen-bonding topologies.

3.3. Methodology

3.3.1. Computational details

The initial configurations of the $HCl(H_2O)_n$ clusters were taken from the PM3-MAIS optimized structures calculated in Ref. [15]. Each configuration was initially equilibrated in the canonical (NVT) ensemble at T = 50 K for 50 ps. The temperature was maintained using the Andersen thermostat with a random rescaling of the atom velocities every 100 steps.[28] The equilibration was followed by production runs of 50 ps in the microcanonical (NVE) ensemble, during which the molecular dipole moments were recorded every 2 fs. In all cases, the equations of motion were propagated according to the leapfrog algorithm with time step $\Delta t = 0.5$ fs. All simulations were carried out with a development version of the AMBER 12 suite of codes.[29] The dipole-dipole autocorrelation functions and IR spectra of the clusters were calculated using an in-house code.

3.3.2. Infrared spectra calculation and frequency assignment

The infrared absorption coefficient as measured in experiments is given by[30]

$$\alpha_{QC}(\omega) = \left[\frac{4\pi^2\omega}{\hbar c n(\omega)}\right](1 - e^{-\beta\hbar\omega}) I_{QC}(\omega) \tag{3.1}$$

where n(ω) is the refractive index of the system at frequency ω. For gas-phase spectroscopy, n(ω) ≈ 1. In Eq. 4, *c* is the speed of light and $I_{QC}(\omega)$ is the quantum-corrected line shape, which can be expressed as

$$I_{QC}(\omega) = Q_{QC}(\omega) I_{cl}(\omega) \tag{3.2}$$

where $I_{cl}(\omega)$ is the Fourier transform of the classical dipole (M) autocorrelation function

$$I_{cl}(\omega) = FFT[C_{cl}(t)] = \frac{1}{2\pi}\int_{-\infty}^{+\infty} e^{-i\omega t}\langle M(0)M(t)\rangle dt \tag{3.3}$$

and $Q_{QC}(\omega)$ is the quantum correction factor that is used to approximate the quantum line shape. In the present study, the harmonic approximation quantum correction factor

$$Q_{QC} = \frac{\beta\hbar\omega}{1 - \exp^{-\beta\hbar\omega}} \tag{3.4}$$

is applied as it is known to perform well for hydrogen-bonded systems.[23,30] Using Eqs. 5 and 7, the infrared absorption coefficient can then be expressed as

$$\alpha_{QC}(\omega) = \frac{4\pi^2\beta\omega^2}{c} I_{cl}(\omega) \tag{3.5}$$

The different IR features were assigned through the analysis of the Fourier transforms of the corresponding (atomic) velocity autocorrelation functions (AVACFs). Specifically, AVACFs associated with the motion of each hydrogen atom in each cluster configuration were calculated along the MD trajectories. The vibrational spectra were

then decomposed in effective normal mode contributions. This analysis allows us to associate individual molecular vibrations with the motion of the relevant hydrogen atoms and, consequently, to assign the corresponding OH stretching and HOH bending modes.

The limitation of an assignment based on AVACFs is that it is difficult to distinguish two vibrational modes associated with a specific hydrogen atom if the modes lie within the same frequency region. In the present study, several vibrational modes corresponding to protonated water complexes are found with frequencies similar to those of the water HOH bending vibration. In order to assign these modes, the atomic velocity projection method (AVPM) was used. AVPM is based on the projection of the atomic velocity vectors on the tangential directions of the trajectories belonging to a predefined internal coordinate (in this study, the OH stretch).[31] In this way, the contributions associated with atomic motions along a given OH bond can be isolated, which allows OH stretching modes appearing in the HOH bending region to be distinguished and assigned. AVACFs and AVPM thus provide complementary information enabling a detailed assignment of the vibrational spectra of the $HCl(H_2O)_n$ clusters.

3.4. Results and discussion

As shown in our previous study,[15] several distinct structural motifs can be identified in $HCl(H_2O)_n$ clusters, which differ in the solvation of both excess proton and chloride ion. The presence of the excess proton results in the appearance of: A) Eigen-type structures, $H_3O^+(H_2O)_3$; B) Eigen-like-type structures, $H_3O^+(H_2O)_2Cl^-$, in which one H_2O molecule of the Eigen structure is replaced by Cl^-; C) Zundel-type structures corresponding to $H_5O_2^+$, with one shared proton, and $H_7O_3^+$-type structures with two

identical shared protons; D) Intermediate Zundel-Eigen-type structures, $H_5O_2^+(H_2O)_3Cl^-$, where one water molecule in $H_5O_2^+$ is H-bonded to Cl^-. The definitions of Zundel-type, Eigen-type, and intermediate Zundel-Eigen-type structures used in the present study to identify different structural arrangements within each cluster are discussed in detail in Ref. [15].

3.4.1. Eigen-type complexes

To unravel the effects of the hydration environment on the IR spectra, $HCl(H_2O)_n$ clusters with Eigen-type structures are first characterized. The calculated IR spectra of five representative $HCl(H_2O)_n$ clusters with Eigen-type structures are shown in Figure 3.1. From a structural point of view, two groups of Eigen-type structures are identified, including those with symmetric (4B1E and 7A1E in Figure 3.1) and asymmetric (5B1E, 8A1E and 8B1E in Figure 3.1) second solvation shells around the H_3O^+ core. The asymmetric arrangement in the second solvation shell is responsible for the splitting of the H_3O^+ asymmetric stretching band (in red in Figure 3.1), with the two peaks being separated by a few hundred wavenumbers. A similar splitting of the H_3O^+ asymmetric stretches was observed in predeuterated $HCl(H_2O)_6$ aggregates using CPMD simulations[23] and in the experimental IR spectra of protonated water.[29,30] These studies show that the asymmetric stretches of the hydronium ion in the $H^+(H_2O)_5$ cluster give rise to two peaks — one blue-shifted by ~200 cm^{-1} and one red-shifted by ~780 cm^{-1} relative to the H_3O^+ asymmetric stretch of the isolated $H^+(H_2O)_4$ Eigen ion.[32,33] As suggested by previous theoretical and experimental studies,[32-34] structural asymmetries in the second solvation shell around the hydronium core result in the preferential localization of the

excess charge on one or two of the H atoms which thus causes the spectral splitting. The H_3O^+ symmetric stretch around 2800 cm^{-1} is shown in green in Figure 3.1. From IR depletion spectra at 0.37 K,[11] a peak at 2667.8 cm^{-1} was assigned to the H_3O^+ symmetric stretch in 4B1E. The H_3O^+ symmetric stretch calculated from the present classical BOMD simulations is ~150 cm^{-1} blue-shifted relative to the experimental value. This difference is likely associated with the neglect of nuclear quantum effects, which are known to move the vibrational spectral features to the red due to the anharmonicity of the underlying potential energy surface.

The peaks shown in blue in Figure 3.1 are associated with the OH stretching modes of H_2O molecules that are hydrogen bonded to the chloride ion. For configurations containing three hydrogen bonds between Cl^- and the water molecules (4B1E, 7A1E, 5B1E and 8A1E), these peaks are located between 3050 cm^{-1} and 3200 cm^{-1}. A blue shift of the corresponding modes is observed in 8B1E where four hydrogen bonds are formed between the Cl^- ion and four water molecules. This blue shift is mainly due to weaker H_2O-Cl^- interactions in 8B1E relative to other isomers. The spectroscopic features near 3750 cm^{-1} can be readily assigned to dangling water OH stretches, and those around 1600 cm^{-1} to intramolecular bends of both water molecules and hydronium ions. The (black) peaks between 2600 cm^{-1} and 3600 cm^{-1} are assigned to OH stretches that are H-bonded to water molecules. It is worth noting that the AD-type (where A is the H-bond acceptor and D is the H-bond donor) H-bonded OH stretches of 5B1E appear at ~2650 cm^{-1}, which is red-shifted by several hundred wavenumbers relative to the OH stretches of H-bonded H_2O molecules. Less red-shifted peaks at ~3000 cm^{-1} associated with ADD-type OH stretching modes are also found in 8A1E and 8B1E. These pronounced red shifts are

caused by the redistribution of the excess charge from the hydronium ion to the neighboring water molecules. The peaks between 3500 and 3600 cm^{-1} are assigned to the OH stretches of ADD type hydrogen-bonded H_2O molecules. Experimentally, a sharp feature near 3600 cm^{-1} was assigned to water molecules acting as ADD sites in large protonated water clusters.[35,36]

3.4.2. Eigen-like-type complexes

Both calculated IR spectra and structures of $HCl(H_2O)_n$ clusters containing Eigen-like-type structures, $H_3O^+(H_2O)_2Cl^-$, are shown in Figure 3.2. In Eigen-like-type structures, the hydronium core is solvated by one Cl^- ion and two water molecules. The asymmetry in the first solvation shell of the hydronium core gives rise to three IR bands associated with the OH stretch modes of the hydronium ion. One mode originates from the OH stretch of H_3O^+ that is H-bonded to the Cl^- ion (in green in Figure 3.2), while two other modes originate from the symmetric and asymmetric OH stretches of H_3O^+ that are H-bonded to the water molecules (in red in Figure 3.2). For isomers containing three hydrogen bonds between Cl^- and the hydronium/water molecules, the OH stretching mode of H_3O^+ that is H-bonded to Cl^- appears at ~3000 cm^{-1}. A blue shift of this mode to ~3200 cm^{-1} is found in the 8E1E isomer in which four hydrogen bonds are formed between the Cl^- ion and hydronium/water molecules. By contrast, a large red shift of the same mode to ~2200 cm^{-1} is seen in the 4D1E isomer where only two hydrogen bonds are formed between the Cl^- ion and the hydronium/water molecules. The blue (red) shift is mainly caused by weaker (stronger) H_3O^+-Cl^- interactions in 8E1E (4D1E) relative to other isomers.

The peaks associated with the OH stretches of H_2O molecules that are H-bonded to the Cl^- ion are shown in blue in Figure 3.2. In this case, only slight shifts are observed in 4D1E and 8E1E compared to other isomers that contain three hydrogen bonds formed between the Cl^- ion and hydronium/water molecules. These results indicate that the OH stretches of H_2O molecules that are H-bonded with Cl^- are less perturbed than those of H_3O^+ H-bonded to Cl^-. The strong perturbation of the OH stretches of H_3O^+ in 4D1E is caused by the strong attraction between the H_3O^+ and Cl^- ions, leading to the large red shift of the corresponding OH spectral feature.

As described in Section 4.4.1, dangling OH stretches are located at ~3750 cm^{-1} while water and hydronium bending modes are found at ~1600 cm^{-1}. The (black) peaks in the region between 2600 cm^{-1} and 3600 cm^{-1} are assigned to the OH stretches of H-bonded water molecules. The bands in the region between 2600 cm^{-1} and 2840 cm^{-1} of each isomer are assigned to H-bonded OH stretches of water molecules next to the hydronium ion. As discussed above, the large red shifts relative to the OH stretch band observed in bulk water (3200~3600 cm^{-1}) are caused by the redistribution of the excess positive charge over the neighboring water molecules. One exception is the peak at ~2900 cm^{-1} in 7A2E which is assigned to the OH stretch of an AAD-type water molecule (this molecule is shown in blue in structure 7A2E in Figure 3.2). In this case, a four-membered ring is formed by the AAD-type water, the hydronium ion, and two water molecules next to the hydronium ion. The ring geometry enables the redistribution of the excess positive charge from the hydronium ion to the neighboring water molecules as well as to the AAD-type water molecule.

3.4.3. Zundel- and $H_7O_3^+$-type complexes

Four representative $HCl(H_2O)_n$ clusters and their corresponding IR spectra are shown in Figure 3.3. Two clusters (4A1Z and 8F1Z) contain Zundel-type structures with one shared proton while the other two clusters (7C1Z and 9D1Z) contain $H_7O_3^+$-type complexes with two identical shared protons. We first focus on the spectroscopic features associated with the two identical shared protons in 7C1Z and 9D1Z. It is important to emphasize that these two protons are identical in a dynamic sense after taking into account their motion within the cluster. In order to characterize their dynamic identity, we have monitored the quantity $\delta = r_{O_aH^*} - r_{O_bH^*}$ along the MD trajectory, where $r_{O_aH^*}$ and $r_{O_bH^*}$ are the distances between the shared proton (H^*) and the two closest oxygen atoms (O_a and O_b), respectively. As an example, the time evolution of δ obtained from NVE simulations of 9D1Z at 50 K is shown in Figure 4. Clearly, δ displays the same periodic, though out-of-phase, oscillation for both protons. Three representative states of this oscillation are shown in Figure 4. In states (a) and (c), one of the two shared protons corresponds to a Zundel-type shared proton with δ = 0 Å, while in state (b), the two shared protons resemble the hydronium protons in Eigen-like-type structures, with δ = 0.07 Å. Based on this analysis, it should be expected to find IR features associated with the two shared protons in both Zundel- and Eigen-like-type frequency ranges. It is straightforward to assign the band around 1200 cm^{-1} to the proton oscillation of the Zundel-type structure in states (a) and (c), and the peak at 2200 cm^{-1} to the OH symmetric stretch of the two shared protons of the Eigen-like-type structure in state (b). A strong peak at ~1420 cm^{-1} (in orange in Figure 3.3) is assigned to the OH asymmetric

stretch of the two shared protons in the Eigen-like-type state. This peak appears at frequencies similar to those of the water HOH bend.

To verify this assignment, we have analyzed the power spectrum obtained from the Fourier transform of the velocity-velocity correlation function calculated using the projection of the shared-proton velocity vector into the corresponding OH stretches. This projection takes into account only the contribution of the shared-proton motion along the OH stretch direction and thus separates the HOH bending and OH stretching modes involving H^*. From this analysis, the peaks appearing at ~1420 cm^{-1} in the IR spectra of 7C1Z and 9D1Z are thus assigned to the asymmetric OH stretch involving the two identical shared protons in the Eigen-like-type configuration. The symmetric and asymmetric OH stretches of the Eigen-like-type state in the $H^+(H_2O)_3$ complex of 7C1Z and 9D1Z appear at ~2200 cm^{-1} and ~1420 cm^{-1}, respectively. Recalling that the symmetric and asymmetric OH stretches of Eigen-type structures in 4B1E and 7A1E (shown in Figure 3.1 and discussed in Section 4.4.1) are located at ~2800 cm^{-1} and ~2200 cm^{-1}, respectively, it is found that both symmetric and asymmetric OH stretches in the $H^+(H_2O)_3$ complex of 7C1Z and 9D1Z have strong red shifts relative to the corresponding modes in Eigen-type structures. Due to the removal of one water molecule from the hydration shell of the hydronium ion in Eigen-type structures, the excess charge is transferred to the other two shared protons, pulling the two solvating water molecules closer to the hydronium core and thereby red-shifting the associated OH stretch bands.[32]

The assignment of the IR spectra associated with both Zundel and the $H_7O_3^+$-type complexes is discussed in the following. The IR bands resulting from the oscillation of the shared proton along the O-O intermolecular axis are located at ~1170 cm^{-1} in both

4A1Z and 8F1Z (in red in Figure 3.3). Weak blue shifts (< 100 cm^{-1}) of the proton oscillations are found in 7C1Z and 9D1Z, with sharp peaks (in orange in Figure 3.3) appearing at ~1420 cm^{-1}. The latter are assigned to the asymmetric OH stretch involving two identical shared protons of Eigen-like-type configurations. The features at ~1600 cm^{-1} are assigned to hydronium and water bending modes. The IR peaks between 2000 and 2300 cm^{-1} (in green in Figure 3.3) are assigned to the OH stretching modes of H_2O molecules in Zundel-type complexes (4A1Z and 8F1Z) as well as to the OH symmetric stretching mode of the two identical shared protons in the $H_7O_3^+$ structures (7C1Z and 9D1Z). The OH stretching modes of water molecules that are H-bonded to the chloride ion are shown in blue. The IR bands in the frequency range between 2600 cm^{-1} and 3600 cm^{-1} are assigned to H-bonded OH stretches of the water molecules. The sharp peak at ~2900 cm^{-1} in 9D1Z is assigned to the H-bonded OH stretch of an AAD-type water molecule (this molecule is shown in blue in structure 9D1Z in Figure 3.3).

3.4.4. Intermediate Zundel-Eigen-type complexes

The IR spectra of $HCl(H_2O)_n$ clusters with intermediate Zundel-Eigen-type structures, $H_5O_2^+(H_2O)_3Cl^-$, are shown in Figure 3.5. All clusters except 4C1I are characterized by the same first solvation shell, consisting of one Cl^- and three water molecules around the $H_5O_2^+$ core. In 4C1I, the $H_5O_2^+$ core is solvated by only two water molecules and the Cl^- ion. Despite these similarities, characteristic bands originating from OH stretches of $H_5O_2^+$ are found over a wide range of frequencies. To unravel the effects of structural changes on the vibrational bands, the water molecules in $H_5O_2^+(H_2O)_3Cl^-$ are labeled based on their location within the cluster as shown in Figure

3.6c. The H_2O molecule labeled as "a" has two OH bonds coordinated with water molecules in the first solvation shell. The IR features associated with these OH stretches (in green in Figure 3.5) are found at frequencies as low as ~2250 cm^{-1} in 10A1I and as high as ~3470 cm^{-1} in 8C1I. The OH bonds of the H_2O molecule labeled as "b" in Figure 3.6c are coordinated to the Cl^- ion and a water molecule, respectively. In small clusters (4C1I, 6D1I and 7E1I) the vibrational frequencies of the OH bond coordinated to Cl^- (in pink in Figure 3.5) are red shifted by several hundred wavenumbers relative to those of the OH bond coordinated to a water molecule (in orange in Figure 3.5). By contrast, large blue shifts of the OH stretches coordinated to Cl^- are found in large clusters (four bottom traces in Figure 3.5). The bands associated with the OH stretching modes of H_2O molecules that are H-bonded to Cl^- are shown in blue in Figure 3.5. As the number of H-bonds to Cl^- increases from two to four, blue shifts of the OH stretches to Cl^- are observed, similarly to those found in Eigen- and Eigen-like-type complexes. The wide distribution of OH frequencies is due to both charge delocalization and subtle changes in the hydrogen-bonding topologies. A detail analysis of the IR features associated with the $H_5O_2^+(H_2O)_3Cl^-$ clusters is discussed in the following section along with the analysis of the IR spectra of the $HCl(H_2O)_{10}$ and $HCl(H_2O)_{21}$ clusters.

An interesting feature of the IR spectra of clusters containing the $H_5O_2^+(H_2O)_3Cl^-$ moiety is associated with the shared-proton oscillation. Since the IR band associated with this mode (in red in Figure 3.5) is located in the same frequency range as the bending modes, the velocity projection method (as described in section 4.4.3) was used to uniquely assign the two vibrations. It has been established experimentally that molecular species that are H-bonded to a water molecule of the $H_5O_2^+$ core lead to an increase in the

proton affinity of the same water molecule, thereby causing a blue shift of the shared-proton oscillation.[33] A similar blue shift is observed here in all isomers containing the $H_5O_2^+(H_2O)_3Cl^-$ moiety due to the asymmetric solvation shell around the $H_5O_2^+$ core. In all cases, bands associated with shared-proton oscillation are 500-600 cm^{-1} blue-shifted relative to the proton oscillation frequency found in the Zundel-type structure 4A1Z.

3.4.5 IR spectra of $HCl(H_2O)_{10}$ and $HCl(H_2O)_{21}$ clusters

To better characterize the spectroscopic features associated with the $H_5O_2^+(H_2O)_3Cl^-$ moiety, the IR spectra corresponding to the global minima of $HCl(H_2O)_{10}$ and $HCl(H_2O)_{21}$ are also analyzed. Both global minima contain the same intermediate Zundel-Eigen-type complex but differ in the location of the excess proton within the cluster: for n = 10 the excess proton is closer to the water molecule "a" in Figure 3.6c while for n = 21 the excess proton is closer to water "b". To investigate the relationship between position of the excess proton and spectroscopic features, the time dependence of $\delta = r_{O_aH^*} - r_{O_bH^*}$ was calculated for the $H_5O_2^+$ core in the $HCl(H_2O)_{10}$ and $HCl(H_2O)_{21}$ clusters along the MD trajectory (Figure 3.7). In both cases, δ exhibits Gaussian distributions with mean values corresponding to -0.1 Å and 0.06 Å for n = 10 and n = 21, respectively. These distributions imply that the excess proton forms hydronium-like-type structures with water "a" when n = 10 cluster and with water "b" when n = 21. Combining this analysis with the power spectra obtained from the relevant atomic velocity autocorrelation functions, the frequency assignment of the vibrational modes associated with the $H_5O_2^+$ core in clusters with n = 10 and 21 becomes straightforward. In both clusters, the excess proton oscillation appears at ~1650 cm^{-1} (in

red in Figure 3.8). The IR peaks found at ~2200 cm^{-1} in both spectra are assigned to OH stretches of water molecules "a" and "b" for n = 10 and n = 21, respectively. This assignment is in agreement with the excess proton dynamics analyzed in Figure 3.7. For n = 10, the OH stretches (H-bonded to molecule "e") of the water molecule "b" appear at 2800 cm^{-1} (in orange in Figure 3.8), while those of the water molecule "a" for n = 21 are found at 2820 and 2870 cm^{-1} (in green in Figure 3.8).

3.5. Conclusions

It is known that the excess-proton-containing "core ion" in $HCl(H_2O)_n$ clusters displays different structural arrangements: the excess proton can either strongly bind a single water molecule forming a hydronium ion (H_3O^+) or be shared between two water molecules forming the Zundel ion ($H_5O_2^+$). Due to the asymmetry of the solvation shells, the "core ion" can then form Eigen-like, $H_7O_3^+$, and intermediate Zundel-Eigen-type structures. In this study, we have analyzed the spectroscopic features associated with the excess proton generated by the HCl dissociation in $HCl(H_2O)_n$ clusters using Born-Oppenheimer molecular dynamics simulations with the PM3-MAIS semiempirical Hamiltonian. The frequencies of the vibrational modes associated with the excess proton are found to vary from ~1175 cm^{-1} for the proton oscillation in Zundel-type configurations, to 1670-1800 cm^{-1} for OH stretches in intermediate Zundel-Eigen-type configurations, and ~2820 cm^{-1} for H_3O^+ stretches in Eigen-type configurations. These pronounced shifts can be explained by considering the different "core ion" structures and charge redistribution. Headrick et al. reported shifts of up to 1600 cm^{-1} for vibrational modes associated with the excess proton in protonated water clusters, with features at

1085 cm^{-1} and 2665 cm^{-1} being assigned to the shared proton oscillation of the Zundel ion and to the OH stretches of the Eigen ion, respectively.[32] A difference of ~1645 cm^{-1} between the Zundel-type proton oscillation the Eigen-type H_3O^+ stretches is found in the IR spectra calculated for the $HCl(H_2O)_n$ clusters, in good agreement with the experimental measurements of Ref. [32].

Some differences between measured and calculated vibrational frequencies exist, which are likely due to inaccuracies of PM3-MAIS. Nonetheless, the calculated IR spectra correctly reproduce the relevant spectroscopic features associated with specific vibrational modes of the $HCl(H_2O)_n$ clusters. In particular, unique spectroscopic signatures are identified for each excess proton-containing "core ion" structure and hydrogen-bonding topology. These unique signatures directly connect structural and dynamical properties, and can thus guide the interpretation of the experimental spectra.

3.6. Acknowledgments

This research was supported by the National Science Foundation through grant CHE-1111364. This work used the Extreme Science and Engineering Discovery Environment (XSEDE), which is supported by National Science Foundation grant number OCI-1053575 (allocation TG-CHE110009).

Chapter 3 contains materials from "Infrared Spectra of $HCl(H_2O)_n$ Clusters: A Born-Oppenheimer Molecular Dynamics Simulations" currently being prepared for submission for publication authored by Wei Lin and Francesco Paesani. All material has been reproduced with the consent of all other authors.

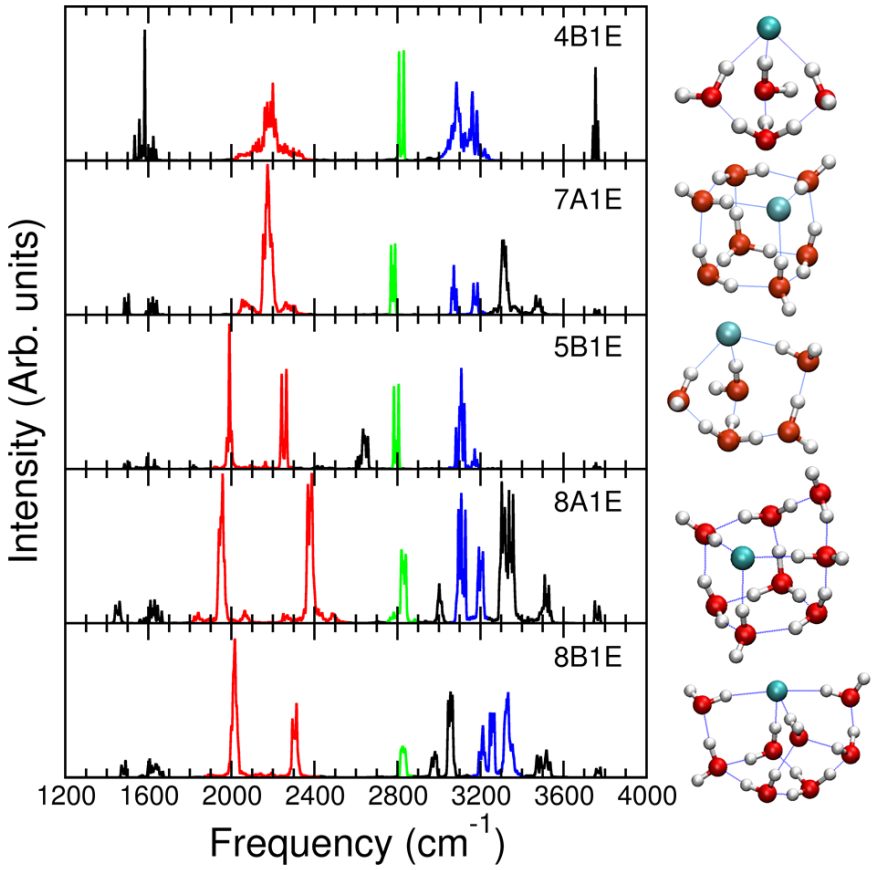

Figure 3.1. Infrared spectra of $HCl(H_2O)_n$ clusters containing Eigen-type structures. The H_3O^+ asymmetric and symmetric stretches are shown in red and green, respectively. The blue feature is assigned to the OH stretch of H_2O that is H-bonded to the chloride ion. The corresponding cluster structures are shown next to each IR spectrum. Cl, O and H atoms are shown in cyan, red and white, respectively.

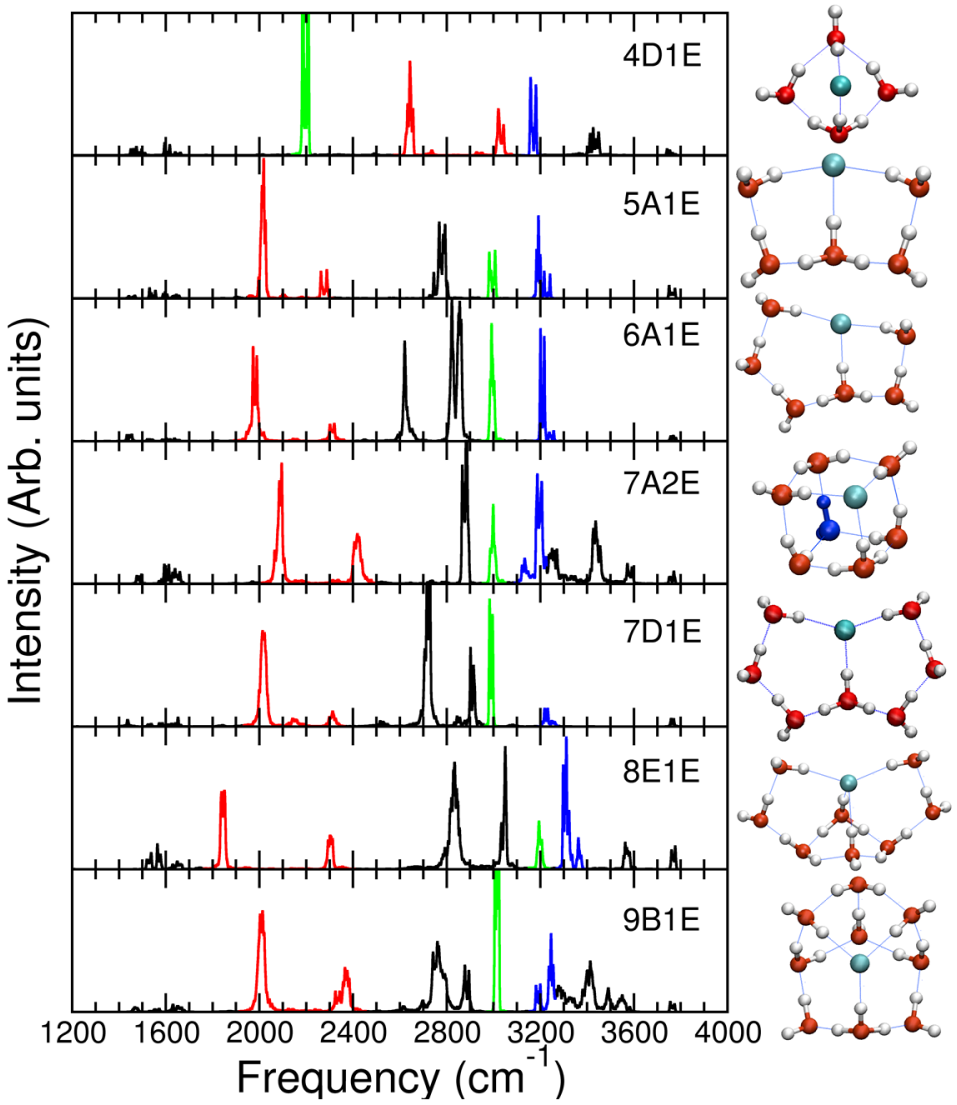

Figure 3.2. IR spectra of $HCl(H_2O)_n$ clusters with Eigen-like-type structures, $H_3O^+(H_2O)_2Cl^-$, in which one H_2O molecule of the Eigen ion is replaced by Cl^-. The H_3O^+ asymmetric stretches are shown in red, and the OH stretch of H_3O^+ H-bonded to the chloride ion is shown in green. The blue feature is assigned to the OH stretch of H_2O that is H-bonded to Cl^-. The corresponding cluster structures are shown next to each IR spectrum. Cl, O and H atoms are shown in cyan, red and white, respectively.

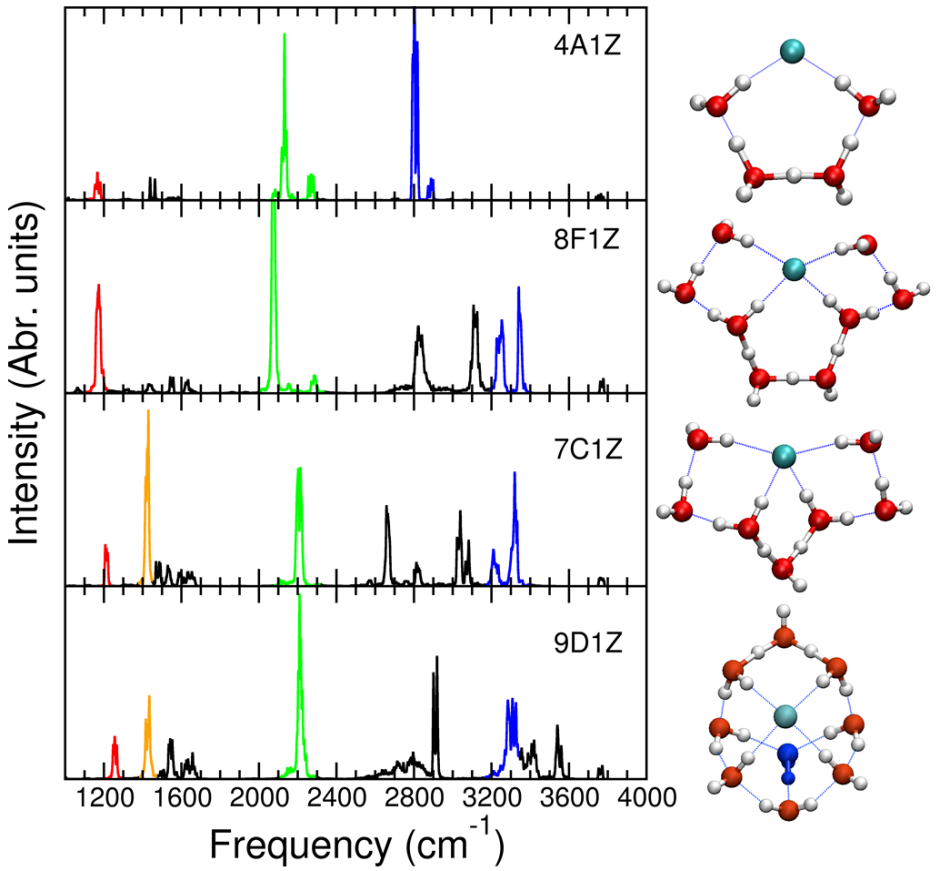

Figure 3.3. IR spectra of $HCl(H_2O)_n$ clusters with Zundel (top two traces) and $H_7O_3^+$ (bottom two traces) type structures. The red feature indicates the shared proton oscillation. OH stretches of H_2O in $H_5O_2^+$ are shown in green. The asymmetric and symmetric stretches of two identical shared protons in $H_7O_3^+$ are shown in orange and green, respectively. The blue feature is assigned to the OH stretch of H_2O that is H-bonded to the chloride ion. The corresponding cluster structures are shown next to each IR spectrum. Cl, O and H atoms are shown in cyan, red and white, respectively.

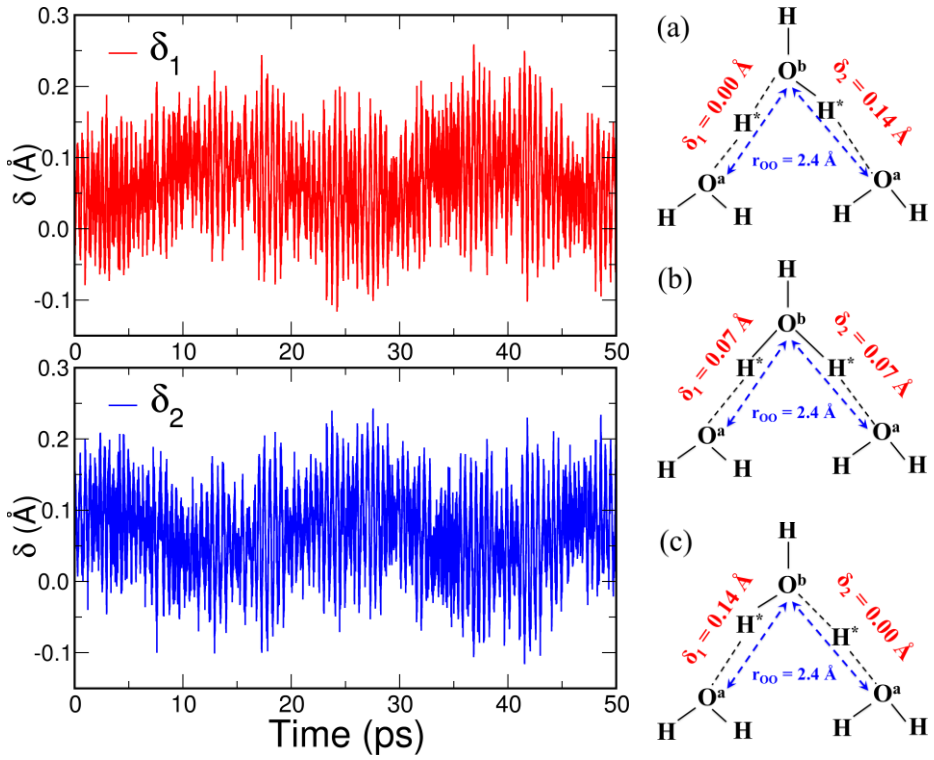

Figure 3.4. Left: $\delta = r_{O_a H^*} - r_{O_b H^*}$ calculated for the $H_7O_3^+$ moiety in the structure 9D1Z of the $HCl(H_2O)_9$ cluster along the MD trajectory. Right: three representative configurations of $H_7O_3^+$.

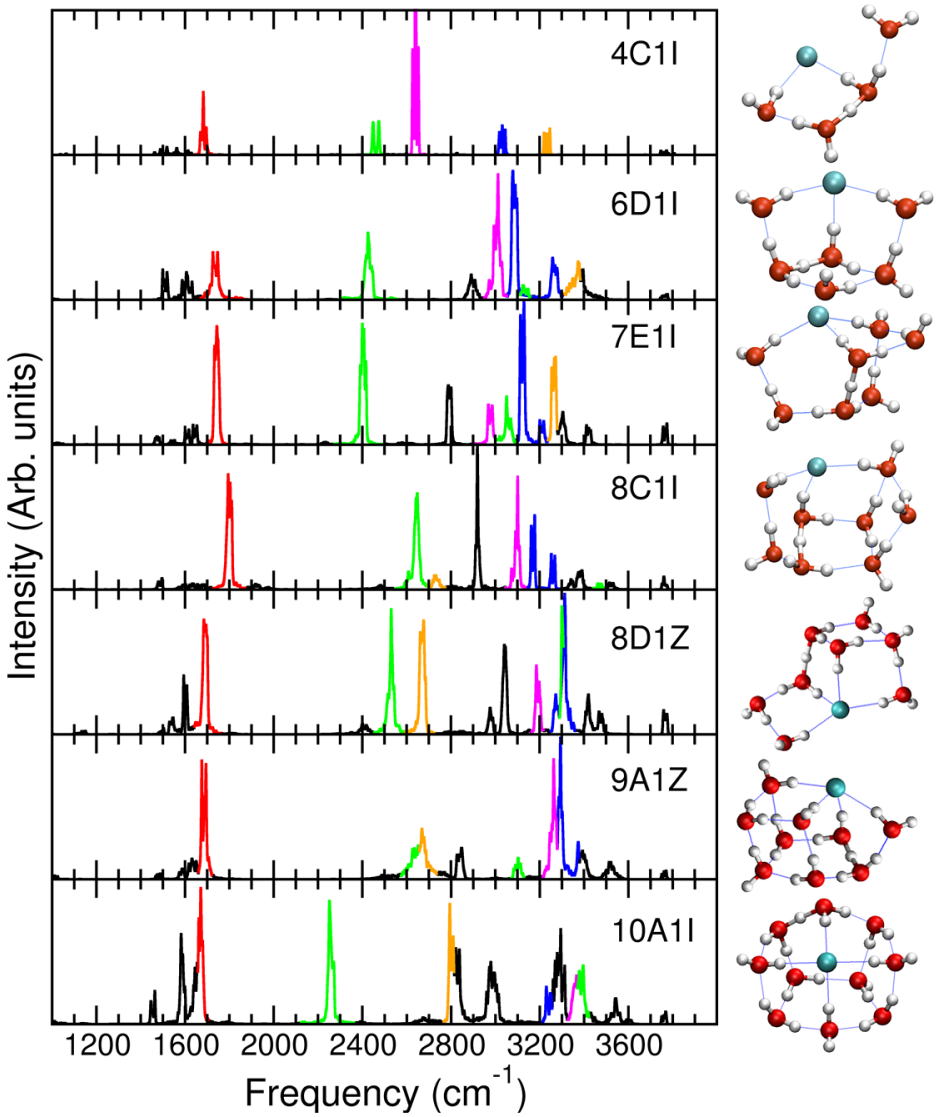

Figure 3.5. IR spectra of the $HCl(H_2O)_n$ clusters with intermediate Zundel-Eigen-type structures. The red feature indicates the shared proton oscillation. The H_2O molecule in $H_5O_2^+$ (water "b" in Figure 3.6c) displays two different stretches: the OH stretch to water "e" is shown in orange, while the OH stretch to the chloride ion is shown in pink. The OH stretches of water "a" in Figure 3.6c are shown in green. The blue feature is assigned to the OH stretch of the H_2O molecule that is H-bonded to Cl^-. The corresponding cluster structures are shown next to each IR spectrum. Cl, O and H atoms are shown in cyan, red and white, respectively.

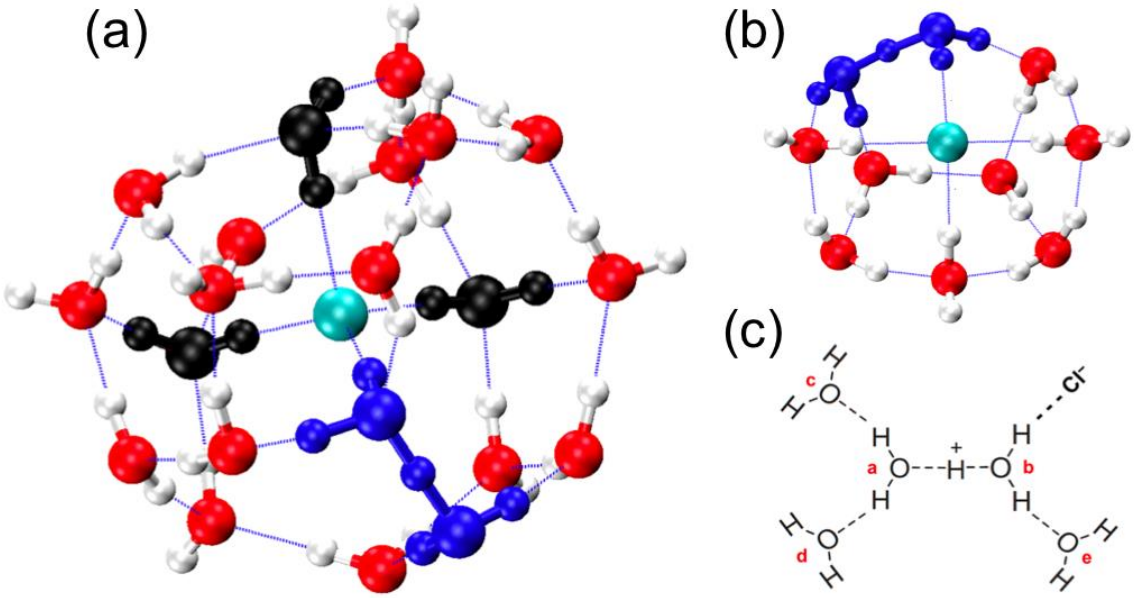

Figure 3.6. (a) Global minimum-energy structure of the $HCl(H_2O)_{21}$ cluster in which the $H_5O_2^+$ complex is shown in blue. The AADD-type (A indicates a H-bond acceptor and D indicates a H-bond donor) water molecule is shown in black. (b) Global minimum-energy structure of the $HCl(H_2O)_{10}$ cluster in which the $H_5O_2^+$ complex is shown in blue. (c) Schematic representation of the $H_5O_2^+$ ion along with its first solvation shell corresponding to the $H_5O_2^+(H_2O)_3Cl^-$ moiety. Labels from "a" to "e" are used to identify the surrounding water molecules.

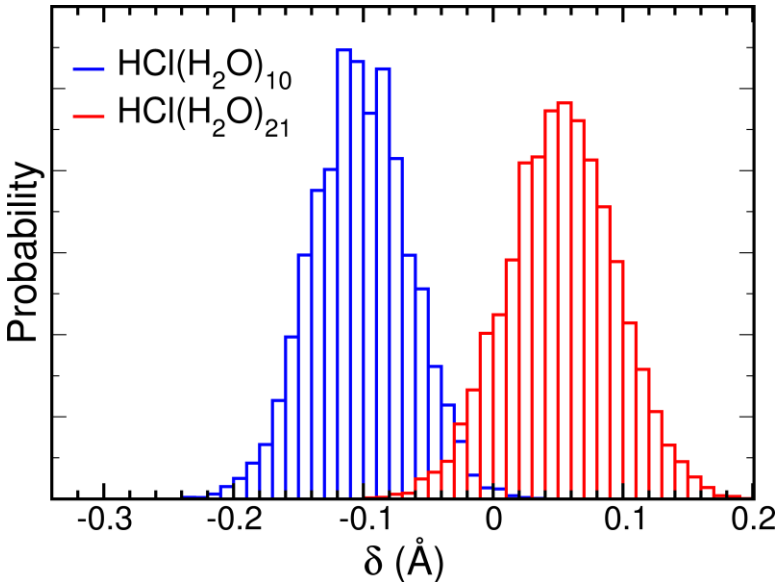

Figure 3.7. Normalized distributions of the quantity $\delta = r_{O_aH^*} - r_{O_bH^*}$ calculated for the $H_5O_2^+$ moiety in the $HCl(H_2O)_{10}$ and $HCl(H_2O)_{21}$ clusters. O_a and O_b indicate the oxygen atoms of the water molecules labeled as "a" and "b" in Figure 3.6c, respectively.

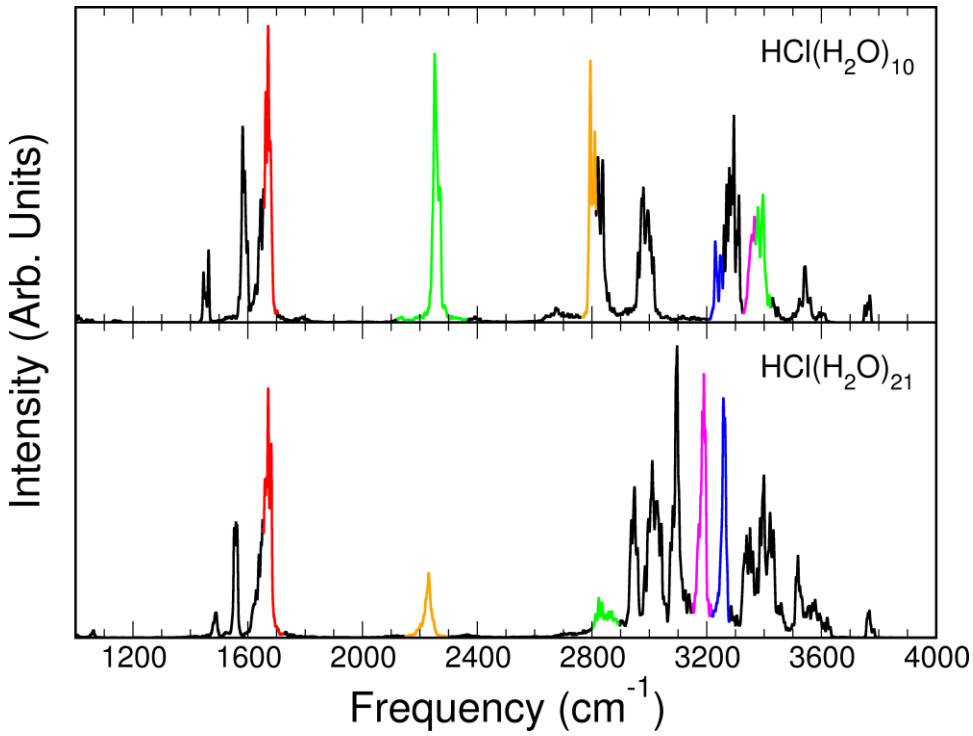

Figure 3.8. Calculated IR spectra for the global minimum-energy structures of the $HCl(H_2O)_{10}$ and $HCl(H_2O)_{21}$ clusters. The red feature indicates the shared proton oscillation in $H_5O_2^+$. The OH stretches of the H_2O molecule "a" in Figure 3.6c are shown in green. The OH stretches of the H_2O molecule "b" in Figure 3.6c are shown in orange (OH H-bonded to a water molecule) and in pink (OH H-bonded to the chloride ion). The blue feature is assigned to the OH stretch of the H_2O molecule that is H-bonded to the chloride ion.

3.7. References

(1) Finlayson-Pitts, B. J.; Pitts, J. N., Jr. *Chemistry of the upper and lower atmosphere: Theory, experiments and applications*; Academic Press: San Diego, CA, 2000.

(2) Leopold, K. R. Hydrated Acid Clusters. *Annu. Rev. Phys. Chem.* **2011**, *62*, 327-349.

(3) Molina, M. J.; Tso, T. L.; Molina, L. T.; Wang, F. C. Y. Antarctic Stratospheric Chemistry of Chlorine Nitrate, Hydrogen-Chloride and Ice - Release of Active Chlorine. *Science* **1987**, *238*, 1253-1257.

(4) McNeill, V. F.; Loerting, T.; Geiger, F. M.; Trout, B. L.; Molina, M. J. Hydrogen chloride-induced surface disordering on ice. *Proc. Natl. Acad. Sci. U.S.A.* **2006**, *103*, 9422-9427.

(5) McNeill, V. F.; Geiger, F. M.; Loerting, T.; Trout, B. L.; Molina, L. T.; Molina, M. J. Interaction of hydrogen chloride with ice surfaces: The effects of grain size, surface roughness, and surface disorder. *J. Phys. Chem. A* **2007**, *111*, 6274-6284.

(6) Ishikawa, Y.; Bacelo, D. E.; Binning, R. C. Ab initio Monte Carlo simulated annealing study of $HCl(H_2O)_n$ (n=3, 4) clusters. *J. Phys. Chem. A* **1999**, *103*, 4631-4640.

(7) Kim, K. S.; Odde, S.; Mhin, B. J.; Lee, S.; Lee, H. M. Dissociation chemistry of hydrogen halides in water. *J. Chem. Phys.* **2004**, *120*, 9524-9535.

(8) Lee, C. T.; Sosa, C.; Planas, M.; Novoa, J. J. A theoretical study of the ionic dissociation of HF, HCl, and H_2S in water clusters. *J. Chem. Phys.* **1996**, *104*, 7081-7085.

(9) Milet, A.; Struniewicz, C.; Moszynski, R.; Wormer, P. E. S. Theoretical study of the protolytic dissociation of HCl in water clusters. *J. Chem. Phys.* **2001**, *115*, 349-356.

(10) Forbert, H.; Masia, M.; Kaczmarek-Kedziera, A.; Nair, N. N.; Marx, D. Aggregation-Induced Chemical Reactions: Acid Dissociation in Growing Water Clusters. *J. Am. Chem. Soc.* **2011**, *133*, 4062-4072.

(11) Gutberlet, A.; Schwaab, G.; Birer, O.; Masia, M.; Kaczmarek, A.; Forbert, H.; Havenith, M.; Marx, D. Aggregation-Induced Dissociation of $HCl(H_2O)_2$ Below 1 K: The Smallest Droplet of Acid. *Science* **2009**, *324*, 1545-1548.

(12) Takayanagi, T.; Takahashi, K.; Kakizaki, A.; Shiga, M.; Tachikawa, M. Path-integral molecular dynamics simulations of hydrated hydrogen chloride cluster $HCl(H_2O)_4$ on a semiempirical potential energy surface. *Chem. Phys.* **2009**, *358*, 196-202.

(13) Sugawara, S.; Yoshikawa, T.; Takayanagi, T.; Tachikawa, M. Theoretical study on mechanisms of structural rearrangement and ionic dissociation in the $HCl(H_2O)_4$

cluster with path-integral molecular dynamics simulations. *Chem. Phys. Lett.* **2011**, *501*, 238-244.

(14) Walewski, L.; Forbert, H.; Marx, D. Quantum Induced Bond Centering in Microsolvated HCl. *J. Phys. Chem. Lett.* **2011**, *2*, 3069-3074.

(15) Lin, W.; Paesani, F. Systematic Study of Structural and Thermodynamic Properties of $HCl(H_2O)_n$ Clusters from Semiempirical Replica Exchange Simulations. *J. Phys. Chem. A* **2013**, *117*, 7131-7142.

(16) Huneycutt, A. J.; Stickland, R. J.; Hellberg, F.; Saykally, R. J. Infrared cavity ringdown spectroscopy of acid–water clusters: HCl–H_2O, DCl–D_2O, and DCl–$(D_2O)_2$. *J. Chem. Phys.* **2003**, *118*, 1221-1229.

(17) Fárník, M.; Weimann, M.; Suhm, M. A. Acidic protons before take-off: A comparative jet Fourier transform infrared study of small HCl– and HBr–solvent complexes. *J. Chem. Phys.* **2003**, *118*, 10120-10136.

(18) Skvortsov, D.; Lee, S. J.; Choi, M. Y.; Vilesov, A. F. Hydrated HCl Clusters, $HCl(H_2O)_{1-3}$, in Helium Nanodroplets: Studies of Free OH Vibrational Stretching Modes. *J. Phys. Chem. A* **2009**, *113*, 7360-7365.

(19) Flynn, S. D.; Skvortsov, D.; Morrison, A. M.; Liang, T.; Choi, M. Y.; Douberly, G. E.; Vilesov, A. F. Infrared Spectra of HCl-H_2O Clusters in Helium Nanodroplets. *J. Phys. Chem. Lett.* **2010**, *1*, 2233-2238.

(20) Weimann, M.; Farnik, M.; Suhm, M. A. A first glimpse at the acidic proton vibrations in HCl-water clusters via supersonic jet FTIR spectroscopy. *Phys. Chem. Chem. Phys.* **2002**, *4*, 3933-3937.

(21) Re, S.; Osamura, Y.; Suzuki, Y.; Schaefer, H. F. Structures and stability of hydrated clusters of hydrogen chloride, $HCl(H_2O)_n$, n=1-5. *J. Chem. Phys.* **1998**, *109*, 973-977.

(22) Odde, S.; Mhin, B. J.; Lee, S.; Lee, H. M.; Kim, K. S. Dissociation chemistry of hydrogen halides in water. *J. Chem. Phys.* **2004**, *120*, 9524-9535.

(23) Masia, M.; Forbert, H.; Marx, D. Connecting structure to infrared spectra of molecular and autodissociated HCl - Water aggregates. *J. Phys. Chem. A* **2007**, *111*, 12181-12191.

(24) Ndongmouo, U. F. T.; Lee, M. S.; Rousseau, R.; Baletto, F.; Scandolo, S. Finite-temperature effects on the stability and infrared spectra of $HCl(H_2O)_6$ clusters. *J. Phys. Chem. A* **2007**, *111*, 12810-12815.

(25) Letzner, M.; Gruen, S.; Habig, D.; Hanke, K.; Endres, T.; Nieto, P.; Schwaab, G.; Walewski, L.; Wollenhaupt, M.; Forbert, H.; Marx, D.; Havenith, M. High resolution spectroscopy of HCl-water clusters: IR bands of undissociated and dissociated clusters revisited. *J. Chem. Phys.* **2013**, *139*, 154304-154311.

(26) Bernal-Uruchurtu, M. I.; Arillo-Flores, O. I.; Ruiz-Lopez, M. F. Can semi-empirical models describe HCl dissociation in water? *Theor. Chem. Acc.* **2007**, *118*, 425-435.

(27) Bernal-Uruchurtu, M. I.; Ruiz-Lopez, M. F. Basic ideas for the correction of semiempirical methods describing H-bonded systems. *Chem. Phys. Lett.* **2000**, *330*, 118-124.

(28) Andrea, T. A.; Swope, W. C.; Andersen, H. C. The Role of Long Ranged Forces in Determining the Structure and Properties of Liquid Water. *J. Chem. Phys.* **1983**, *79*, 4576-4584.

(29) Case, D. A.; Darden, T. A.; Cheatham, T. E., III ; Simmerling, C. L.; Wang, J.; Duke, R. E.; Luo, R.; Walker, R. C.; Zhang, W.; Merz, K. M.; Roberts, B.; Hayik, S.; Roitberg, A.; Seabra, G.; Swails, J.; Gotez, A. W.; Kolossváry, I.; Wong, K. F.; Paesani, F.; Vaníček, J.; Wolf, R. M.; Liu, J.; Wu, X.; Brozell, S. R.; Steinbrecher, T.; Gohlke, H.; Cai, Q.; Ye, X.; Wang, J.; Hsieh, M.-J.; Cui, G.; Roe, D. R.; Mathews, D. H.; Seetin, M. G.; Salomon-Ferrer, R.; Sagui, C.; Babin, V.; Luchko, T.; Gusarov, S.; Kovalenko, A.; Kollman, P. A.; AMBER 12 ed.; University of California - San Francisco: San Francisco, 2012.

(30) Ramirez, R.; Lopez-Ciudad, T.; Kumar, P.; Marx, D. Quantum corrections to classical time-correlation functions: Hydrogen bonding and anharmonic floppy modes. *J. Chem. Phys.* **2004**, *121*, 3973-3983.

(31) Van Speybroeck, V.; Van Houteghem, M.; Verstraelen, T.; Van Neck, D.; Kirschhock, C.; Martens, J. A.; Waroquier, M. Atomic Velocity Projection Method: A New Analysis Method for Vibrational Spectra in Terms of Internal Coordinates for a Better Understanding of Zeolite Nanogrowth. *J. Chem. Theory Comput.* **2011**, *7*, 1045-1061.

(32) Headrick, J. M.; Diken, E. G.; Walters, R. S.; Hammer, N. I.; Christie, R. A.; Cui, J.; Myshakin, E. M.; Duncan, M. A.; Johnson, M. A.; Jordan, K. D. Spectral signatures of hydrated proton vibrations in water clusters. *Science* **2005**, *308*, 1765-1769.

(33) Olesen, S. G.; Guasco, T. L.; Roscioli, J. R.; Johnson, M. A. Tuning the intermolecular proton bond in the $H_5O_2^+$ 'Zundel ion' scaffold. *Chem. Phys. Lett.* **2011**, *509*, 89-95.

(34) Marx, D.; Tuckerman, M. E.; Hutter, J.; Parrinello, M. The nature of the hydrated excess proton in water. *Nature* **1999**, *397*, 601-604.

(35) Shin, J. W.; Hammer, N. I.; Diken, E. G.; Johnson, M. A.; Walters, R. S.; Jaeger, T. D.; Duncan, M. A.; Christie, R. A.; Jordan, K. D. Infrared signature of structures associated with the $H^+(H_2O)_n$ (n=6 to 27) clusters. *Science* **2004**, *304*, 1137-1140.

(36) Miyazaki, M.; Fujii, A.; Ebata, T.; Mikami, N. Infrared spectroscopic evidence for protonated water clusters forming nanoscale cages. *Science* **2004**, *304*, 1134-1137.

Chapter 4. Negative ion photoelectron spectroscopy reveals thermodynamic advantage of organic acids in facilitating formation of bisulfate ion clusters: atmospheric implications

4.1. Abstract

Recent lab and field measurements have indicated critical roles of organic acids in enhancing new atmospheric aerosol formation. Such findings have stimulated theoretical studies with the aim of understanding interaction of organic acids with common aerosol nucleation precursors like bisulfate (HSO_4^-). In this chapter, we report a combined negative ion photoelectron spectroscopic and theoretical investigation of molecular clusters formed by HSO_4^- with succinic acid (SUA, $HO_2C(CH_2)_2CO_2H$), $HSO_4^-(SUA)_n$ (n = 0-2), along with $HSO_4^-(H_2O)_n$ and $HSO_4^-(H_2SO_4)_n$. It is found that one SUA molecule can stabilize HSO_4^- by ca. 39 kcal/mol, triple the corresponding value that one water molecule is capable of (ca. 13 kcal/mol). Molecular dynamics simulations and quantum chemical calculations reveal the most plausible structures of these clusters and attribute the stability of these clusters due to formation of strong hydrogen bonds. This work provides direct experimental evidence showing significant thermodynamic advantage by involving organic acid molecules to promote formation and growth in bisulfate clusters and aerosols.

4.2. Introduction

Atmospheric aerosols have received intense research attention last several decades as their importance in influencing climate change[1-3] and human health[4-7] has been gradually recognized. Aerosol formation and growth often begin with homogeneous nucleation, in which the first step involves two (binary) or three (ternary) gaseous species interacting with each other to form stable clusters and complexes to decrease nucleation free energy barriers.[8,9] Field measurements[10] have indentified sulfuric acid including bisulfate ion as key atmospheric nucleation precursors in several nucleation mechanisms, including binary H_2SO_4-H_2O,[11] ternary H_2O–H_2SO_4–NH_3[12,13] where NH_3 can also be replaced by amines,[14,15] and ion-mediated nucleation.[16,17] The roles of ions and organics in atmospheric nucleation have attracted researchers' interests recently, especially after atmospheric field measurements have revealed that aerosols often contain a considerable amount of organic matter[18-20] and ambient ions.[16,21,22] In 2004, Zhang and co-workers performed a landmark experiment indicating that nucleation rates of sulfuric acid aerosols can be considerably enhanced by the presence of a trace amount of aromatic acids.[23] This pioneering work has stimulated several experimental studies aimed at characterizing critical roles of different organic compounds in aerosol formations.[24-28]

Size-selected clusters with tunable compositions provide ideal model systems to

probe and untangle often complex intermolecular interactions important to formation of critical nuclei and nucleation embryos. Atmospherically relevant hydrated bisulfate/sulfuric acid clusters have been investigated using IR action spectroscopy,[29,30] mass spectrometry,[31-34] and quantum chemistry calculations.[35,36] Theoretical computations on several hydrogen-bonded clusters consisting of organic species with atmospheric nucleation precursors have been carried out very recently,[37-42] aimed at providing a molecular-level understanding of the mechanisms that allow organic acids to enhance (often significantly) aerosol formation and growth. One important finding from these calculations is that organic acids can form strong hydrogen bonds with nucleation precursors,[37-42] resulting in significant stabilization in energy and reducing nucleation free energy barriers.[8,43]

In this chapter, we report a low-temperature negative ion photoelectron spectroscopy (PES) study on solvation of HSO_4^- by a common dicarboxylic acid, succinic acid (SUA)[18] ($HO_2C(CH_2)_2CO_2H$, H_2DC_2 where DC_2 refers to dicarboxylate with two CH_2 groups) to help understand and experimentally probe the first nucleation step of bisulfate aerosols containing organic acids. Like IR spectroscopy that can directly provide the structural information, PES can determine the stabilization energy of HSO_4^- upon addition of the acid molecules through measurements of the associated the spectral electron binding energy (EBE) increase. In addition, molecular dynamics simulations and ab initio quantum calculations reveal the plausible structures for these clusters, and

provide the electron binding energies and association energies to compare with the experimental data. To determine the thermodynamic effects due to organic acids in the initial stage of nucleation, we also carried out PES investigations on $HSO_4^-(H_2O)_{1-2}$ and $HSO_4^-(H_2SO_4)_{1-2}$ (where H_2O and H_2SO_4 are important nucleation species in the atmosphere) and the results are directly compared with those obtained with SUA.

The $HSO_4^-(Sol)_n$ (Sol = SUA, H_2O, and H_2SO_4, n = 0-2) clusters were produced in the gas phase via electrospray ionization (ESI) of ~0.4 mM aqueous solutions of $(NBu_4)_2SO_4$ / SUA (1:1) or $NaHSO_4$ / H_2SO_4 (1:1) diluted three times in CH_3CN, and characterized by a low-temperature PES (The detailed description of this instrument was given in a recent publication,[44]). This ESI-PES combined with gas-phase theoretical calculations has been shown to be a powerful approach to obtain the geometric and electronic structures of clusters involving sulfate ions, water molecules, and various organic acids.[45-48]

4.3. Combination of experimental and computational results

Figure 4.1 presents the 20 K PE spectra of $HSO_4^-(Sol)_{0-2}$ (Sol = SUA, H_2SO_4, and H_2O) at 157 nm (7.867 eV). The 193 nm (6.424 eV) PE spectrum of HSO_4^- has been reported by Wang et al. in 2000,[49] and here its 157 nm spectrum shows two more band features (labeled as B, C). Interestingly, a vibrational progression was clearly resolved for

the C band with a frequency of 800 ± 40 cm^{-1}. We assigned this frequency to S–OH stretching mode according to the reported vibrational frequencies of the bisulfate ion,[29,30] which is also confirmed by our theoretical analysis (*vide infra*). On the basis of the rapidly rising onset energies for all $HSO_4^-(Sol)_1$ species, estimates of the adiabatic electron detachment energies (ADEs) of 4.75 (HSO_4^-), 6.45 ($HSO_4^{-\bullet}SUA$), 6.55 ($HSO_4^{-\bullet}H_2SO_4$), and 5.35 eV ($HSO_4^{-\bullet}H_2O$) were obtained (Table 4.1). One most surprising finding is that addition of one SUA or H_2SO_4 molecule has induced a huge electron binding energy (EBE) increase of ca. 1.7~1.8 eV for $HSO_4^-(SUA)$ and $HSO_4^-(H_2SO_4)$ from that of HSO_4^-, whereas one H_2O only induced about ca. 0.6 eV EBE increase. These EBE increases correspond to the binding energy differences between HSO_4^- and $HSO_4^\bullet$ with each solvent molecule, reflecting lower limits for the stabilization of the bisulfate anion by one SUA, sulfuric acid, and water molecule, i.e., 39.2, 41.5, and 13.8 kcal/mol respectively. The larger EBE increase brought by first SUA and H_2SO_4 than H_2O reflects the extent of the stabilization of the bisulfate ion by these two foreign molecules. This is the first direct experimental observation showing the remarkable thermodynamic advantage by involving organic acids in initial nucleation steps, and also in agreement with the much higher stability of $HSO_4^-(H_2SO_4)_n$ vs. $HSO_4^-(H_2O)_n$ found in recent computations and mass spectrometric measurements.[34,50,51]

The PE spectra of $HSO_4^-(Sol)_2$ exhibit further stabilization upon association of the second SUA, H_2SO_4, and H_2O molecules onto the respective mono-solvated clusters,

i.e. 0.15, 0.65, and 0.20 eV EBE increases, respectively, albeit at much smaller paces (Figure 4.1). There is a very long rising onset for the spectrum of $HSO_4^-(SUA)_2$, indicating either existence of multiple isomers (X′ and X) or large geometric changes upon photodetachment. The signal-to-noise ratio of the PE spectrum of $HSO_4^-(H_2SO_4)_2$ is poor, presumably due to its extremely high EBE considering it was taken under similar conditions (ion intensity and photon flux) as the other two clusters ($HSO_4^-(H_2O)_2$ and $HSO_4^-(SUA)_2$). Nevertheless, two spectral features at the extremely high EBE side, i.e., X′ of 7.2 eV and X with EBE >7.5 eV, can be identified in the spectrum. The experimentally estimated ADEs of all bisulfate clusters, along with their vertical detachment energies (VDEs), measured from the rising onset peak maxima, are listed in Table 4.1.

To better understand the experimentally observed spectra and obtain insights into the first nucleation step of atmospheric aerosols, we conducted structural analysis using replica exchange molecular dynamics (REMD) simulations[52] and quantum chemical calculations[53]. The potential energy surfaces of the clusters were first explored using REMD simulations using the semiempirical RM1 Hamiltonian.[54] The low-lying isomers (within 10 kcal/mol) obtained from the REMD simulations were further optimized using the B3LYP functional[55] with Pople's basis set 6-311++G(3df, 3pd)[56] followed by single point energy calculations using both MP2[57] and DFT (M06-2X)[58] methods. The validity and accuracy of the theoretical methods were confirmed by comparison of the calculated

geometries of H_2O, HSO_4^-, H_2SO_4, H_2DC_2 and HDC_2^- with the available experimental values and previous calculations.

The most stable structures along with the low-lying isomers that provide good agreement with the EBE measurements for $HSO_4^-(Sol)_n$ (Sol = SUA (H_2DC_2), H_2O and H_2SO_4) are shown in Figure 4.2. We only present our results for HSO_4^- for comparison, since this system has been studied thoroughly by Wang et al[49] and others[59]. The calculated geometric structures, vibrational frequencies as well as the ADE and VDE (X) are in excellent agreement with the experimental values.

There are two intermolecular H bonds between HSO_4^- and H_2DC_2, and one intramolecular H bond in H_2DC_2 in our optimized most stable structure of $HSO_4^-(H_2DC_2)_1$. It is interesting to note there is proton transfer from SUA acid (with the O—H bond length increasing from 0.969 Å in free SUA to 1.529 Å in the complex) to bisulfate ion upon forming cluster. The bond length of the newly formed (S)O—H is 1.030 Å, similar to the other one of 1.012 Å, and both being just slightly longer than that found in free sulfuric acid (0.967 Å). Proton transfer results in a very strong H-bond that can be understood by considering that the proton affinity of HSO_4^- (311.1/306.4±3.1 kcal/mol)[16] is very close to that of HDC_2^- (322.8 kcal/mol).[16] A similar proton transfer mechanism has been observed previously by Ehn et al[16] in $HSO_4^-\cdot C_3H_4O_4$.

As shown in Figure 4.2, the O···H···O contact distances are 2.558 and 2.617 Å

for the two intermolecular H bonds between SUA and HSO_4^-, and 2.593 Å for the intramolecular H bond of SUA. Therefore all three H bonds correspond to strong H bonds.[60] The complexation leads to a stronger intramolecular H bond (*d*(O⋯O) from 2.754 Å to 2.593 Å), which can be attributed to the increased negative electron density on $O_{c=o}$ (from -0.643 in H_2DC_2 to -0.795 in the cluster) due to proton transfer. Simultaneously, the charge of the shared transferred H_s increases from 0.498 to 0.512. Therefore, the molecular formula of this cluster can effectively be written as $(HSO_4^-)(H^+)(HDC_2^-)$ or $H_2SO_4(HDC_2^-)$ instead of $HSO_4^-(H_2DC_2)$.

The ADE and VDE calculated with the M06-2X functional are 6.27 eV and 7.19 eV, in good agreement with the experimental data and significantly larger than the corresponding values measured for free HSO_4^- (Table 4.1). This stabilization is due to the formation of multiple strong H bonds in the cluster.

The optimized structure of $HSO_4^-(H_2SO_4)$ possesses three intermolecular H bonds (Figure 4.2). Such structure has been identified in $HSO_4^-(H_2SO_4)(H_2O)_n$ by Froyd and Lovejoy.[34] Also in this case, the calculated ADE and VDE are in good agreement with the experimental values. Other isomers with two H bonds are all turned out to be energetically very high (> 5 kcal/mol) (Fig.S2).

Two nearly iso-energetic isomers of $HSO_4^-(H_2O)$ have been found (Figure 4.2). In isomer A, the H_2O molecule acts as double donor and single acceptor in forming 3 H

bonds, whereas in isomer B, the single H_2O molecule interacts with bisulfate via bifurcated H bonds. All H bonds in $HSO_4^-(H_2O)$ are not optimal due to the constrained O···H—O angles that are appreciably different from the ideal value of 180°. The comparison between the measured and calculated ADEs and VDEs suggests that both isomers A and B are present in the experiments. Similar conclusion has been drawn in an IRMPD study of $HSO_4^-(H_2O)_n$ by Yacovitch et al.[29]

Several low-lying isomers (within 4 kcal/mol at the B3LYP/6-311++G (3df, 3pd) level of theory) have been identified for $HSO_4^-(H_2DC_2)_2$, among which the two most stable structures are shown in Figure 4.2. Structure A has a linear configuration with HSO_4^- staying on one side and two H_2DC_2 molecules connected by one strong intermolecular H bond (d(O···O)=2.591 Å). This configuration is similar as the structure of $(C_2H_2O_4)_2(HSO_4^-)$ obtained by Xu et al.[37] Compared to $HSO_4^-(H_2DC_2)$, it appears that proton transfer from H_2DC_2 to HSO_4^- is more significantly. This can be attributed to the formation of the hydrogen bond between the two acid molecules that decreases the proton affinity of the carboxylic acid group. As a consequence, the molecular formula of this structure should probably be written as $(H_2SO_4)(HDC_2^-)(H_2DC_2)$. Isomer B also displays a linear structure, with HSO_4^- now lying between two H_2DC_2 molecules. A similar structure has been predicted for (H_2SO_4)(pinonic acid)$_2$ by Zhao et al[38] and has been shown to enable further growth of the cluster by addition of other nucleated species on both sides. The computed M06-2X ADEs for A (6.11 eV) and B (7.15 eV) fit well with

the experimental features of X′ (6.6 eV) and X (7.1 eV).

Six minima have been obtained for $HSO_4^-(H_2SO_4)_2$, several of which are also reported by Herb et al.[61] and by Froyd and Lovejoy[34](in monohydrated clusters). The two most stable structures are isomer A, where each H_2SO_4 molecule interacts with bisulfate via 2 H bonds and connects with each other via 1 H bond, and structure B, where one H_2SO_4 associates with bisulfate via 3 H bonds as in the case for $HSO_4^-(H_2SO_4)_1$ while the other H_2SO_4 solvates the empty side of bisulfate. The M06-2X ADE is ca. 7 eV for A and ca. 7.4 eV for B, in good agreement with the experimental X′ (7.2 eV) and X (7.5 eV) features.

Up to 12 isomers for $HSO_4^-(H_2O)_2$ are identified, with some of them being already reported in the literature.[29,35,50,62] The most stable clusters are isomer A_1 which can be viewed as a water dimer (connected by 1 H bond) interacting with the anion core, and isomer B_1 in which each H_2O molecule interacts only with one side of HSO_4^-. Again the calculated M06-2X ADEs for both isomers fit the observed spectrum well, suggesting that both isomers likely exist under the experimental conditions, which supports the observations of Yacovitch et al. derived from the IRMPD experiments.[29]

In order to further understand the roles of organic diacids in aerosol nucleation, we calculated the thermochemical parameters (e.g. binding energy, enthalpy, entropy, and Gibbs free energy) for the complex formation at 1 atm and 298K for the most stable

isomers shown in Figure 4.2. Our calculations show very large binding energies of 32 kcal/mol for $HSO_4^-(SUA)_1$ and ~50 kcal/mol for $HSO_4^-(SUA)_2$. These values are much larger than that of $HSO_4^-(H_2O)$ (~11 kcal/mol) and $HSO_4^-(H_2O)_2$ (~21 kcal/mol), in accord with the conclusions derived from the EBE increase that SUA can induce a larger stabilization of the bisulfate ion than H_2O. The Gibbs free energy changes (ΔG) for bisulfate associated with one and two SUA are calculated to be ca. -20 and -27 kcal/mol, respectively, much larger than the corresponding values, ca. -2.5 and -4.7 kcal/mol, for one and two water molecules. The large binding energies and negative Gibbs free energy changes for bisulfate-SUA clusters indicate that these complexes are very stable, thermodynamically favorable to form, and can survive for long times at atmospheric conditions. Consequently they may contribute to reducing nucleation barriers[17,63] and facilitate further growth into larger particles. Considering the abundance of organic dicarboxylic acid in the atmosphere[18,20], it is likely that organic dicarboxylic acids will play critical roles in stabilizing gaseous sulfuric acid/bisulfate ion by forming highly stable complex and promoting the aerosol nucleation.

4.4. Conclusions

In summary, the anionic complex clusters formed by key atmospheric nucleation species, such as sulfuric acid/bisulfate ion and a common organic diacid (succinic acid),

have been successfully produced by ESI, and their energetics and structures have been investigated by using low-temperature PES combined with theoretical calculations. The observed PE spectra show that these complexes possess very high EBEs, with a huge EBE increase (by 1.7 eV for the first SUA) relative to EBE of HSO_4^-, compared to the 0.6 eV EBE increase measured for the first H_2O. Replica exchange simulations and electronic structure calculations identify 3 strong H bonds in HSO_4^-(SUA), which serve as the driving force for the complex formation and account for the high stability of the complex. Comparison with other pre-nucleation species reveals that the formation of $HSO_4^-(SUA)_n$ anionic complexes is thermodynamically much more favorable than $HSO_4^-(H_2O)_n$. Given the abundance of organic diacids in the atmosphere, their complexion with sulfuric acid/bisulfate ion can significantly reduce the nucleation barrier, which will facilitate further growth of the new aerosol particles.

4.5. Acknowledgments

The experimental work done at Richland was supported by the Division of Chemical Sciences, Geosciences, and Biosciences, Office of Basic Energy Sciences, U. S. Department of Energy (DOE), and performed using EMSL, a national scientific user facility sponsored by DOE's Office of Biological and Environmental Research and located at Pacific Northwest National Laboratory, which is operated by Battelle

Memorial Institute for the DOE. FP was supported by the National Science Foundation through Grant CHE-1038028 (CCI Center for Aerosol Impacts on Climate and the Environment). The calculations were conducted on the ScGrid and Deepcomp7000 of the Supercomputing Center, Computer Network Information Center of Chinese Academy of Sciences, as well as on the Extreme Science and Engineering Discovery Environment (XSEDE) computational resources, which are supported by National Science Foundation Grant Number OCI-1053575 (allocation TG-CHE110009).

This chapter contains materials from "Negative Ion Photoelectron Spectroscopy Reveals Thermodynamic Advantage of Organic Acids in Facilitating Formation of Bisulfate Ion Clusters: Atmospheric Implications" published in 2013 in *Journal of Physical Chemistry Letters (Volume* 4, pages 779 to 785), authored by Gao-Lei Hou, Wei Lin, Shi-Hu Deng, Jian Zhang, Wei-Jun Zheng, Francesco Paesani, Xue-Bin Wang. All material has been reproduced with the consent of all other authors.

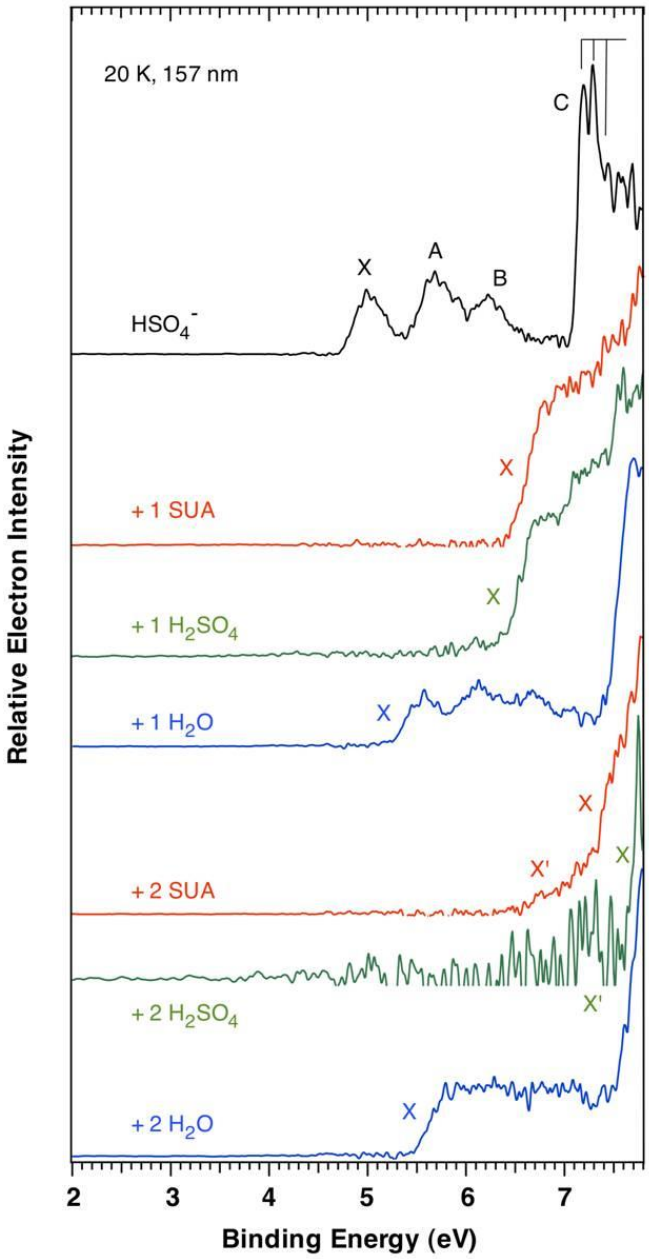

Figure 4.1. The 20 K photoelectron spectra of $HSO_4^-(Sol)_{0-2}$ (Sol = SUA, H_2SO_4, and H_2O) at 157 nm (7.867 eV). The vibrational progression of the C band of HSO_4^- is indicated.

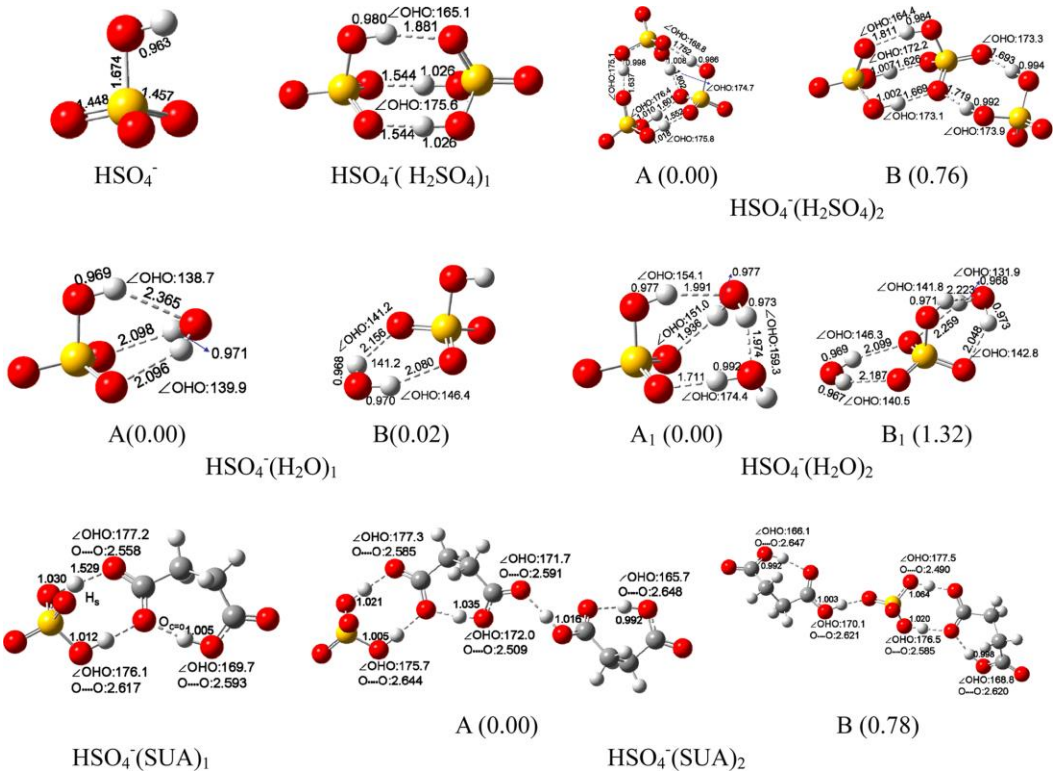

Figure 4.2. The most stable structures and low-lying isomers that show good agreement with the experiments of $HSO_4^-(Sol)_{0-2}$ (Sol = H_2DC_2 (SUA), H_2SO_4 and H_2O) at the B3LYP/6-311++G(3df, 3pd) level. Selected bond lengths (Å), bond angles (^{o}) and relative energies (kcal/mol) are indicated.

Table 4.1. The experimentally measured and theoretically calculated adiabatic (ADE) and vertical detachment energy (VDE) for $HSO_4^-(Sol)_n$ (Sol = SUA, H_2O and H_2SO_4) (n = 0-2) (in eV).

		ADE				VDE		
		Expt.[a]	Calc.[c]			Expt.[a]	Calc.[c]	
				B3LYP	M06-2X		B3LYP	M06-2X
HSO_4^-	X	4.75(10)		4.61	5.00	5.0(1)	4.86	5.36
	A	5.4(1)				5.68(10)		
	B	~5.8				6.22(10)		
	C	7.18(2)				7.28 (2)		
	Freq.(cm^{-1})	800(40)						
				821.6[d]				
$HSO_4^-(SUA)_1$	X	6.45(10)		5.87	6.27	6.78(10)	6.23	7.19
$HSO_4^-(H_2SO_4)_1$	X	6.55(10)		5.96	6.42	6.8(1)	6.50	7.20
$HSO_4^-(H_2O)_1$	X	5.35(10)	A	4.68	5.13	5.6(1)	5.39	5.90
			B	5.07	5.47		5.46	6.00
$HSO_4^-(SUA)_2$	X′	~6.6	A	5.78	6.11		6.59	7.71
	X	~7.1	B	6.26	7.15		6.51	7.65
$HSO_4^-(H_2SO_4)_2$	X′	~7.2	A	6.53	6.93		7.25	8.05
	X	~7.5	B	6.90	7.37		7.41	8.44
$HSO_4^-(H_2O)_2$	X	5.55(10)	B_1	5.10	5.57	5.8(1)	5.86	6.44
			A_1	4.79	5.20		5.57	6.11

[a]Numbers in parentheses represent experimental uncertainty in last digits.
[b]B3LYP/6-311++G(3df,3pd) level of theory with zero point vibrational energy difference corrections for ADEs, and numbers in brackets represent calculated values at M06-2X/aug-cc-PVT(+d)Z//B3LYP/6-311++G(3df,3pd) level of theory. For $HSO_4^-(H_2O)_{1,2}$, $HSO_4^-(H_2SO_4)_{1,2}$ and $HSO_4^-(SUA)_1$, we also performed single point energy calculations at MP2//B3LYP/6-311++G(3df,3pd) level.
[c]Optimized structures are given in Figure 4.2.
[d]The listed theoretical vibrational frequency is after 0.970 scaling factor.

4.6. References

(1) Kulmala, M. How Particles Nucleate and Grow. *Science* **2003**, *302*, 1000-1001.

(2) Charlson, R. J.; Schwartz, S. E.; Hales, J. M.; Cess, R. D.; Coakley, J. A.; Hansen, J. E.; Hofmann, D. J. Climate Forcing by Anthropogenic Aerosols. *Science* **1992**, *255*, 423-430.

(3) Power, H. C. The geography and climatology of aerosols. *Pro.Phys.Geography* **2003**, *27*, 502-547.

(4) Dockery, D. W.; Schwartz, J.; Spengler, J. D. Air pollution and daily mortality: Associations with particulates and acid aerosols. *Environ. Res.* **1992**, *59*, 362-373.

(5) Dockery, D. W.; Pope, C. A. Acute Respiratory Effects of Particulate Air Pollution. *Annu. Rev. Public Health* **1994**, *15*, 107-132.

(6) Saxon, A.; Diaz-Sanchez, D. Air pollution and allergy: you are what you breathe. *Nature Immunol.* **2005**, *6*, 223-226.

(7) Kittelson, D. B.; Watts, W. F.; Johnson, J. P. Nanoparticle emissions on Minnesota highways. *Atmos. Environ.* **2004**, *38*, 9-19.

(8) Zhang, R. Y.; Khalizov, A.; Wang, L.; Hu, M.; Xu, W. Nucleation and Growth of Nanoparticles in the Atmosphere. *Chem. Rev.* **2012**, *112*, 1957-2011.

(9) Kathmann, S. M.; Schenter, G. K.; Garrett, B. C.; Chen, B.; Siepmann, J. I. Thermodynamics and Kinetics of Nanoclusters Controlling Gas-to-Particle Nucleation. *J. Phys. Chem. C* **2009**, *113*, 10354-10370.

(10) Sipilä, M.; Berndt, T.; Petäjä, T.; Brus, D.; Vanhanen, J.; Stratmann, F.; Patokoski, J.; Mauldin, R. L. I.; Hyvärinen, A.-P.; Lihavainen, H.; Kulmala, M. The Role of Sulfuric Acid in Atmospheric Nucleation. *Science* **2010**, *327*, 1243-1246.

(11) Hamill, P.; Turco, R. P.; Kiang, C. S.; Toon, O. B.; Whitten, R. C. An analysis of various nucleation mechanisms for sulfate particles in the stratosphere. *J. Aerosol Sci.* **1982**, *13*, 561-585.

(12) Kulmala, M.; Korhonen, P.; Napari, I.; Karlsson, A.; Berresheim, H.; O'Dowd, C. D. Aerosol formation during PARFORCE: Ternary nucleation of H_2SO_4, NH_3, and H_2O. *J. Geophys. Res.* **2002**, *107*, 8111.

(13) Napari, I.; Noppel, M.; Vehkamäki, H.; Kulmala, M. Parametrization of ternary nucleation rates for H_2SO_4-NH_3-H_2O vapors. *J. Geophys. Res.* **2002**, *107*, 4381.

(14) Loukonen, V.; Kurtén, T.; Ortega, I. K.; Vehkamäki, H.; Pádua, A. A. H.; Sellegri, K.; Kulmala, M. Enhancing effect of dimethylamine in sulfuric acid nucleation in the presence of water – a computational study. *Atmos. Chem. Phys.* **2010**, *10*, 4961-4974.

(15) DePalma, J. W.; Bzdek, B. R.; Doren, D. J.; Johnston, M. V. Structure and Energetics of Nanometer Size Clusters of Sulfuric Acid with Ammonia and Dimethylamine.

J.Phys.Chem.A **2012**, *116*, 1030-1040.

(16) Ehn, M.; Junninen, H.; Petäjä, T.; Kurtén, T.; Kerminen, V. M.; Schobesberger, S.; Manninen, H. E.; Ortega, I. K.; Vehkamäki, H.; Kulmala, M.; Worsnop, D. R. Composition and temporal behavior of ambient ions in the boreal forest. *Atmos. Chem. Phys.* **2010**, *10*, 8513-8530.

(17) Yu, F.; Turco, R. P. Ultrafine aerosol formation via ion-mediated nucleation. *Geophys. Res. Lett.* **2000**, *27*, 883-886.

(18) Prenni, A. J.; DeMott, P. J.; Kreidenweis, S. M.; Sherman, D. E. The Effects of Low Molecular Weight Dicarboxylic Acids on Cloud Formation. *J. Phys. Chem. A* **2001**, *105*, 11240-11248.

(19) Marti, J. J.; Weber, R. J.; McMurry, P. H.; Eisele, F.; Tanner, D.; Jefferson, A. New particle formation at a remote continental site: Assessing the contributions of SO_2 and organic precursors. *J. Geophys. Res.* **1997**, *102*, 6331-6339.

(20) Limbeck, A.; Puxbaum, H.; Otter, L.; Scholes, M. C. Semivolatile behavior of dicarboxylic acids and other polar organic species at a rural background site (Nylsvley, RSA). *Atmos. Environ.* **2001**, *35*, 1853-1862.

(21) Hõrrak, U.; Salm, J.; Tammet, H. Bursts of intermediate ions in atmospheric air. *J. Geophys. Res.* **1998**, *103*, 13909-13915.

(22) Keesee, R. G.; Castleman, A. W. J. Ions and Cluster Ions: Experimental Studies and Atmospheric Observations. *J. Geophys. Res.* **1985**, *90*, 5885-5890.

(23) Zhang, R. Y. Atmospheric New Particle Formation Enhanced by Organic Acids. *Science* **2004**, *304*, 1487-1490.

(24) Zhang, R.; Wang, L.; Khalizov, A. F.; Zhao, J.; Zheng, J.; McGraw, R. L.; Molinac, L. T. Formation of nanoparticles of blue haze enhanced by anthropogenic pollution. *Proc. Natl. Acad. Sci. U.S.A.* **2009**, *106*, 17650-17654.

(25) Wang, L.; Xu, W.; Khalizov, A. F.; Zheng, J.; Qiu, C.; Zhang, R. Y. Laboratory Investigation on the Role of Organics in Atmospheric Nanoparticle Growth. *J. Phys. Chem. A* **2011**, *115*, 8940-8947.

(26) Lal, V.; Khalizov, A. F.; Lin, Y.; Galvan, M. D.; Connell, B. T.; Zhang, R. Y. Heterogeneous Reactions of Epoxides in Acidic Media. *J. Phys. Chem. A* **2012**, *116*, 6078-6090.

(27) Peckhaus, A.; Grass, S.; Treuel, L.; Zellner, R. Deliquescence and Efflorescence Behavior of Ternary Inorganic/Organic/Water Aerosol Particles. *J. Phys. Chem. A* **2012**, *116*, 6199-6210.

(28) Wang, L.; Khalizov, A. F.; Zheng, J.; Xu, W.; Ma, Y.; Lal, V.; Zhang, R. Y. Atmospheric nanoparticles formed from heterogeneous reactions of organics. *Nature Geoscience* **2010**, *3*, 238-242.

(29) Yacovitch, T. I.; Wende, T.; Jiang, L.; Heine, N.; Meijer, G.; Neumark, D. M.;

Asmis, K. R. Infrared Spectroscopy of Hydrated Bisulfate Anion Clusters: $HSO_4^-(H_2O)_{1-16}$. *J. Phys. Chem. Lett.* **2011**, *2*, 2135-2140.

(30) Yacovitch, T. I.; Heine, N.; Brieger, C.; Wende, T.; Hock, C.; Neumark, D. M.; Asmis, K. R. Communication: Vibrational spectroscopy of atmospherically relevant acid cluster anions: Bisulfate versus nitrate core structures. *J. Chem. Phys.* **2012**, *136*, 241102.

(31) Zatula, A. S.; Andersson, P. U.; Ryding, M. J.; Uggerud, E. Proton mobility and stability of water clusters containing the bisulfate anion, $HSO_4^-(H_2O)_n$. *Phys. Chem. Chem. Phys.* **2011**, *13*, 13287-13294.

(32) Lovejoy, E. R.; Curtius, J. Cluster Ion Thermal Decomposition (II): Master Equation Modeling in the Low-Pressure Limit and Fall-Off Regions. Bond Energies for $HSO_4^-(H_2SO_4)_x(HNO_3)_y$. *J. Phys. Chem. A* **2001**, *105*.

(33) Curtius, J.; Froyd, K. D.; Lovejoy, E. R. Cluster Ion Thermal Decomposition (I): Experimental Kinetics Study and ab Initio Calculations for $HSO_4(H_2SO_4)_x(HNO_3)_y$. *J. Phys. Chem. A* **2001**, *105*, 10867-10873.

(34) Froyd, K. D.; Lovejoy, E. R. Experimental Thermodynamics of Cluster Ions Composed of H_2SO_4 and H_2O. 2. Measurements and ab Initio Structures of Negative Ions. *J. Phys. Chem. A* **2003**, *107*, 9812-9824.

(35) Husar, D. E.; Temelso, B.; Ashworth, A. L.; Shields, G. C. Hydration of the Bisulfate Ion: Atmospheric Implications. *J. Phys. Chem. A* **2012**, *116*, 5151-5163.

(36) Temelso, B.; Morrell, T. E.; Shields, R. M.; Allodi, M. A.; Wood, E. K.; Kirschner, K. N.; Castonguay, T. C.; Archer, K. A.; Shields, G. C. Quantum Mechanical Study of Sulfuric Acid Hydration: Atmospheric Implications. *J. Phys. Chem. A* **2012**, *116*, 2209-2224.

(37) Xu, Y.; Nadykto, A. B.; Yu, F.; Jiang, L.; Wang, W. Formation and properties of hydrogen-bonded complexes of common organic oxalic acid with atmospheric nucleation precursors. *J. Mol. Struct.: THEOCHEM* **2010**, *951*, 28-33.

(38) Zhao, J.; Khalizov, A.; Zhang, R. Y.; McGraw, R. Hydrogen-Bonding Interaction in Molecular Complexes and Clusters of Aerosol Nucleation Precursors. *J. Phys. Chem. A* **2009**, *113*, 680-689.

(39) Xu, Y.; Nadykto, A. B.; Yu, F.; Herb, J.; Wang, W. Interaction between Common Organic Acids and Trace Nucleation Species in the Earth's Atmosphere. *J. Phys. Chem. A* **2010**, *114*, 387-396.

(40) Xu, W.; Zhang, R. Y. Theoretical Investigation of Interaction of Dicarboxylic Acids with Common Aerosol Nucleation Precursors. *J. Phys. Chem. A* **2012**, *116*, 4539-4550.

(41) Nadykto, A. B.; Yu, F. Strong hydrogen bonding between atmospheric nucleation precursors and common organics. *Chem. Phys. Lett.* **2007**, *435*, 14-18.

(42) Weber, K. H.; Morales, F. J.; Tao, F.-M. Theoretical Study on the Structure and

Stabilities of Molecular Clusters of Oxalic Acid with Water. *J. Phys. Chem. A* **2012**, *116*, 11601-11617.

(43) Zhang, R. Y. Getting to the Critical Nucleus of Aerosol Formation. *Science* **2010**, *328*, 1366-1367.

(44) Wang, X.-B.; Wang, L.-S. Development of a low-temperature photoelectron spectroscopy instrument using an electrospray ion source and a cryogenically controlled ion trap. *Rev. Sci. Instrum.* **2008**, *79*, 073108.

(45) Wang, X. B.; Wang, L. S. Bulk-Like Features in the Photoemission Spectra of Hydrated Doubly Charged Anion Clusters. *Science* **2001**, *294*, 1322-1325.

(46) Murdachaew, G.; Valiev, M.; Kathmann, S. M.; Wang, X.-B. Study of Ion Specific Interactions of Alkali Cations with Dicarboxylate Dianions. *J. Phys. Chem. A* **2012**, *116*, 2055-2061.

(47) Minofar, B.; Mucha, M.; Jungwirth, P.; Yang, X.; Fu, Y.-J.; Wang, X.-B.; Wang, L.-S. Bulk versus Interfacial Aqueous Solvation of Dicarboxylate Dianions. *J. Am. Chem. Soc.* **2004**, *126*, 11691-11698.

(48) Woo, H.-K.; Wang, X.-B.; Lau, K.-C.; Wang, L.-S. Low-temperature Photoelectron Spectroscopy of Aliphatic Dicarboxylate Monoanions, $HO_2C(CH_2)_nCO_2^-$ (n=1-10): Hydrogen Bond Induced Cyclization and Strain Energies. *J. Phys. Chem. A* **2006**, *110*, 7801-7805.

(49) Wang, X.-B.; Nicholas, J. B.; Wang, L.-S. Photoelectron Spectroscopy and Theoretical Calculations of SO_4^- and HSO_4^-: Confirmation of High Electron Affinities of SO_4 and HSO_4. *J. Phys. Chem. A* **2000**, *104*, 504-508.

(50) Kurt´en, T.; Noppel, M.; Vehkam¨aki, H.; Salonen, M.; Kulmala, M. Quantum Chemical Studies of Hydrate Formation of H_2SO_4 and HSO_4^-. *Boreal Env. Res.* **2007**, *12*, 431-453.

(51) Eisele, F. L.; Hanson, D. R. First Measurement of Prenucleation Molecular Clusters. *J. Phys. Chem. A* **2000**, *104*, 830-836.

(52) Yuji Sugitaa; Okamoto, Y. Replica-exchange molecular dynamics method for protein folding. *Chem. Phys. Lett.* **1999**, *314*, 141-151.

(53) M. J. Frisch, G. W. Trucks, H. B. Schlegel, Gaussian 09. Gaussian Inc.Wallingford CT, 2009.

(54) Rocha, G. B.; Freire, R. O.; Simas, A. M.; Stewart, J. J. P. RM1: A reparameterization of AM1 for H, C, N, O, P, S, F, Cl, Br, and I. *J. Comput. Chem.* **2006**, *27*, 1101-1111.

(55) (a) Becke, A. D. Density-functional thermochemistry. III. The role of exact exchange. *J. Chem. Phys.* **1993**, *98*, 5648-5652; (b) Lee, C.; Yang, W.; Parr, R. G. Development of the Colle-Salvetti correlation-energy formula into a functional of the electron density. *Phys.*

Rev. B **1988**, *37*, 785-789.

(56) Krishnan, R.; Binkley, J. S.; Seeger, R.; Pople, J. A. Self-consistent molecular orbital methods. XX. A basis set for correlated wave functions. *J. Chem. Phys.* **1980**, *72*, 650-654.

(57) Head-Gordon, M.; Pople, J. A.; Frisch, M. J. MP2 energy evaluation by direct methods. *Chem. Phys. Lett.* **1988**, *153*, 503-506.

(58) Zhao, Y.; Truhlar, D. G. Density Functionals with Broad Applicability in Chemistry. *Acc. Chem. Res.* **2008**, *41*, 157-167.

(59) Vchirawongkwin, V.; Kritayakornupong, C.; Rode, B. M. Structural and Dynamical Properties and Vibrational Spectra of Bisulfate Ion in Water: A Study by Ab Initio Quantum Mechanical Charge Field Molecular Dynamics. *J. Phys. Chem. B* **2010**, *114*, 11561-11569.

(60) Gilli, P.; Bertolasi, V.; Ferretti, V.; Gilli, G. Covalent Nature of the Strong Homonuclear Hydrogen Bond. Study of the O•••H•••O System by Crystal Structure Correlation Methods. *J. Am. Chem. Soc.* **1994**, *116*, 909-915.

(61) Herb, J.; Xu, Y.; Yu, F.; Nadykto, A. B. Large Hydrogen-Bonded Pre-nucleation $(HSO_4^-)(H_2SO_4)_m(H_2O)_k$ and $(HSO_4^-)(NH_3)(H_2SO_4)_m(H_2O)_k$ Clusters in the Earth's Atmosphere. *J. Phys. Chem. A* **2013**, *117*, 133-152.

(62) Nadykto, A. B.; Yu, F.; Herb, J. Theoretical analysis of the gas-phase hydration of common atmospheric pre-nucleation and $(H_3O^+)(H_2SO_4)(H_2O)_n$ cluster ions. *Chem. Phys.* **2009**, *360*, 67-73.

(63) Curtius, J.; Lovejoy, E. R.; Froyd, K. D. Atmospheric Ion-induced Aerosol Nucleation. *Space Sci. Rev.* **2006**, *125*, 159-167.

Chapter 5. A refined MS-EVB model for proton transport in aqueous environments

5.1 Abstract

In order to improve the description of proton mobility in aqueous environments, a revised multistate empirical valence bond model (*a*MS-EVB3) is developed. The new *a*MS-EVB3 model is built upon an anharmonic water force field (*a*SPC/Fw) in which the OH bond potential is described through a quartic approximation to a Morse potential. First, it is shown that the *a*SPC/Fw anharmonic water model provides an accurate description of water at ambient conditions and reproduces the available experimental data for several structural, thermodynamic and dynamical properties. Second, it is shown that, when applied to the study of proton solvation and transport in bulk water, the new *a*MS-EVB3 model accurately describes the solvation structure around the excess proton. Importantly, the new *a*MS-EVB3 model predicts a significantly larger proton diffusion coefficient than previous models, which largely improves the agreement with the available experimental data.

5.2. Introduction

Since water plays a central role in a many fundamental phenomena (e.g., reactive, transport and diffusion processes in solution and at interfaces, and hydration of biomolecules), it is not surprising that much experimental and theoretical effort has been

devoted in the past to the development of a molecular-level understanding of its unique properties.[1,2] On the other hand, proton solvation and transport processes take place in a variety of chemical reactions in solution that have important implications in many different areas including atmospheric chemistry, energy transduction, and the development of proton exchange membrane fuel cells, just to mention a few.[3,4] It is thus apparent that an accurate modeling of the structural, thermodynamic and dynamical properties of pure and protonated water plays a key role for a complete understanding of the molecular mechanisms that govern several important physicochemical processes in the condensed phase.

From a computational standpoint, numerous water force fields have been developed, which include minimalistic models based on coarse-grained representations of the molecular interactions,[5,6] atomistic models based on fixed partial charges and rigid bonds,[7-10] and more sophisticated models that explicitly take into account for molecular flexibility,[11] three-body contributions,[12-14] and electronic polarization.[15-17] Specialized models have also been developed to account for nuclear quantum effects.[18-20] When employed in computer simulations, each of these models has shown a certain degree of success in reproducing at least some of the properties of liquid water. In this regard, since water often represents the most abundant component in fully atomistic computer simulations of condensed phase systems (e.g., biomolecules in solution), the largest fraction of CPU time used to model these systems is effectively spent in the calculation of the interactions between water molecules. As a consequence, it is highly desirable to have access to water models that can accurately describe the structural, thermodynamic and dynamical properties of the liquid phase and, at the same time, can still be

computationally affordable. These requirements become even more critical for molecular simulations of the behavior of excess protons in aqueous environments. Because of the high mobility of protons in water, realistic computer models must be capable of describing the hopping dynamics of protons between water molecules within the hydrogen-bond network. This implies that both the Grotthuss mechanism[21] and the associated delocalization of the excess charge over multiple water molecules[22] have to be correctly taken into account. Although both these features can in principle be captured in ab initio molecular dynamics (AIMD) simulations, current approaches based on density functional theory (DFT) have been limited so far to relatively small systems due to the associated high computational cost.[4] It should also be noted that the choice of the most appropriate functional for describing the water properties is still matter of debate, with recent studies highlighting the importance of the dispersion interactions, which instead are usually neglected in the most common DFT implementations.[23-26]

Alternatively, reactive force fields can also be used to describe the physicochemical properties of protons in aqueous environments. Among the most effective approaches based on a force field representation of the molecular interactions is the multistate empirical valence bond (MS-EVB) method.[27-32] Built upon the original two-state empirical valence bond (EVB) method introduced by Warshel,[33] the MS-EVB method enables the description of proton solvation and transport by evolving the system on a reactive potential energy surface defined by a linear combination of multiple diabatic potentials. Each diabatic state corresponds to a limiting "state" of the system, with the total number of all possible states representing an effective basis set for the system Hamiltonian. By construction, the MS-EVB method captures the main features of

the Grotthuss mechanism in which the proton hopping events are strictly connected to both the molecular diffusion and the rearrangement of the water hydrogen-bond network.[3,4] Since its initial development, the MS-EVB method has been applied with success to study proton solvation and transport in many different environments and under different conditions (see Ref.[3] for a recent review). Recently, the latest version of the MS-EVB model, MS-EVB3, has also been employed to elucidate the elementary steps associated with proton transfer in bulk water.[34] Despite much success in reproducing the essential features and molecular mechanisms of proton transport and solvation in aqueous environments, all previous MS-EVB models have been found to underestimate the diffusion coefficient associated with the proton mobility in bulk water. The only exception is represented by a polarizable version of the MS-EVB approach for which, however, some of the properties such as energy conservation remain to be assessed.[35]

In order to provide a more quantitative description of proton transport in aqueous environments, a refined version of the (nonpolarizable) MS-EVB3 model is developed in this work. The new model is based on an anharmonic water force field in which the OH intramolecular vibrations are represented by a quartic approximation to the Morse potential. This functional form has been shown to provide a reasonable representation of the OH stretching frequencies in pure water when nuclear quantum effects are explicitly taken into account.[20,36] The introduction of vibrational anharmonicity into the original SPC/Fw water force field,[11] which is employed in the MS-EVB3 model,[30,37] leads to a new anharmonic water model, *a*SPC/Fw. The latter clearly satisfies the requirement to be simple and fast to calculate using standard algorithms for molecular simulations and, importantly, provides a more realistic description of the water motion. In turn, the explicit

account of the vibrational anharmonicity in the description of the water interactions also leads to a refined anharmonic MS-EVB3 model, *a*MS-EVB3. When applied to the study of proton solvation and transport in bulk water, the new *a*MS-EVB3 predicts a proton diffusion coefficient that is significantly larger (~40%) than the value calculated with the original MS-EVB3 model and, consequently, in better agreement with the available experimental data. However, some differences still exist between the experimental and MS-EVB results, which may be due to several factors that are discussed in this study.

5.3. Computational methodologies

5.3.1 The anharmonic aSPC/Fw water model

Taking as a reference the original (harmonic) SPC/Fw water model,[11] an anharmonic force field (*a*SPC/Fw) was developed in order to accurately reproduce several structural, thermodynamic and dynamical properties of bulk water at room temperature (T = 298.15 K). The functional form of the *a*SPC/Fw force field is expressed as

$$V = V^{bond} + V^{angle} + V^{inter} \tag{5.1}$$

where

$$\begin{aligned} V^{bond} = {} & D_{OH}\left[\alpha_{OH}^{2}\left(r_{OH_1} - r_{OH}^{eq}\right)^{2} - \alpha_{OH}^{3}\left(r_{OH_1} - r_{OH}^{eq}\right)^{3} + \frac{7}{12}\alpha_{OH}^{4}\left(r_{OH_1} - r_{OH}^{eq}\right)^{4}\right] \\ & + D_{OH}\left[\alpha_{OH}^{2}\left(r_{OH_2} - r_{OH}^{eq}\right)^{2} - \alpha_{OH}^{3}\left(r_{OH_2} - r_{OH}^{eq}\right)^{3} + \frac{7}{12}\alpha_{OH}^{4}\left(r_{OH_2} - r_{OH}^{eq}\right)^{4}\right] \end{aligned} \tag{5.2}$$

$$V^{angle} = \frac{K_{HOH}}{2}\left(\theta_{HOH} - \theta_{HOH}^{eq}\right)^{2} \tag{5.3}$$

and

$$V^{inter} = \sum_{i,j} \left\{ 4\varepsilon_{ij} \left[\left(\frac{\sigma_{ij}}{R_{ij}} \right)^{12} - \left(\frac{\sigma_{ij}}{R_{ij}} \right)^{6} \right] + \frac{q_i q_j}{R_{ij}} \right\} \quad (5.4)$$

In Eqs. (5.1)-(5.4), V^{bond} represents the anharmonic OH stretching potential, V^{angle} describes the HOH bending potential, and V^{inter} describes the intermolecular interactions that include both the Lennard-Jones and Coulomb terms between all pairs of nonbonded atoms. In Eqs. (5.2) and (5.3), r_{OH}^{eq} and θ_{HOH}^{eq} are the equilibrium bond length and angle of an isolated water molecule, respectively, while R_{ij} in Eq. (5.4) is the distance between atom *i* and *j*. The parameters D_{OH} and α_{OH} entering the expression of the quartic potential describing the OH stretching motion were taken from Ref.[20]. These parameters were shown to provide a reasonable description of the OH stretching frequencies when employed in quantum dynamical simulations of the infrared spectrum of liquid water.[20,36] In this regard, it is important to note that an accurate description of the OH infrared intensities also requires a proper description of the induced dipole interactions that cannot be accurately represented by any fixed charge models. The bending force constant K_{HOH} was kept fixed at the original value of the SPC/Fw model.[11] All other parameters that appear in Eqs. (5.2) - (5.4) were optimized using classical molecular dynamics (MD) simulations until an overall good agreement between the computed and the available experimental values was achieved for a relatively large set of water properties at 298.15 K, including radial distribution functions, density, enthalpy of vaporization, dielectric constant, diffusion coefficient, and orientational relaxation times. The final set of parameters that define the *a*SPC/Fw model is listed in Table 5.1.

All classical MD simulations were carried out with a development version of the

AMBER suite of codes[38] and DL_POLY 2[39] for a system consisting of 256 water molecules in a periodic cubic box. The short-range interactions were truncated at an atom-atom distance of 9.0 Å, while the electrostatic interactions were treated using the particle mesh Ewald method.[40] After 1 ns of equilibration, the structural and thermodynamic properties were calculated from a classical MD simulation of 5 ns performed in the isothermal-isobaric (NPT) ensemble with temperature and pressure maintained via Langevin dynamics and a Berendsen barostat,[40] respectively. The dielectric constant was instead calculated from a 4 ns simulation in the canonical (NVT) ensemble with the density held fixed at the corresponding calculated value. All the dynamical properties were obtained by averaging over 100 trajectories of 25 ps each carried out in the microcanonical (NVE) ensemble.

5.3.2 The anharmonic aMS-EVB3 model

In the multistate empirical valence bond method the electronic wavefunction of a protonated system is represented by a linear combination of valence bond states that describe all possible molecular configurations of the hydronium ion (H_3O^+).[27-30] In practice, the valence bond configurations are generated by identifying first the "pivot hydronium" and then allowing the oxygen atoms of all water molecules located in the first three solvation shells of the pivot hydronium to also form hydronium ions. As in the MS-EVB3 model,[30,37] the solvation shells in the *a*MS-EVB3 model are determined using a geometric definition of the hydrogen bonds that involve the O---H distance (with a cutoff of 2.5 Å) between oxygen and hydrogen atoms of different molecules and the O-H---O angle (with a cutoff of 130°). In the parameterization of the new *a*MS-EVB3

model, the same functional form of the Hamiltonian is adopted as in the original MS-EVB3 model.[30,37] This implies that individual oxygen atoms are allowed to participate in more than one hydronium ion, which, as described in Ref.[30], is particularly important when the oxygen atoms of the water molecules are involved in two acceptor hydrogen bonds.

Following Refs.[30,37], the Hamiltonian matrix of the *a*MS-EVB3 model contains diagonal elements (H_{ii}), which describe both the intramolecular and intermolecular interactions of all molecules in each valence bond state, and off-diagonal elements (H_{ij}), which couple different states and effectively enable proton hopping events from one water molecule to another. The diagonal terms take the form[30,37]

$$H_{ii} = V^{intra}\left(H_3O^+\right) + \sum_{k}^{N_{H_2O}} V_k^{intra}\left(H_2O\right) + \sum_{k}^{N_{H_2O}} V_k^{inter}\left(H_3O^+ - H_2O\right) + \sum_{k<k'}^{N_{H_2O}} V_{kk'}^{inter}\left(H_2O - H_2O\right) \tag{5.5}$$

where $V^{intra}\left(H_3O^+\right)$ is the intramolecular potential of the hydronium ion expressed as

$$V^{intra}\left(H_3O^+\right) = \sum_{j}^{3} D_{OH}\left[1 - e^{-a_{OH}\left(r_{j,OH} - r_{OH}^{eq}\right)}\right]^2 + \frac{1}{2}\sum_{j}^{3} k_{\phi}\left(\phi_{j,HOH} - \phi_{HOH}^{eq}\right)^2 \tag{5.6}$$

with $r_{j,OH}$ and $\phi_{j,HOH}$ being the j-th OH bond length and the j-th HOH angle of the hydronium ion. The terms $V_k^{intra}\left(H_2O\right)$ and $V_{kk'}^{inter}\left(H_2O\right)$ are respectively the intra- and intermolecular potentials of the *a*SPC/Fw water model described in Section 5.3.1. Finally the term $V_{kk'}^{inter}\left(H_3O^+ - H_2O\right)$ describes the interaction between the hydronium ion and the water molecules, and takes the form

$$V_k^{inter}\left(H_3O^+ - H_2O\right) = 4\varepsilon_{OO_W}\left[\left(\frac{\sigma_{OO_W}}{R_{OO_W}}\right)^{12} - \left(\frac{\sigma_{OO_W}}{R_{OO_W}}\right)^{6}\right] + 4\varepsilon_{HO_W}\left[\left(\frac{\sigma_{HO_W}}{R_{HO_W}}\right)^{12} - \left(\frac{\sigma_{HO_W}}{R_{HO_W}}\right)^{6}\right] + \sum_{m}^{4}\sum_{n_k}^{3}\frac{q_m^{H_3O^+} q_{n_k}^{H_2O}}{R_{mn_k}} + V_{OO_k}^{rep} + V_{HO_k}^{rep} \tag{5.7}$$

This term includes the Lennard-Jones and Coulomb interactions between all pairs of nonbonded atoms as well as the two repulsive terms that were introduced in the MS-EVB3 model to correctly describe the interactions between the hydronium ion and the water molecules in the first solvation shell.[30] These latter terms are expressed as

$$V_{OO_k}^{rep} = B\, e^{-b\left(R_{OO_k} - d_{OO}^0\right)} \sum_{j}^{3} e^{-b' \bullet q_{H_jO_k}^2} \tag{5.8}$$

and

$$V_{HO_k}^{rep} = C\, e^{-c\left(R_{HO_k} - d_{OH}^0\right)} \tag{5.9}$$

Following Ref.[30], the off-diagonal elements (H_{ij}) of the Hamiltonian matrix are defined as

$$H_{ij} = \left[V_{ij}^{(const)} + V_{ij}^{(ex)}\right] A\left(R_{OO}, q\right) \tag{5.10}$$

if the two valence bond states $|i\rangle$ and $|j\rangle$ share a common hydrogen atom, and $H_{ij} = 0$ otherwise. In Eq. (10), $V_{ij}^{(const)}$ is a constant, while $V_{ij}^{(ex)}$ describes the electrostatic interaction between the Zundel complex ($H_5O_2^+$) and the remaining N_{H_2O}-1 water molecules and takes the form

$$V_{ij}^{(ex)} = \sum_{m}^{7}\sum_{k}^{N_{H_2O}-1}\sum_{n_k}^{3}\frac{q_{n_k}^{H_2O} q_m^{ex}}{R_{mn_k}} \tag{5.11}$$

Here, q_m^{ex} and $q_{n_k}^{H_2O}$ are the exchange charges of the $H_5O_2^+$ complex and the atomic charges of the k-th water molecule, respectively. The term $A\left(R_{OO},q\right)$ is instead a geometry dependent scaling factor defined in Ref.[30] as

$$A\left(R_{OO},q\right)=e^{-\gamma q^2}\left[1+Pe^{-k\left(R_{OO}-D_{OO}\right)^2}\right]\left\{\frac{1}{2}\left\{1-\tanh\left[\beta\left(R_{OO}-R_{OO}^0\right)\right]\right\}+P'e^{-\alpha\left(R_{OO}-r_{OO}^0\right)}\right\} \quad (5.12)$$

where R_{OO} is the distance between the two oxygen atoms of the $H_5O_2^+$ complex, and $q=\frac{r_O+r_{O'}}{2}-r_{H^*}$ is the asymmetric stretch coordinate of the complex, with r_O and $r_{O'}$ being the position vectors of the two oxygen atoms and r_{H^*} being the corresponding vector of the central hydrogen atom. For a detailed description of all terms appearing in Eqs. (5.5)-(5.12) the interested reader is referred to Refs.[30,37].

Among the 33 parameters of the original MS-EVB3 model,[30] 25 parameters were re-optimized to represent the ab initio structures and binding energies of selected protonated water clusters. Eight parameters, including those associated with the intramolecular potential of the hydronium ion and the partial charge of the oxygen atom of the hydronium ion as well as the parameters describing the smooth cut-off of the OO and HO repulsive terms in Eqs. (5.8) and (5.9), were kept fixed at the corresponding values of the MS-EVB3 model because the overall optimization procedure was found to be essentially insensitive to these parameters. The multi-dimensional optimization of the *a*MS-EVB3 parameters was performed with the genetic algorithm,[41,42] and the following target quantities were used: 1) Ab initio geometries and binding energies of four different protonated water clusters shown in Figure 1, including the Zundel and Eigen structures as

well as the cluster with 3 H_2O molecule and an excess proton; 2) Ab initio potential energy surface (PES) associated with the proton shuttling between two water molecules in the Zundel configuration. The geometries of the water, hydronium ion and protonated water clusters were optimized at the MP2/aug-cc-pVTZ level of theory. Single point energy corrections at the CCSD(T)/aug-cc-pVTZ level of theory were then performed in order to obtain more accurate binding energies and proton shuttling PESs. All the ab initio calculations were performed using Gaussian 09.[43] The final set of parameters for the *a*MS-EVB3 model is listed in Table 5.2.

The bulk properties of protonated water calculated with the *a*MS-EVB3 model were obtained using classical MD simulations for a system consisting of 256 water molecules and an excess proton in a periodic cubic box. Starting from an equilibrated configuration of 256 *a*SPC/Fw water molecules at T = 298.15 K and P = 1 atm, an excess proton was added to the simulation box and the combined system was further equilibrated for 1 ns at constant temperature and volume. The structural and thermodynamic properties were then calculated from a 1 ns long simulation in the NVT ensemble with the temperature controlled by a Nosé-Hoover thermostat with a relaxation time of 0.5 ps. The self-diffusion coefficient of the excess proton was instead calculated from an additional 5 ns simulation carried out in the NVE ensemble.

5.4. Results and Discussion

5.4.1 aSPC/Fw model

Several structural, thermodynamic and dynamical properties were computed with the new *a*SPC/Fw model in order to assess its accuracy in reproducing the corresponding

experimental values. First, the radial distribution functions (RDFs), calculated at T = 298.15 K, are compared in Figure 5.2 with the available data extracted from neutron and x-ray scattering measurements of the water structure factor.[44-46] It is worth mentioning that the precise determination of the local structure of liquid water is currently matter of intense debate. The generally accepted picture of water as a liquid in which the molecules are on average four-fold coordinated has been recently challenged by a different interpretation of x-ray absorption and emission spectra.[47-49] According to the new analysis, the arrangement of the water molecules within the first solvation shell is characterized by two distinct motifs that correspond respectively to tetrahedral and strongly distorted hydrogen-bonded configurations with a 1:2 ratio. The new proposed picture of the water structure is still highly controversial (e.g., see Refs.[50]). The lack of consensus on a unique set of experimental data makes the direct comparison between simulation and experiment difficult. In an attempt to provide a general comparison, Figure 5.2 shows the RDFs calculated with the *a*SPC/Fw model along with the three experimentally derived sets that are most commonly employed in the literature. In all cases the calculated RDFs qualitatively reproduce the main features of the corresponding experimental data although they predict a slightly more structured liquid. This is particularly evident in the first peak of the OH RDF describing the correlation between oxygen and hydrogen atoms that are involved in hydrogen-bonded configurations. Due to the light mass of the hydrogen atoms, this peak is particularly sensitive to nuclear quantum effects that are neglected in this study. In this regard, it has been shown that, when nuclear quantization is explicitly taken into account in the molecular dynamics simulations, the agreement with the experimental data is significantly improved.[19] A

similar reasoning can also be used to explain the differences between the calculated and experimental HH RDFs. Although the explicit inclusion of nuclear quantum effects is expected to improve the agreement with the experimental data for the OH and HH RDFs, the case of the OO RDF is somewhat different. As it is possible to see in the bottom panel of Figure 5.2, significant differences exist between the three sets of experimental data. Based on the calculations performed with the quantum qSPC/Fw model in Ref.[19], it may be expected that the inclusion of nuclear quantum effects will lower the height of the first peak located at ~2.8 Å. However, the overall impact will be much smaller than that observed for the OH and HH RDFs due to the larger mass of the oxygen atoms.[19] Therefore, from a simple and qualitative analysis, it appears to be unlikely that, after inclusion of nuclear quantum effects, the OO RDF calculated with the new *a*SPC/Fw model could reproduce the experimentally derived data of Ref.[46]. On the other hand, it may be expected that the quantum OO RDF can effectively reproduce the curves obtained in Refs.[44,45] If the present results are put in the context of other simulation studies, the RDFs calculated here with the *a*SPC/Fw model are similar to those obtained with other water force fields, including the empirical and nonpolarizable SPC/Fw,[11] TIP4P, E3B[14] models, and the ab-initio-based and polarizable TTM3-F model.[15]

Individual molecular properties were also calculated with the *a*SPC/Fw model. In particular, the average OH bond and HOH angle as well as the average molecular dipole moment are compared in Table III with the corresponding values obtained from simulations with the SPC/Fw model and from experiment. In all cases the present results are found to be in better agreement with the experimental data. The calculated dipole moment is still underestimated, which is common to all empirical force fields that, based

on fixed partial atomic charges, are not able to correctly reproduce the molecular polarization arising in the bulk.

Besides the structural properties analyzed above, several thermodynamic quantities calculated with the *a*SPC/Fw model are also listed in Table III. Similarly to the SPC/Fw model, the density (ρ) of liquid water at T = 298.15 K is overestimated by ~2%. It must be noted, however, that the explicit inclusion of nuclear quantum effects has been shown to improve the agreement with the experimental value.[19] The enthalpy of vaporization was calculated according to the formula $\Delta H_{vap} \approx -\langle E \rangle + RT$, where $\langle \mathrm{E} \rangle$ is the average potential energy and R is the gas constant. In order to make a direct comparison with the data reported in Ref.[11] for the SPC/Fw model, the corrections terms that are often applied to ΔH_{vap} were neglected. For a flexible, 3-point charge model these corrections amount to ~0.5 kcal mol^{-1}.[19] The static dielectric constant (ε) was instead computed according to the following expression

$$\varepsilon = 1 + \frac{4\pi}{3k_B VT}\left(\langle \mathbf{M}^2 \rangle - \langle \mathbf{M} \rangle^2\right) \tag{5.13}$$

where **M** is the total dipole moment of the system, k_B is the Boltzmann constant and V is the volume of the simulation box. The heat capacity at constant pressure was calculated as $C_P \approx \frac{\Delta H}{\Delta T}$, where H is the enthalpy of the system. For this purpose, two additional simulations of 1 ns each were carried out at T = 288.15 K and T = 308.15 K in the NPT ensemble. A correction factor that effectively takes into account for the quantum nature of the water vibrations is generally added to the classical C_P value. In the case of the *a*SPC/Fw model, this correction amounts to ~2 cal mol^{-1} and was determined numerically

from path-integral molecular dynamics simulations. While both ΔH_{vap} and C_P calculated with the *a*SPC/Fw model are very similar to the corresponding values obtained with the SPC/Fw model, the dielectric constant is somewhat larger. This is likely due to the larger atomic partial charges (and, consequently, dipole moment) that are used in the present anharmonic model. Table III indicates that both the heat capacity and the dielectric constant calculated with the *a*SPC/Fw model are slightly larger than the corresponding experimental data. However, it has been shown that the inclusion of nuclear quantum effects generally leads to a decrease of the classical values, which results in a better agreement with the experimental data.[19]

Finally, the thermal expansion coefficient (α) and the isothermal compressibility (κ_T) for liquid water at T = 298.15 K were also calculated using the following expressions

$$\alpha = \frac{1}{V}\left(\frac{\partial V}{\partial T}\right)_P \approx \left[\frac{\ln(\rho_2 / \rho_1)}{T_2 - T_1}\right]_P \tag{5.14}$$

and

$$k_T = -\frac{1}{V}\left(\frac{\partial V}{\partial P}\right)_T \approx \left[\frac{\ln(\rho_2 / \rho_1)}{P_2 - P_1}\right] \tag{5.15}$$

In order to compute α via Eq.(14), two additional NPT simulations of 1 ns each were carried out at T_1 = 288.15 K and T_2 = 308.15 K which were used to determine the corresponding densities. For the calculation of κ_T, two additional NVT simulations of 1 ns each were performed at T = 298.15 K to determine the corresponding pressure values that were used in Eq.(5.15). As shown in Table III, both α and κ_T calculated with the *a*SPC/Fw model are in remarkably good agreement with the corresponding experimental

results.

Several quantities associated with the dynamics of the water molecules in the bulk were also computed with the *a*SPC/Fw model. In particular, the diffusion coefficient was calculated through the velocity autocorrelation function according as

$$D = \frac{1}{3}\int \left\langle \mathbf{v}(0)\cdot\mathbf{v}(t)\right\rangle dt, \tag{5.16}$$

where **v** is the center-of-mass velocity of a water molecule. The relaxation time (τ_2) associated with the reorientation of the water molecules within the hydrogen-bond network was instead obtained from the exponential fit of the long-time decay of the following orientational correlation function

$$C_2(t) = \left\langle P_2\left[\mathbf{e}_{OH}(0)\cdot\mathbf{e}_{OH}(t)\right]\right\rangle \tag{17}$$

Here, P_2 is the second Legendre polynomial and **e** is a unit vector along the OH bonds of a water molecule. As shown in Table III, both D and τ_2 calculated with the *a*SPC/Fw model are in good agreement with the corresponding experimental data. Furthermore, while the diffusion coefficient is similar to the value obtained with the SPC/Fw model, the new *a*SPC/Fw model clearly provides a more accurate description of the water orientational dynamics.

The comparison reported in Table III thus indicates that the new *a*SPC/Fw model provides an overall better description of bulk water relative to the SPC/Fw model. This is particular evident from the analysis of the properties that are associated to individual molecules (such as the equilibrium geometry and dipole moment) as well as to the dynamics of the hydrogen-bond network (such the C_2 orientational correlation function). In the next section, it will be shown that this improved description of the water properties

lead to a significantly more accurate description of the mobility of excess protons in water.

5.4.2 aMS-EVB3 model

The optimized geometries of the protonated water clusters calculated with the *a*MS-EVB3, MS-EVB3, and MP2/aug-cc-pVTZ methods are listed in Table 5.4, which also includes the data for the protonated clusters containing 5 H_2O molecules (Figure 5.1) that were not part of the training set used to parameterized the new *a*MS-EVB3 model. In all cases, the values obtained with the *a*MS-EVB3 model for the structural properties are in good agreement with the corresponding ab initio data, with the largest bond and angle differences being 0.04 Å for the O-H bond of the Eigen ion ($H_9O_4^+$) and 6.3° for the O---O---O angle of the protonated water trimer, respectively. All ab initio binding energies of the protonated water clusters, including those with 5 H_2O molecules that were not used in the parameterization, are accurately reproduced by the *a*MS-EVB3 model (Table 5.5). Tables 5.4 and 5.5 also indicate that overall both the structural properties and energetics calculated with the new *a*MS-EVB3 model are in better agreement with the corresponding ab initio values than those obtained with the original MS-EVB3 model.

Four curves describing radial cuts of the PES associated with the shuttling motion of the excess proton in the Zundel configuration were calculated for O---O separations corresponding to 2.2, 2.4, 2.6 and 2.8 Å, respectively. Following Ref.[30], the coordinate *q* describing the proton shuttling motion was defined as the distance of the central hydrogen atom from its equilibrium position while keeping the O---O distance fixed. For each value of the O---O distance, the scan along *q* was carried out at the CCSD(T)/aug-

cc-pVTZ level of theory with all the internal coordinates being kept fixed at the optimized values obtained with MP2/aug-cc-pVTZ. All four curves were included in the parameterization of the *a*MS-EVB3 model. Figure 3 shows a comparison between the ab initio data and the results obtained with the *a*MS-EVB3 model. In all cases, an excellent agreement is achieved, with the largest difference between the ab initio and *a*MS-EVB3 curves being ~1 kcal/mol for an O---O separation of 2.6 Å.

In order to analyze the structural properties of protonated water, several RDFs were calculated which are compared in Figure 4 with the corresponding experimental data of Ref.[51]. Both the O-O* RDF describing the spatial correlation between the oxygen atoms (O) of the water molecules and the oxygen atom (O*) of the pivot hydronium ion, and the O-H* RDF describing the spatial correlation between the oxygen atoms of the water molecules and the hydrogen atoms (H*) of the pivot hydronium ion calculated with the *a*MS-EVB3 model are similar to the corresponding RDFs obtained with the original MS-EVB3 model.[30] This is not completely unexpected since both models provide a similar description of the protonated water clusters as described above.

A significant improvement is instead provided by the new *a*MS-EVB3 model in the description of the proton mobility in bulk water. Following Ref.[30], the self-diffusion coefficient of the excess proton was calculated from the mean-square displacement (MSD) of the center of excess charge (CEC) defined as

$$\mathbf{r}_{CEC} = \sum_{i}^{N} c_i^2 \mathbf{r}^i{}_{COC} \tag{5.18}$$

where $\mathbf{r}^i_{COC}$ is the center of charge of the hydronium ion in the i-th EVB state. The Einstein relation, defined in Eq. (19), was then used to calculate the self-diffusion

coefficient of the center of excess charge (D_{CEC})

$$D_{CEC} = \lim_{t\to\infty} \frac{\left\langle \left| \mathbf{r}_{CEC}(t) - \mathbf{r}_{CEC}(0) \right|^2 \right\rangle}{6t} \tag{5.19}$$

The self-diffusion coefficient calculated with the *a*MS-EVB3 model is D_{CEC} = 0.410 ± 0.002 Å^2/ps (the error is from 95% confidence bounds after the linear least square fit), which is ~40% larger than the corresponding value obtained with the original MS-EVB3 model as shown in Figure 5. This difference can be qualitatively explained by calculating the free-energy for proton transfer expressed as $\Delta F = -kT \ln\left(c_1^2 - c_2^2\right)$, where c_1 and c_2 are the largest and second largest amplitudes in the MS-EVB expansion of the total wavefunction. Although it has been shown that the actual reaction coordinate describing proton transfer in water involve the collective rearrangement of the hydrogen bond network, the free-energy calculated within the MS-EVB framework as a function of $c_1^2 - c_2^2$ still provides useful insights into the associated energetics since the pivot state has to change identity when $c_1^2 - c_2^2 = 0$, which effectively corresponds to a proton hopping event. As shown in Fig. 6, the free-energy barrier calculated with the present *a*MS-EVB3 model is appreciably lower than that obtained in Ref.[30] with the original MS-EVB3 model, which correlates well with the difference in the corresponding self-diffusion coefficients of the center of excess charge.

The present results thus suggest that a description of the O-H stretching motion of the water molecules in terms of a more physically realistic anharmonic potential is an important component for a more quantitative molecular-level representation of the dynamical properties of the excess proton in aqueous environments. However, although

the significant improvement over the original MS-EVB3 model, the value of the self-diffusion coefficient calculated with the *a*MS-EVB3 model is still somewhat smaller than the corresponding experimental value of 0.94 ± 0.01 $Å^2$/ps. One possible reason for this difference can be related to the fact that the present *a*MS-EVB3 model has been specifically developed for classical simulations, which implies that nuclear quantum effects are neglected. As shown in Ref.[30], the explicit inclusion of nuclear quantum effects in the MS-EVB method combined with a specialized water model designed for quantum simulations results in a ~70% increase of the self-diffusion coefficient. If a similar scaling factor is applied to the value calculated here with the *a*MS-EVB3 model, it would bring D_{CEC} within ~25% of the experimental value. In this regard, it may also be expected that nuclear quantum effects are more pronounced in the case of the *a*MS-EVB3 model due to the anharmonicity of the underlying water model. Another possible reason for the difference between the value calculated with the *a*MS-EVB3 model and the experimental estimate can be related to the fact that polarization effects are only partially taken into account within the *a*MS-EVB3 representation of the system Hamiltonian. A quantitative analysis of the impacts of both polarization and nuclear quantum effects on the mobility of protons in aqueous environments clearly deserves further investigation in future developments of the MS-EVB models.

5.5. Conclusions

In this study a refined MS-EVB model (*a*MS-EVB3) has been developed in order to improve the description of the proton mobility in aqueous environments. The new *a*MS-EVB3 model is built upon an anharmonic water force field (*a*SPC/Fw) in which the

OH stretching motion is described by a quartic approximation to a Morse potential. Through an extended analysis of several structural, thermodynamic and dynamical properties, it is shown that the anharmonic *a*SPC/Fw model provides an improved description of the behavior of water at ambient conditions relative to its harmonic counterpart. In particular, single molecule structural properties such as the equilibrium bond distance and angle are in better agreement with the corresponding experimental values. Importantly, the new model also provides a more accurate representation of the orientational dynamics of water molecules in the liquid phase, which is directly connected with the rearrangements of the hydrogen-bond network.

The anharmonic *a*SPC/Fw water force field is used as a basis for developing an improved version of the multistate empirical valence bond model, the *a*MS-EVB3 model. The latter is shown to provide an accurate description of the solvation structure of an excess proton in bulk water, which is in good agreement with the available experimental data as well as with the results obtained with the previous (harmonic) MS-EVB3 model. Importantly, the new *a*MS-EVB3 model predicts a significantly larger (~40%) proton diffusion coefficient compared to MS-EVB3, which improves the agreement with the experimental estimate of proton mobility in water. This indicates that a more physically correct description of the water properties plays an important role in the description of the hopping events associated with the motion of excess protons in aqueous environments. Although the present result represents an appreciable improvement over previous calculations within the nonpolarizable MS-EVB framework, a noticeable difference still exists between the calculated value and the experimental estimate. Possible reasons for this difference can be associated with nuclear quantum effects and explicit polarization

effects which are neglected in the *a*MS-EVB3. In this regard, it has been shown that the inclusion of nuclear quantum effects into a specifically designed quantum version of the MS-EVB3 model leads to a ~70% increase of the proton diffusion coefficients relative to the classical counterpart. Since nuclear quantum effects are more pronounced for anharmonic potentials, a similar or even larger factor may be expected from quantum simulations with an appropriate quantum version of the *a*MS-EVB3 model. A more detailed analysis of the role played by both polarization and nuclear quantum effects on the mobility of protons in aqueous environments clearly deserves further investigation in future developments of the MS-EVB models. In this regard, the use of more sophisticated water models derived from high level ab initio calculations[52,53] could lead to an overall more accuarte description of proton solvation and transport in the condensed phase.

5.6. Acknowledgments

This research was supported by the National Science Foundation through grant CHE-1111364. We are grateful to the National Science Foundation for a generous allocation of computing time on Teragrid resources as well as to the San Diego Supercomputer Center for a computing time allocation on the Triton Computing Cluster through the TRO program.

Chapter 5 contains materials from “A Refined MS-EVB Model for Proton Transport in Aqueous Environments” published in 2012 in *Journal of Physical Chemistry B. (Volume* 116, pages 343 to 352), authored by Kyoyeon Park, Wei Lin and Francesco Paesani. All material has been reproduced with the consent of all other authors.

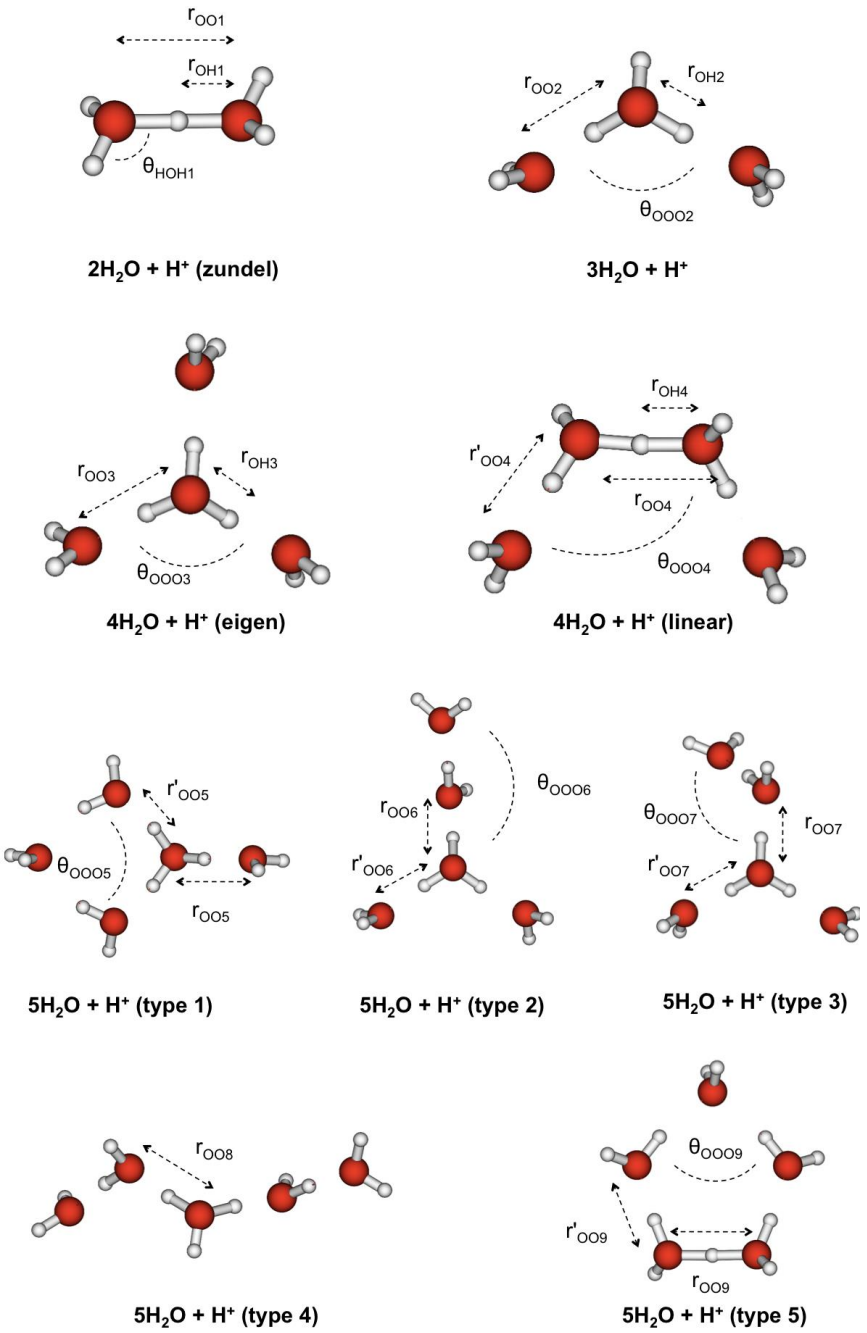

Figure 5.1. Geometries of protonated water dimer (Zundel ion), trimer, tetramers (Eigen ion and linear structure) and pentamers. The geometrical parameters indicated in the figure are listed in Table 5.4.

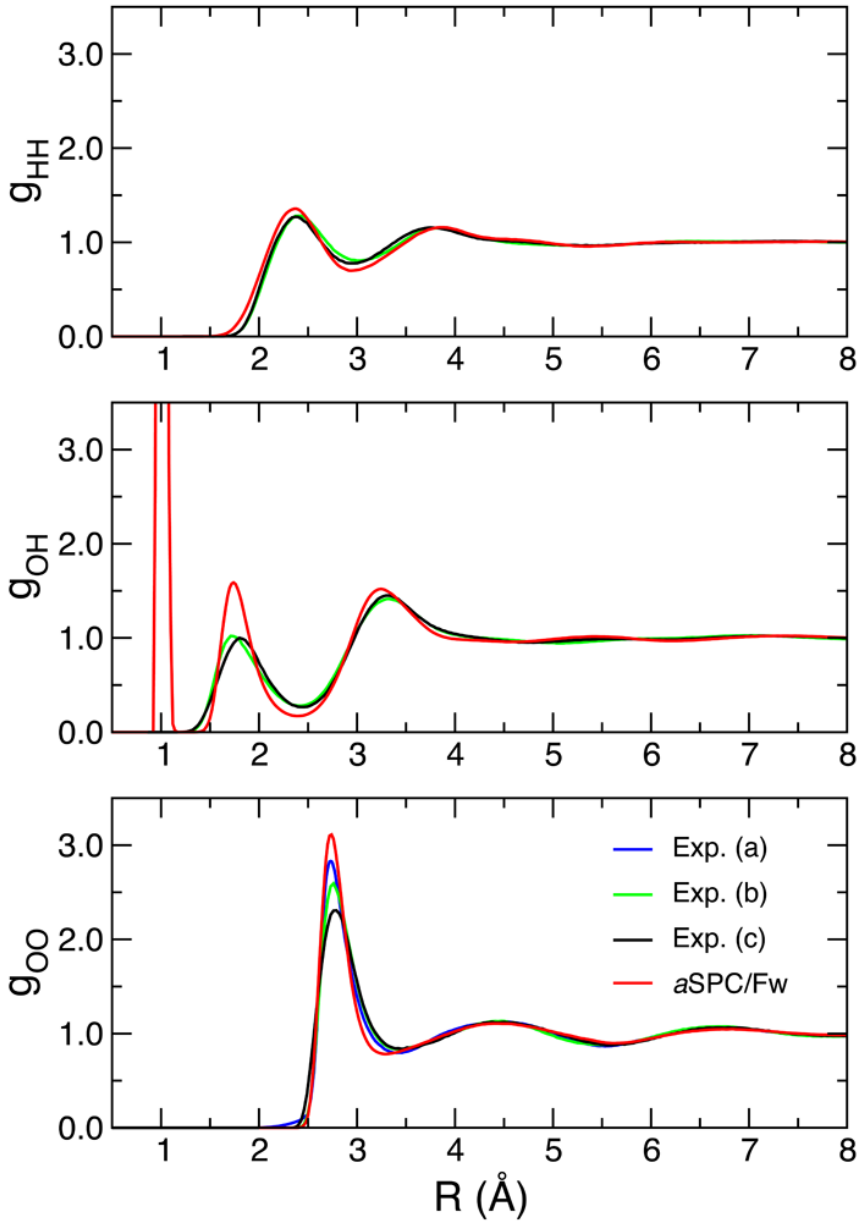

Figure 5.2. Radial distribution functions for oxygen-oxygen (bottom), oxygen-hydrogen (middle panel), and hydrogen-hydrogen (top panel) atom pairs computed with the *a*SPC/Fw water model. The experimental data for the set (a) are from Ref.[44], for the set (b) are from Ref.[45], and for set (c) are from Ref.[46]

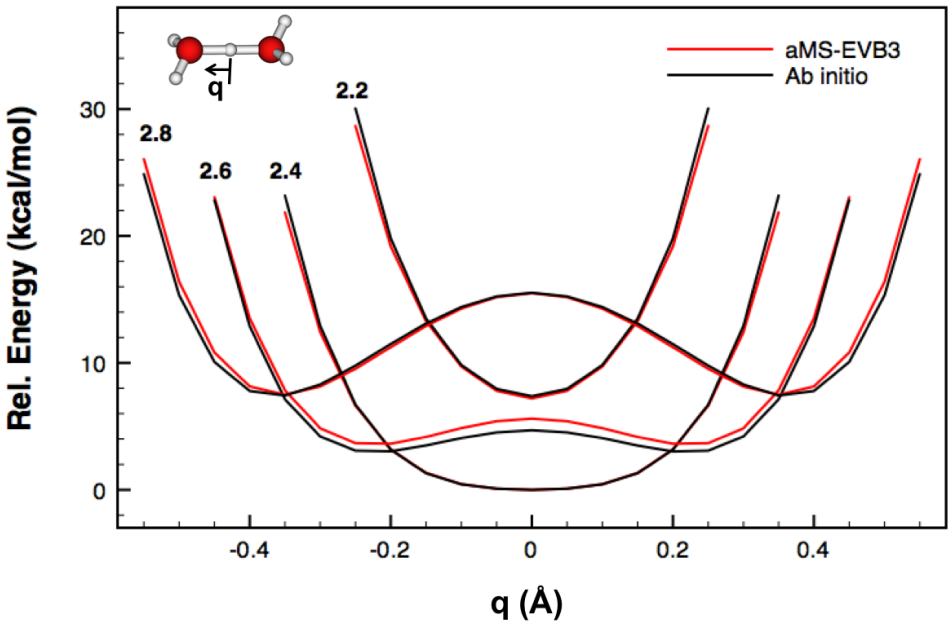

Figure 5.3. PES curves for the proton shuttling in the Zundel ion with O---O distances of 2.2, 2.4, 2.6 and 2.8 Å. The proton shuttling coordinate, *q*, is defined as the difference in the distance of the central hydrogen from its position at the center. See the section 5.4.2 for the details.

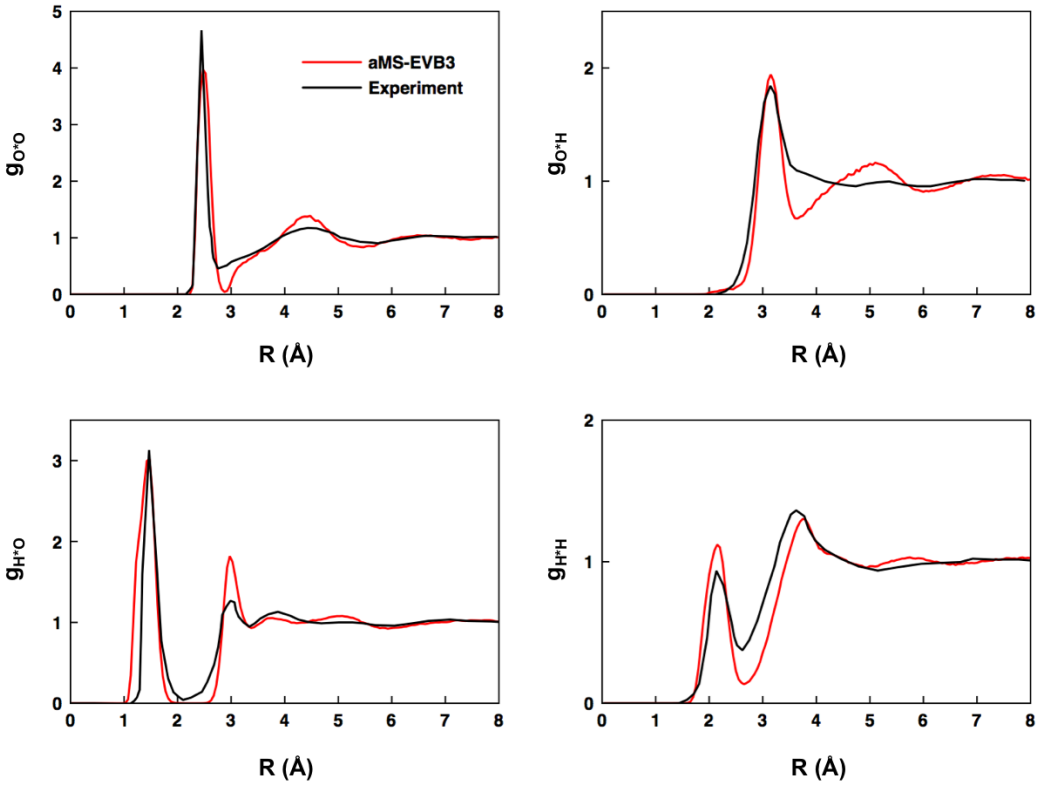

Figure 5.4. RDF curves of bulk water with an excess proton. a) Top left curve: RDF describing the spatial correlation between the oxygen atom of the pivot hydronium ion (O*) and the water oxygen atoms (O); b) Top right curve: RDF describing the spatial correlation between the oxygen atom of the pivot hydronium ion (O*) and the water hydrogen atoms (H); c) Bottom left curve: RDF describing the spatial correlation between the hydrogen atoms of the pivot hydronium ion (H*) and the water oxygen atoms (O); d) Bottom right curve: RDF describing the spatial correlation between the hydrogen atoms in the pivot hydronium ion (H*) and the water hydrogen atoms (H). The experimental data are from Ref.[51].

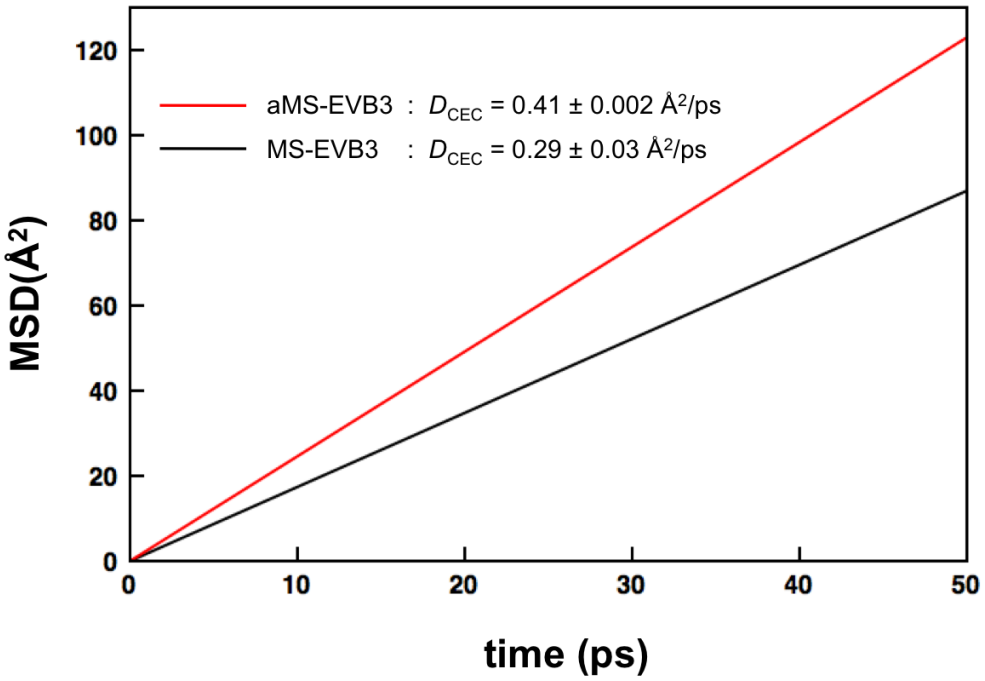

Figure 5.5. Mean-square displacement (MSD) of the excess proton center of the excess charge as a function of time. The data for the MS-EVB3 model are from Ref.[30].

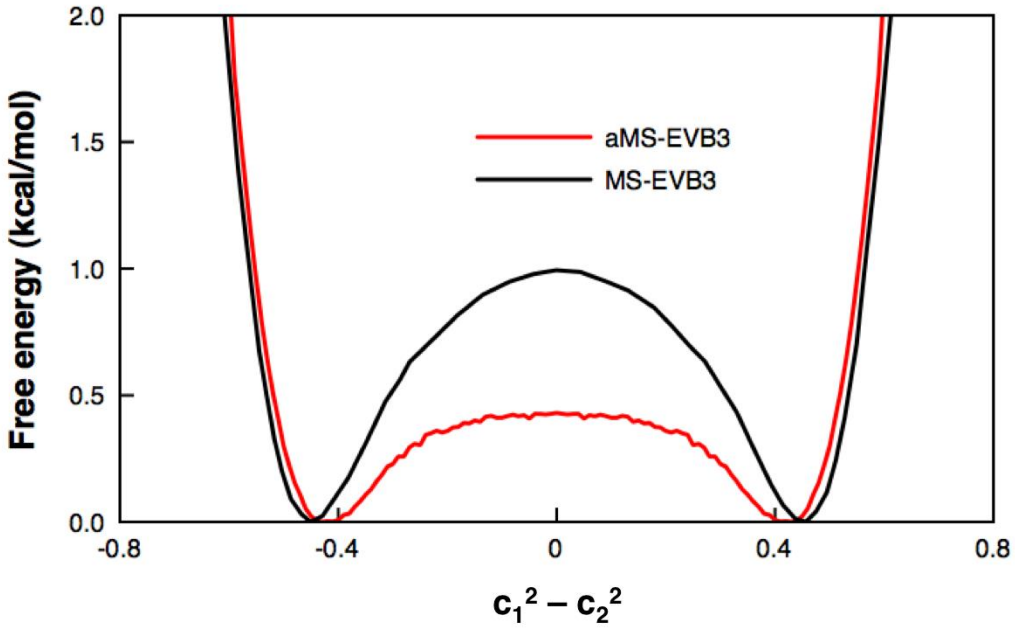

Figure 5.6. Comparison of the *a*MS-EVB3 (red) and MS-EVB3 (black) free energy profiles for the proton-transfer reaction calculated as a function of the difference between the two largest MS-EVB amplitudes, $c_1^2 - c_2^2$. The MS-EVB3 results are from Ref.[30].

Table 5.1. Parameters for the *a*SPC/Fw model.

r_{OH}^{eq}	(Å)	0.995
D_{OH}	(kcal mol^{-1})	116.09
α_{OH}	(Å $^{-1}$)	2.287
K_{HOH}	(kcal mol^{-1} rad^{-2})	75.9
θ_{HOH}^{eq}	(degree)	112.5
q_O	(e)	-0.8350
q_H	(e)	0.4175
ε_{OO}	(kcal mol^{-1})	0.1554253
σ_{OO}	(Å)	3.165492

Table 5.2. Parameters for the *a*MS-EVB3 model.

D_{OH}	(kcal/mol)	94.40010014	$r_{OO}^{sm,1\ a}$	(Å)	2.85
a_{OH}	($Å^{-1}$)	2.26724650	$r_{OO}^{sm,2\ b}$	(Å)	3.05
r_{OH}^{eq}	(Å)	1.0	$r_{OH}^{sm,1\ c}$	(Å)	2.50
k_{ϕ}	(kcal/mol/rad^2)	77.4868	$r_{OH}^{sm,2\ d}$	(Å)	3.00
φ_{HOH}^{eq}	(degree)	111.7269	V^{ij}_{const}	(kcal/mol)	-24.29325513
ε_{OOw}	(kcal/mol)	0.12074169	q_O^{ex}	(*e*)	-0.09290503
σ_{OOw}	(Å)	3.11941063	q_H^{ex}	(*e*)	0.03181478
ε_{HOw}	(kcal/mol)	0.00212056	$q_{H^*}^{ex}$	(*e*)	0.05855095
σ_{HOw}	(Å)	1.58086145	γ	($Å^{-2}$)	1.47116944
$q_O^{H_3O^+}$	(*e*)	-0.5	P		0.10342117
$q_H^{H_3O^+}$	(*e*)	0.5	k	($Å^{-2}$)	9.56531102
B	(kcal/mol)	11.28233555	D_{OO}	(Å)	3.00673285
b	($Å^{-1}$)	3.01657850	β	($Å^{-1}$)	7.05386835
b'	($Å^{-2}$)	2.40174399	R^0_{OO}	(Å)	3.04448208
d^0_{OO}	(Å)	2.40206347	P'	($Å^{-1}$)	7.58446749
C	(kcal/mol)	6.47644661	α	($Å^{-1}$)	7.19736309
c	($Å^{-1}$)	0.95362792	r^0_{OO}	(Å)	1.80176071
d_0^{OH}	(Å)	1.04900956			

[a] $r_{OO}^{sm,1}$: smooth cut-off starting distance for O-O repulsive term
[b] $r_{OO}^{sm,2}$: smooth cut-off ending distance for O-O repulsive term
[c] $r_{OH}^{sm,1}$: smooth cut-off starting distance for H-O repulsive term
[d] $r_{OH}^{sm,2}$: smooth cut-off ending distance for H-O repulsive term

Table 5.3. Comparison between the water properties calculated with the *a*SPC/Fw model and the corresponding experimental data. Also shown are the results obtained in Ref.[11] with the SPC/Fw model. All properties are described in the text.

Property		*a*SPC/Fw	Experiment	SPC/Fw
$\langle r_{OH} \rangle$	(Å)	1.0150 ± 0.0002	0.970[a]	1.0310 ± 10^{-6}
$\langle \theta_{HOH} \rangle$	(deg)	106.80 ± 0.05	106[b]	107.69 ± 0.33
$\langle \mu \rangle$	(D)	2.420 ± 0.005	2.9[c]	2.39 ± 0.19
ρ	(g cm^{-3})	1.01 ± 0.01	0.997[d]	1.012 ± 0.016
ΔH_{vap}	(kcal mol^{-1})	10.7 ± 0.1	10.52[e]	10.72 ± 0.12
C_p	(kcal mol^{-1} K^{-1})	27.1 ± 0.1	17.99[f]	27.37
ε		88 ± 2	78.5[g]	79.63
α	(10^{-4} K^{-1})	4.3 ± 0.1	2.0[h]	4.90
κ_T	(10^{-5} atm^{-1})	4.6 ± 0.1	4.58[i]	4.50
D	(Å ^{2} ps^{-1})	0.233 ± 0.001	0.229[l]	0.232 ± 0.05
τ_2	(ps)	2.7 ± 0.1	2.5[m]	1.86

[a] From Ref.[54]
[b] Derived from Ref.[54]
[c] From Ref.[55]
[d] From Ref.[56]
[e] From Ref.[57]
[f] From Ref.[58]
[g] From Ref.[58]
[h] From Ref.[59]
[i] From Ref.[59]
[l] From Ref.[60]
[m] From Ref.[61]

Table 5.4. Geometries of protonated water clusters[a]

	int. coord.[b]	*a*MS-EVB3	MS-EVB3[c]	MP2/aug-cc-pVTZ
$2H_2O + H^+$ (Zundel)	r_{OO1}	2.37	2.39	2.40
	r_{OH1}	1.19	1.20	1.20
	θ_{HOH1}	117.6	117.3	115.8
$3H_2O + H^+$	r_{OO2}	2.49	2.50	2.49
	r_{OH2}	1.07	1.07	1.04
	θ_{OOO2}	110.8	110.6	117.1
$4H_2O + H^+$ (Eigen)	r_{OO3}	2.53	2.55	2.55
	r_{OH3}	1.05	1.07	1.01
	θ_{OOO3}	108.4	108.4	114.1
$4H_2O + H^+$ (linear)	r_{OO4}	2.37	2.37	2.39
	r'_{OO4}	2.59	2.59	2.59
	r_{OH4}	1.18	1.19	1.20
	θ_{OOO4}	115.7	114.7	119.1
$5H_2O + H^+$ (type 1)	r_{OO5}	2.54	2.55	2.57
	r'_{OO5}	2.54	2.51	2.54
	θ_{OOO5}	78.1	75.6	79.0
$5H_2O + H^+$ (type 2)	r_{OO6}	2.44	2.46	2.47
	r'_{OO6}	2.55	2.56	2.59
	θ_{OOO6}	120.2	120.2	117.4
$5H_2O + H^+$ (type 3)	r_{OO7}	2.45	2.46	2.47
	r'_{OO7}	2.56	2.57	2.59
	θ_{OOO7}	125.2	125.0	121.9
$5H_2O + H^+$ (type 4)	r_{OO8}	2.49	2.48	2.46
$5H_2O + H^+$ (type 5)	r_{OO9}	2.37	2.37	2.39
	r'_{OO9}	2.57	2.58	2.57
	θ_{OOO9}	85.7	85.0	91.3

[a] Units are in Å for distances and degree for angles.
[b] All coordinates are defined Figure 5.1.
[c] From Ref.[30]. The MS-EVB3 geometries for the $5H_2O + H^+$ clusters were directly computed using the force field parameters reported in Ref.[30,37]

Table 5.5. Comparison of Binding Energies of Protonated Water Clusters[a]

	*a*MS-EVB3	MS-EVB3[b]	CCSD(T)//MP2 /aug-cc-pVTZ
$2H_2O + H^+$ (Zundel)	-32.83	-33.05	-33.47
$3H_2O + H^+$	-56.64	-57.18	-57.65
$4H_2O + H^+$ (Eigen)	-79.05	-79.70	-77.55
$4H_2O + H^+$ (linear)	-73.89	-73.90	-73.68
$5H_2O + H^+$ (type 1)	-91.93	-93.64	-92.21
$5H_2O + H^+$ (type 2)	-93.52	-93.85	-91.15
$5H_2O + H^+$ (type 3)	-93.56	-93.96	-91.17
$5H_2O + H^+$ (type 4)	-87.67	-87.67	-87.63
$5H_2O + H^+$ (type 5)	-89.14	-89.41	-88.61

[a] Units are in kcal mol^{-1}.
[b] From Ref.[30]

5.7. References

(1) Maréchal, Y. *The hydrogen bond and the water molecule: The physics and chemistry of water, aqueous and bio-media*; Elsevier: Amsterdam, 2006.

(2) Ball, P. *Life's matrix: A biography of water*; U. of California Press, 2001.

(3) Swanson, J. M. J.; Maupin, C. M.; Chen, H.; Petersen, M. K.; Xu, J.; Wu, Y.; Voth, G. A.; Proton solvation and transport in aqueous and biomolecular systems: Insights from computer simulations; *J. Phys. Chem. B* **2007**, *111*, 4300-4314.

(4) Marx, D.; Proton transfer 200 years after von Grotthuss: Insights from ab initio simulations; *Chemphyschem* **2006**, *7*, 1848-1870.

(5) Molinero, V.; Moore, E. B.; Water Modeled As an Intermediate Element between Carbon and Silicon; *Journal of Physical Chemistry B* **2009**, *113*, 4008-4016.

(6) Izvekov, S.; Parrinello, M.; Burnham, C. J.; Voth, G. A.; Effective force fields for condensed phase systems from ab initio molecular dynamics simulation: A new method for force-matching; *J. Chem. Phys.* **2004**, *120*, 10896-10913.

(7) Abascal, J. L. F.; Vega, C.; A general purpose model for the condensed phase of water: TIP4P/2005; *J. Chem. Phys.* **2005**, *123*, 234505.

(8) Berendsen, H. J. C.; Grigera, J. R.; Straatsma, T. P.; The missing term in effective pair potentials; *Journal of Physical Chemistry* **1987**, *91*, 6269.

(9) Jorgensen, W. L.; Chandrasekhar, J.; Madura, J. D.; Impey, R. W.; Klein, M. L.; Comparison of simple potential functions for simulating liquid water; *The Journal of Chemical Physics* **1983**, *79*, 926-935.

(10) Horn, H. W.; Swope, W. C.; Pitera, J. W.; Madura, J. D.; Dick, T. J.; Hura, G. L.; Head-Gordon, T.; Development of an improved four-site water model for biomolecular simulations: TIP4P-Ew; *J. Chem. Phys.* **2004**, *120*, 9665-9678.

(11) Wu, Y. J.; Tepper, H. L.; Voth, G. A.; Flexible simple point-charge water model with improved liquid-state properties; *J. Chem. Phys.* **2006**, *124*, 024503.

(12) Bukowski, R.; Szalewicz, K.; Groenenboom, G. C.; van der Avoird, A.; Polarizable interaction potential for water from coupled cluster calculations. II. Applications to dimer spectra, virial coefficients, and simulations of liquid water; *Journal of Chemical Physics* **2008**, *128*, 094314.

(13) Wang, Y.; Bowman, J. M.; Towards an ab initio flexible potential for water, and post-harmonic quantum vibrational analysis of water clusters; *Chemical Physics Letters* **2010**, *491*, 1-10.

(14) Tainter, C. J.; Pieniazek, P. A.; Lin, Y. S.; Skinner, J. L.; Robust three-body water simulation model; *Journal of Chemical Physics* **2011**, *134*, 184501.

(15) Fanourgakis, G. S.; Xantheas, S. S.; Development of transferable interaction potentials for water. V. Extension of the flexible, polarizable, Thole-type

model potential (TTM3-F, v. 3.0) to describe the vibrational spectra of water clusters and liquid water; *Journal of Chemical Physics* **2008**, *128*, 074506.

(16) Burnham, C. J.; Anick, D. J.; Mankoo, P. K.; Reiter, G. F.; The vibrational proton potential in bulk liquid water and ice; *J. Chem. Phys.* **2008**, *128*, 154519.

(17) Mankoo, P. K.; Keyes, T.; POLIR: Polarizable, flexible, transferable water potential optimized for IR spectroscopy; *J. Chem. Phys.* **2008**, *129*, 034504-034509.

(18) Lobaugh, J.; Voth, G. A.; A quantum model for water: Equilibrium and dynamical properties; *J. Chem. Phys.* **1997**, *106*, 2400-2410.

(19) Paesani, F.; Zhang, W.; Case, D. A.; Cheatham, T. E., III; Voth, G. A.; An accurate and simple quantum model for liquid water; *J. Chem. Phys.* **2006**, *125*, 184507.

(20) Habershon, S.; Markland, T. E.; Manolopoulos, D. E.; Competing quantum effects in the dynamics of a flexible water model; *J. Chem. Phys.* **2009**, *131*, 024501.

(21) de Grotthuss, C. J. T.; Sur la décomposition de l'eau et des corps qu' elle tient en dissolution à l'aide de l'électricité galvanique; *Annales de Chimie* **1806**, *58*, 54.

(22) Swanson, J. M. J.; Simons, J.; Role of Charge Transfer in the Structure and Dynamics of the Hydrated Proton; *J. Phys. Chem. B* **2009**, *113*, 5149-5161.

(23) Lin, I. C.; Seitsonen, A. P.; Coutinho-Neto, M. D.; Tavernelli, I.; Rothlisberger, U.; Importance of van der Waals interactions in liquid water; *J. Phys. Chem. B* **2009**, *113*, 1127-1131.

(24) Murdachaew, G.; Mundy, C. J.; Schenter, G. K.; Improving the density functional theory description of water with self-consistent polarization; *Journal of Chemical Physics* **2010**, *132*, 164102.

(25) Yoo, S.; Xantheas, S. S.; Communication: The effect of dispersion corrections on the melting temperature of liquid water; *Journal of Chemical Physics* **2011**, *134*, 121105.

(26) Wang, J.; Roman-Perez, G.; Soler, J. M.; Artacho, E.; Fernandez-Serra, M. V.; Density, structure, and dynamics of water: The effect of van der Waals interactions; *Journal of Chemical Physics* **2011**, *134*, 024516.

(27) Schmitt, U. W.; Voth, G. A.; Multistate empirical valence bond model for proton transport in water; *Journal of Physical Chemistry B* **1998**, *102*, 5547-5551.

(28) Schmitt, U. W.; Voth, G. A.; The computer simulation of proton transport in water; *The Journal of Chemical Physics* **1999**, *111*, 9361-9381.

(29) Day, T. J. F.; Soudackov, A. V.; Cuma, M.; Schmitt, U. W.; Voth, G. A.; A second generation multistate empirical valence bond model for proton transport in aqueous systems; *Journal of Chemical Physics* **2002**, *117*, 5839-5849.

(30) Wu, Y.; Chen, H.; Wang, F.; Paesani, F.; Voth, G. A.; An improved multistate empirical valence bond model for aqueous proton solvation and transport; *Journal of Physical Chemistry B* **2008**, *112*, 467-482.

(31) Vuilleumier, R.; Borgis, D.; *J. Phys. Chem. B* **1998**, *102*, 4261.

(32) Vuilleumier, R.; Borgis, D.; *J. Chem. Phys.* **1999**, *111*, 4251.

(33) Warshel, A. *Computer Modeling of Chemical Reactions in Enzymes and Solutions*; Wiley-Interscience: New York, 1991.

(34) Markovitch, O.; Chen, H.; Izvekov, S.; Paesani, F.; Voth, G. A.; Agmon, N.; Special Pair Dance and Partner Selection: Elementary Steps in Proton Transport in Liquid Water; *Journal of Physical Chemistry B* **2008**, *112*, 9456-9466.

(35) Brancato, G.; Tuckerman, M. E.; A polarizable multistate empirical valence bond model for proton transport in aqueous solution; *Journal of Chemical Physics* **2005**, *122*.

(36) Paesani, F.; Voth, G. A.; A quantitative assessment of the accuracy of centroid molecular dynamics for the calculation of the infrared spectrum of liquid water; *Journal of Chemical Physics* **2010**, *132*, 014105.

(37) Wu, Y.; Chen, H.; Wang, F.; Paesani, F.; Voth, G. A.; An improved multistate empirical valence bond model for aqueous proton solvation and transport (vol 112B, pg 467, 2008); *Journal of Physical Chemistry B* **2008**, *112*, 7146-7146.

(38) Case, D. A.; et al.; Amber 11; University of California - San Francisco: San Francisco, 2010.

(39) Smith, W.; Forester, T.; *J. Molec. Graphics* **1996**, *14*, 136.

(40) Frenkel, D.; Smit, B. *Understanding molecular simulation: From algorithms to applications*; Academic Press, 2001.

(41) Goldberg, D. E. *Genetic Algorithms in Search, Optimization and Machine Learning*; 1st ed.; Addison-Wesley Longman Publishing Co..: Boston, 1989.

(42) Carroll, D. L.Fortran code: Genetric Algorithm

(43) Frisch, M. J.; et al..; Gaussian, Inc.: Wallingford, CT, 2009.

(44) Hura, G.; Russo, D.; Glaeser, R. M.; Head-Gordon, T.; Krack, M.; Parrinello, M.; Water structure as a function of temperature from X-ray scattering experiments and ab initio molecular dynamics; *PhysChemChemPhys* **2003**, *5*, 1981-1991.

(45) Soper, A. K.; Benmore, C. J.; Quantum differences between heavy and light water; *Physical Review Letters* **2008**, *101*, 065502.

(46) Wikfeldt, K. T.; Leetmaa, M.; Ljungberg, M. P.; Nilsson, A.; Pettersson, L. G. M.; On the Range of Water Structure Models Compatible with X-ray and Neutron Diffraction Data; *Journal of Physical Chemistry B* **2009**, *113*, 6246-6255.

(47) Wernet, P.; Nordlund, D.; Bergmann, U.; Cavalleri, M.; Odelius, M.; Ogasawara, H.; Näslund, L. Å.; Hirsh, T. K.; Ojamäe, L.; Glatzel, P.; Pettersson, L. G. M.; Nilsson, A.; The structure of the first coordination shell in liquid water; *Science* **2004**, *304*, 995-999.

(48) Tokushima, T.; Harada, Y.; Takahashi, O.; Senba, Y.; Ohashi, H.;

Pettersson, L. G. M.; Nilsson, A.; Shin, S.; High resolution X-ray emission spectroscopy of liquid water: The observation of two structural motifs; *Chemical Physics Letters* **2008**, *460*, 387-400.

(49) Huang, C.; Wikfeldt, K. T.; Tokushima, T.; Nordlund, D.; Harada, Y.; Bergmann, U.; Niebuhr, M.; Weiss, T. M.; Horikawa, Y.; Leetmaa, M.; Ljungberg, M. P.; Takahashi, O.; Lenz, A.; Ojamae, L.; Lyubartsev, A. P.; Shin, S.; Pettersson, L. G. M.; Nilsson, A.; The inhomogeneous structure of water at ambient conditions; *Pro. Nati. Acad. Sci. USA* **2009**, *106*, 15214-15218.

(50) Clark, G. N. I.; Cappa, C. D.; Smith, J. D.; Saykally, R. J.; Head-Gordon, T.; The structure of ambient water; *Molecular Physics* **2010**, *108*, 1415-1433.

(51) Botti, A.; Bruni, F.; Imberti, S.; Ricci, M. A.; Soper, A. K.; Ions in water: The microscopic structure of a concentrated HCl solution; *Journal of Chemical Physics* **2004**, *121*, 7840-7848.

(52) Cencek, W.; Szalewicz, K.; Leforestier, C.; van Harrevelt, R.; van der Avoird, A.; An accurate analytic representation of the water pair potential; *Physical Chemistry Chemical Physics* **2008**, *10*, 4716-4731.

(53) Wang, Y.; Shepler, B. C.; Braams, B. J.; Bowman, J. M.; Full-dimensional, ab initio potential energy and dipole moment surfaces for water; *The Journal of Chemical Physics* **2009**, *131*, 054511-054518.

(54) Ichikawa, K.; Kameda, Y.; Yamaguchi, T.; Wakita, H.; Misawa, M.; Neutron-diffraction investigation; *Molecular Physics* **1991**, *73*, 79-86.

(55) Badyal, Y. S.; Saboungi, M. L.; Price, D. L.; Shastri, S. D.; Haeffner, D. R.; Soper, A. K.; Electron distribution in water; *Journal of Chemical Physics* **2000**, *112*, 9206-9208.

(56) Kell, G. S.; Precise representatino of volume properties of water; *Journal of Chemical and Engineering Data* **1967**, *12*, 66-&.

(57) Wagner, W.; Pruss, A.; The IAPWS formulation 1995 for the thermodynamic properties of ordinary water substance for general and scientific use; *Journal of Physical and Chemical Reference Data* **2002**, *31*, 387-535.

(58) *Handbook of Chemistry and Physics*; Haynes, W. M., Ed.; CRC, 2011.

(59) *Water: A comprehensive treatise*; Franks, F., Ed.; Plenum: NY, 1972.

(60) Krynicki, K.; Green, C. D.; Sawyer, D. W.; Pressure and temperature-dependence of self-diffusion in water; *Faraday Discussions* **1978**, *66*, 199-208.

(61) Bakker, H. J.; Rezus, Y. L. A.; Timmer, R. L. A.; Molecular reorientation of liquid water studied with femtosecond midinfrared spectroscopy; *J. Phys. Chem. A* **2008**, *112*, 11523-11534.

Chapter 6. Fast and slow proton transfer in ice: The role of the quasi-liquid layer and hydrogen-bond network

6.1. Abstract

The proton mobility in ice is studied through molecular dynamics simulations carried out with a newly developed ab initio-based reactive force field, *a*MS-EVB3/ice. The analysis of both structural and dynamical properties of protonated ice as a function of temperature indicates that the mobility of excess protons at the surface is largely suppressed, with protons becoming essentially immobile at temperatures below 200 K. In contrast, fast proton transfer/transport can exist in bulk ice I_h at low temperature through connected regions of the proton-disordered hydrogen-bond network. Based on the simulation results, it is shown that the mechanisms associated with proton transfer/transport in both bulk and interfacial regions of ice are largely dependent on the local hydrogen-bond structure surrounding the charge defect. A molecular-level picture of the mechanisms responsible for proton transfer/transport in ice is then developed and used to interpret the available experimental data.

6.2. Introduction

The characterization of both physical and chemical properties of ice at the molecular level is key to the understanding of the mechanisms associated with several fundamental processes that take place in the environment.[1,2] For example, ice properties,

including structure, reactivity, and conductivity, play important roles in cloud formation and charging in the troposphere as well as in the stratospheric ozone cycle.[3-6] As a consequence, the behavior of ice under different conditions has been the subject of numerous experimental and theoretical studies.[3,4,7-15] In particular, the proton activity of ice has attracted much interest because of its direct implication in charge transport phenomena,[3,4] cloud charging, and stratospheric chemistry.[5,6] Although conductivity measurements have been used extensively to characterize proton transfer and transport in ice, the considerable variability of the experimental conditions (e.g., presence of impurities, sample preparation, and detection techniques) has led to several hypotheses about the molecular mechanisms responsible for the observed proton mobility.

In hexagonal ice (ice I_h), water molecules are arranged in a tetrahedral network, with each molecule establishing four hydrogen bonds (H-bonds) with its four closest neighbors. Although the crystalline structure of ice I_h is characterized by a substantial amount of proton disorder,[3,4] the number of donating and accepting H-bonds associated with each water molecule must satisfy the so-called Bernal-Fowler rules.[16] Any violation of these rules results in the creation of local defects (known as point defects or Bjerrum defects) within the H-bond network.[4,17] Unlike in the bulk region, both the positions of the oxygen atoms and the orientations of the water molecules at the surface of ice I_h show a significant amount of disorder. This interfacial region, known as the quasi-liquid layer (QLL),[18-21] has important implications in heterogeneous processes taking place in the environment.[1,2]

Two distinct mechanisms for proton transport in ice have been described in the literature: the Bjerrum-defect (or orientational-defect) transfer and the proton-hopping

relay (ionic-defect transfer).[4,17] The Bjerrum-defect transfer mechanism involves rotations of the water molecules within the ice lattice with the consequent creation of local defects and charge densities. In the hopping-relay mechanism, proton transfer events occur through the cleavage and subsequent formation of O-H bonds between adjacent water molecules. In mid-1980s, Devlin and co-workers showed that the proton mobility measured in hydrogen/deuterium (H/D) exchange experiments on ice nanoparticles could be explained by considering the combination of both Bjerrum-defect transfer and proton-hopping relay events.[8] Based on the spectroscopic data, the time scale for both processes was estimated to be on the order of minutes. The molecular mechanisms and energy barriers associated with H/D exchange reactions were also studied on ice surfaces by Kang and co-workers.[11-13] It was found that, although H/D exchange reactions on the surface of thin ice films could occur via the same mechanisms as in bulk ice, the time scale associated with proton-hopping events was significantly shorter than that required for Bjerrum-defect transfers measured for ice films grown after HCl deposition.[12] Further evidence for the time scale associated with proton-hopping events was provided by quasi-elastic neutron scattering experiments in which extremely fast non-vibrational proton motions were observed on the picosecond time scale over a wide temperature range (5 – 270 K) for both pure and HCl-doped ice.[22,23] In this regard, it is believed that proton hopping events can transport the excess charge only over relatively short distances[4,12] since longer length scales require the concerted motion of several water molecules within the ice lattice.[4,7,12,24]

It has been found that ice media with different physical morphologies display significantly different electric conductivity values. High charge transport was measured

on the surface of doped ice near the melting temperature.[4] It was observed that proton activity in bulk ice could be controlled by acid and base adsorbates, which implies that excess charges can effectively be transported from the surface to the interior regions.[10] However, soft-landing experiments in which hydronium (H_3O^+) ions were deposited on ice films showed no surface-to-bulk charge transport at low temperature ($T < 190$ K).[7] Interestingly, high proton mobility was found at the surface of thin ice films grown after acid deposition even below 140 K.[11] To explain the low mobility of the excess charge in the interfacial regions of ice, it was suggested that H_3O^+ ions could have higher affinity to the ice surface compared to the interior regions.[12,25] However, this is in apparent contradiction with data collected from quasi-elastic neutron scattering measurements[22,23] and more recent experiments showing no obvious affinity of hydronium ions for the ice surface.[26]

In this chapter, we report on atomistic simulations of structural and dynamical properties of excess protons in both hexagonal and amorphous ice in the temperature range between 100 K and 265 K.

6.3. Computational methodology

6.3.1. The anharmonic aSPC/Fw/ice model

Simulation studies of the ice properties as a function of temperature require water models capable of correctly reproducing the melting/freezing behavior. To this end, the *a*SPC/Fw water model described in ref [27] was specifically re-parameterized for ice simulations. The new model (called *a*SPC/Fw/ice) predicts a melting point of 267.5 ± 2.5 K for ice I_h at atmospheric pressure, which is in reasonably good agreement with the

corresponding experimental value. The parameterization of the *a*SPC/Fw/ice model was performed through a series of water-ice coexistence simulations carried out at different temperatures. Following ref [28], an initial configuration of ice I_h containing 768 water molecules was prepared according to the Bernal-Fowler rules.[16] A water box, also containing 768 molecules, was then placed in contact with the basal (0001) plane of the ice I_h box. At each temperature, the ice/water system was equilibrated for 2 ns in the isobaric-isothermal (NPT) ensemble after which an 8 ns-long NPT simulation was used to monitor the temperature variations of the oxygen-oxygen (O-O) radial distribution functions (RDFs) calculated independently for molecules initially located in the ice and water phases. In these simulations, the temperature was controlled by a Langevin thermostat with a collision frequency of 20 ps^{-1} while the pressure was maintained by a Berendsen barostat with a relaxation time of 0.1 ps. Periodic boundary conditions were employed in all directions. Both intra- and inter-molecular parameters of the original *a*SPC/Fw model were re-optimized to reproduce the melting point of ice determined from the ice/water coexistence simulations. The optimized parameters for the *a*SPC/Fw/ice model are listed in Table 6.3 in the Supporting Information. Snapshots of both initial and final ice/water configurations at T = 265, 270 and 275 K are shown in Figure 6.9, while the corresponding O-O RDFs are shown in Figure 6.10 in the Supporting Information.

6.3.2. The anharmonic aMS-EVB3/ice model

The multi-state empirical valence bond (MS-EVB) method[27,29-32] was used to model proton transfer and transport in ice. It has been shown that MS-EVB provides accurate descriptions of structural, thermodynamic, and dynamical properties of hydrated

protons in water[32-38] as well as in complex aqueous environments.[39-46] Because of its computationally efficiency compared to *ab initio* approaches, the MS-EVB method enables relatively longer simulations that are necessary for the statistical analysis of molecular observables associated with slow dynamical processes.

The aMS-EVB3/ice model employed in the simulations described in the next section was developed by re-parameterizing the third generation of MS-EVB models[27,32] using the aSPC/Fw/ice model to represent the water interactions. The aMS-EVB3/ice parameters obtained following the protocol described in ref [27] are listed in Table 6.4 in the Supporting Information. Comparisons between aMS-EVB3/ice and *ab initio* results calculated for both geometries and binding energies of small protonated water clusters as well as for the proton shuttling potential energy surface are reported in the Supporting Information (Tables 6.5 and 6.6, and Figure 6.8).

6.3.3 Ice I_h and amorphous ice configurations

The initial configurations of ice I_h were prepared according to the following procedure: 1) the oxygen (O) atoms of the water molecules were placed in an orthorhombic unit cell[4] with cell parameters taken from synchrotron radiation experiments;[47] 2) the unit cell was replicated along the three Cartesian directions; 3) two hydrogen (H) atoms were assigned to each O atom with random OH orientations; 4) the number of Bjerrum defects was minimized by rotating the OH bonds until all molecules satisfied Bernal-Fowler's rules; 5) the total dipole moment of the resulting ice configuration was calculated. Steps 3 to 5 were repeated until the total dipole moment of the system was minimized. A protocol similar to that proposed in Refs.[28] and [48] was used

in steps 3 and 4. The final (proton-disordered) configurations of ice I_h contained 896 water molecules (8 bilayers, 112 water molecules per bilayer). The initial configurations of amorphous ice were instead prepared by cooling an equilibrated box of liquid water containing 1000 molecules from 298 K to the target temperatures used in the ice simulations. These was accomplished through a series of NPT simulations in which the temperature was gradually reduced at a cooling rate of 0.05 K / ps. The initial configurations of ice I_h and amorphous ice were equilibrated for 2 ns at temperatures ranging from 100 K to 265 K through a series of NVT and NPT simulations.

After equilibration, the simulation boxes were extended in the z-direction to create extended slab configurations. For ice I_h, the (0001) surface (basal plane) was chosen since it is considered to be the most relevant ice surface in the atmosphere.[49] To relax the surface region, NVT simulations for all slab configurations were carried out at each temperature for additional 2 ns. The positions of all water molecules located in the bottommost bilayer of the ice I_h slab and within 4 Å of the bottom of amorphous ice slab kept fixed at their initial locations in order to reproduce bulk continuum. The dimensions of both ice I_h and amorphous ice slabs were approximately 32 Å × 31 Å × 30 Å.

6.3.4 Molecular dynamics simulations of protonated ice

Three different systems were investigated: 1) the surface of ice I_h with an excess proton in the temperature range 100 K – 265 K; 2) the surface of amorphous ice with an excess proton at 190 K, 250 K, and 265 K; 3) bulk ice I_h with an excess proton at 190 K. For the slab simulations, the excess proton was introduced in the system by randomly protonating one water molecule within the top bilayer (for ice I_h) or within 3 Å of the

surface (Figure 6.1). The resulting protonated ice configurations were then accepted if the distance between the excess proton and any other atom was larger than 1.5 Å. After protonation, NVT simulations were carried out for 1 ns in order to equilibrate the surface structures. At each temperature, the structural and dynamical properties of the protonated ice surfaces were calculated from additional 1-ns NVE simulations.

For simulations of bulk ice I_h with an excess proton, the initial (pure) ice configuration was equilibrated at 190 K and 1 bar for 1 ns in the NPT ensemble. After equilibration, the excess proton was added to the system by randomly protonating one water molecule. A total of 500 different configurations were prepared. Since each water molecule in bulk ice I_h accepts and donates two H-bonds, the insertion of an extra proton results in the creation of a D-defect, in which two OH bonds point toward each other. For each initial configuration, the artificially created D-defects were relaxed for 50 ps in the NVT ensemble. This was then followed by 50-ps NVE simulations during which all structural and dynamical properties of the excess proton were calculated.

All simulations were carried out with a modified version of DL_POLY2.[50] A Nosé-Hoover thermostat with a relaxation time of 0.5 ps was used in the NVT simulations, and Nosé-Hoover thermostat and barostat (with relaxation times of 0.5 ps) were used in the NPT simulations.[51,52] A time step of 0.5 fs was used in all NVE, NVT, and NPT simulations. The self-diffusion coefficient of the excess proton was calculated from the Einstein's relation[53]

$$D_{CEC} = \lim_{t\to\infty} \frac{\left\langle \left| \mathbf{r}_{CEC}(t) - \mathbf{r}_{CEC}(0) \right|^2 \right\rangle}{6t} \tag{7.1}$$

where $\mathbf{r}_{CEC}$ is the center of excess charge (CEC),[27]

$$\mathbf{r}_{CEC} = \sum_{i=1}^{n} c_i^2 \, \mathbf{r}_{COC}^i \tag{7.2}$$

Here, $\mathbf{r}^i_{COC}$ is the center of charge of the i-th EVB state. For all slab simulations, two distinct coefficients were calculated corresponding to proton diffusion parallel, $D^{\parallel}_{CEC}$ and perpendicular, $D^{\perp}_{CEC}$, to the ice surface,

$$D^{\parallel}_{CEC} = \lim_{t\to\infty} \frac{\left\langle \left| \mathbf{r}_{CEC,xy}(t) - \mathbf{r}_{CEC,xy}(0) \right|^2 \right\rangle}{4t} \tag{7.3}$$

$$D^{\perp}_{CEC} = \lim_{t\to\infty} \frac{\left\langle \left| \mathbf{r}_{CEC,z}(t) - \mathbf{r}_{CEC,z}(0) \right|^2 \right\rangle}{2t} \tag{7.4}$$

6.4. Results

6.4.1 Proton mobility on ice surfaces

The temperature dependence of proton mobility on ice surfaces is illustrated in Figure 6.2 and the calculated self-diffusion coefficients are listed in Table 6.1. On ice I_h surfaces, proton mobility is non-negligible only near the melting point of the aSPC/Fw/ice model (267.5 K) and slows down substantially as the temperature decreases, with the proton becoming essentially immobile below 200 K. At 265 K, the in-plane component of the calculated CEC self-diffusion coefficient $\left(D^{\parallel}_{CEC}\right)$ is 8.5×10^{-3} Å^2 / ps. The corresponding value calculated for water molecules in the quasi-liquid layer $\left(D^{\parallel}_{WAT}\right)$ is 8.6×10^{-3} Å^2 / ps, which is in good agreement (within the reported uncertainty)

with the available experimentally data.[54] Based on the *a*MS-EVB3 simulations, the ratio $D^{\|}_{CEC}/D^{\|}_{WAT}$ is ~1 on the ice I_h surface and ~1.8 in liquid water at 298 K,[27] suggesting that the mobility of protons on the I_h surface is more tightly connected with that of the surrounding water molecules. Since the observed fast diffusion of protons in liquid water results from the combination of both vehicular and hopping (Grotthuss) mechanisms,[24] the calculated ratio $D^{\|}_{CEC}/D^{\|}_{WAT}$ indicates that the hopping mechanism on the ice I_h surface is largely suppressed.

Qualitatively similar results are also obtained for proton diffusion on the surface of amorphous ice (Figure 6.2 and Table 6.1). In this case, $D^{\|}_{CEC} = 1.0 \times 10^{-2}$ Å^2 / ps and $D^{\|}_{WAT} = 1.3 \times 10^{-2}$ Å^2 / ps at 265 K, with $D^{\|}_{CEC}/D^{\|}_{WAT}$ ~0.8. As mentioned above, $D^{\|}_{WAT}$ for amorphous ice was calculated considering all water molecules lying within 4 Å of the surface. The similarity between proton mobility on ice I_h and amorphous ice surfaces at T = 265 K can be explained by analyzing the structure and dynamics of the corresponding H-bond networks. As schematically shown in Figure 6.1, both surfaces do not display long-range structural order. The high similarity between the two H-bond networks can be assessed quantitatively from the analysis of the following quantities: (1) average number of H-bonds per molecule (NHB_{WAT}), (2) average number of H-bonds of the hydronium ion (NHB_{HYDRO}), and (3) average number of H-bonds per molecule calculated for H_2O molecules within the first solvation shell of the hydronium ion (NHB_{WAT_FS}). For the ice I_h surface at 265 K, NHB_{WAT} = 3.6, NHB_{HYDRO} = 3.0, and NHB_{WAT_FS} = 3.1, which are very close to the corresponding values calculated for the amorphous ice surface (NHB_{WAT} = 3.7, NHB_{WAT} = 3.0, and NHB_{WAT_FS} = 3.0).

The dynamical behavior of the water molecules at both ice I_h and amorphous ice surfaces is also comparable. As discussed above, water diffusion in the two interfacial regions is largely suppressed compared to the liquid phase. Further insights into the dynamical properties of the H-bond networks can be gained from the analysis of the rotational relaxation time (τ_R) extracted from the exponential fit to the long-time decay of the orientational time autocorrelation function $C_2(t) = \left\langle P_2\left[\mathbf{e}(0)\cdot\mathbf{e}(t)\right]\right\rangle$ where $P_2\left[\mathbf{e}(0)\cdot\mathbf{e}(t)\right]$ is the second Legendre polynomial of the angle spanned in time by the unit vector $\mathbf{e}(t)$ lying along one OH bond of each H_2O molecule, and the brackets indicate an ensemble average over both OH bonds and water molecules.[55] In liquid water at 298 K, NVE simulations with the aSPC/Fw water model provides $\tau_R = 2.7 \pm 0.1$ ps.[27] The time scale associated with the reorientation of the water molecules increases significantly at both ice surfaces, with $\tau_R = 110 \pm 10$ ps for ice I_h and $\tau_R = 84 \pm 5$ ps for amorphous ice at 265 K. The correlation between the structure of the H-bond network and time scale associated with the water dynamics as well as the implications to the underlying proton transfer/transport mechanisms in ice are further discussed in Section 6.5.3.

6.4.2 Proton mobility in bulk ice I_h

Proton mobility in bulk ice I_h is studied at 190 K. The self-diffusion coefficients calculated using eqs 6.1-4 in bulk ice I_h, and both ice I_h and amorphous ice surfaces are compared in Table 6.1. The aMS-EVB3 simulations predict that proton diffusion in bulk

ice I_h is ~2800 faster than at the surface. Importantly, D_{CEC} calculated for ice I_h at 190 K is appreciably larger than the corresponding value obtained for protonated at 298 K.[27]

To gain further insights into the proton transfer/transport process in bulk ice I_h, the distribution of proton-hopping frequencies (PHF) was also investigated. This analysis neglects all transfer events associated with the rattling motion of the excess proton between two adjacent water molecules which does not result in long-range transport. The calculated PHF distribution (Figure 6.3 and Table 6.1) is clearly bimodal, with the main peak corresponding to dynamical trajectories with an average proton-hopping frequency of 1.7 ps^{-1}. For this group of trajectories, $D_{CEC} = 0.6 \pm 0.1$ $Å^2$ / ps, which is ~56 % higher than the corresponding value obtained from aMS-EVB3 simulations of protonated water at 298 K. The average PHF value for the second group of trajectories is 0.3 ps^{-1}, resulting in $D_{CEC} = 4.2 \times 10^{-2} \pm 1 \times 10^{-3}$ $Å^2$ / ps.

6.4.3 Fast and trapped protons in bulk ice I_h

Two representative trajectories belonging to the groups introduced in Section 6.4.2 are shown in Figures 6.4 and 6.5. In one case (Figure 6.4), the trajectory is characterized by fast proton-hopping events, while the second trajectory (Figure 6.5) is associated with the formation of a "trapped" proton configuration. In bulk (crystalline) ice I_h, water molecules are found in a symmetric solvating environment, with each molecule accepting and donating two H-bonds. As a consequence, the intermolecular O-O distance between all water pairs is ~2.8 Å. When a hydronium ion is incorporated in the crystal, the perfectly tetrahedral arrangement is locally disrupted in the neighborhood of the excess charge. Although four water molecules are still located within the first

solvation shell of the hydronium ion, one of the four O*--O_i distances (where O* and O_i indicate the oxygen atoms of the hydronium ion and four water molecules, respectively) becomes significantly longer (~3.1 Å). This corresponds to a H-bonded pair in which the water molecule donates one H-bond to the hydronium ion. The remaining three O*---O_i distances instead become shorter (~ 2.5 Å), leading to the formation of H-bonded pairs in which each water molecule accepts one H-bond from the hydronium ion. In the trajectory shown in Figure 6.4, one proton transfer event occurs at ~24.8 ps and results in an identity change of O_a (Figure 6.4a) that becomes the new hydronium oxygen. When the excess proton is transferred to O_a, one O*---O_i distance becomes larger due to the repulsion between the hydronium ion and the donor water molecule. After a few successful transfer events, O_a recovers its symmetric H-bond environment at ~26.6 ps. The average lifetime of the hydronium ion (excluding proton rattling) extracted from these aMS-EVB3 fast-hopping trajectories is ~1 ps.

The fast proton transfer process can be interrupted by the formation of a "proton trap" (Figure 6.5). As illustrated in Figure 6.4a, one the H-bon donor water molecules is pushed away from the hydronium ion at ~31.5 ps while reorienting in order to create a local structure where none of its two O-H bonds points to the oxygen atom of the hydronium ion, Figure 6.5b. This creates a local defect in the lattice that breaks the crystalline structure of ice I_h. Once the local defect is created, hopping or shuttling motions are largely suppressed, and the excess proton is trapped next to the defect site.

Both experimental[56] and theoretical[57] studies have predicted that local defects could trap excess protons in bulk ice I_h. However, the molecular mechanisms associated with the trapping events remain poorly understood. The local structure that "traps" the

excess proton can be described as a hydronium / L-defect (H/L) complex.[56,57] The creation of the H/L defect is closely associated with the thermal fluctuations of the H-bond network around the excess proton. Although the lifetime of broken H-bonds in ice is extremely due to the structural constraints imposed by the crystalline environment, in some cases, the local structure around a broken H-bond can distort significantly relative to the corresponding crystalline arrangement, creating a long-lived structural defect in the lattice. A schematic representation of a proton-trapping event that leads to the formation of a long-lived H/L complex is depicted in Figure 6.6.

6.5. Discussion

6.5.1. Fast proton transfer/transport in bulk ice I_h

Due to the presence of low energy barriers for proton transfer between adjacent molecules and the existence of predefined proton-transfer pathways along the underlying H-bond network, the crystalline structure of ice I_h provides a favorable environment for fast proton transfer/transport. In this regard, Ohmine and co-workers investigated the potential energy surfaces associated with proton transfer using quantum mechanics / molecular mechanics (QM/MM) simulations for both proton ordered and disordered ice configurations.[58] Unlike in liquid water, the formation of stable Zundel cations[59] in ice I_h is prevented by the constraints imposed by the lattice structure on the O---O distance between neighboring water molecules. On the other hand, although similar, the local structure of an excess proton in ice is clearly distinct from typical Eigen-type structures observed in protonated liquid water. Specifically, a hydronium ion in bulk ice I_h is coordinated with four water molecules. The three nearest molecules accept H-bonds from

the hydronium ion, while the fourth molecule, which is usually not present in the first solvation shell of H_3O^+ in liquid water, donates one H-bond to the hydronium ion. The interaction between the donor water molecule and the hydronium ion is relatively unfavorable because of the low charge density localized on the hydronium oxygen. However, due to the lattice constraints, the donor water molecule cannot be excluded from the first solvation shell of the hydronium ion in ice. This leads to an increase of the potential energy around the hydronium ion in the ice crystal, which thus lowers the energy barriers associated with proton transfer down to ~1.5 kcal/mol.[58]

A second element associated with fast proton transfer/transport processes in ice I_h is the confined nature of the water molecules in the ice crystal. Several studies have demonstrated that proton transfer rates in water increase upon confinement.[40,60-63] In particular, it was shown that water diffusion and reorientation slow down in polar and non-polar confining environments. As a consequence, the average H-bond lifetime increases,[62,63] which, in turn, decreases the vehicular contribution to the overall proton transport process.[40,64] In this context, bulk ice can be considered as a limiting example of water under confinement in which water diffusion is completely suppressed. Due to the extremely slow water orientational dynamics, proton transfer/transport in ice occur via the hopping-relay mechanism through the long-range H-bond network confined within the lattice structure without involving the rearrangement of the H-bond network itself.

Previous experimental[22] and theoretical studies on protonated ice[14,15] and water[65-67] have provided important insights on the mechanisms associated with proton mobility in aqueous systems. Based on quasi-elastic neutron scattering data, it was established that proton hopping can persist down to 5 K in proton-disordered crystals (ice I_h and I_c).[22]

However, no proton activity was observed in proton-ordered crystals (ice VIII) under the same experimental conditions. Non-negligible proton activity at very low temperature was predicted by path integral molecular dynamics[15] and quantum electrodynamics simulations.[14] The simulations of refs. [14] and [15] also indicated that explicit inclusion of nuclear quantum effects (e.g., zero-point energy and tunneling) results in proton-hopping events at 0 K in proton-disordered ice crystals (ice I_h and VII). Since it has been established that the proton-hopping (Grotthuss) mechanism requires a collective rearrangement of the H-bond network around the hydronium ion,[24,37,65,66] it is likely that nuclear quantum effects combined with the proton-disordered structure of ice I_h can provide the necessary distortion of the local (H-bond) environment around the hydronium ion to promote fast proton hopping at 0 K.

6.5.2 Proton hopping relay vs. Bjerrum defect transfer: Length and time scales

Although the energy barriers for proton transfer in ice I_h have been shown to be relatively low (~1.5 kcal/mol),[13,22,58] it is often assumed that hopping relay can only be effective over short distances, which can be associated with the rattling motion of the excess proton between two adjacent water molecules.[24] However, the present aMS-EVB3 simulations suggest that the hopping-relay mechanism can be effective in transporting the excess proton in ice I_h over relatively longer distances than previously predicted.[4,12] In particular, the aMS-EVB3 simulations predict that proton transfer via the hopping-relay mechanism occurs in a step-wise fashion so that the location of the charge defect (hydronium ion) at any given instant can be identified with the specific location of a water molecule within the lattice, although the lifetime of each of these configurations is

relatively short (~1 ps). Since the lattice structure prevents the formation of stable Zundel ions, after a successful hop, the three (H-bond) acceptor molecules around the new hydronium ion are completely equivalent and the direction of a following hopping event is thus determined by thermal fluctuations.

The short time scales (~1 ps) for proton hopping derived from the aMS-EVB3 simulations carried out for ice I_h at 190 K are in agreement with recent quasi-elastic neutron scattering measurements.[22,23] Since the lifetime of a H/L complex is significantly longer than the simulation time accessible by aMS-EVB3, it was not possible to determine the time scale associated with transfer/transport of Bjerrum defects in ice I_h. As observed in refs [8,56], the time scale associated with the transfer/transport of a Bjerrum defect are extremely long since this process requires the concerted motion of several water molecules within the lattice. Evidence for the long time scales associated with Bjerrum-defect transfer/transport was provided in previous theoretical studies.[68]

6.5.3 Proton transfer/transport and the role of the quasi-liquid layer

The present aMS-EVB3 simulations predict significantly different proton mobility in the bulk and interfacial regions of ice. The difference is directly related to the concentration of point defects and structure of the H-bond network in the two regions. Since proton diffusion at ice surfaces is also lower than water diffusion in the liquid phase, structural diffusion associated with proton-hopping events (Grotthuss mechanism) is largely suppressed at the interface. This can be explained by considering that water dynamics in the QLL becomes extremely slow below the melting temperature.

Furthermore, unlike in bulk ice I_h, the tetrahedral H-bond network is disrupted at the interface, which implies that the long-range connectivity is lost.

Since it has been shown that the excess proton can hop between two water molecules only after the proton-accepting molecule has assumed a hydration structure compatible with the final stage of the transfer process, the slow water dynamics and lack of long-range H-bond connectivity at ice surfaces can explain the calculated low proton mobility. Although several successful proton-hopping events are observed in the interfacial regions of ice (Table 6.1), these hops mostly occur between water molecules within the closest solvation shells of the hydronium ion. This leads to many recurring events that eventually cause the excess proton to be trapped in a confined region until a collective rearrangement of the H-bond network induced by the concerted motion of several water molecules occurs.

The present aMS-EVB3 results thus provide further molecular-level insights into the measurements of proton activity carried out under different experimental conditions. Since proton transfer/transport in ice is a thermal process in absence of external fields, proton mobility is expected to increase with temperature.[23] However, the physical mechanisms associated with the transfer/transport process largely depend on the structure of the underlying H-bond network. The analysis of Section 6.4 thus suggests that if the excess proton is (softly) deposited on the ice surface, it would take a significant amount of time for the charge defect to diffuse in the bulk region.[8] If heat is released during the collision between the charged species and the ice surface, the thickness of the interfacial disordered layer can instead increase, resulting in the formation of a local proton trap.[7] On the other hand, if the excess proton is incorporated into the lattice before the crystal

can grow, fast proton hopping can be observed in the bulk region as shown by the present aMS-EVB3 simulations.[11,23]

6.6. Summary

The mechanism of proton transfer/transport in ice is studied through molecular dynamics simulations carried out with a specifically parameterized MS-EVB model (*a*MS-EVB3/ice). On both ice I_h and amorphous ice surfaces, the excess proton is found to have non-negligible mobility only near the melting temperature, becoming effectively immobile at temperatures below 200 K. The similar mobility of the excess proton on both types of ice surfaces can be explained by considering the similarity between the structure of the underlying H-bond network and water dynamics. Although the interfacial region displays quasi-liquid properties, structural diffusion (i.e., proton transfer/transport via the Grotthuss mechanism) is largely suppressed on both ice surfaces due to the disordered structure of the H-bond network and extremely slow water reorientation.

Proton mobility is instead predicted to be faster in bulk ice I_h at low temperatures (190 K). The analysis of proton hopping frequencies indicates that two distinct mechanisms are responsible for proton transfer/transport in bulk ice I_h. In aMS-EVB3 trajectories displaying high hopping frequencies, proton transfer/transport is found to occur via the hopping-relay mechanism. This is promoted by (1) the confining environment around the excess proton that effectively lowers the energy barrier for proton transfer, and (2) the long-range connectivity of the underlying H-bond network. The fast-hopping trajectories can terminate in a local proton trap corresponding to the

creation of a H/L defect. The H/L defect is characterized by a longer lifetime, which manifests itself in the second peak in the distribution of proton-hopping frequencies.

6.7. Acknowledgments

This research was supported by the National Science Foundation through grant CHE-1111364. This work used the Extreme Science and Engineering Discovery Environment (XSEDE), which is supported by National Science Foundation grant number OCI-1053575 (allocation TG-CHE110009).

Chapter 6 contains materials from "Fast and Slow Proton Transfer in ice: the Role of the Quasi-liquid Layer and Hydrogen-bond Network" published in 2014 in *Journal of Physical Chemistry B. (***DOI:** 10.1021/jp501116d), authored by Kyoyeon Park, Wei Lin and Francesco Paesani. All material has been reproduced with the consent of all other authors.

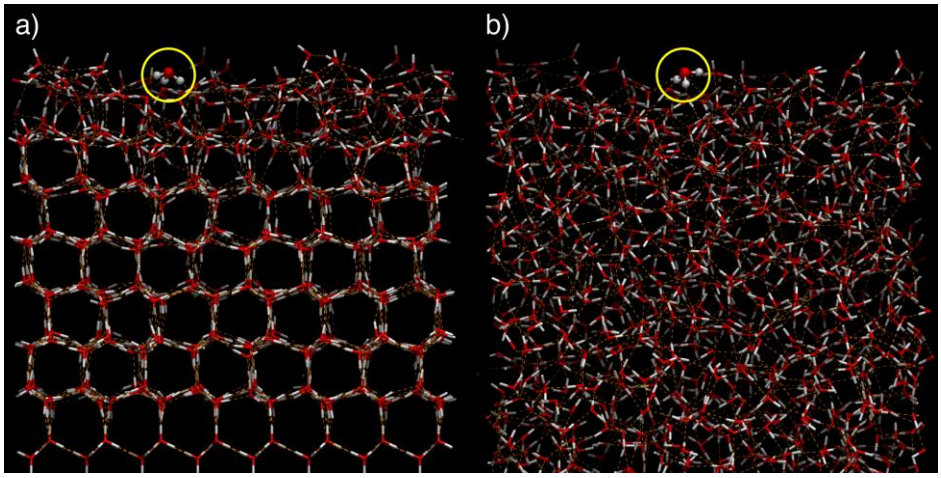

Figure 6.1. Snapshots from aMS-EVB3 simulations of an excess proton on the surface of ice I_h (a) and amorphous ice (b) at 265 K. The yellow circles identify the instantaneous location of the hydronium ion on both surfaces, while the dashed orange lines correspond to hydrogen bonds between the water molecules.

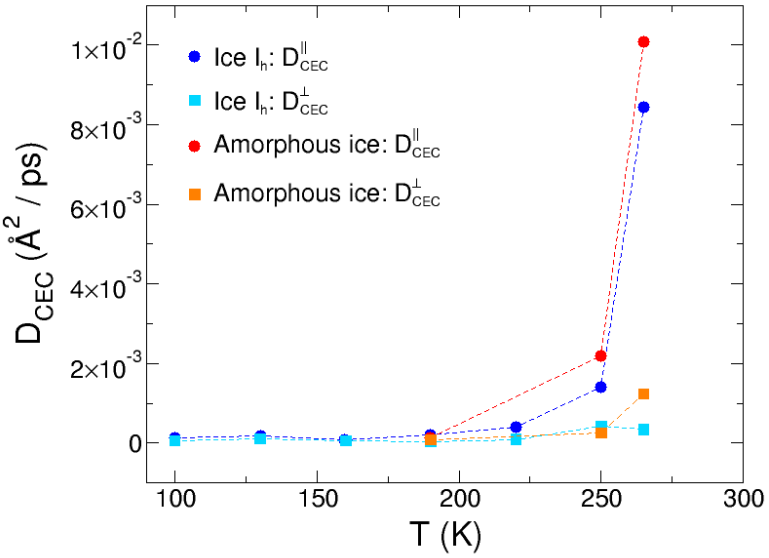

Figure 6.2. Parallel and perpendicular components of the self-diffusion coefficient of the center of excess charge calculated from aMS-EVB3 simulations of ice I_h (cold colors) and amorphous ice (warm colors) surfaces.

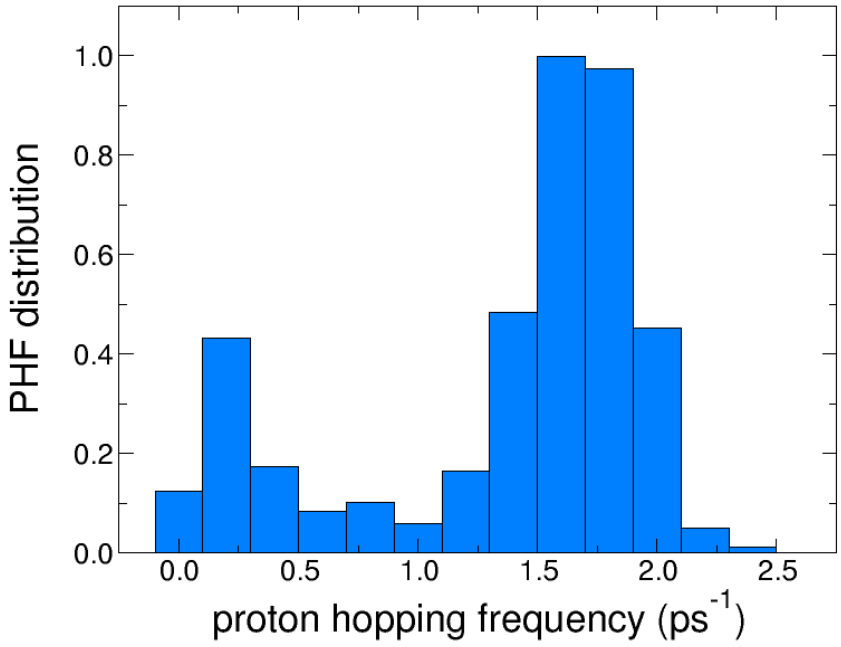

Figure 6.3. Distribution of proton hopping frequencies in bulk ice I_h calculated at 190 K by averaging over 500 aMS-EVB3 trajectories of 50 ps each.

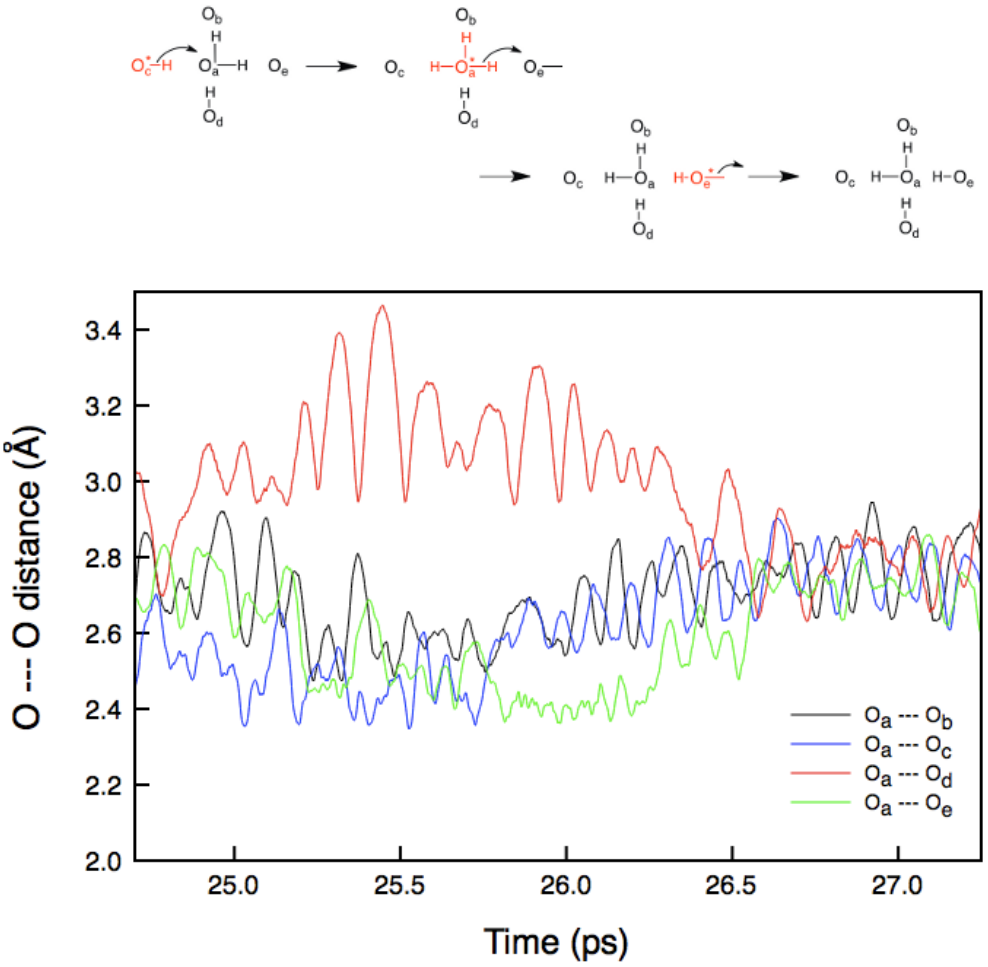

Figure 6.4. a) Schematic representation of proton hopping in ice I_h. b) Variation of the O-O distances along an aMS-EVB3 trajectory displaying fast proton-hopping events in ice I_h. O_c corresponds to the oxygen atom of the initial hydronium ion while O_a is the oxygen atom of the final hydronium ion that is formed after proton hopping. O_b and O_d are the oxygen atoms of the water molecules hydrogen bonded to O_a, and O_e is the oxygen atom of the hydronium ion that is formed after a subsequent hopping event.

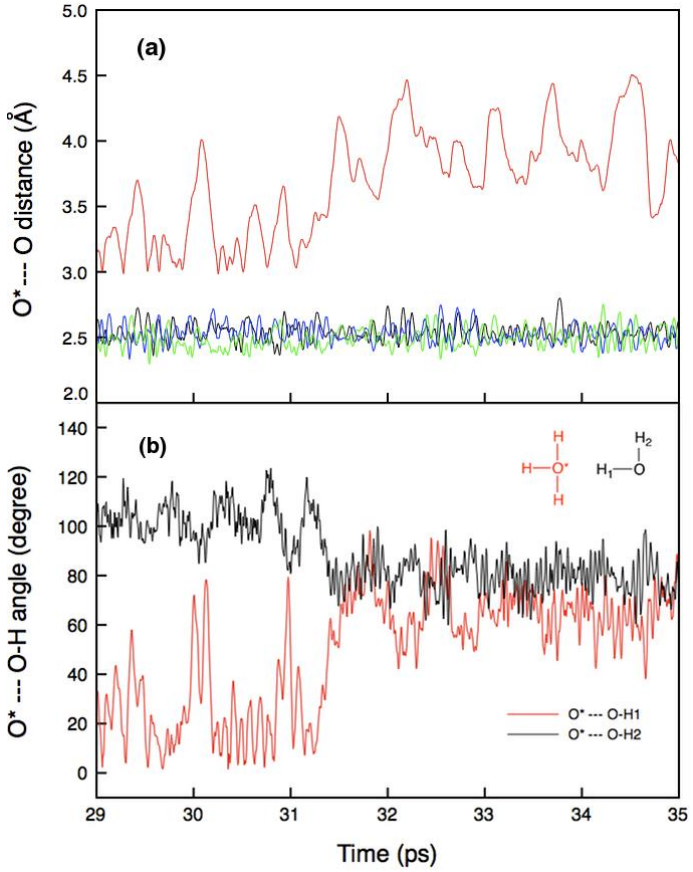

Figure 6.5. (a) Variation of O*-O_i distances along an aMS-EVB3 trajectory displaying a proton-trapping event. O* indicates the oxygen atom in the hydronium ion, and O_i corresponds to the oxygen atom of each of the four water molecules coordinated with the hydronium ion within the lattice. (b) Variation of the O*---O-$H_{1,2}$ angles along an aMS-EVB3 trajectory displaying a proton-trapping event. H_1 and H_2 correspond to the hydrogen atoms of the H-bond donor water molecule. The H-bond donor water molecule is pushed away from the hydronium ion at ~31.5 ps, leading to the formation of a long-lived H/L complex.

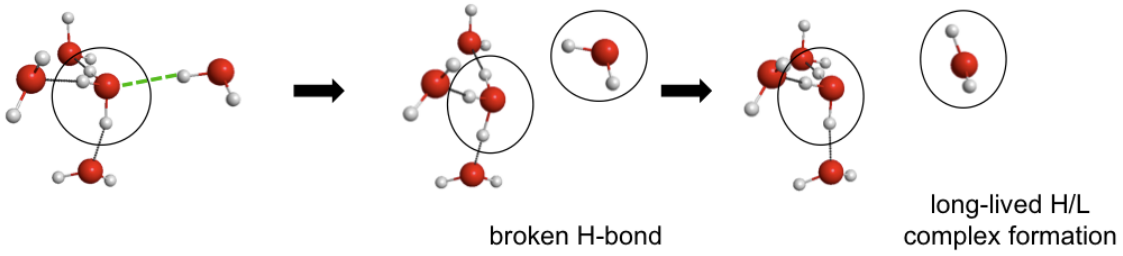

Figure 6.6. Schematic representation of the formation of a long-lived H/L complex (proton tramp) in ice I_h.

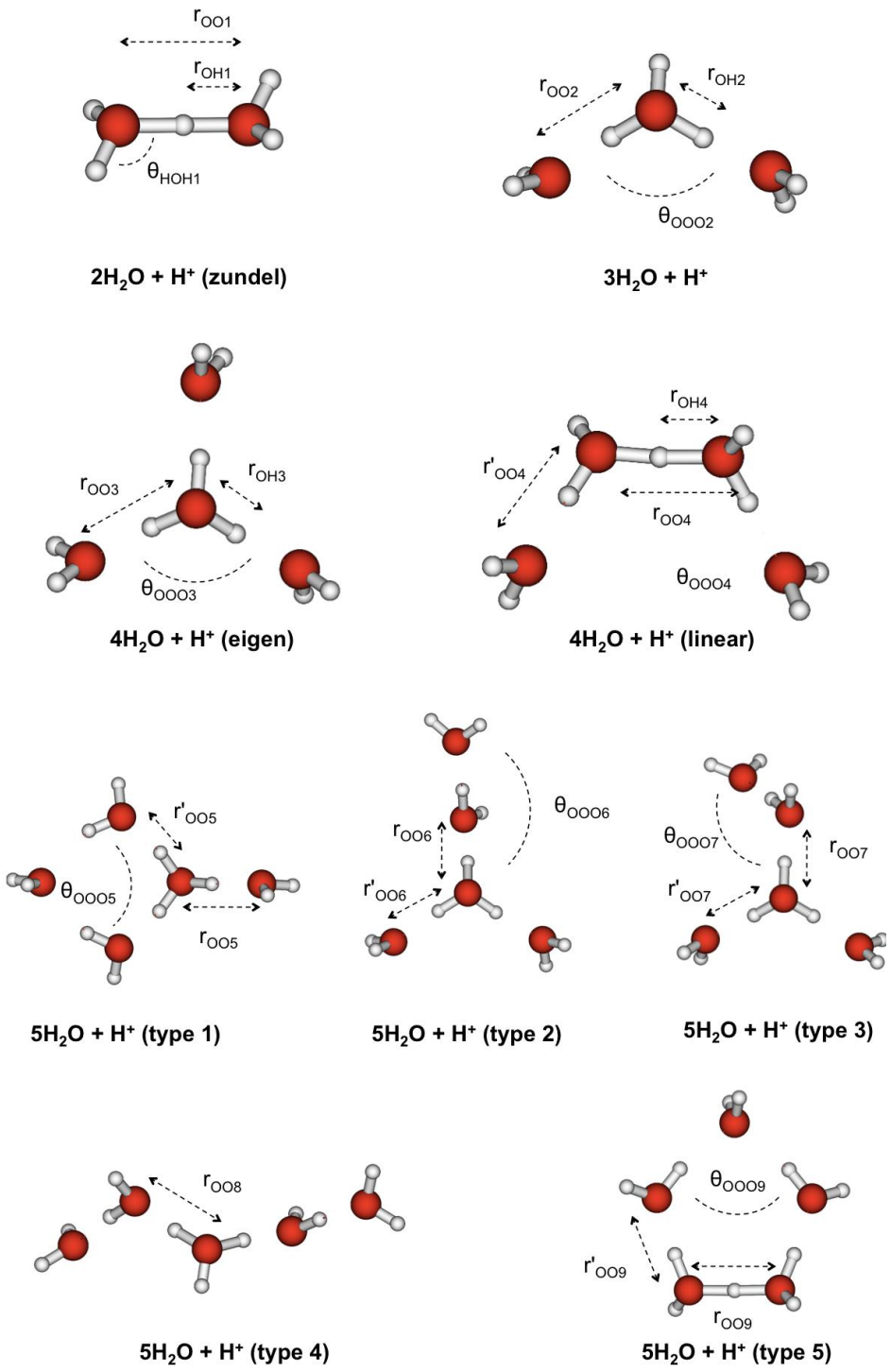

Figure 6.7. Small protonated water clusters. All values for the indicated bonds and angles are listed in Table 7.5.

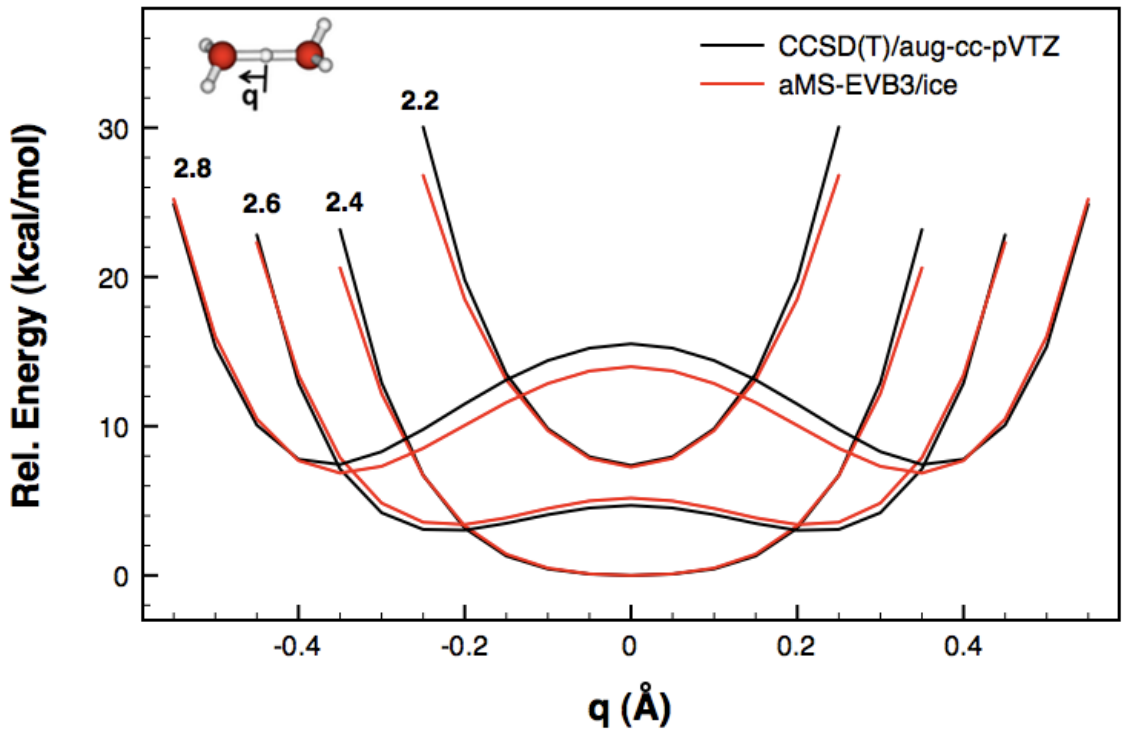

Figure 6.8. Potential energy curves corresponding to proton shuttling in the Zundel ion ($H_5O_2^+$)calculated for different O_a---O_b distances (R_{OO} = 2.2, 2.4, 2.6, and 2.8 Å), where O_a and O_b are the oxygen atoms of the two water molecules. The proton shuttling coordinate is defined as $q = R_{OaH^*} - R_{ObH^*}$, where H* is the shared proton.

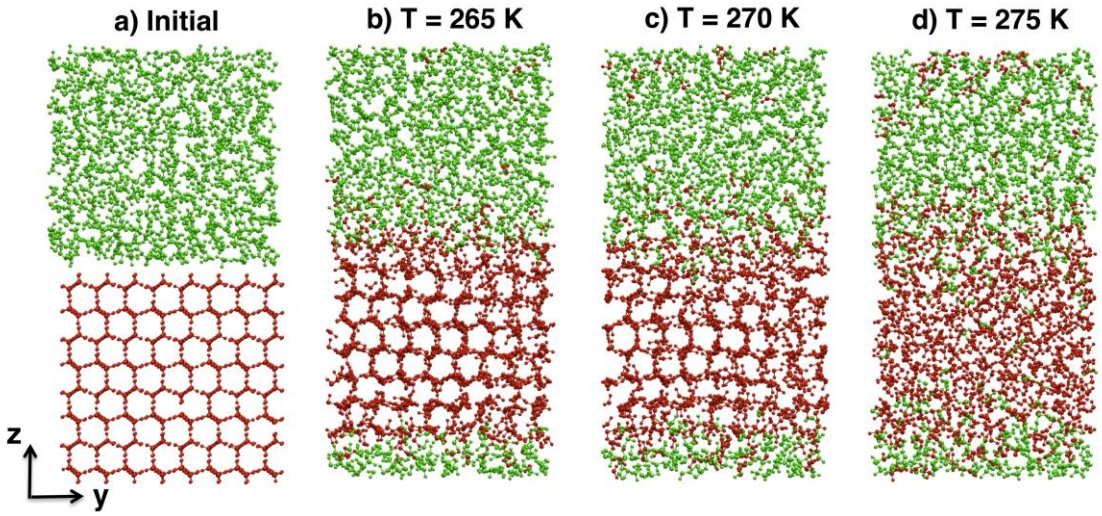

Figure 6.9. 2-dimensional projections of ice-water coexistence structures extracted from aSPC/Fw/ice simulations. a) Initial configuration. b) Final configuration after a 10 ns long NPTsimulation at T = 265 K. c) Final configuration after a 10 ns long NPT simulation at T = 270 K. d) Final configuration after a 10 ns long NPT simulation at T = 275 K.

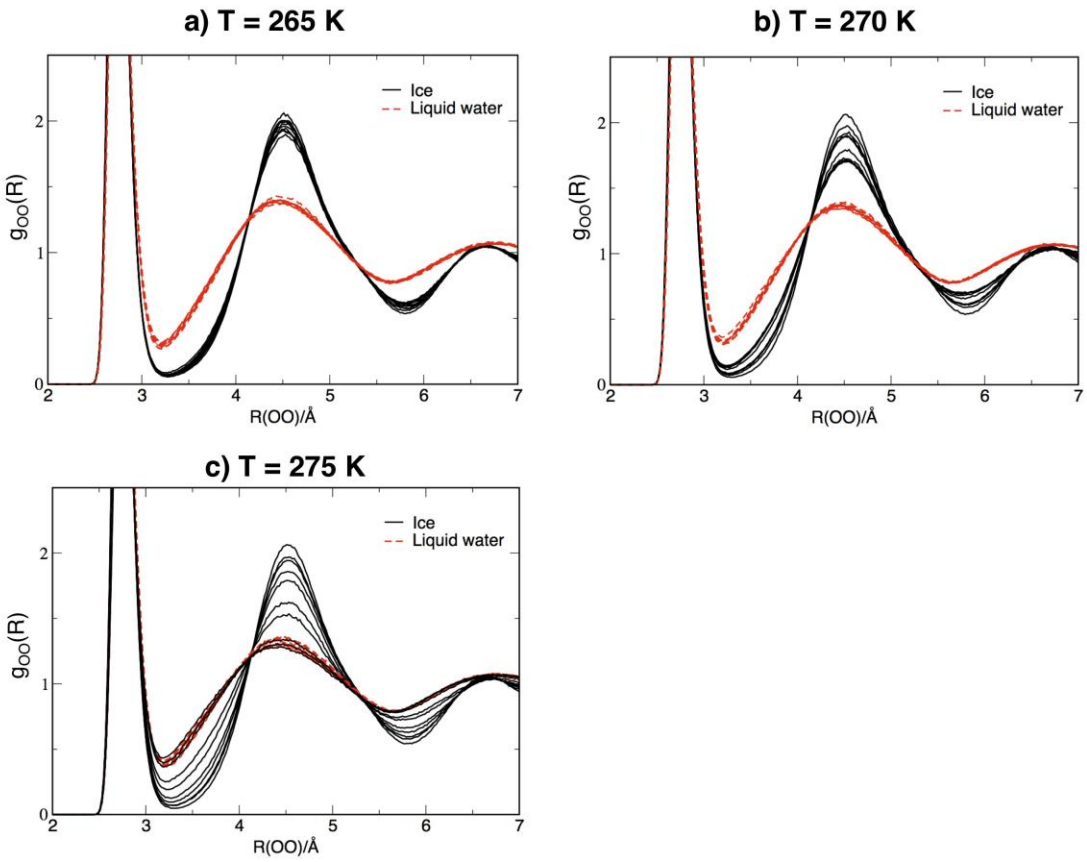

Figure 6.10. Ice (black solid lines) and liquid water (red dashed lines) oxygen-oxygen RDFs calculated from ice-water coexistence simulations at: a) T = 265K, b) T = 270K and c) T = 275K. Each RDF curve was obtained by averaging over each 1 ns interval of a 10 ns long simulation. For T = 275 K, the curve shows that ice molecules are completely melted after 8 ns.

Table 6.1. Parallel $\left(D_{CEC}^{\parallel}\right)$ and perpendicular $\left(D_{CEC}^{\perp}\right)$ components of the center of excess charge self-diffusion coefficient (eqs 6.2 and 6.3), and average proton hopping frequency (PHF) calculated from aMS-EVB3 simulations of an excess proton on ice I_h and amorphous ice surfaces. The values in parenthesis represent the associated statistical uncertainties corresponding to 95% confidence limits calculated from linear least-squares fits.

		$D_{CEC}^{\parallel}$ (Å^2 / ps)	$D_{CEC}^{\perp}$ (Å^2 / ps)	PHF (ps^{-1})
T = 190 K	Ice I_h	1.8×10^{-4} (1×10^{-5})	5.1×10^{-5} (1×10^{-6})	0.030
	Amorphous ice	1.5×10^{-4} (1×10^{-5})	8.8×10^{-5} (1×10^{-6})	0.003
T = 265 K	Ice I_h	8.5×10^{-3} (1×10^{-4})	3.5×10^{-4} (1×10^{-5})	0.090
	Amorphous ice	1.0×10^{-2} (1×10^{-4})	1.2×10^{-3} (1×10^{-4})	0.110

Table 6.2. Isotropic $\left(D_{CEC}\right)$ center of excess charge self-diffusion coefficient and average proton hopping frequency (PHF) calculated from aMS-EVB3 simulations of an excess proton in bulk ice I_h. For comparison, the corresponding values obtained in ref. for an excess proton in liquid water are also reported. The values in parenthesis represent the associated statistical uncertainties corresponding to 95% confidence limits calculated from linear least-squares fits.

	D_{CEC} (Å^2 / ps)	PHF (ps^{-1})
Ice I_h at 190 K	0.52 (0.02)	1.42
Liquid water at 298 K	0.41 (0.02)	0.70

Table 6.3. Parameters for the *a*SPC/Fw model for ice[a].

r_{OH}^{eq}	(Å)	0.995
D_{OH}	(kcal mol^{-1})	116.09
α_{OH}	(Å $^{-1}$)	2.287
K_{HOH}	(kcal mol^{-1} rad^{-2})	75.9
θ_{HOH}^{eq}	(degree)	112.5
q_O	(e)	-0.950
q_H	(e)	0.475
ε_{OO}	(kcal mol^{-1})	0.22
σ_{OO}	(Å)	3.17

a. The functional form of the *a*SPC/Fw model is same as in ref [1].

Table 6.4. Parameters for the *a*MS-EVB3 model for ice[a].

D_{OH}	(kcal/mol)	98.89230623	$r_{OO}^{sm,1}$ [b]	(Å)	2.85
a_{OH}	($Å^{-1}$)	2.19209766	$r_{OO}^{sm,2}$ [c]	(Å)	3.05
r_{OH}^{eq}	(Å)	1.0	$r_{OH}^{sm,1}$ [d]	(Å)	2.50
k_ϕ	(kcal/mol/rad^2)	77.4868	$r_{OH}^{sm,2}$ [e]	(Å)	3.00
ϕ_{HOH}^{eq}	(degree)	111.7269	V^{ij}_{const}	(kcal/mol)	-22.27009513
ε_{OOw}	(kcal/mol)	0.16289756	q_O^{ex}	(*e*)	-0.07069382
σ_{OOw}	(Å)	3.12290299	q_H^{ex}	(*e*)	0.02292276
ε_{HOw}	(kcal/mol)	0.00215410	q_{H*}^{ex}	(*e*)	0.04969661
σ_{HOw}	(Å)	1.54481081	γ	($Å^{-2}$)	1.68860167
$q_O^{H_3O^+}$	(*e*)	-0.5	P		0.23675646
$q_H^{H_3O^+}$	(*e*)	0.5	k	($Å^{-2}$)	9.14365210
B	(kcal/mol)	9.39821186	D_{OO}	(Å)	3.08818425
b	($Å^{-1}$)	1.20946227	β	($Å^{-1}$)	7.48386620
b'	($Å^{-2}$)	2.40425368	R^0_{OO}	(Å)	3.07912414
d^0_{OO}	(Å)	2.68866090	P'	($Å^{-1}$)	9.48446320
C	(kcal/mol)	8.37438428	α	($Å^{-1}$)	9.83488544
c	($Å^{-1}$)	2.43824819	r^0_{OO}	(Å)	1.88108986
d_0^{OH}	(Å)	0.95179458			

a. The functional form of the *a*MS-EVB3 model is same as in ref [1].
b. $r_{OO}^{sm,1}$: smooth cut-off starting distance for O-O repulsive term
c. $r_{OO}^{sm,2}$: smooth cut-off ending distance for O-O repulsive term
d. $r_{OH}^{sm,1}$: smooth cut-off starting distance for H-O repulsive term
e. $r_{OH}^{sm,2}$: smooth cut-off ending distance for H-O repulsive term

Table 6.5. Geometries of protonated water clusters. Bonds in Å and angles in degrees.

	Coordinates[a]	*a*MS-EVB3/ice	MP2/aug-cc-pVTZ
$2H_2O + H^+$ (Zundel)	r_{OO1}	2.38	2.40
	r_{OH1}	1.19	1.20
	θ_{HOH1}	118.0	115.8
$3H_2O + H^+$	r_{OO2}	2.50	2.49
	r_{OH2}	1.07	1.04
	θ_{OOO2}	110.5	117.1
$4H_2O + H^+$ (Eigen)	r_{OO3}	2.55	2.55
	r_{OH3}	1.06	1.01
	θ_{OOO3}	108.0	114.1
$4H_2O + H^+$ (linear)	r_{OO4}	2.38	2.39
	r'_{OO4}	2.62	2.59
	r_{OH4}	1.19	1.20
	θ_{OOO4}	115.7	119.1
$5H_2O + H^+$ (type 1)	r_{OO5}	2.55	2.57
	r'_{OO5}	2.52	2.54
	θ_{OOO5}	88.6	79.0
$5H_2O + H^+$ (type 2)	r_{OO6}	2.48	2.47
	r'_{OO6}	2.56	2.59
	θ_{OOO6}	122.2	117.4
$5H_2O + H^+$ (type 3)	r_{OO7}	2.48	2.47
	r'_{OO7}	2.57	2.59
	θ_{OOO7}	127.6	121.9
$5H_2O + H^+$ (type 4)	r_{OO8}	2.46	2.46
$5H_2O + H^+$ (type 5)	r_{OO9}	2.38	2.39
	r'_{OO9}	2.60	2.57
	θ_{OOO9}	83.7	91.3

[a] All coordinates are defined Figure 6.8.

Table 6.6. Binding energies for small protonated water clusters.

	*a*MS-EVB3	CCSD(T)//MP2 /aug-cc-pVTZ
$2H_2O + H^+$ (Zundel)	-31.69	-33.47
$3H_2O + H^+$	-56.13	-57.65
$4H_2O + H^+$ (Eigen)	-78.45	-77.55
$4H_2O + H^+$ (linear)	-74.56	-73.68
$5H_2O + H^+$ (type 1)	-94.48	-92.21
$5H_2O + H^+$ (type 2)	-94.88	-91.15
$5H_2O + H^+$ (type 3)	-94.88	-91.17
$5H_2O + H^+$ (type 4)	-91.04	-87.63
$5H_2O + H^+$ (type 5)	-92.86	-88.61

6.8. References

(1) Finlayson-Pitts, B. J.; Pitts, J. N., Jr. *Chemistry of the upper and lower atmosphere: Theory, experiments and applications*; Academic Press, 2000.

(2) Seinfeld, J. H.; Pandis, S. N. *Atmospheric Chemistry and Physics: From Air Pollution to Climate Change*; Wiley: Hoboken, N.J., 2006.

(3) Hobbs, P. V. *Ice physics*; Clarendon Press: Oxford, 1974.

(4) Petrenko, V. F.; Whitworth, R. W. *Physics of ice*; Oxford University Press, USA, 1999.

(5) Molina, M. J.; Tso, T. L.; Molina, L. T.; Wang, F. C. Y. Antarctic Stratospheric Chemistry of Chlorine Nitrate, Hydrogen-Chloride and Ice - Release of Active Chlorine. *Science* **1987**, *238*, 1253.

(6) McNeill, V. F.; Loerting, T.; Geiger, F. M.; Trout, B. L.; Molina, M. J. Hydrogen chloride-induced surface disordering on ice. *Proc. Natl. Acad. Sci. U. S. A.* **2006**, *103*, 9422.

(7) Cowin, J. P.; Tsekouras, A. A.; Iedema, M. J.; Wu, K.; Ellison, G. B. Immobility of protons in ice from 30 to 190 K. *Nature* **1999**, *398*, 405.

(8) Collier, W. B.; Ritzhaupt, G.; Devlin, J. P. Spectroscopically Evaluated Rates and Energies for Proton-Transfer and Bjerrum Defect Migration in Cubic Ice. *J. Phys. Chem.* **1984**, *88*, 363.

(9) Uras-Aytemiz, N.; Joyce, C.; Devlin, J. P. Protonic and Bjerrum defect activity near the surface of ice at T < 145 K. *J. Chem. Phys.* **2001**, *115*, 9835.

(10) Devlin, J. P.; Buch, V. Evidence for the surface origin of point defects in ice: Control of interior proton activity by adsorbates. *J. Chem. Phys.* **2007**, *127*, 091101.

(11) Lee, C. W.; Lee, P. R.; Kang, H. Protons at ice surfaces. *Angew. Chem. Int. Ed.* **2006**, *45*, 5529.

(12) Lee, C. W.; Lee, P. R.; Kim, Y. K.; Kang, H. Mechanistic study of proton transfer and H/D exchange in ice films at low temperatures (100-140 K). *J. Chem. Phys.* **2007**, *127*, 084701.

(13) Moon, E. S.; Yoon, J.; Kang, H. Energy barrier of proton transfer at ice surfaces. *J. Chem. Phys.* **2010**, *133*, 044709.

(14) Neto, A. H. C.; Pujol, P.; Fradkin, E. Ice: A strongly correlated proton system. *Phys. Rev. B* **2006**, *74*, 024302.

(15) Benoit, M.; Marx, D.; Parrinello, M. Tunnelling and zero-point motion in high-pressure ice. *Nature* **1998**, *392*, 258.

(16) Bernal, J. D.; Fowler, R. H. A theory of water and ionic solution, with particular reference to hydrogen and hydroxyl ions. *J. Chem. Phys.* **1933**, *1*, 515.

(17) Bjerrum, N. Structure and Properties of Ice. *Science* **1952**, *115*, 385.

(18) Kroes, G. J. Surface Melting of the (0001) Face of Tip4p Ice. *Surf. Sci.* **1992**, *275*, 365.

(19) Li, Y.; Somorjai, G. A. Surface premelting of ice. *J. Phys. Chem. C* **2007**, *111*, 9631.

(20) Paesani, F.; Voth, G. A. Quantum effects strongly influence the surface premelting of ice. *J. Phys. Chem. C* **2008**, *112*, 324.

(21) Wei, X.; Miranda, P. B.; Shen, Y. R. Surface vibrational spectroscopic study of surface melting of ice. *Phys. Rev. Lett.* **2001**, *86*, 1554.

(22) Bove, L. E.; Klotz, S.; Paciaroni, A.; Sacchetti, F. Anomalous Proton Dynamics in Ice at Low Temperatures. *Phys. Rev. Lett.* **2009**, *103*.

(23) Presiado, I.; Lal, J.; Mamontov, E.; Kolesnikov, A. I.; Huppert, D. Fast Proton Hopping Detection in Ice I(h) by Quasi-Elastic Neutron Scattering. *J. Phys. Chem. C* **2011**, *115*, 10245.

(24) Agmon, N. The Grotthuss Mechanism. *Chem. Phys. Lett.* **1995**, *244*, 456.

(25) Devlin, J. P. Relating the current science of ion-defect behavior in ice to a plausible mechanism for directional charge transfer during ice particle collisions. *Phys. Chem. Chem. Phys.* **2011**, *13*, 19707.

(26) Wren, S. N.; Donaldson, D. J. Laboratory study of pH at the air-ice interface. *J. Phys. Chem. C* **2012**, *116*, 10171.

(27) Park, K.; Lin, W.; Paesani, F. A Refined MS-EVB Model for Proton Transport in Aqueous Environments. *J. Phys. Chem. B* **2012**, *116*, 343.

(28) Buch, V.; Sandler, P.; Sadlej, J. Simulations of H2O solid, liquid, and clusters, with an emphasis on ferroelectric ordering transition in hexagonal ice. *J. Phys. Chem. B* **1998**, *102*, 8641.

(29) Schmitt, U. W.; Voth, G. A. Multistate empirical valence bond model for proton transport in water. *J. Phys. Chem. B* **1998**, *102*, 5547.

(30) Schmitt, U. W.; Voth, G. A. The computer simulation of proton transport in water. *J. Chem. Phys.* **1999**, *111*, 9361.

(31) Day, T. J. F.; Soudackov, A. V.; Cuma, M.; Schmitt, U. W.; Voth, G. A. A second generation multistate empirical valence bond model for proton transport in aqueous systems. *J. Chem. Phys.* **2002**, *117*, 5839.

(32) Wu, Y.; Chen, H.; Wang, F.; Paesani, F.; Voth, G. A. An improved multistate empirical valence bond model for aqueous proton solvation and transport. *J. Phys. Chem. B* **2008**, *112*, 467.

(33) Lapid, H.; Agmon, N.; Petersen, M. K.; Voth, G. A. A bond-order analysis of the mechanism for hydrated proton mobility in liquid water. *J. Chem. Phys.* **2005**, *122*, 014506.

(34) Day, T. J. F.; Schmitt, U. W.; Voth, G. A. The mechanism of hydrated proton transport in water. *J. Am. Chem. Soc.* **2000**, *122*, 12027.

(35) Chen, H. N.; Voth, G. A.; Agmon, N. Kinetics of Proton Migration in Liquid Water. *J. Phys. Chem. B* **2010**, *114*, 333.

(36) Kim, J.; Schmitt, U. W.; Gruetzmacher, J. A.; Voth, G. A.; Scherer, N. E. The vibrational spectrum of the hydrated proton: Comparison of experiment, simulation, and normal mode analysis. *J. Chem. Phys.* **2002**, *116*, 737.

(37) Markovitch, O.; Chen, H.; Izvekov, S.; Paesani, F.; Voth, G. A.; Agmon, N. Special pair dance and partner selection: Elementary steps in proton transport in liquid water. *J. Phys. Chem. B* **2008**, *112*, 9456.

(38) Wang, F.; Izvekov, S.; Voth, G. A. Unusual "Amphiphilic" association of hydrated protons in strong acid solution. *J. Am. Chem. Soc.* **2008**, *130*, 3120.

(39) Iyengar, S. S.; Petersen, M. K.; Day, T. J. F.; Burnham, C. J.; Teige, V. E.; Voth, G. A. The properties of ion-water clusters. I. The protonated 21-water cluster. *J. Chem. Phys.* **2005**, *123*, 084309.

(40) Dellago, C.; Naor, M. M.; Hummer, G. Proton transport through water-filled carbon nanotubes. *Phys. Rev. Lett.* **2003**, *90*.

(41) Laria, D.; Marti, J.; Guardia, E. Protons in supercritical water: A multistate empirical valence bond study. *J. Am. Chem. Soc.* **2004**, *126*, 2125.

(42) Petersen, M. K.; Iyengar, S. S.; Day, T. J. F.; Voth, G. A. The hydrated proton at the water liquid/vapor interface. *J. Phys. Chem. B* **2004**, *108*, 14804.

(43) Swanson, J. M. J.; Maupin, C. M.; Chen, H.; Petersen, M. K.; Xu, J.; Wu, Y.; Voth, G. A. Proton solvation and transport in aqueous and biomolecular systems: Insights from computer simulations. *J. Phys. Chem. B* **2007**, *111*, 4300.

(44) Li, H.; Chen, H. N.; Steinbronn, C.; Wu, B. H.; Beitz, E.; Zeuthen, T.; Voth, G. A. Enhancement of Proton Conductance by Mutations of the Selectivity Filter of Aquaporin-1. *J. Mol. Biol.* **2011**, *407*, 607.

(45) Feng, S.; Voth, G. A. Proton Solvation and Transport in Hydrated Nafion. *J. Phys. Chem. B* **2011**, *115*, 5903.

(46) Yamashita, T.; Voth, G. A. Insights into the Mechanism of Proton Transport in Cytochrome c Oxidase. *J. Am. Chem. Soc.* **2012**, *134*, 1147.

(47) Rottger, K.; Endriss, A.; Ihringer, J.; Doyle, S.; Kuhs, W. F. Lattice-Constants and Thermal-Expansion of H2o and D2o Ice Ih between 10 and 265 K. *Acta Crystallogr. B* **1994**, *50*, 644.

(48) Rick, S. W.; Haymet, A. D. J. Dielectric constant and proton order and disorder in ice Ih: Monte Carlo computer simulations. *J. Chem. Phys.* **2003**, *118*, 9291.

(49) Colbeck, S. C. Temperature-Dependence of the Equilibrium Form of Ice. *J. Cryst. Growth* **1985**, *72*, 726.

(50) Smith, W.; Forester, T. *J. Molec. Graphics* **1996**, *14*, 136.

(51) Nose, S. A Molecular-Dynamics Method for Simulations in the Canonical Ensemble. *Mol. Phys.* **1984**, *52*, 255.

(52) Hoover, W. G. Constant-Pressure Equations of Motion. *Phys. Rev. A* **1986**, *34*, 2499.

(53) McQuarrie, D. A. *Statistical Mechanics*, 1st ed.; University Science Books, 2000.

(54) Nasello, O. B.; de Juarez, S. N.; Di Prinzio, C. L. Measurement of self-diffusion on ice surface. *Scripta Mater.* **2007**, *56*, 1071.

(55) Pieniazek, P. A.; Lin, Y. S.; Chowdhary, J.; Ladanyi, B. M.; Skinner, J. L. Vibrational Spectroscopy and Dynamics of Water Confined inside Reverse Micelles. *J. Phys. Chem. B* **2009**, *113*, 15017.

(56) Wooldridge, P. J.; Devlin, J. P. Proton Trapping and Defect Energetics in Ice from FT-IR Monitoring of Photoinduced Isotopic Exchange of Isolated D_2O. *J. Chem. Phys.* **1988**, *88*, 3086.

(57) Kobayashi, C.; Saito, S.; Ohmine, I. Mechanism of proton transfer in ice. II. Hydration, modes, and transport. *J. Chem. Phys.* **2001**, *115*, 4742.

(58) Kobayashi, C.; Saito, S. J.; Ohmine, I. Mechanism of fast proton transfer in ice: Potential energy surface and reaction coordinate analyses. *J. Chem. Phys.* **2000**, *113*, 9090.

(59) Zundel, G.; Fritsch, J. In *The Chemical Physics of Solvation*; Dogonadze, R. R., Kálmán, E. A. K. A., Ulstrup, J., Eds.; Elsevier: Amsterdam, The Netherlands, 1986; Vol. Part B.

(60) Brewer, M. L.; Schmitt, U. W.; Voth, G. A. The formation and dynamics of proton wires in channel environments. *Biophys J* **2001**, *80*, 1691.

(61) Cao, Z.; Peng, Y. X.; Yan, T. Y.; Li, S.; Li, A. L.; Voth, G. A. Mechanism of Fast Proton Transport along One-Dimensional Water Chains Confined in Carbon Nanotubes. *J. Am. Chem. Soc.* **2010**, *132*, 11395.

(62) Rasaiah, J. C.; Garde, S.; Hummer, G. Water in nonpolar confinement: From nanotubes to proteins and beyond. *Annu Rev Phys Chem* **2008**, *59*, 713.

(63) Paesani, F. Water in metal-organic frameworks: Structure and diffusion of H_2O in MIL-53(Cr) from quantum simulations. *Mol. Simul.* **2012**, in press.

(64) Bankura, A.; Chandra, A. Hydroxide Ion Can Move Faster Than an Excess Proton through One-Dimensional Water Chains in Hydrophobic Narrow Pores. *J. Phys. Chem. B* **2012**, *116*, 9744.

(65) Tuckerman, M.; Laasonen, K.; Sprik, M.; Parrinello, M. Ab-Initio Molecular-Dynamics Simulation of the Solvation and Transport of Hydronium and Hydroxyl Ions in Water. *J. Chem. Phys.* **1995**, *103*, 150.

(66) Tuckerman, M.; Laasonen, K.; Sprik, M.; Parrinello, M. Ab-Initio Molecular-Dynamics Simulation of the Solvation and Transport of H_3O^+ and OH^- Ions in Water. *J. Phys. Chem.* **1995**, *99*, 5749.

(67) Marx, D.; Tuckerman, M. E.; Hutter, J.; Parrinello, M. The nature of the hydrated excess proton in water. *Nature* **1999**, *397*, 601.

(68) Podeszwa, R.; Buch, V. Structure and dynamics of orientational defects in ice. *Phys. Rev. Lett.* **1999**, *83*, 4570.

Chapter 7. Effect of lipid complexity on the phase behavior and physical properties of Langmuir monolayers: implications for atmospheric chemistry

7.1. Abstract

In this chapter the phase behavior of three different monolayers, namely palmitic acid (PA), dipalmitoyl phosphatidic acid (DPPA), and Lipid-A monolayers, at the air/water interface is investigated through molecular dynamics simulations with atomistic force fields. The complexity of both (hydrophobic) tail and (hydrophilic) head groups increases from PA to DPPA and Lipid-A. Our results show that at T = 300 K a second-order phase transition appears as a kink in the PA isotherm as the monolayer transitions from the uniformly tilted condensed to the untilted condensed phase, in agreement with the available experimental data. The analysis of the structural properties indicates that the conformation of the acyl chains is more disordered in the Lipid-A monolayer than in the PA and DPPA monolayers, which is attributed to the presence of a larger number of gauche defects. The electron density profiles of PA and DPPA monolayers show that the hydrophobic tails keep packing efficiently during the compression process due to their larger size compared to the head groups. In contrast, Lipid-A has a larger hydrophilic head group and requires more surface area. The tail groups of Lipid-A are then kept farther apart at both high and low surface pressures and the lateral cohesive interactions or efficient packing of the tail groups are prevented. It is also found that the tilt angles calculated for the acyl chains with respect to the interface normal increase in all

monolayers as the surface area increases (i.e., as the surface pressure decreases). Our simulations provide fundamental insights into the molecular structure and physical properties of Langmuir monolayers at the air/water interface that may affect chemical processes on aerosol particles in the atmosphere.

7.2. Introduction

Marine aerosols constitute one of the most important natural aerosol systems and are known to play an important role in regulating the Earth's climate.[1] Marine aerosols are comprised of primary and secondary aerosol components. The primary aerosol components originate from the interaction of wind stress at the ocean surface and result in the mechanical production of sea-spray aerosol.[2] Sea salts and organic compounds are the main components of these aerosols.[3,4] The fraction of organic components depends upon the seasonality of biological productivity in the ocean and leads to markedly different physical and chemical properties.[5,6] The organic composition plays an important role in determining morphological, optical, and chemical properties of aerosols.[7-12] For example, the organic composition affects aerosol's ability to act as cloud condensation nuclei and to scatter light.[13-15]

Several different organic compounds have been detected in aerosol particles,[16] including alkanes,[17,18] alcohols,[19] polycyclic aromatic hydrocarbons (PAHs),[20] sterols,[21] free fatty acids (FFAs),[22-24] and carbohydrates[25]. Palmitic acid (PA), a saturated 16 carbon chain, is the most abundant FFA that has been identified on aerosol surfaces. Recent studies have indicated that lipopolysaccharides are also found in atmospheric aerosols.[26-29] Chemical composition is ultimately responsible for both physical and

chemical properties of aerosol particles. For example, surface morphology of an aerosol is dependent upon the nature of the organic film, as soluble and insoluble surfactants form expanded and close-packed films, respectively.[30] The packing structure of surface film affects water uptake and evaporation, which can then alter other aerosol properties.[12]

Lipid monolayers at the air/water interface exhibit different physical properties, depending on the type of lipid and surface area. Physical properties can be changed by varying the monolayer area at the interface or by applying an external surface pressure.[31] For example, the dipalmitoylphosphatidylcholine (DPPC) monolayer at the air/water interface, which has been intensively studied because DPPC is the primary component of lung surfactants, exhibits a liquid condensed to liquid expanded transition at ambient conditions as the monolayer area increases.[32]

Since the monolayer composition at the surface of marine aerosols has been shown to be extremely variable, a systematic study of various monolayers was carried out to understand the effect of lipid complexity on the properties of the monolayers. Three abundant lipid monolayers selected from fatty acid, phospholipid and a lipopolysaccharide are studied. The three monolayers are palmitic acid (PA), dipalmitoyl phosphatidic acid (DPPA), and Lipid-A monolayers. The complexity of both hydrophobic tail and hydrophilic head groups in these systems increases from PA to DPPA and Lipid-A. The molecular structures of PA, DPPA, and Lipid-A are shown in Figure 7.1.

7.3. Computational methodology

In order to build the starting configurations of monolayers, lipid bilayers are first generated. The initial configuration of a DPPA bilayer was generated by the CHARMM-GUI program,[33] where 128 DPPAs were distributed in a 8 × 8 arrangement per layer. Starting configurations for PA and Lipid-A bilayers were created using the Packmol software,[34] in which 288 PAs or 128 Lipid-A molecules were distributed in a 12 × 12 or 8 × 8 arrangement per layer, respectively. In order to neutralize the DPPA and Lipid-A systems, 128 or 256 sodium cations were placed in the vicinity of the phosphate groups of the DPPA or Lipid-A molecules, respectively. The structure of each bilayer was optimized using the steepest descent algorithm without constraints for 10000 steps. The optimized structures were heated up to 300 K and the final structures at the end of the heating process were used as the initial configurations of the lipid bilayer simulations. Each lipid bilayer was simulated in the constant temperature and constant surface tension ensemble with a negative surface tension (-10 mN/m). The temperature was controlled using the Langevin thermostat with a collision frequency of 1 ps^{-1}.[35] During the simulations, the surface area decreased due to the low surface tension of the system. The molecular configurations at specific values of the surface area were extracted from the simulations and modified to form monolayers by adding vacuum regions (see Figure 7.1d).

The monolayer simulations were carried out in the NVT ensemble using a Langevin thermostat to control the temperature with a collision frequency of 1 ps^{-1}.[35] The surface pressure of the systems at each fixed surface area was obtained from $\Pi(A,T) = \gamma_w(T) - \gamma_m(A,T)$, where A is the surface area per lipid molecule, γ_w(T) is the surface

tension of water at 300 K, and γ_m(A, T) is the surface tension of the monolayer at surface area *A* and 300 K. The surface tensions of the monolayer were extracted every 1 ps from the NVT simulations.

All simulations were performed using the GPU-accelerated version of PMEMD available in the Amber 12 suite of codes.[36] The Lipid 11 force field was used to describe the molecular interactions of PA and DPPA.[37] The Glycam-based force field for lipopolysaccharide membranes was used to describe all interactions of Lipid-A, except the partial atomic charges.[38] In order to generate the charges, Lipid-A was separated into six residues, as defined in Ref. [38]. RESP-derived partial atomic charges were computed for the six residues of Lipid-A by fitting to the HF/aug-cc-pVDZ molecular electrostatic potentials (MEPs).[38] Details of the protocol used to generate the partial atomic charges are reported in Ref. [38]. The TIP4P/2005 model was used to model the water interactions.[39] It should be noted that the surface tension of water (γ_w) is an important parameter for calculating the corresponding surface pressure of the monolayer. Most of the non-polarizable water models predict a lower vacuum/water surface tension than the experimental value (~72 mN/m). For example, the TIP3P and SPC models predict a surface tension of approximately 53 mN/m and 55 mN/m, respectively.[40,41] The underestimated surface tension of the vacuum/water interface has only marginal effects on the monolayer properties at high surface pressure with small surface area per lipid, when the vacuum/water contact is negligible. However, at low surface pressure and high surface area, the underestimation of the surface tension of water has much larger effects, artificially promoting pore formation and therefore preventing the actual expansion of the

monolayer. Hence, the TIP4P/2005 water model, which provides an accurate vacuum/water surface tension (~ 68 mN/m), was used in this work.

7.4. Results and discussion

7.4.1. Surface pressure-area isotherms

The surface pressure-area isotherms of Langmuir monolayers on aqueous surfaces can be used to reveal the underlying phase information of the corresponding monolayer. Experimental studies have shown that PA and DPPA monolayers with water subphase at ambient temperature exhibit a second order phase transition.[42-44] The compression isotherms of the PA monolayers on a pure (neat) water subphase surface were investigated by Allen and co-workers.[42,45] A second order phase transition appears as a kink at 25 mN/m on the isotherms when the PA monolayers transition from the tilted condensed (TC) to the untilted condensed (UC) phase.[42] Our atomistic simulations also predict a kink at 25 mN/m in the isotherm, as shown in Figure 7.2a. The snapshots of equilibrium PA monolayers at surface pressures higher and lower than the transition region (kink), as shown in Figure 7.3, clearly indicate the existence of untilted and tilted condensed phases.

The isotherm of DPPA monolayers with pure water subphase is similar to those of fatty acids, where the strong van der Waals attractions among the tails make a condensed phase energetically favorable. Several experiments have shown that the isotherm of DPPA monolayers on a water subphase exhibits a kink at Π = 15 ~ 20 mN/m corresponding to oblique-rectangular-hexagonal lattice phase transitions.[43,44] de Meijere

et al. have studied the progression of the DPPA monolayer structure from oblique to rectangular and hexagonal lattices by performing X-ray diffraction measurements.[44] They also showed that the interaction of a positively charged polyelectrolyte with the negative charge of DPPA head group leads to a local lattice expansion, with the lattice exhibiting a rectangular structure with a uniform chain tilt.[44] As shown in Figure 7.2b, the simulated isotherm of the DPPA monolayer on a Na^+/water subphase shows increasing surface pressure as the monolayer is compressed and no kink is observed. Furthermore, the electron density profiles of the DPPA monolayer in Figure 7.6b indicate that the sodium ions remain close to head groups. The strong interaction of the ions with the head groups can perturb the lattice structures of DPPA monolayers, similarly to the effect of the positively charged polyelectrolyte reported in X-ray diffraction measurements.[44]

The Lipid-A monolayer surface pressure-area isotherm has been experimentally measured, and a plateau indicating a liquid expanded (LE) to liquid condensed (LC) phase transition has been observed.[46,47] Neville et al. have reported that the surface pressure of the LE-LC phase transition plateau region is 17 - 20 mN/m at T = 295 K.[47] In our study, a small phase coexistence plateau occurs in the interval of Π = 15 - 18 mN/m. Usually, a transition from a liquid expanded to a condensed phase with a plateau indicates a first-order transition. Therefore, the hysteresis effect is expected to be observed in the simulations, since the release or absorption of energy is required to change phase in a first-order transition. Since addressing the hysteresis effect and phase coexistence property are out of the main vision of current work, we will present the corresponding study elsewhere with the combination of atomistic and coarse-grained approaches.

Our preliminary results on the isotherms of PA, DPPA, and Lipid-A monolayers elucidate the effect of lipid complexity and ions on the phase transition of Langmuir monolayers. Mean-field theory descriptions of phase transition in monolayers will be used to further address the phase behavior of these three model monolayers.[48]

7.4.2. Structural properties of PA monolayers

The snapshots of PA monolayers shown in Figure 7.3 clearly indicate the existence of untilted and tilted condensed phases at high and low surface pressures, respectively. The average tilt angle of the acyl chains of the representative untilted condensed phase at 34.6 mN/m is 5.7 degrees and the tilted condensed phase at 5.6 mN/m is 28.7 degrees, as shown in Table 7.1 and Figure 7.5.

The radial distribution functions (RDF) of the carboxyl carbons in the PA monolayers are shown in Figure 7.4. For the monolayers with surface pressure higher than the transition pressure (19.00 – 19.50 $Å^2$/mole), only a single peak is observed around R_{C-C} = 4.5 Å. The peak represents the distance of the carboxyl carbon with the nearest-neighbor carboxyl carbons. A shoulder peak appears at around R_{C-C} = 5.4 Å when the monolayers are in a tilted condensed phase (20.00 – 22.00 $Å^2$/mole). To better characterize the change in structures, the positions of the carboxyl carbons are projected onto a plane parallel to the interface and the collective center of mass motion is removed. The results show that the carboxyl carbons of monolayers in the untilted condensed phase are arranged in a lattice with a hexagonal unit cell, whereas in the tilted condensed phase the carboxyl carbons form a lattice with a rectangular unit cell. These two types of unit

cells are consistent with grazing incidence x-ray diffraction measurements on PA monolayers at the air/water interface.[49]

In order to characterize the interactions among the head groups (carboxyl groups) of the PA monolayers, RDFs between carboxyl carbon and hydroxyl hydrogen of the PA monolayers are calculated and shown in Figure 7.8a. Two peaks at ~2.00 and ~2.85 Å corresponding to intramolecular *trans* and *cis* conformers of carboxyl groups are observed. The peak intensity of the *trans* conformers is larger than that of *cis* conformers, which indicates that *trans* conformers are lower in energy than *cis* conformers. With increasing surface area (decreasing surface pressure), the intensity of *trans* conformers decreases and that of *cis* conformers increases. A shoulder peak at ~1.70 Å is present in the RDFs, which clearly reveals the formation of intermolecular hydrogen bonds between the carbonyl (-C=O, as hydrogen-bond acceptor) and hydroxyl (-OH, as hydrogen-bond donor) groups in the PA monolayers.

Structural information of the PA monolayers at selected untilted (Π = 34.6 mN/m) and tilted (Π = 5.6 mN/m) condensed phases are shown in Table 7.1, where the thicknesses and electron densities of the tail groups and the whole monolayers are calculated from the electron density profiles (more details will be discussed in section 7.4.3). The experimental structural parameters of PA monolayers at Π = 15 mN/m fitted to X-ray reflectivity data are also listed in Table 7.1. Overall the calculated structural parameters of the PA monolayer with the tilted condensed phase agree well with the available X-ray reflectivity data.[49]

7.4.3. Electron density profile

Electron density profiles measure the probability of finding electrons at a specific location. To characterize the monolayer structures, electron density profiles along the direction normal to the interface of the PA, DPPA, and Lipid-A monolayers are shown in Figure 7.6, where water, ions, head groups, tail groups, and total electron density profiles are colored in blue, orange, red, green, and black, respectively. The Gibbs dividing surfaces are used to define the interfacial water and set as the zero point along the direction normal to the interface (z-axis). The thickness of the interfacial water layer in the PA, DPPA, and Lipid-A monolayers (the region where the water electron density is smaller than that of bulk water) is 4, 8, and 12 Å, respectively. Changes in the surface pressure do not affect the thickness of interfacial water in any of the three Langmuir monolayers. The sodium ions are preferentially located at the interface as indicated by the electron density profiles of ions in the DPPA and Lipid-A monolayers. In all three monolayers, the tail groups are shorter at low surface pressure than those at high surface pressure. In the PA and DPPA monolayers, this is attributed to the increase of the tilt angles of the tail groups, as shown in Figure 7.5. In the Lipid-A monolayer, the change is attributed to the effects of both tilt angles and gauche defects. Details of the gauche defects observed in the tail groups of the monolayers will be discussed in Section 7.4.4.

The most interesting feature of the electron density profiles shown in Figure 7.6 is the variation of the intensities of both head and tail groups at different surface pressures. The electron density intensities of tail groups of the PA and DPPA monolayers are unperturbed by changing the surface pressure, while the intensities associated with the

head groups are lower at the low surface pressure than at high surface pressure. In contrast, the intensity associated with the tail groups of the Lipid-A monolayer decreases with decreasing of surface pressure, while the intensity of the corresponding head groups remains unchanged. The difference can be explained by comparing the sizes of head and tail groups in PA, DPPA, and lipid-A molecules. Since the head groups of both PA and DPPA molecules are smaller than the corresponding tail groups, the latter pack efficiently throughout the compression process, as shown in Figure 7.6d. In contrast, Lipid-A has a hydrophilic head group that is larger than its tail group. The tails in Lipid-A are therefore kept farther apart at both high and low surface pressures and the lateral cohesive interactions that lead to efficient packing of the tails do not occur, resulting in more flexible tails, as shown in Figure 7.6e. The structural properties of the tail groups of the PA, DPPA, and Lipid-A monolayers will be discussed in the following subsection.

7.4.4. Structures of tail groups: Gauche defects

The structures of the tail groups (acyl chains) can be characterized by measuring the distribution of *trans* and *gauche* configurations along the carbon chains. Figure 7.7 shows the fractions of *trans* states of the acyl chains along the tail groups of the monolayers. The dihedral angle ϕ_i is defined by four consecutive carbon atoms (C_i, C_{i+1}, C_{i+2}, C_{i+3}) in acyl chains to measure the rotation about $C_{i+1} - C_{i+2}$ bond. The *trans* state corresponds to the potential minimum at $\phi_i = 180^o$ and the gauche state corresponds to the minima at $\phi_i = 60^o$ and 120^o. As shown in Figure 7.7, almost all-trans chains are found in the PA monolayers at both high and low surface pressures, which is consistent with the

results of sum frequency generation spectra showing a barely noticeable υ_s-CH_2 mode (methylene symmetric stretch).[42] In the DPPA monolayers, the gauche defects among the carbon atoms in the middle of the chains are negligible. Significant gauche defects (~ 30% at Π = 37.8 mN/m and ~ 40% at Π = 5.6 mN/m) are observed for the carbon atoms (C_2 – C_3) next to the carboxyl groups of DPPA. In contrast, large numbers of gauche defects are observed in Lipid-A, with the largest values corresponding to the acyl chain carbon atoms (C_2 – C_3) next to the head group. The large size of the head groups of Lipid-A reduces the steric effect among acyl chains and increases the corresponding gauche defect probability. This analysis shows that the acyl chains of the Lipid-A monolayer are more flexible than those of the PA and DPPA monolayers, consistent with the analysis of the corresponding electron density profiles.

7.5. Conclusions

The phase behavior and structural properties of three Langmuir monolayers, palmitic acid (PA), dipalmitoyl phosphatidic acid (DPPA), and Lipid-A monolayers, at the air/water interface have been investigated through molecular dynamics simulations. At T=300 K, a second-order phase transition appears as a kink in the surface pressure-area isotherm of PA monolayer, with the transition occurring from the uniformly tilted condensed to the untilted condensed phase. The head groups of the PA molecules in the untilted condensed phase form a hexagonal unit cell, while in the tilted condensed phase the PA molecules lie in a collective tilt and form a lattice with a rectangular unit cell. The

overall simulated structural properties of the PA monolayers are in excellent agreement with the available experimental data.

The electron density profiles of PA and DPPA monolayers indicate that the tails keep packing efficiently during the compression process since the tail groups are larger than the head groups. In contrast, Lipid-A has a larger hydrophilic head group and the tail groups are kept farther apart at both high and low surface pressure. The analysis of the lipid structures indicates that the acyl chains of the Lipid-A monolayer are more flexible than those of the PA and DPPA monolayers. It is also found that the tilt angles of the acyl chains increase in all monolayers as the surface area increases. Overall, the simulations show that lipid complexity and surface pressure are important in determining the physical and chemical properties of Langmuir monolayers at air/water interfaces, and therefore will be important in understanding chemical processes at the surfaces of sea spray aerosol particles in the atmosphere.

7.6. Acknowledgments

This research was supported by the National Science Foundation through grant CHE-1111364. This work used the Extreme Science and Engineering Discovery Environment (XSEDE), which is supported by National Science Foundation grant number OCI-1053575 (allocation TG-CHE110009).

Chapter 7 includes materials from “The Effect of Lipid Complexity and Surface Pressure on the Structural Properties of Langmuir Monolayers: Atmospheric Implications” currently being prepared for submission for publication authored by Wei

Lin, Anthony J. Clark and Francesco Paesani. All material has been reproduced with the consent of all other authors.

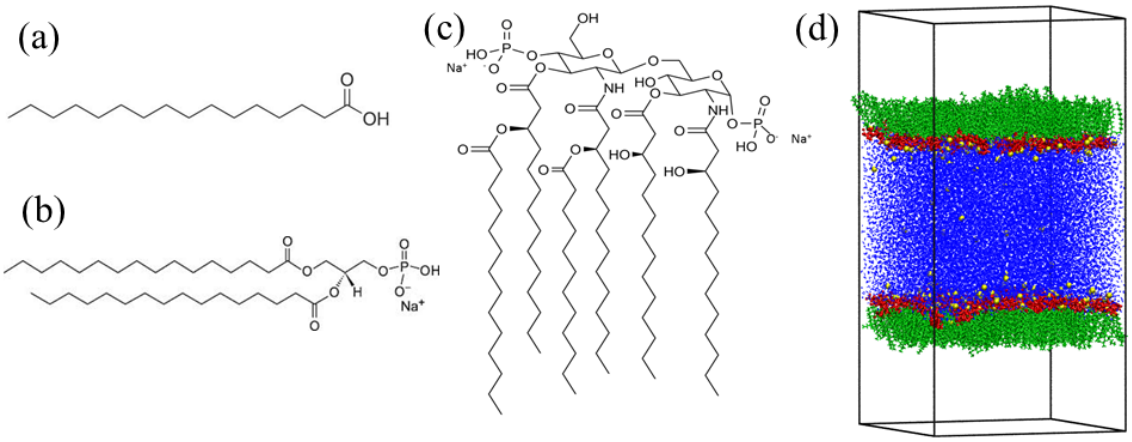

Figure 7.1. Structures of (a) PA, (b) DPPA, (c) Lipid-A and (d) DPPA monolayers for molecualr dynamics simulations. In (d), the water molecules are in blue, the tail groups of DPPA are in green, the head groups of DPPA are in red and the Na^+ ions are in yellow.

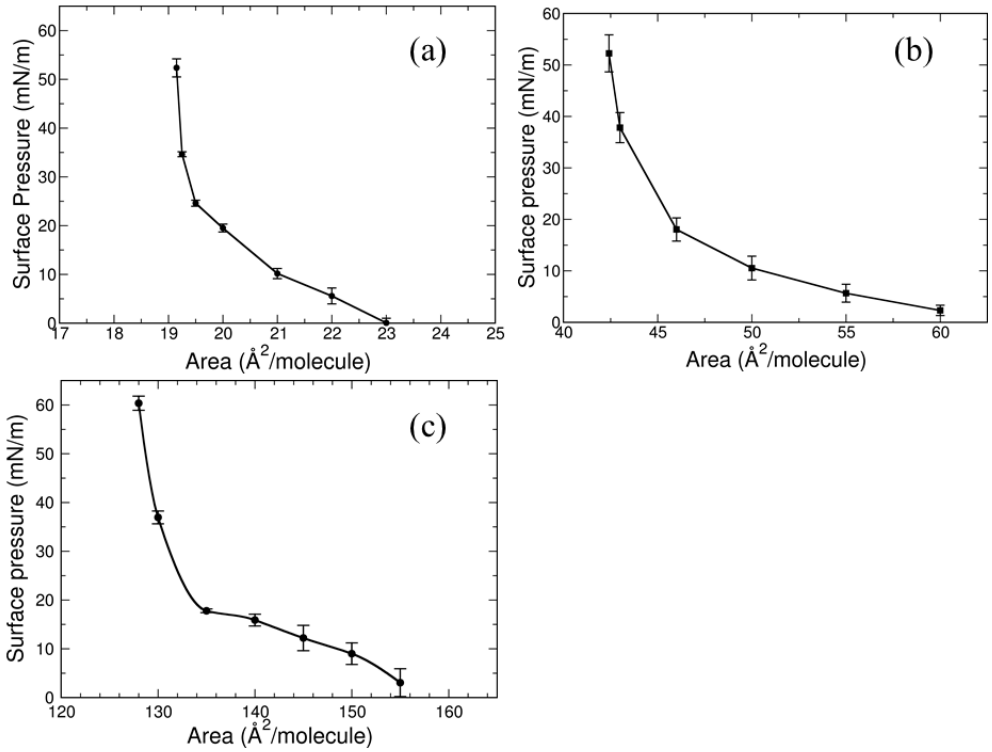

Figure 7.2. Surface pressure-area isotherms of monolayers at T = 300 K: (a) the PA monolayer with water subphase, (b) the DPPA monolayer with Na^+/water subphase, and (c) the Lipid-A monolayers with Na^+/water subphase.

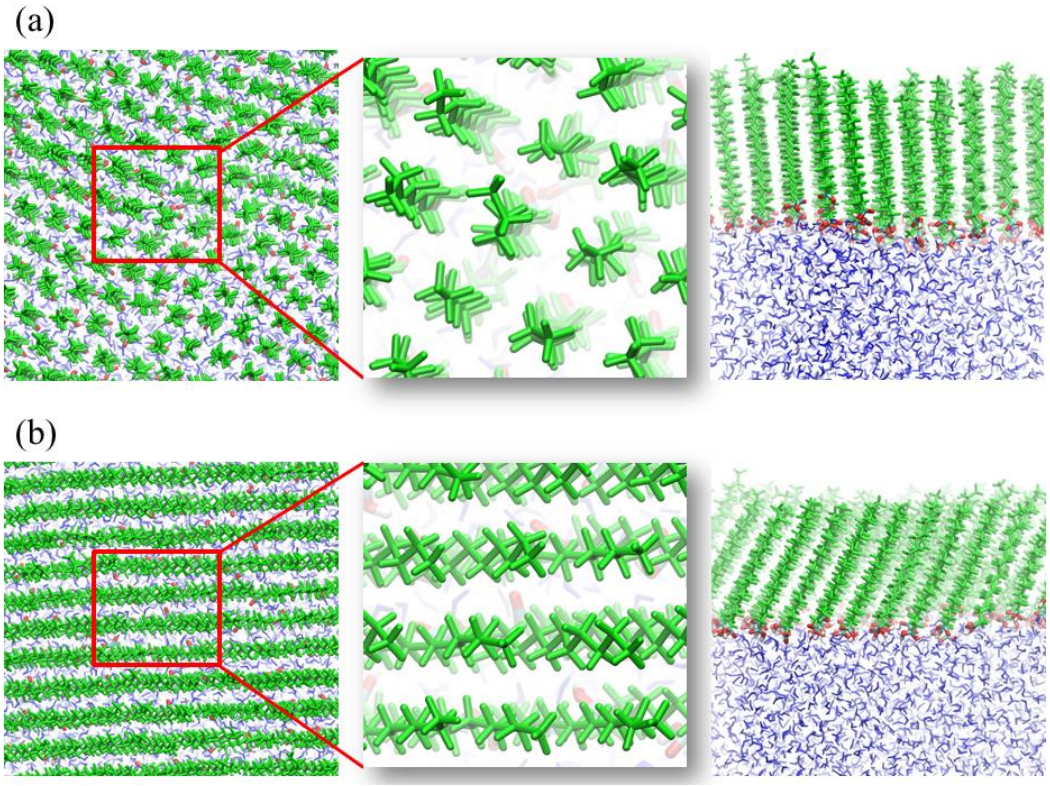

Figure 7.3. Snapshots of PA monolayers. (a) PA monolayers at untilted condensed phase with surface pressure at 34.6 mN/m and surface area per PA molecule at 19.25 $Å^2$. (b) PA monolayers at tilted condensed phase with surface pressure at 5.6 mN/m and surface area per PA molecule at 22.00 $Å^2$. Left column: top view of monolayers; Middle column: enlarge of top view; Right column: side view of monolayers.

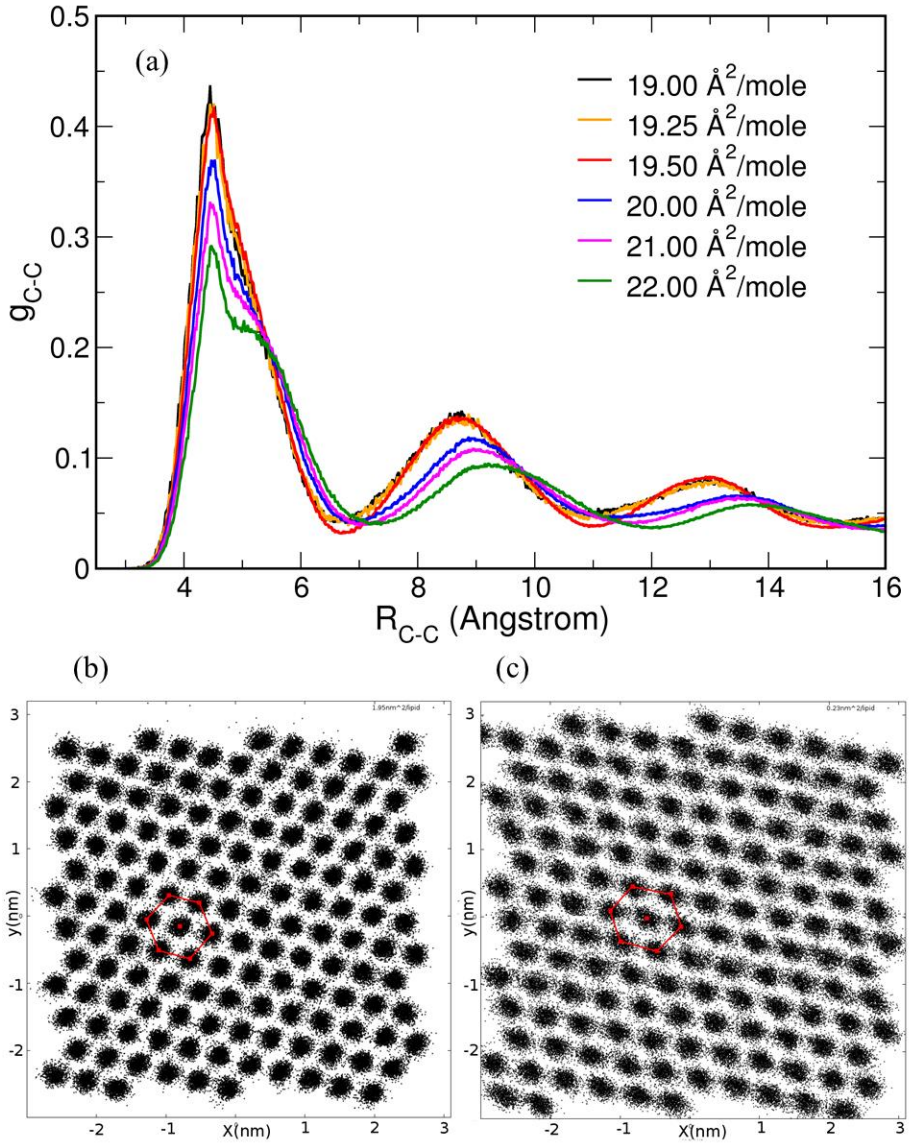

Figure 7.4. (a) The radial distribution functions of carboxyl groups of PA monolayers. The 2D density plot of carboxyl carbon of PA monolayers at (b) high surface pressure (34.6 mN/m, 19.25 Å^2/mole) and (c) low surface pressure (5.6 mN/m, 22.00 Å^2/mole) along the molecular dynamics simulation trajectories.

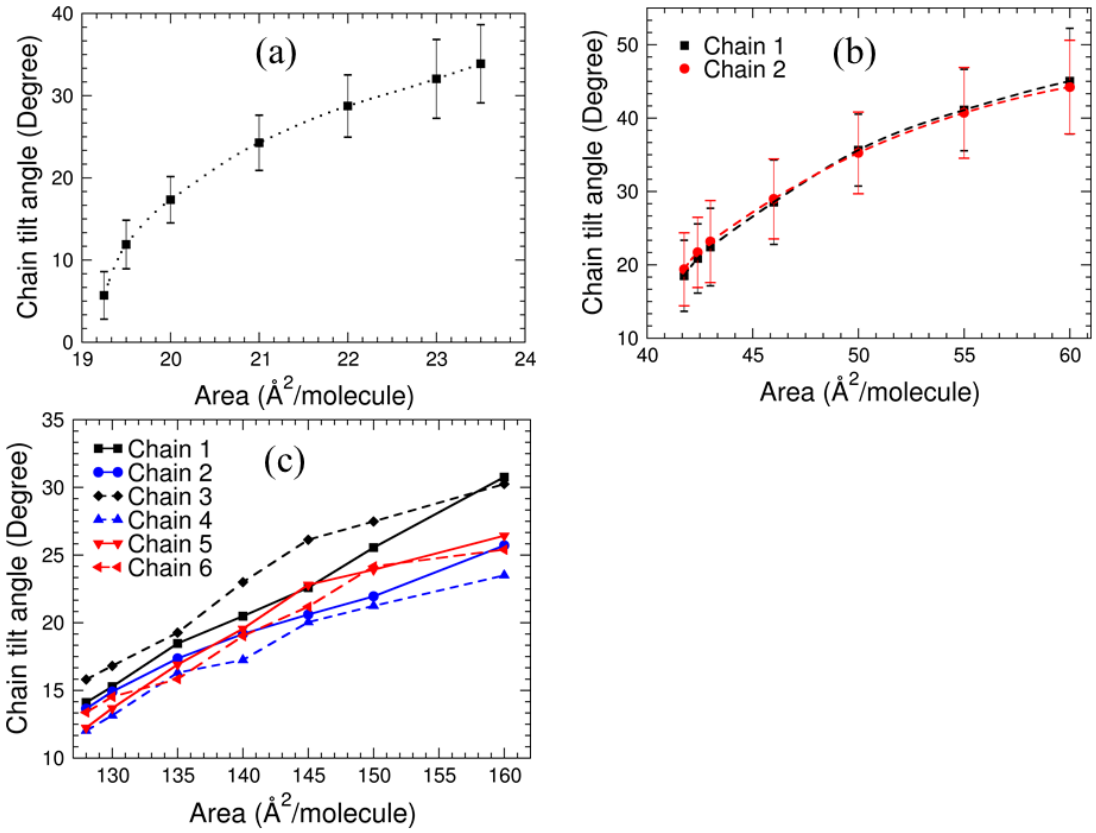

Figure 7.5. Tilt angle of the acyl chains (tail groups) of the (a) PA, (b) DPPA, and (c) Lipid-A monolayers.

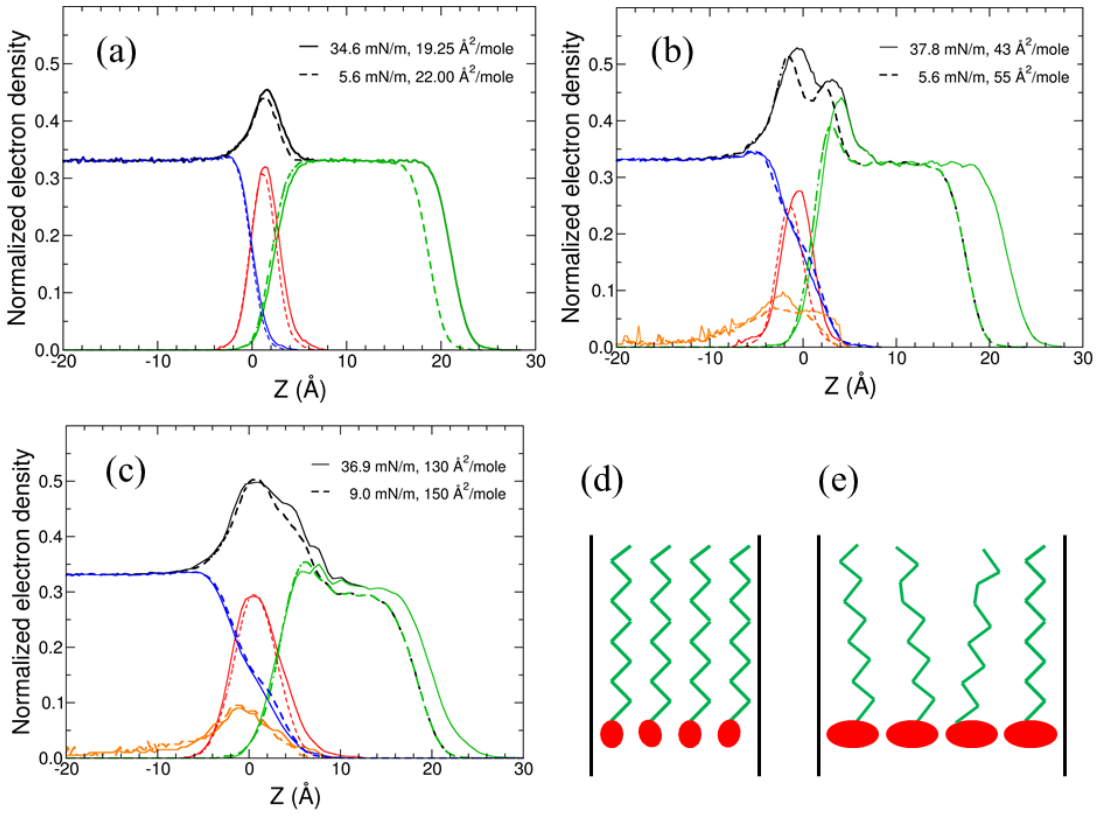

Figure 7.6. Electronic density profiles along z-axis of the (a) PA, (b) DPPA, and (c) Lipid-A monolayers. The water, sodium ions, head groups, tail groups and the total electron density profiles are colored in blue, orange, red, green and black respectively. For clarification, the intensities of electron density of sodium ions are enlarged by 2.5 and 5 times in DPPA and Lipid-A monolayers, respectively. The cartons demonstrate the (d) tail and (e) head group dominations along the packing process.

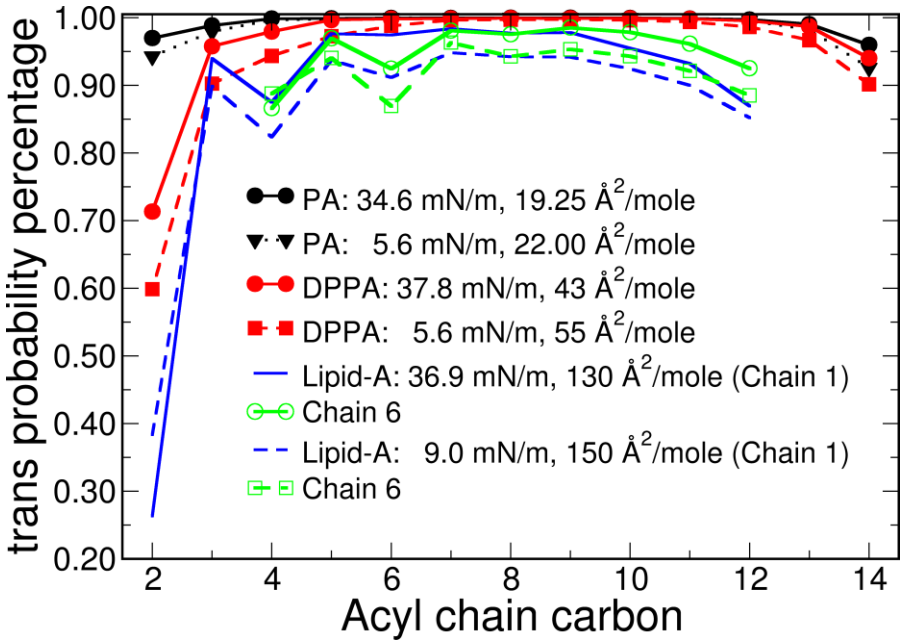

Figure 7.7. The *trans* probabilities of acyl chains of the PA, DPPA, and Lipid-A monolayers.

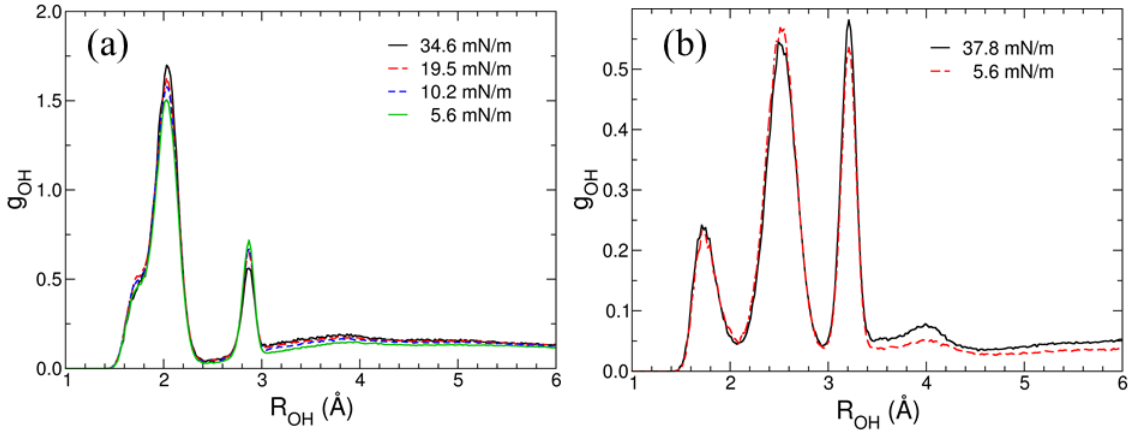

Figure 7.8. The radial distribution functions of O---H distances of head groups of the PA and DPPA monolayers. (a) Distance of hydrogen and carbonyl oxygen of carboxyl group of PA monolayers and (b) distance of hydrogen and phosphate oxygen of hydrogen phosphate group of DPPA monolayers.

Table 7.1. Structure information of PA monolayers.[a]

Surface pressure	Area ($Å^2$/mole)	Tail		Total		Tilt angle (^{o})
		Thickness(Å)	ρ ($e^-/Å^3$)[b]	Thickness(Å)	ρ ($e^-/Å^3$)[b]	
5.6 mN/m	22.00	16.8	0.98	19.1	1.33	28.7
34.6 mN/m Exp.[c]	19.25	18.6	0.98	21.5	1.38	5.7
15 mN/m	21.4	17.6	0.96	19.8	1.53	21.5

[a.] All Thicknesses are calculated from full width of half maximum (FWHM) of electron density profiles of PA monolayers.
[b.] All electron densities (ρ) shown in table are normalized by the electron density of water ($\rho_{water} = 0.334\ e^-/Å^3$)
[c.] experimental data from Ref. [50]

7.7. References

(1) Finlayson-Pitts, B. J.; Pitts, J. N., Jr. *Chemistry of the upper and lower atmosphere: Theory, experiments and applications*; Academic Press, 2000.

(2) Ellison, G. B.; Tuck, A. F.; Vaida, V.; Atmospheric processing of organic aerosols; *Journal of Geophysical Research-Atmospheres* **1999**, *104*, 11633-11641.

(3) Jimenez, J. L.; Canagaratna, M. R.; Donahue, N. M.; Prevot, A. S. H.; Zhang, Q.; Kroll, J. H.; DeCarlo, P. F.; Allan, J. D.; Coe, H.; Ng, N. L.; Aiken, A. C.; Docherty, K. S.; Ulbrich, I. M.; Grieshop, A. P.; Robinson, A. L.; Duplissy, J.; Smith, J. D.; Wilson, K. R.; Lanz, V. A.; Hueglin, C.; Sun, Y. L.; Tian, J.; Laaksonen, A.; Raatikainen, T.; Rautiainen, J.; Vaattovaara, P.; Ehn, M.; Kulmala, M.; Tomlinson, J. M.; Collins, D. R.; Cubison, M. J.; Dunlea, E. J.; Huffman, J. A.; Onasch, T. B.; Alfarra, M. R.; Williams, P. I.; Bower, K.; Kondo, Y.; Schneider, J.; Drewnick, F.; Borrmann, S.; Weimer, S.; Demerjian, K.; Salcedo, D.; Cottrell, L.; Griffin, R.; Takami, A.; Miyoshi, T.; Hatakeyama, S.; Shimono, A.; Sun, J. Y.; Zhang, Y. M.; Dzepina, K.; Kimmel, J. R.; Sueper, D.; Jayne, J. T.; Herndon, S. C.; Trimborn, A. M.; Williams, L. R.; Wood, E. C.; Middlebrook, A. M.; Kolb, C. E.; Baltensperger, U.; Worsnop, D. R.; Evolution of Organic Aerosols in the Atmosphere; *Science* **2009**, *326*, 1525-1529.

(4) Rinaldi, M.; Decesari, S.; Finessi, E.; Giulianelli, L.; Carbone, C.; Fuzzi, S.; O'Dowd, C. D.; Ceburnis, D.; Facchini, M. C.; Primary and Secondary Organic Marine Aerosol and Oceanic Biological Activity: Recent Results and New Perspectives for Future Studies; *Advances in Meteorology* **2010**.

(5) O'Dowd, C. D.; Facchini, M. C.; Cavalli, F.; Ceburnis, D.; Mircea, M.; Decesari, S.; Fuzzi, S.; Yoon, Y. J.; Putaud, J. P.; Biogenically driven organic contribution to marine aerosol; *Nature* **2004**, *431*, 676-680.

(6) Wojciechowski, J. C.; Schumacher, M. V.; Pires, C. A. D.; Madruga, P. R. D.; Kilca, R. D.; Brun, E. J.; da Silva, C. R. S.; Vaccaro, S.; Neto, R. M. R.; Geostatistics

Applied to the Study of Soil Physiochemical Characteristics in Seasonal Deciduous Forest Areas; *Ciencia Florestal* **2009**, *19*, 383-391.

(7) Laurain, A. M. C.; Reid, J. P.; Characterizing Internally Mixed Insoluble Organic Inclusions in Aqueous Aerosol Droplets and Their Influence on Light Absorption; *J Phys Chem A* **2009**, *113*, 7039-7047.

(8) Sierra-Hernandez, M. R.; Allen, H. C.; Incorporation and Exclusion of Long Chain Alkyl Halides in Fatty Acid Monolayers at the Air-Water Interface; *Langmuir* **2010**, *26*, 18806-18816.

(9) Quinn, P. K.; Kapustin, V. N.; Bates, T. S.; Covert, D. S.; Chemical and optical properties of marine boundary layer aerosol particles of the mid-Pacific in relation to sources and meteorological transport; *Journal of Geophysical Research-Atmospheres* **1996**, *101*, 6931-6951.

(10) Beaver, M. R.; Freedman, M. A.; Hasenkopf, C. A.; Tolbert, M. A.; Cooling Enhancement of Aerosol Particles Due to Surfactant Precipitation; *J Phys Chem A* **2010**, *114*, 7070-7076.

(11) Novakov, T.; Corrigan, C. E.; Penner, J. E.; Chuang, C. C.; Rosario, O.; Bracero, O. L. M.; Organic aerosols in the Caribbean trade winds: A natural source?; *Journal of Geophysical Research-Atmospheres* **1997**, *102*, 21307-21313.

(12) Garland, R. M.; Wise, M. E.; Beaver, M. R.; DeWitt, H. L.; Aiken, A. C.; Jimenez, J. L.; Tolbert, M. A.; Impact of palmitic acid coating on the water uptake and loss of ammonium sulfate particles; *Atmospheric Chemistry and Physics* **2005**, *5*, 1951-1961.

(13) Abbatt, J. P. D.; Broekhuizen, K.; Kumal, P. P.; Cloud condensation nucleus activity of internally mixed ammonium sulfate/organic acid aerosol particles; *Atmospheric Environment* **2005**, *39*, 4767-4778.

(14) Fuzzi, S.; Andreae, M. O.; Huebert, B. J.; Kulmala, M.; Bond, T. C.; Boy, M.; Doherty, S. J.; Guenther, A.; Kanakidou, M.; Kawamura, K.; Kerminen, V. M.; Lohmann, U.; Russell, L. M.; Poschl, U.; Critical assessment of the current state of scientific knowledge, terminology, and research needs concerning the role of organic aerosols in the atmosphere, climate, and global change; *Atmospheric Chemistry and Physics* **2006**, *6*, 2017-2038.

(15) Rudich, Y.; Laboratory perspectives on the chemical transformations of organic matter in atmospheric particles; *Chemical Reviews* **2003**, *103*, 5097-5124.

(16) Rogge, W. F.; Mazurek, M. A.; Hildemann, L. M.; Cass, G. R.; Simoneit, B. R. T.; Quantification of Urban Organic Aerosols at a Molecular-Level - Identification, Abundance and Seasonal-Variation; *Atmospheric Environment Part a-General Topics* **1993**, *27*, 1309-1330.

(17) Simoneit, B. R. T.; Application of Molecular Marker Analysis to Reconcile Sources of Carbonaceous Particulates in Tropospheric Aerosols; *Science of the Total Environment* **1984**, *36*, 61-72.

(18) Sicre, M. A.; Marty, J. C.; Saliot, A.; N-Alkanes, Fatty-Acid Esters, and Fatty-Acid Salts in Size Fractionated Aerosols Collected over the Mediterranean-Sea; *Journal of Geophysical Research-Atmospheres* **1990**, *95*, 3649-3657.

(19) Gogou, A. I.; Apostolaki, M.; Stephanou, E. G.; Determination of organic molecular markers in marine aerosols and sediments: one-step flash chromatography compound class fractionation and capillary gas chromatographic analysis; *Journal of Chromatography A* **1998**, *799*, 215-231.

(20) Gogou, A.; Stratigakis, N.; Kanakidou, M.; Stephanou, E. G.; Organic aerosols in Eastern Mediterranean: Components source reconciliation by using molecular markers and atmospheric back trajectories; *Organic Geochemistry* **1996**, *25*, 79-96.

(21) Barbier, M.; Tusseau, D.; Marty, J. C.; Saliot, A.; Sterols in Aerosols, Surface Microlayer and Subsurface Water in the Northeastern Tropical Atlantic; *Oceanologica Acta* **1981**, *4*, 77-84.

(22) Barger, W. R.; Garrett, W. D.; Surface Active Organic Material in Marine Atmosphere; *Journal of Geophysical Research* **1970**, *75*, 4561-&.

(23) Barger, W. R.; Garrett, W. D.; Surface-Active Organic Material in Air over Mediterranean and over Eastern Equatorial Pacific; *Journal of Geophysical Research-Oceans and Atmospheres* **1976**, *81*, 3151-3157.

(24) Duce, R. A.; Mohnen, V. A.; Zimmerman, P. R.; Grosjean, D.; Cautreels, W.; Chatfield, R.; Jaenicke, R.; Ogren, J. A.; Pellizzari, E. D.; Wallace, G. T.; Organic Material in the Global Troposphere; *Reviews of Geophysics* **1983**, *21*, 921-952.

(25) Crahan, K. K.; Hegg, D. A.; Covert, D. S.; Jonsson, H.; Reid, J. S.; Khelif, D.; Brooks, B. J.; Speciation of organic aerosols in the tropical mid-pacific and their relationship to light scattering; *Journal of the Atmospheric Sciences* **2004**, *61*, 2544-2558.

(26) Lass, K.; Friedrichs, G.; Revealing structural properties of the marine nanolayer from vibrational sum frequency generation spectra; *Journal of Geophysical Research-Oceans* **2011**, *116*.

(27) Hawkins, L. N.; Russell, L.; Polysaccharides, Proteins, and Phytoplankton Fragments: Four Chemically Distinct Types of Marine Primary Organic Aerosol Classified by Single Particle Spectromicroscopy; *Advances in Meteorology* **2010**.

(28) Russell, L. M.; Hawkins, L. N.; Frossard, A. A.; Quinn, P. K.; Bates, T. S.; Carbohydrate-like composition of submicron atmospheric particles and their production from ocean bubble bursting; *P Natl Acad Sci USA* **2010**, *107*, 6652-6657.

(29) Facchini, M. C.; Rinaldi, M.; Decesari, S.; Carbone, C.; Finessi, E.; Mircea, M.; Fuzzi, S.; Ceburnis, D.; Flanagan, R.; Nilsson, E. D.; de Leeuw, G.; Martino, M.; Woeltjen, J.; O'Dowd, C. D.; Primary submicron marine aerosol dominated by insoluble organic colloids and aggregates; *Geophysical Research Letters* **2008**, *35*.

(30) Donaldson, D. J.; Vaida, V.; The influence of organic films at the air-aqueous boundary on atmospheric processes; *Chemical Reviews* **2006**, *106*, 1445-1461.

(31) Baoukina, S.; Marrink, S. J.; Tieleman, D. P.; Structure and Dynamics of Lipid Monolayers: Theory and Applications; *Handb Mod Biophys* **2009**, *2*, 75-99.

(32) Mohammad-Aghaie, D.; Mace, E.; Sennoga, C. A.; Seddon, J. M.; Bresme, F.; Molecular Dynamics Simulations of Liquid Condensed to Liquid Expanded Transitions in DPPC Monolayers; *J Phys Chem B* **2010**, *114*, 1325-1335.

(33) Kumar, R.; Iyer, V. G.; Im, W.; CHARMM-GUI: A graphical user interface for the CHARMM users; *Abstr Pap Am Chem S* **2007**, *233*, 273-273.

(34) Martinez, L.; Andrade, R.; Birgin, E. G.; Martinez, J. M.; PACKMOL: A Package for Building Initial Configurations for Molecular Dynamics Simulations; *J Comput Chem* **2009**, *30*, 2157-2164.

(35) Uberuaga, B. P.; Anghel, M.; Voter, A. F.; Synchronization of trajectories in canonical molecular-dynamics simulations: Observation, explanation, and exploitation; *J Chem Phys* **2004**, *120*, 6363-6374.

(36) Case, D. A.; Darden, T. A.; Cheatham, T. E., III ; Simmerling, C. L.; Wang, J.; Duke, R. E.; Luo, R.; Walker, R. C.; Zhang, W.; Merz, K. M.; etal.; 12 ed.; University of California - San Francisco: San Francisco, 2012.

(37) Skjevik, A. A.; Madej, B. D.; Walker, R. C.; Teigen, K.; LIPID11: A Modular Framework for Lipid Simulations Using Amber; *J Phys Chem B* **2012**, *116*, 11124-11136.

(38) Kirschner, K. N.; Lins, R. D.; Maass, A.; Soares, T. A.; A Glycam-Based Force Field for Simulations of Lipopolysaccharide Membranes: Parametrization and Validation; *J Chem Theory Comput* **2012**, *8*, 4719-4731.

(39) Abascal, J. L. F.; Vega, C.; A general purpose model for the condensed phases of water: TIP4P/2005; *J Chem Phys* **2005**, *123*.

(40) Jorgensen, W. L.; Chandrasekhar, J.; Madura, J. D.; Impey, R. W.; Klein, M. L.; Comparison of Simple Potential Functions for Simulating Liquid Water; *J Chem Phys* **1983**, *79*, 926-935.

(41) Hermans, J.; Berendsen, H. J. C.; Vangunsteren, W. F.; Postma, J. P. M.; A Consistent Empirical Potential for Water-Protein Interactions; *Biopolymers* **1984**, *23*, 1513-1518.

(42) Tang, C. Y.; Allen, H. C.; Ionic Binding of Na+ versus K+ to the Carboxylic Acid Headgroup of Palmitic Acid Monolayers Studied by Vibrational Sum Frequency Generation Spectroscopy; *J Phys Chem A* **2009**, *113*, 7383-7393.

(43) Wang, X. L.; He, Q.; Zheng, S. P.; Brezesinski, G.; Mohwald, H.; Li, J. B.; Structural changes of phospholipid monolayers caused by coupling of human serum albumin: A GIXD study at the air/water interface; *J Phys Chem B* **2004**, *108*, 14171-14177.

(44) deMeijere, K.; Brezesinski, G.; Mohwald, H.; Polyelectrolyte coupling to a charged lipid monolayer; *Macromolecules* **1997**, *30*, 2337-2342.

(45) Adams, E. M.; Allen, H. C.; Palmitic Acid on Salt Subphases and in Mixed Monolayers of Cerebrosides: Application to Atmospheric Aerosol Chemistry; *Atmosphere-Basel* **2013**, *4*, 315-336.

(46) Gidalevitz, D.; Ishitsuka, Y. J.; Muresan, A. S.; Konovalov, O.; Waring, A. J.; Lehrer, R. I.; Lee, K. Y. C.; Interaction of antimicrobial peptide protegrin with biomembranes; *P Natl Acad Sci USA* **2003**, *100*, 6302-6307.

(47) Neville, F.; Hodges, C. S.; Liu, C.; Konovalov, O.; Gidalevitz, D.; In situ characterization of lipid A interaction with antimicrobial peptides using surface X-ray scattering; *Bba-Biomembranes* **2006**, *1758*, 232-240.

(48) Kaganer, V. M.; Mohwald, H.; Dutta, P.; Structure and phase transitions in Langmuir monolayers; *Rev Mod Phys* **1999**, *71*, 779-819.

(49) Lee, H.; Kandasamy, S. K.; Larson, R. G.; Molecular dynamics simulations of the anchoring and tilting of the lung-surfactant peptide SP-B1-25 in palmitic acid monolayers; *Biophys J* **2005**, *89*, 3807-3821.

(50) Lee, K. Y. C.; Majewski, J.; Kuhl, T. L.; Howes, P. B.; Kjaer, K.; Lipp, M. M.; Waring, A. J.; Zasadzinski, J. A.; Smith, G. S.; Synchrotron X-ray study of lung surfactant-specific protein SP-B in lipid monolayers; *Biophys J* **2001**, *81*, 572-585.